Synthesis of Carbon Nanotube Materials from a Microwave Plasma

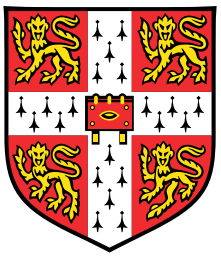

Brian Mackenzie Graves

Department of Engineering
University of Cambridge

This dissertation is submitted for the degree of
Doctor of Philosophy

Churchill College September 2019

Declaration

I hereby declare that this dissertation is the result of my own work and includes nothing which is the outcome of work done in collaboration except as declared in the Acknowledgements and specified in the text. This dissertation is not substantially the same as any other that I have submitted, or, is being concurrently submitted for any degree, diploma or other qualification at the University of Cambridge or any other University or similar institution. I further state that no substantial part of this dissertation has already been submitted, or, is being concurrently submitted for any degree, diploma or other qualification at the University of Cambridge or any other University or similar institution. This dissertation does not exceed the prescribed word limit.

Brian Mackenzie Graves
September 2019

Abstract

Synthesis of Carbon Nanotube Materials from a Microwave Plasma
Brian Graves

Carbon nanotubes (CNTs) possess numerous exceptional structural, thermal, and electrical properties that have the potential to be highly disruptive and impactful in many areas of technology. Unfortunately, synthesis methods of CNT-containing materials are often complex, expensive, and require prefabricated precursors. For CNT-based materials to experience widespread adoption, they must be produced by simple, inexpensive, and scalable means. The outcome of this work presents straightforward, fast, and industrially-relevant processes using microwave plasma for synthesis of CNT materials starting from widely-available, inexpensive precursor materials.

The plasma system has been developed to accommodate multiple gases including mixtures with hydrogen fractions of at least 50%. Stabilization has been accomplished with custom ceramic "axial" and "swirl" torches which result in low background particle generation and the ability to operate nearly indefinitely with little to no component wear. The excitation temperature and electron density of the plasma were characterized using the Boltzmann plot method with a rubidium aerosol as a tracer species.

The first application of the plasma system was to produce a metal oxide-CNT hybrid material for lithium-ion battery anodes. The process is both fully continuous and fast ($\sim$5 seconds from raw precursors to final product). The metal oxide particles are formed from readily-available coarse powders using a bespoke powder feeder and the final product was well-characterized using aerosol methods that agreed well with microscopy results. This anode material eliminated the need for a conductive additive in the electrode, and showed both good capacity recovery from high-rate cycling and promising long-term stability.

Finally, work towards a high mass throughput CNT production process is also presented. High-quality CNTs were synthesized using the axial torch. Using the swirl torch, higher hydrogen fractions could be achieved and the carbon precursor could be introduced through the front of the reactor. This led to abundant growth of long CNTs (tens of μm) with diameters of $\sim$50 nm. Given additional parameter optimization, it is likely that mass throughput could be increased further and aerogel formation may be possible. Fast, scalable processes such as those presented here may contribute to the widespread integration of CNTs in the next generation of high performance materials.

This thesis is dedicated to my parents, for their unwavering support and encouragement, and for being role models through every stage of my life.

Acknowledgements

I would first like to acknowledge my supervisor, Adam Boies, for his support, insight, wisdom, and inspiration. I have been fortunate to work under someone so enthusiastic and passionate about expanding the boundaries of knowledge. I have learned a great deal from his mentorship, both academic and otherwise, and I am grateful for everything he has invested in me.

I would also like to acknowledge others who have contributed significantly to my academic work. In particular, I would like to thank Michael De Volder, my advisor, for his invaluable expertise on the battery project. Additionally, I want to acknowledge Lee Weller for his collaboration on the temperature measurement work, as well as his regular assistance in the lab. I would also like to extend a very big thank you to Fiona Smail for her extensive help planning and troubleshooting, as well as the large amount of general support she has provided me, both inside the lab and beyond the walls of the department.

I am also appreciative of the many others who have contributed to the success of this work. I would like to thank Liron Issman for his experimental contributions to the high throughput CNT project, Andreas Kattamis for his help developing the powder feeder, Simon Engelke and Changshin Jo for the electrochemical tests, Herme Baldovi for the TEM, Filip Gökstorp for the CFD model, and Xiao Zhang for his wide experimental insight, particularly in characterization techniques. I would also like to acknowledge the friends and colleagues who have indirectly contributed to my success through camaraderie and fruitful discussion including Robert, Tyler, Christian, Jean, and Alex.

Importantly, much of this heavily experimental project would not have been possible if it weren't for the support from the workshop. In particular I would like to thank Mick Underwood and Mark Garner for their innovation and skilled craftsmanship. I was regularly in awe of the speed and precision with which they work, as well as their comprehensive understanding of the science behind the projects. Additionally, I want to acknowledge the Churchill Society of Edmonton, the Cambridge Trust, and the Natural Sciences and Engineering Research Council of Canada (NSERC) for my personal funding. I would also like to extend my gratitude to Rebecca Sawalmeh at Churchill College who has been an invaluable resource, particularly as I was settling in.

Finally, and perhaps most importantly, I want to thank my friends and family for their support, encouragement, patience, and understanding during my time in the UK. I value these relationships immensely and am thankful to have maintained so many despite the timezones and the miles. I am also thankful to have gained many new friendships and I am confident these will also stand the test of time. What an unforgettable experience this has been.

Table of contents

List of figures

List of tables

Nomenclature

Roman Symbols

A	Area, m^2; Einstein coefficient, s^{-1}
C	Empirical constant
c	Speed of light in vacuum, m s^{-1}
d	Diameter, m
D_α	Empirical constant
D_m	Mass-mobility exponent
E	Electric field strength, V m^{-1}; Energy, J
e	Electron charge, 1.602×10^{-19} C
E_H	Rydberg constant, 13.6 eV
F	Atomic fraction
f	Frequency, Hz
G	Gibbs free energy, J; Product of internal partition functions
g	Acceleration due to gravity, 9.81 m s^{-2}; Degeneracy of states
H	Enthalpy, J
h	Planck's constant, 6.626×10^{-34} J s
I	Emission intensity
k	Thermal conductivity, W m^{-1} K^{-1}; Empirical constant
k_a	Empirical constant
k_b	Boltzmann's constant, 1.38×10^{-23} J K^{-1}
L	Length / depth, m
M	Mass concentration, kg m^{-3}
m	Mass, kg; Chirality vector
$\dot{m}$	Mass flow rate, kg s^{-1}
M_m	Molar mass, kg mol^{-1}

N	Number concentration / number density, m^{-3}
n	Number of moles, mol; Chirality vector; Principal quantum number
N_a	Avogadro's number, 6.023×10^{23} mol^{-1}
$\dot{n}$	Molar flow rate, mol s^{-1}
P	Pressure, Pa
p	Power, W
Q	Volumetric flow rate, m^3 s^{-1}
r	Radius, m; Angle relative to radial vector, °
S	Entropy, J K^{-1}
T	Temperature, K
t	Time, s
u	Velocity, m s^{-1}
V	Volume, m^3; Voltage, V
x	Mass fraction
z	Angle relative to tube axis, °; Relative charge acting on electron

Greek Symbols

$< \sigma >$	Collision cross-section, m^2
ε_0	Vacuum permittivity, 8.85×10^{-12} F m^{-1}
λ	Wavelength, m
μ	Dynamic viscosity, kg m^{-1} s^{-1}
ν	Collision frequency, s^{-1}
ω	Angular frequency / angular velocity, s^{-1}
Φ	Oxygen uptake fraction
Ψ	CNT mass fraction
ρ	Density, kg m^{-3}
σ	Standard deviation

Subscripts

+	Ion
0	Standard conditions; Neutral
1	Singly charged
a	Atomic / Neutral

b	Bulk
bev	Beverloo
c	Cutoff
e	Electron
en	Electron-neutral
exc	Excitation
gas	Gas
g	Geometric
gr	Ground
i	Index
∞	Ionization
in	Inner
j	Index
k	Index
LTE	Local thermodynamic equilibrium
met	Metal
m	Mobility-equivalent
o	Orifice
out	Outer
pad	Paddle
p	Particle
pp	Primary Particle
rot	Rotational
r	Radial
s	Skin
θ	Circumferential
th	Thermal
trans	Translational
t	Terminal
vib	Vibrational
z	Axial

Acronyms / Abbreviations

CFD	Computational Fluid Dynamics
CNT	Carbon Nanotube
CPC	Condensation Particle Counter
CPMA	Centrifugal Particle Mass Analyzer
CV	Cyclic Voltammetry
DMA	Differential Mobility Analyzer
EIS	Electrochemical Impedance Spectroscopy
FEC	Fluoroethylene Carbonate
FEG	Field Emission Gun
HRTEM	High-Resolution Transmission Electron Microscopy
LIB	Lithium-Ion Battery
LPM	Litres Per Minute
LTE	Local Thermodynamic Equilibrium
LTO	Lithium Titanium Oxide
MW	Microwave
MWNT	Multi-walled Nanotube
NMP	N-Methyl-2-Pyrrolidone
OD	Outer Diameter
OES	Optical Emission Spectroscopy
PDE	Partial Differential Equation
PTFE	Polytetrafluoroethylene
PVDF	Polyvinylidene Difluoride
RBM	Radial Breathing Mode
SEI	Solid Electrolyte Interphase
SEM	Scanning Electron Microscopy
SLPM	Standard Litres Per Minute
SMPS	Scanning Mobility Particle Spectrometer
SWNT	Single-Walled Nanotube
TEM	Transmission Electron Microscopy
TGA	Thermogravimetric Analysis

UV	Ultraviolet
XPS	X-ray Photoelectron Spectroscopy

Chapter 1

Introduction

1.1 Carbon Nanotubes

Carbon nanotubes (CNTs), first discovered by Iijima [1] have the potential to revolutionize multiple areas of science by virtue of their many unique and fascinating properties, yet their widespread adoption remains elusive. They consist of one or several concentric graphitic layers of carbon wrapped into a cylindrical geometry. CNTs are typically several nanometres in diameter but can easily be grown to lengths of tens or hundreds of micrometres [2–6] resulting in aspect ratios of 10^5 and have even been grown as long as half a metre [7]. Unlike most traditional manufacturing processes, CNTs and their greater structures are produced from additive or bottom-up processes, allowing for more efficient material usage. CNTs exhibit exceptional mechanical, thermal, and electrical properties, and these properties make CNTs a leading candidate for the next generation of technology in industries such as automotive, aerospace, energy, and computing. Today, CNTs are used in some niche, high-end applications but their adoption in the mass market has been obstructed by their high production cost. For CNTs to realize their potential impact on future technologies, they must be produced with *inexpensive processes* and should be available in a *range of forms* beyond simple stand-alone powders. Once these processes and materials are developed, it is likely we will witness CNTs used in many areas of daily life.

1.1.1 Individual CNT Properties

While the majority of this thesis focuses on mass-production of CNTs for industrial use, it is first useful to understand the structure and properties of individual CNTs. The simplest type of CNT is a single-walled nanotube (SWNT). These possess the smallest diameters among CNTs, typically between 1 and 2 nm but may even be below 1 nm [8, 9]. Alternatively, CNTs may have two walls (double-walled nanotube) or

more (multi-walled nanotube, MWCNT), and diameters for the latter are typically in the range of 5 to 20 nm but can also be much larger [8]. In general, the number of walls scales with the CNT diameter.

In addition to its diameter (and particularly relevant for SWNTs), a CNT can also be characterized by the angle between its axis and the orientation of its lattice, known as chirality. The chirality of a CNT is represented as (n,m) and is expressed as the number of steps in each of the two lattice vectors required to traverse the circumference of the tube, perpendicular to its axis. If only one vector is required to traverse the tube circumference i.e. $(n,0)$, the chiral angle is 0° which is known as a "zigzag" tube. Conversely, if an equal number of lattice steps are required for each vector i.e. (n,n) then the chiral angle assumes its maximum value of 30°, known as "armchair".

Electrical properties: The chirality of a SWNT dictates its electronic properties such that when $n-m$ is evenly divisible by 3 the CNT is metallic, otherwise it is semiconducting. The bandgap of a semiconducting CNT is also determined by its chirality. Chirality is less important for MWNTs since the CNT will be metallic even if a single wall is metallic. Metallic CNTs have been shown to exhibit excellent electrical and thermal transmission properties. Electrically, they can accommodate a current density as high as 10^9 A cm^{-2} [10]. Interestingly, the electrical resistance of a perfectly crystalline CNT is approximately 12.9 kΩ regardless of its length [11].

Thermal properties: Thermally, CNTs exhibit extremely high on-axis conductivity. MWNTs have been observed to have a thermal conductivity of 3180 W m^{-1} K^{-1} [12] and SWNTs have been seen to have a conductivity of 3500 W m^{-1} K^{-1} [13]. Further, SWNTs have been theorized to have a thermal conductivity of up to 6000 W m^{-1} K^{-1} [14]. Despite these extreme values which are an order of magnitude higher than those of metals, the off-axis thermal conductivity is very low, measured by Sinha et al. [15] to be 1.52 W m^{-1} K^{-1}.

Mechanical properties: Structurally, CNTs possess similarly impressive properties. Models have predicted that a pristine SWNT should have a tensile strength of at least 100 GPa and a modulus of approximately 1 TPa [16–20], although in practice these values have been notably lower, in part since even minimal defects have been shown to decrease strength considerably [16]. A single SWNT has been found to have a tensile strength in excess of 60 GPa [21] and an elastic modulus of 915 GPa [22]. Dependencies of SWNT tensile strength on diameter and chirality have been observed, with small diameter armchair CNTs exhibiting the highest strengths [21]. MWNTs have been measured to have tensile strengths of 11 to 63 GPa [23], during which failure occurred at the outer walls. These walls had a modulus of elasticity of 270 to 950 GPa.

1.2 Existing CNT Synthesis

1.2.1 General CNT Growth Process

Catalyst particles are traditionally deposited on a substrate resulting in a batch process, but particles may also be suspended in the gas resulting in a floating catalyst process that can be continuous. Both methods are examined in the subsequent sections. Two components are required to produce CNTs: a catalyst and a carbon source. Transition metals are most commonly used as catalysts [24]. Iron and nickel are widely seen as some of the most effective metals for CNT growth and while there have been claims that nickel is the most effective of all [24], iron is more commonly used since its precursor compounds tend to be cheaper and less toxic. CNTs can grow on catalyst particles according to two mechanisms: tangential growth or perpendicular growth [25]. Tangential growth results in the CNT walls being tangent to the catalyst surface, i.e. the CNT diameter matches the catalyst particle diameter. Conversely, perpendicular growth produces a CNT with a diameter smaller than that of the catalyst, such that the angle of the CNT walls to the comparatively broad catalyst particle surface approaches 90°.

Carbon can be introduced as nearly any hydrocarbon; however there are indications that the hydrocarbon itself is not effective for growth, but instead, intermediate C_2 species containing double or triple bonds are the primary source [26, 27]. Growth will continue until either the catalyst surface is blinded by carbon or the temperature is reduced below the point where the reaction can proceed.

1.2.2 Substrate Growth

Historically, CNTs have most commonly been grown from substrates. Catalyst particles are deposited on the substrate beforehand and the substrate is then exposed to heat and a carbon-rich atmosphere where CNT growth occurs. Catalysts may be prefabricated and then deposited on the substrate [28], or they may be formed on the substrate itself [9]. It is even possible to grow CNTs on substrates without the use of a catalyst if nanofeatures can first be etched into the substrate from which the CNT growth can begin [29].

Substrate growth is often referred to as forest or carpet growth since the CNTs are typically tightly-packed and vertically-aligned similar to the growth of trees or grass. It is well understood and can be finely controlled to manipulate CNT properties and even to grow the CNTs into three-dimensional structures on the substrate [30, 31]. Nevertheless, substrate growth also exhibits several limitations. The first limitation is that when CNTs are grown via the root growth mechanism, the catalyst particle remains fixed to the substrate and mass is added to the CNT at its root. Penetration of

additional gaseous carbon through the dense network of CNTs can be difficult and the growth rate is hindered. This diffusion-limited growth restricts the maximum growth rate between 0.2 and 17 μm s^{-1} [2–5]. Moreover, additional complexity is added to the overall CNT synthesis process since the CNTs must be removed from the substrate after growth. It is for these reasons that substrate growth is not an ideal process for large-scale CNT production. Methods that are better suited to a continuous process and those that are not limited by low carbon diffusion are required to increase the production rate of CNTs to the point that the availability and cost are suitable for their widespread adoption.

1.2.3 Floating Catalyst and Continuous Throughput

Floating catalyst processes circumvent many of the limitations associated with substrate growth since they can easily be made into continuous processes. In a floating catalyst process, the catalyst nanoparticles are suspended in the carrier gas and travel through the furnace or heating medium rather than being fixed on a substrate. As a result, the particles have ample exposure to the gaseous carbon atmosphere where diffusion is fast. CNT growth from floating catalysts proceeds at a rate of at least several μm s^{-1} [32] and has even been estimated to exceed 100 μm s^{-1} [6]. Secondly, floating catalyst processes are able to operate continuously so large mass throughputs can easily be achieved. These processes often contain fewer steps than their corresponding substrate-based alternatives since the CNTs are not fixed to anything except their host catalyst particle.

1.2.4 Aerogel Formation

Even in a floating catalyst process, unique macroscopic structures can be created. One type of floating catalyst process is the Windle process [33] in which CNTs are grown in a hot-wall reactor at sufficient length and number concentration that they self assemble into a continuous network known as an aerogel. The aerogel can be removed continuously from the effluent of the reactor and wound onto a bobbin to form a fibre or a mat. In this way, bulk CNT materials can be produced in a single-step process. The Windle process is likely highly scalable since it has already been proven successful using precursor input rates that span three orders of magnitude [34]. The formation of an aerogel consists of three phases: catalyst particle production, CNT growth, and agglomeration. Each of these phases is discussed below.

Aerogel formation requires CNTs to grow as long as possible within the relatively short residence time of several seconds, and consequently, efficient catalysts must be used (most commonly iron from ferrocene). A small quantity of sulphur is also required in the catalyst chemistry, and this is normally introduced as thiophene, a

hydrocarbon ring (liquid at room temperature). Other elements in addition to sulphur have been used in this role including selenium and tellurium [35].

The steps of the Windle process are shown in Figure 1.1, along with the typical temperature profile of a hot-wall furnace. The precursor materials enter the hot zone of the reactor where they decompose, resulting in iron and sulphur vapours. As the vapour pressure reaches saturation, nanoparticles begin to nucleate. A small amount of CNT growth occurs at this point but as the particles move towards the hottest section of the furnace they vaporize [36]. It is only after passing through the peak of the temperature profile that the particles renucleate as the reactant gases cool. Therefore, a key point regarding this process is that the input size distribution (i.e. mean diameter or number concentration) of catalyst material is irrelevant as all particles evaporate. Instead, it is only the mass concentration of catalyst material entering the reactor that dictates whether or not an aerogel is able to form. The inclusion of sulphur in the catalyst chemistry increases the onset of renucleation, making the catalyst particles available farther upstream and allowing CNTs to be grown both for a longer period of time and at higher temperature. Sulphur is also thought to increase surface carbon mobility on the catalysts by lowering the surface tension of iron [34, 37].

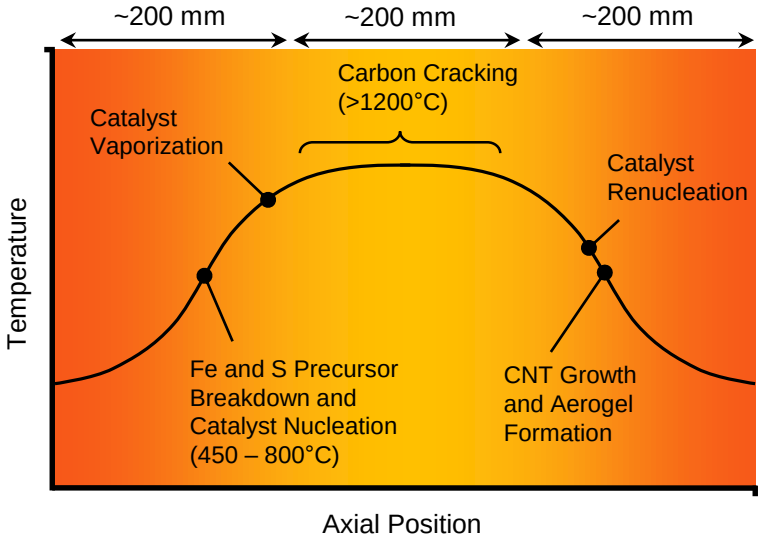

Fig. 1.1 Windle process schematic

The second phase of the process begins when carbon becomes available for CNT growth. This can either be done by physically introducing the carbon at this stage, or through the decomposition of a carbon-containing compound that is already present. Many sources of carbon have been used in this process including methane [38–41], toluene [38], xylene [14, 39], benzene [42], hexane [33, 43, 44], and mesitylene [33]. Alcohols such as methanol [41], ethanol [41, 44, 45], propanol [41], butanol [41, 46], and pentanol [41] have also been used, in addition to other oxygen containing molecules such as diethyl ether, ethylene glycol, polyethylene glycol, acetone, and

ethylformate [33, 40, 43, 44]. Importantly, it is believed that it is not the primary hydrocarbon that is responsible for the majority of CNT growth but instead secondary intermediate C_2 compounds that form as the primary hydrocarbon is cracked [26, 27]. This is another reason the majority of the CNT growth occurs near the exit of the reactor: the carbon source must pass through the hottest portion of the furnace first so it can crack and the intermediate compounds can form. The presence of these intermediate C_2 compounds increases the growth rate such that an aerogel may form.

It is also ideal if the molecules react catalytically on the surface of the particles as opposed to decomposing thermally. In this way, the temperature of the reactor must be sufficiently high so as to support this catalytic breakdown, but not so high that the molecules decompose by themselves. Thermal decomposition results in the production of amorphous carbon and soot, which contribute little to the final material's properties, yet their presence increases the material's mass. Despite the effectiveness of iron catalysts, CNT growth has been found to occur on only a small fraction of catalyst particles. Still, many of these unused catalyst particles can be contained in the CNT fibres [38]. Moreover, the conversion rate of carbon is typically only 1 to 10% [34] (although conversions for industrially-produced material have been anecdotally reported to be as high as 60 to 80%). There is also typically a compromise between higher carbon yield and decreased quality of the CNT material (higher amorphous carbon fraction). In addition to increasing this conversion rate, one of the key aims of research in CNT synthesis is to increase the reaction density (potentially by several orders of magnitude) - and thus production rate - while maintaining a high-quality end product.

As the CNTs become longer and more numerous, the frequency of their collisions increases. A collision between two individual CNTs results in reorientation and alignment as the van der Waals forces attempt to reduce surface energy of the system [47]. This reorientation process continues as additional CNTs collide, resulting in the formation of CNT bundles. With each additional CNT, the bundle becomes stiffer and more massive and if two sufficiently large bundles collide, they are not able to reorient before additional collisions occur and a network of bundles is created. It is this network that ultimately forms into the aerogel. The aerogel typically forms at a specific radius within the reactor tube [45] but there is currently no consensus on why this phenomenon occurs. It can then be removed continuously from the reactor and wound directly onto a bobbin to form a mat. Alternatively, spraying the aerogel with a volatile liquid such as acetone condenses the aerogel as the liquid evaporates and condenses the CNTs into a fibre via capillary forces. In either case, this can be done immediately upon exiting the reactor and the process can operate nearly indefinitely. The Windle process is appealing not only because it is a method of continuously producing CNTs, but also since they self-assemble directly into a useful macroscopic structure. In fact,

some CNT applications may only be possible with a pre-formed material. For example, efforts have been made to disperse powdered CNTs into a resin to form composites. However, at concentrations required to achieve a significant benefit in mechanical, electrical, or thermal properties, the viscosity increases exponentially making it nearly impossible to evenly disperse the CNTs and create a homogeneous composite [14]. This issue can be mitigated by introducing the resin to the already-formed CNT fibres or mats, since in these forms the CNTs already form a continuous network. As a result, the products of this process have the potential to satisfy unique roles in next-generation technology.

1.2.5 Bulk CNT Properties

Despite the impressive properties of CNTs, it is important to note that the values discussed so far pertain to individual tubes. When larger structures are constructed, it is often the connections between CNTs that impose the limits of material performance. Material properties for state of the art bulk CNT materials are displayed in Figure 1.2 [34] including (a) modulus of elasticity, (b) electrical conductivity, (c) tensile strength, and (d) thermal conductivity. Note the extremely low density of the aerogel itself as well as the dramatic changes in properties once formed into mats and fibres. Mechanically, direct spun mats from the Windle process exhibit elastic moduli of several GPa whereas direct spun fibres have moduli approximately an order of magnitude higher. Likewise, the strength of the CNT materials (particularly the fibres) is equal to or greater than aluminum or copper and may even be comparable to silicon. Both the specific strength and specific stiffness (N tex^{-1}) of typical fibres spun from the Windle process to date are approximately 70% of the those compared to carbon fibre and Kevlar. Nevertheless, the best performing CNT fibres have nearly double the strength and stiffness of these materials [6]. The combination of high strength and stiffness along with the high strains which bulk CNT materials can withstand (approaching 10% [48]) gives them very high toughness since a large amount of energy is required to pull CNT fibres apart due to their high surface area and considerable van der Waals forces between individual tubes. In addition, the flexibility of the CNT bundles allows the fibre to be woven or knotted, yet the material will display no loss in strength. This is highly unique for high-stiffness fibres. By comparison, most other fibres experience a reduction in strength after knotting, to only 25-50% of their unknotted values in the case of Kevlar and Dyneema, or less than 5% for carbon fibre [6, 49].

Electrically, the mats and fibres exhibit similar upper limits of conductivity although the fibres have a lower bound several orders of magnitude higher than that for the mats. At present, these materials are somewhat less conductive than aluminum and copper. Average CNT fibre electrical conductivity is between one and one and a half orders of magnitude lower than that for copper, yet it still outperforms the

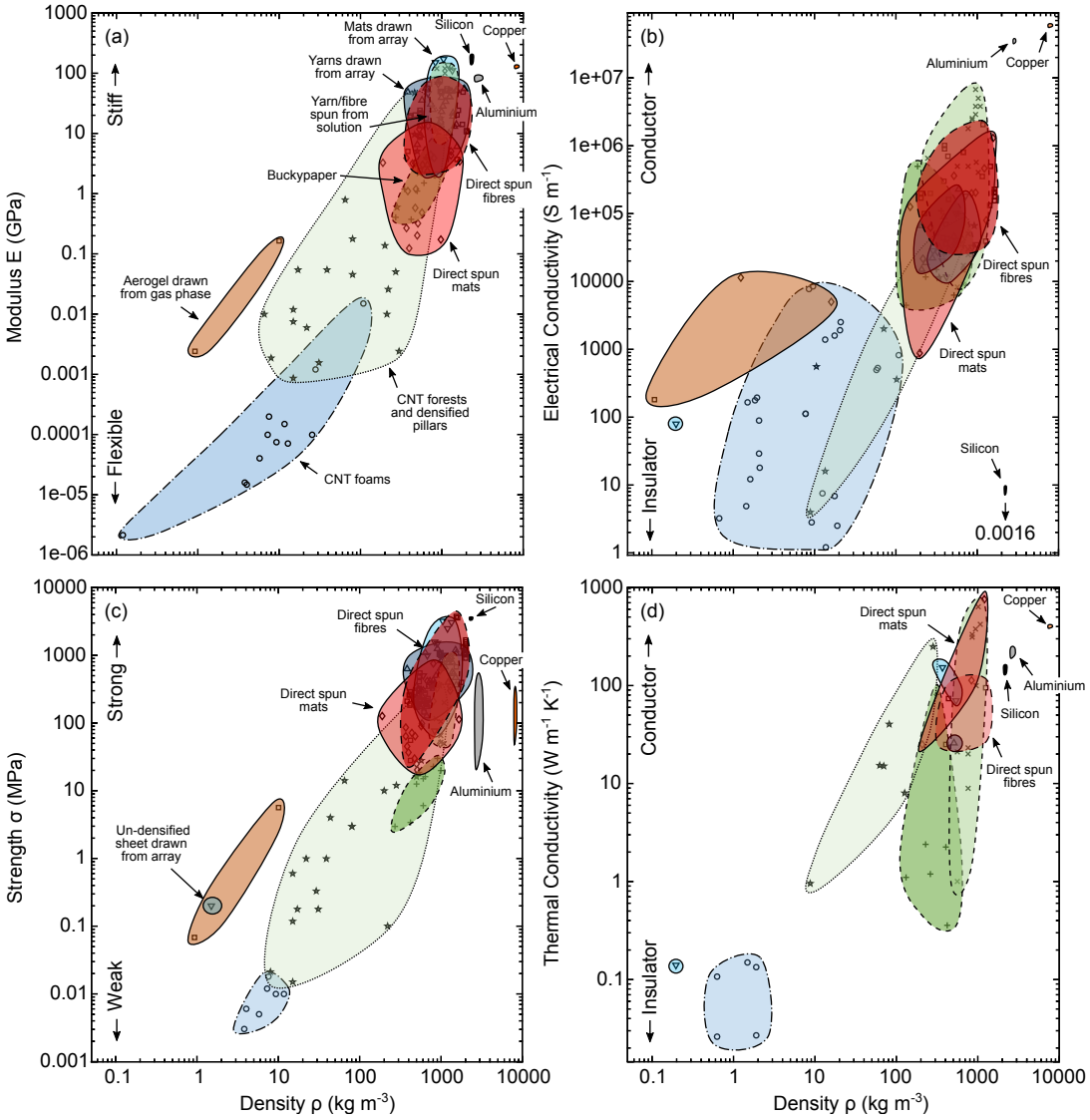

Fig. 1.2 Properties of various forms of bulk CNT materials including (a) modulus of elasticity, (b) electrical conductivity, (c) tensile strength, and (d) thermal conductivity [34]

electical conductivity of carbon fibre by nearly 20 times [6]. Thermally, the mats exhibit a higher thermal conductivity than the fibres, and have already surpassed the performance of copper. For comparison, CNT fibres are two orders of magnitude more thermally conductive than carbon fibre [6]. Note that these properties represent what is possible at present, and increases in these values are likely possible if features such as the CNT alignment or inter-CNT conductivity can be improved.

1.2.6 CNT Applications

Due to their high mechanical strength and thermal conductivity, as well as their unique electrical properties and large anisotropy, CNTs are potential candidates for a plethora of applications. Aerogel-derived CNT fibres may be used as an addition to or

replacement for carbon fibre in the next generation of composites. High performance composites may be used for automobiles, aircraft, spacecraft, defense, and any other device in which a high strength and low mass must be achieved. CNTs are already used in composites for sports equipment such as bicycle frames and tennis rackets [8]. Given the high toughness of the mats and fibres attributed to resistive forces from CNTs shearing past one another during deformation, these materials could also be used in safety components such as crash barriers, crumple zones, and body armour.

The high conductivity and low mass of metallic CNTs may allow them to be used in wires, electronics, and electromagnetic interference shielding [8] where traditional metals may be too heavy. An additional benefit is that the high thermal conductivity allows the CNTs to carry high electrical current without heating significantly, and as a result smaller wires can be used. Similarly, the CNTs can be used as a conductive additive, increasing electrical conductivity of a material even at loadings as small as 0.01 wt% [8]. Use as a conductive additive has been particularly successful for battery applications in which the CNTs are mixed with the active anode or cathode material. Conductive additives are often essential for electrodes since they dramatically increase the cell's longevity and stability, particularly at high charge and discharge rates. In certain instances CNTs can be doubly effective, also acting as the electrode's binder [50]. The use of CNTs as a battery active material additive has been sufficiently successful, resulting in these cells having been adopted in commercially-sold devices [51, 52].

The large on-axis and small off-axis thermal conductivity allows CNT materials to be used for solid-state heat conduction elements. A simple heat pipe can be constructed - again from aerogel-derived fibres or mats - where traditionally convective cooling (liquid or gas) may otherwise be required that would be both more complicated and heavier. CNTs are also used to improve thermal conduction and heat dissipation of electronic components such as amplifiers [8].

On the nanoscale, individual CNTs can be used for conductive circuits and semiconducting CNTs can be used as transistors. This could be a very high-impact application since the $\sim$1 nm diameter of SWNTs allows them to be packed tightly on a substrate. As a result, a higher transistor density than silicon may be achievable which may be a method of circumventing the slowing of Moore's law that has been observed in recent years [53, 54]. Fully-functioning processors using CNT transistors have already been proven successful [55] and their areal density and speed are likely to increase rapidly in the future.

Other unique applications of CNTs are those that employ several of their properties at once. For example, CNTs could be used in electronics in a fighter pilot's helmet and simultaneously as a structural component. Alternatively, the piezoelectric property of CNTs could be exploited by fitting them as integrated strain gauges in an aircraft wing.

They can simultaneously act as a load-bearing member while conveying information on the fitness and integrity of the wing itself.

While it is unlikely that all of these applications will be realized, the diversity in which CNT materials can be applied means that these materials have the potential to be responsible for a multitude of advances in engineering and technology, and demand for CNTs in varying forms and morphologies is likely to continue increasing. It is for this reason that innovative methods for CNT production are necessary, so CNTs can be made in *sufficiently high quantities and at sufficiently low cost* for their adoption and application to be widespread.

1.2.7 CNTs in Energy Storage Applications

One application of particular interest that is already being realized is the use of CNTs in energy storage, which includes both electrochemical cells and supercapacitors. In particular, these applications use CNTs in the electrodes and can be used either as the active material itself or as a conductive additive to enhance the performance of other materials. Given their high electrical conductivity, charge transfer within the electrode is facilitated and the device may be suitable for applications which require high charge and discharge rates such as in an electric vehicle. Moreover, the high thermal conductivity of CNTs means they are also able to effectively remove the heat generated during the charge and discharge processes. This is a vital capability for any applications that require high power since overheating can cripple the device and can pose serious safety risks to those using it.

The use of CNTs has been demonstrated in supercapacitors [56] and have been shown to provide excellent stability and a very long cycle life. In conventional electrochemical cells such as lithium-ion batteries (LIBs), CNTs have been shown to provide some degree of energy storage capacity [57] and are widely used as conductive additives as described above [58, 59]. CNTs have been particularly useful in this regard when paired with metal oxide electrodes. In the anode for example, metal oxides are an attractive choice for the next generation of batteries since they can be used as near drop-in replacements to standard and conventional anode materials like graphite and lithium titanium oxide (LTO). Metal oxide anodes offer several considerable advantages over existing anodes, with one such advantage being that they offer specific capacities that can be several times higher. They also do not suffer from lithium dendrite formation, as does graphite, which can be heavily detrimental to the cell. Additionally, metal oxide anodes also possess an ability to withstand much higher charge and discharge rates without sustaining irreversible damage. In theory, metal oxide anodes could be prevalent in the next generation of electrochemical cells and are particularly attractive considering the quickly growing market for electric vehicles.

Despite the numerous advantages of metal oxide anodes, they also possess some limitations that must be addressed. The primary limitation is that metal oxides experience a significant volume change during charging and discharging as lithium reacts chemically with the oxide. As a result, the material degrades in a process known as pulverization and the cell's capacity severely decreases. Secondly, metal oxides typically possess low electrical conductivity; it can be difficult to extract all the potential energy from the cell since portions can be electrically disconnected from the remainder of the anode.

The addition of CNTs to the metal oxides can improve both of these issues. A network of CNTs can create significant structural support to prevent pulverization and can dramatically extend the cell's cycle life and stability. Furthermore, the CNTs improve the anode's conductivity, ensuring that all metal oxide mass is contributing to energy storage. In this way, CNTs are able to render metal oxide anodes for LIBs an attractive and near-term alternative for energy storage technology. With the increasing demand for energy storage, particularly with the accelerating production of electric vehicles, methods are required that can produce these energy storage materials cost-effectively at large scale. At present, many methods described in the literature do not synthesize the materials from raw ingredients and instead combine pre-fabricated materials such as CNT or metal oxide nanopowders. The products of materials that are mixed during post production typically have poorer quality than co-synthesized products. Further, nearly all of the co-synthesis to date involves complex and time-consuming wet chemistry. While the co-synthesized products perform well, they are not economically viable when produced by these methods. Techniques are instead required which can provide *straightforward synthesis of materials using only inexpensive, raw ingredients that are readily available*.

1.3 Process Heat Addition Mechanisms

The majority of synthesis processes are conducted using hot-wall furnaces in which the reactor tube is heated externally by heating coils. The heat is then conducted from the reactor tube to the carrier gas and reagents. From this heating mechanism, several key characteristics can be associated with hot-wall furnace processes. The first is that since heat flows from the outside radially in, the reactor tube is, by definition, hotter than the carrier gas which can lead to accelerated growth of unwanted material on the tube walls. This is particularly an issue for species with high mass diffusivity since they are able to quickly diffuse through the internal tube volume. An example of this effect is observed in the aerogel formation process at the stage where ferrocene is decomposed. Since the tube wall is hotter than the carrier gas, any ferrocene near the wall will decompose first and will often deposit there. The deposits remove precursors

from the system and reduce process efficiency and in extreme cases, can block the reactor tube entirely. The process must be periodically stopped to remove the deposits. If the carrier gas were to be hotter than the tube, breakdown would occur in the gas phase first and deposits would form much more slowly.

Another effect of the outside-in heat diffusion of a hot-wall furnace is the existence of a thermal entry length. As heat diffuses radially inwards, the carrier gas is also moving further down the tube, meaning that physical space is required to bring the gas and precursors to thermal equilibrium and the required temperature. Thermal entry length is a well-characterized area of heat transfer and while this value is only on the order of centimetres for a lab-scale furnace, it approaches and may exceed one metre even at a modest industrial scale. As a result, the process and equipment (particularly the furnace) must be larger and this can add considerable cost. A more effective means of heat addition that does not rely purely on conduction would be ideal since it reduces the thermal entry length and therefore the size of the process and potentially its cost.

In addition to the thermal entry length, the size of a process is also dictated by its energy density. Those with higher energy densities can produce more material in a smaller volume. Unfortunately, the energy density of a hot-wall furnace is low. Its power input must be distributed over its entire heated volume, and for a typical lab-scale furnace the energy density is approximately 10 W cm^{-3}. *If the energy density could be increased by several orders of magnitude* a significantly smaller setup would be required for comparable mass throughput or alternatively, a comparably sized process could produce much larger masses of material.

Several technologies exist which are suitable alternatives to traditional furnaces. One such technique is heating using lasers. Extremely high temperatures can be achieved and very high heating rates are possible. Indeed, CNTs have been synthesized in this way [60]. Laser based synthesis is only feasible at small scales however, and is therefore not an industrially-relevant technique. Conversely, plasmas are used widely for large-scale materials synthesis and are an excellent candidate for CNT production. In a plasma, the energy is input into the carrier gas directly and therefore the thermal gradient is reversed in comparison to a hot-wall furnace; heat will flow from the gas to the reactor tube, and eventually to the surroundings. Precursor breakdown will occur in the plasma itself rather than on the walls. Because atmospheric pressure plasmas are small (on the order of centimetres), they exhibit a very small thermal entry length, meaning that gases and precursors are heated very quickly. This is largely because plasmas possess very high energy densities and can therefore heat their contents much faster than would be possible in a furnace. A lab-scale atmospheric pressure plasma may have an energy density of 1000 W cm^{-3} - two orders of magnitude larger than that of a furnace.

Plasma is also often characterized by large temperature gradients which can be used for greater control over a process [61]. For example, a fast reduction in temperature can be used to stop a reaction at a specific point. Also, the ion generation in plasma may allow more effective reactions between species and could mean smaller quantities of reactants can be used. Hydrogen is often added when a reducing atmosphere is required, and a plasma process could allow for a smaller molar fraction of hydrogen to be used since reactive ions are actively being generated.

Plasmas are able to produce large quantities of material with a small process footprint and can make efficient use of precursors and process gases, making them an attractive option for CNT synthesis. The work in this thesis accomplishes just that: the use of an atmospheric pressure microwave (MW) plasma for synthesis of several CNT-based materials.

1.4 Plasma

1.4.1 Plasma Definition and Examples

Plasma is often referred to as the fourth state of matter. While it is in many ways similar to a gas, plasma is comprised of charged particles including electrons and atomic and molecular ions, in addition to a fraction of neutral species. As a consequence, a plasma is responsive to electromagnetic fields which can dramatically affect its behaviour and this is its key distinguishing feature from a gas. The two most important properties when describing a plasma are its temperature and electron density. Higher electron densities can be achieved either by increasing the pressure of the system (more particles present per unit volume) or by increasing the temperature of the system. If the plasma is in equilibrium, its charge states will correspond to its temperature as described by the Saha equation. Just as an increase in temperature corresponds to atoms possessing more kinetic energy, so too does it correspond to electrons with more energy. As such, increasing temperature increases the fraction of electrons with enough energy to occupy higher energy states within an atom as well as the fraction that can be liberated from their host atom altogether; increasing the charge fraction of the population. In this way, the ion charge states can include not only neutral and +1 but also any number beyond this, provided the atom still has electrons that can be liberated. The general Saha equation is:

$$\frac{N_{k+1}}{N_k} = \frac{2}{N_\mathrm{e}}\left(\frac{2\pi m_\mathrm{e} k_\mathrm{b} T}{h^2}\right)^{\frac{3}{2}} \frac{G_{k+1}}{G_k} \exp\left(-\frac{E_{\infty,k+1} - E_{\infty,k}}{k_\mathrm{b} T}\right), \tag{1.1}$$

where N_{k+1} and N_k are the number densities of the $(k+1)^{\mathrm{th}}$ and k^{th} charge state respectively, N_e is electron density, m_e is electron mass, k_b is Boltzmann's constant, T

is temperature, h is Planck's constant, G is the product of internal partition functions, and E_∞ is ionization energy required to reach a given charge state. In this work however, the plasma is not energetic enough to produce significant quantities of charge states beyond +1 (discussed further in Chapter 4) and therefore the Saha equation can be simplified to include only the neutral species (N_0) and singly ionized species (N_1). Further, in this case since each +1 ion corresponds to one electron, $N_1 = N_e$. This equation can be useful for determining the electron density from a known temperature, and this is performed in Chapter 4.

Plasmas occur naturally in a variety of forms in nature under a wide range of conditions. Flames are a type of low energy plasma with small charge fractions and relatively low temperatures. Lightning is an example of a very high energy, transient plasma. Gas molecules in the air are heated to tens of thousands of Kelvin (accompanied by very high electron densities) as millions of amps are discharged. Conversely, another atmospheric plasma phenomenon - the aurora caused by collisions between energetic particles emitted from the sun and gas molecules at high altitude - shows very low concentrations of ionized particles. Plasmas are seen commonly beyond Earth as well, with the majority of the matter in stars being believed to exist as plasma. Conditions vary widely even within a given star. In the case of the sun, the surface is a relatively cool 5800 K while its corona region is lower density but much higher energy at around one million Kelvin. Further still, the stellar core where the fusion reactions occur is extremely dense, highly charged and extremely hot (15 million K). Despite the fact that all these phenomena are classified as plasmas, their behaviour and properties are undeniably eclectic.

1.4.2 Plasma Generation Mechanisms

Plasma can be generated in many ways, all of which include the application of an electromagnetic field. In many senses the simplest method of plasma generation is with a DC current to produce a sustained arc, known as arc discharge. Similar to any naturally occurring arc such as lightning, electrons are accelerated in the electric field and as they travel between electrodes, they collide with neutral particles and may ionize them. These plasmas can be very hot and larger systems may require hundreds of amps [62]. Nevertheless, basic operation is relatively straightforward since ultimately all that is required is a potential difference. One particular drawback of arc discharge systems is that since the plasma is in contact with the electrodes, their ablation can introduce impurities into the system and also the process must also be stopped periodically to replace worn electrodes.

Alternatively, oscillating electromagnetic fields can be used. Radio frequency (RF) or inductively coupled plasmas do not require direct contact between their electrodes and the plasma. Instead, plasma is generated using an oscillating field produced by

a conductive coil positioned around the reactor tube. These plasmas also tend to be very hot ($\sim$10 000 K) but have the benefit of naturally centralizing in their reactor tube and therefore do not contaminate the flow with wall impurities and do not need stabilization from particular gas flow patterns. RF systems are often limited in the gas compositions they can process, and may only accommodate $\sim$5% H_2 by volume which is often not sufficient for good quality CNT synthesis. Note that all gas fractions in this thesis are on a volume basis.

Microwave plasmas are similar to RF systems in that they are powered by an oscillating electromagnetic field; however, the means by which this is accomplished is notably different. Rather than an induction coil, microwave systems typically position the reactor tube inside a perpendicular cavity containing the microwave field. These systems are known as surface wave plasma systems. In comparison to RF plasmas, microwave plasmas are slightly cooler and require a torch or well-controlled gas flow to stabilize the plasma in the tube centre, although they are able to operate with a wide range of gas mixtures (e.g. beyond 50% H_2) and may be significantly less expensive than RF plasma systems. In both RF and microwave systems, the gas molecules are not directly ionized by the electromagnetic energy but are instead ionized from collisions with free electrons that are accelerated in the electromagnetic field. This mechanism is discussed in more detail in Chapter 3.

Plasmas have been used previously to synthesize CNTs, and much of this work is examined in detail in section 2.4 of Chapter 2. The plasmas are often employed for substrate growth, and while good quality CNTs can be produced this way, this method is likely not scalable since it typically occurs at low pressure and as discussed above, substrate growth is most commonly a batch process. CNTs have also been grown from floating catalyst plasma processes, and given the high temperatures, solid precursors such as carbon black [63] have been used in addition to more traditional liquid and gaseous precursors. Mass throughputs for these processes can be high [63], although to date the quality of the CNT material is typically low. This is largely due to the fact that precursors are passed directly through the plasma and this results in the formation of soot or other undesirable morphologies such as "stacked cup" CNTs, nano-necklaces, or onion-like structures [64, 65]. Scalable plasma production of high-quality CNTs is challenging since the large temperature gradients require precise introduction of carbon to the system. Injection into an area that is too hot results in thermal decomposition and leads to a low-quality product, whereas injection into an area that is too cool will not allow activation of the carbon at all, and no CNT growth will occur. Despite the difficulty, the advantages of plasma synthesis are considerable and thus it is worth investing effort to overcome the challenges.

1.5 Aims

This section has provided a brief overview of CNTs and their abilities, their present and future applications, and the means by which they can be synthesized. It has also identified the shortfalls of current production, particularly that furnaces possess low energy densities, are limited in the types of precursors they can accept, and many of their processes are not continuous. Opportunities for improvements in scalable CNT synthesis have also been presented, particularly highlighting that plasma-based processes are intriguing alternatives to furnace-based production. This is because plasmas have energy densities that can be up to two orders of magnitude larger than that of a furnace, are capable of operating continuously, and can accept a wide range of precursors including solids. Consequently, these types of plasma processes may be capable of cost-effectively producing large throughputs of CNT material. In doing so, they may increase the availability of CNTs in a range of forms and make them a viable option for an array of future applications. At this point, the broad aims of this work can be defined.

The overarching long-term goal of this project is to produce CNT materials using new scalable processes. Numerous existing CNT synthesis techniques are suitable for a lab scale, yet many of these processes are not viable for larger mass throughputs. So while scientifically valuable, they are often not economically relevant. For a process to be capable of synthesizing CNT materials cost-effectively at large scale, it should be able to operate continuously and should maximize its reactor density since a smaller footprint will translate into a significantly cheaper process. Specifically, reactor density should be increased by one to two orders of magnitude relative to a standard tube furnace. The new processes should also contain the fewest steps possible and be compatible with precursor materials which are inexpensive and widely available. Plasma processes are good candidates since they fulfil these criteria. Therefore, the immediate aim is to develop plasma-based processes which are able to produce multiple CNT products with precursors and conditions which could be effectively scaled-up to quantities that would be economically relevant.

Chapter 2

Literature Review

2.1 Introduction

This section discusses the state of the literature relevant to the developments presented in this thesis. The literature can be broadly divided into two categories: plasma characterization and CNT synthesis. The plasma characterization section focuses primarily on determination of the two most meaningful properties, namely temperature and electron density. Quantification of these two properties provides a good overall understanding of the plasma since additional properties such as the ionization fraction can be inferred. Plasma temperature in particular is an important value since this is ultimately responsible for driving the synthesis processes described in Chapters 5 and 6.

The CNT synthesis literature can also be divided in two categories, each concerning a material or process developed here. Specifically, a process for production of a CNT-metal oxide material for battery anodes has been developed and literature presented here explores the state of the art in CNT-metal oxide anodes. Further, the plasma system has also been used to develop a process for high-mass throughput of CNTs for a range of applications. The existing field of plasma-synthesized CNTs is also examined. In exploring this existing literature, gaps can be identified which present opportunities for further development. This thesis aims to exploit these opportunities in a way that results in valuable contributions to the academic community and produce knowledge that can someday be adopted by industry to maximize the positive impact of these processes on society.

2.2 Measurement of Plasma Temperature and Electron Density

One of the reasons plasma processes are used for large-scale synthesis of carbon nanotubes and other nanomaterials [66] is because their temperature is often extremely high and can allow for vaporization of precursors that would otherwise not be possible. Additionally, their elevated ion concentrations can facilitate chemical processes involved in chemical vapour deposition or cleaning. For these applications to be effective, the plasma must first be quantified and characterized in terms of its temperature and ion/electron concentrations.

Plasma temperature itself is in fact, a nuanced concept. Most plasmas are not in complete thermodynamic equilibrium and as a result, some species may exist at different temperatures than others. For example, while not in equilibrium, the vibrational, rotational, and translational temperatures of gas molecules could all be different values. Free electrons and positive ions also exist in a plasma and have their own respective temperatures. Finally, the plasma's excitation temperature represents the temperature (at local thermodynamic equilibrium or "LTE") that corresponds to the relative ratios of electron states in a Boltzmann temperature distribution.

In most cases, electrons are more responsive to the method of energy input than are atoms, molecules, or ions. For example, electrons are the species most easily accelerated between electrodes in an arc discharge plasma and the most responsive to the microwave field in a surface wave plasma. As a result, the electron temperature will normally be higher than the gas temperature(s). Excitation temperature should be bounded by electron temperature and gas temperature; therefore, the following temperature inequality holds for most plasmas [67, 68]:

$$T_{\mathrm{e}} \geq T_{\mathrm{exc}} \geq T_{\mathrm{vib}} \geq T_{\mathrm{rot}} \approx T_{\mathrm{tra}} \approx T_{\mathrm{gas}} \ , \tag{2.1}$$

where T_{e} is electron temperature, T_{exc} is excitation temperature, T_{vib} is vibrational temperature, T_{rot} is rotational temperature, T_{tra} is translational temperature, and T_{gas} is the gas temperature - a less nuanced term for the temperature of atoms and molecules in the system. In perfect thermodynamic equilibrium, the net energy transfer between the populations of electrons, ions, and neutrals is zero. Consequently, the respective temperatures for these species are all equal. This is known as a thermal plasma. Conversely, plasmas that possess large differences in population temperatures - typically more than an order of magnitude - are described as nonthermal plasmas. Microwave plasmas tend to be close to but not completely thermal since their electron temperatures are commonly several times higher than their gas temperatures [67, 69–

71]. For the remainder of this work, unless otherwise stated the plasmas in question are taken to be nearly thermal.

Plasma temperature - particularly T_{gas} - can exist within a wide range, even at ambient temperature [72], or near absolute zero [73]. Conversely, gas temperature has also been observed to surpass 10 000 K (14 500 K in the case of Snyder et al. [62]), and can even exceed 10 million K in extreme environments such as those suited for nuclear fusion [74, 75].

Various physical techniques exist to measure plasma temperature, but this is only feasible when the rate of heat transfer to the probe is not too severe. Low to moderate heat transfer is observed for low pressure plasmas since the thermal conductivity of the plasma is lower than that at atmospheric pressure. For atmospheric pressure plasmas, physical measurements may be possible if the plasma gas temperature is below $\sim$2000 K [72, 73, 76, 77]. Electron temperature can be measured with a Langmuir probe [78] although again, the plasma pressure must be well below atmospheric pressure. High energy-density systems including those at atmospheric pressure must be assessed using minimally-invasive techniques such as optical emission spectroscopy (OES). Gas temperatures of many plasma applications have been studied extensively with OES techniques including van der Waals broadening [79–81], Rayleigh scattering [82, 83], and by comparison to theoretical models [67, 69, 77, 83–90].

Excitation temperature is a useful plasma property since it represents an upper limit on gas temperature and a lower limit on electron temperature. As the definition of excitation temperature is based on the relative populations of electrons in various states of the atoms, the Boltzmann plot method is frequently employed. This technique involves comparing the intensities of emission lines at various electron energy levels and correlating this with a temperature value. A requirement of the Boltzmann plot method is that the transitions considered are in LTE. An example plot is presented in Figure 2.1. The natural logarithm of emission line intensity (normalized by wavelength and transition strength) is plotted against the energy of the upper state of the given transition. The slope of the resulting regression line is then equal to $-1/\left(k_{\text{b}}T_{\text{exc}}\right)$, where k_{b} is Boltzmann's constant. This method is described in more detail in Chapter 4.

It is common to apply the Boltzmann plot method to emission lines of the plasma gas itself, most commonly argon [67, 70, 78, 90–93], although other gases have been used as well including helium [67, 94], oxygen [69], hydrogen [95–97], mercury [68], and xenon [98]. Other atomic species such as iron [71, 99], lead [94], magnesium [97], zinc [97], palladium [100], and titanium [89] have also been introduced into the plasma, and the excitation temperature has been measured from these species rather than from the major plasma medium itself. The electron number density can be measured using Stark broadening [67, 70, 71, 79, 82, 87–89, 92, 101], often of hydrogen lines. This requires a high-end spectrometer since fine resolution in wavelength is required to

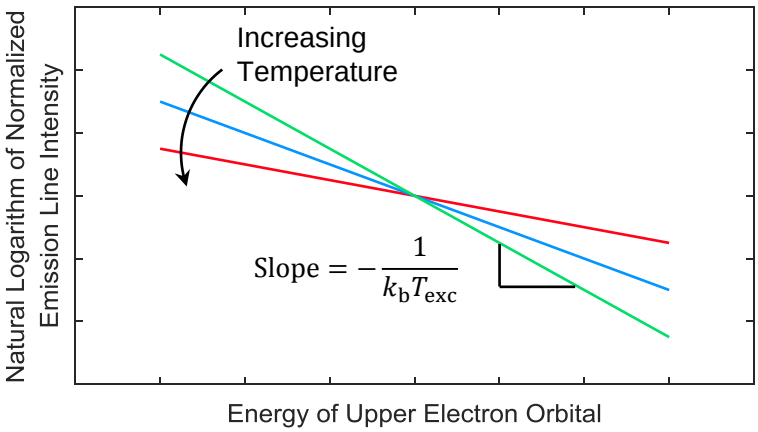

Fig. 2.1 Example Boltzmann plot

accurately quantify the emission line width. Nevertheless, the advantage of Stark broadening is that it provides a direct and independent measurement of electron density. Conversely, using a calculated temperature value, the Saha equation can be used to compute the corresponding electron number density [69, 71]. This approach is straightforward since it does not require additional measurement, though its results will only be meaningful if the plasma is in LTE. Therefore, if using the Saha equation to determine electron density, the LTE condition must then be verified.

The use of group I elements as "tracer" species for OES is attractive since these elements produce relatively simple emission spectra because they possess only a single electron in their outer electron shell and consequently their emission spectra are very well characterised. Rubidium, in particular, has been used in vapour cells along with laser-based techniques to extract temperature values up to 350°C with very high accuracy [102–105]. Moreover, introduction of rubidium into a plasma is straightforward since many of its compounds are soluble and can be spray-dried. Some studies have in fact introduced group I elements into plasma environments. Yubero et al. [81] measured gas temperature of an atmospheric pressure microwave plasma using van der Waals broadening of a sodium emission line sourced from impurities in the quartz tube wall. The presence and effects of other group I elements in plasma has been reported as well. Bings et al. [71] introduced both lithium and caesium into their plasma and determined that the presence of these metals decreased excitation temperature by 300 - 700 K and 1000 - 1500 K respectively, likely due to the low ionization energy of group I elements functioning as a latent heat sink. Conversely, Jovicevic et al. [106] performed a two dimensional temperature map and determined that adding potassium (in the form of KCl) increased the highest observed excitation temperature by 1300 K.

In this work the excitation temperature of an atmospheric pressure microwave plasma is measured using the Boltzmann plot method for rubidium and these results

are compared to similar measurements of the plasma gas itself, such as argon. The Boltzmann plot method exhibits some disadvantages such as the need for LTE and a low time resolution (at best on the order of milliseconds). Despite these limitations, the Boltzmann plot method is an attractive technique for plasma temperature measurement because it does not require complicated computer models or an array of high-end optics, and instead can be performed with a simple optical probe and spectrometer for less than £1000. Naturally, this gives the Boltzmann plot method a small experimental footprint and the potential to be used widely in labs and industrial processes. Despite the fact that some literature suggests that the presence of a group I element in the plasma can affect the plasma temperature, the addition of a tracer species such as rubidium allows measurement of non-monatomic plasmas in which this technique is normally not easily applied. This is particularly relevant to the body of work presented here since the majority of the processes use nitrogen (a diatomic gas) which possesses a broad spectrum rather than discrete lines, making the Boltzmann plot method difficult to employ.

2.3 CNT-Metal Oxide Anodes for Lithium-Ion Batteries

Traditional manufacturing techniques for energy storage materials are often slow and complex. Wet chemistry approaches can contain an extensive series of steps and regularly require hours or even days to execute. Also, many existing energy storage material synthesis processes begin with precursors that are challenging and costly to produce such as nanoparticles or CNTs. Nevertheless, the use of structured combinations of nanomaterials within energy storage devices enables fast diffusion rates through high surface areas, control of crystal size, unique chemistries and structures that make simultaneous use of conductive and insulating materials. Unfortunately, given the added complexity of their fabrication, most processes that include nanomaterials such as CNTs in energy storage materials begin with those that are prefabricated. Components that are fabricated separately and later mixed provide weak interactions between the active materials and those included for conductive enhancements. Further, this multi-step supply chain places limits on the lower bound of the final product's price and may inhibit its widespread adoption in the consumer market.

Optimization of anode design for enhanced LIBs is paramount for automotive, electronic, and energy storage applications since the anode is one of the primary drivers of the cell's total capacity, multi-cycle stability, as well as the maximum charge and discharge rates. A schematic of a typical LIB is shown in Figure 2.2a. Upon charging, lithium ions move within the electrolyte and through the separator towards the anode, where they are stored. Storage can occur through three mechanisms: (1) intercalation

in which lithium is deposited within the spaces of the active material lattice, (2) an alloying reaction with the active material, or (3) a conversion reaction where lithium reduces the active material. The metal oxide active material used in this work employs the conversion mechanism.

The anode itself (shown schematically in Figure 2.2b) is comprised of a current collector - usually copper - on which the active material for lithium storage is situated. The active material is typically mixed with a conductive additive (e.g. CNTs) and the mixture is held together using a polymer binder. The amount of lithium contained by the anode dictates the upper limit of the battery's energy storage capacity. The maximum rate at which the lithium can be added to or removed from the anode determines the limiting rates for charging and discharging the cell, and it is the chemical and structural stability of the anode which contribute to the long-term cyclability of the battery. As such, the anode has a significant influence on the utility of the battery and its potential uses in the wider consumer market.

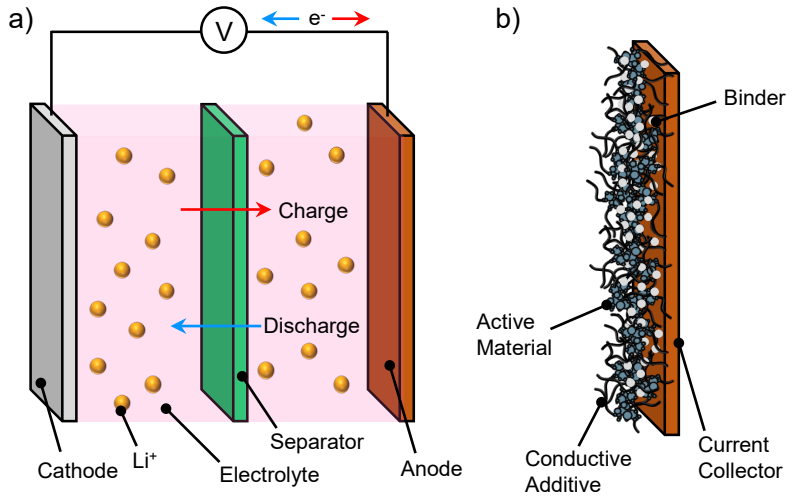

Fig. 2.2 Electrochemical schematics including (a) lithium-ion cell and (b) anode microstructure

Recent advancements in metal oxide conversion anodes have shown that higher capacities can be achieved for metal oxides, e.g. 926 mAh g^{-1} for Fe_3O_4 and 1008 mAh g^{-1} for Fe_2O_3, when compared to graphite and lithium titanium oxide which are 372 mAh g^{-1} and 175 mAh g^{-1} respectively. It should be noted that metal oxides are not prone to the lithium dendrite formation which degrades graphite anode performance. Existing studies on metal oxide anodes have confirmed their effectiveness as a near drop-in replacement for conventional LIB formulations. Reported energy densities can often be in excess of 800 mAh g^{-1} [50, 58, 59, 107–110], with studies demonstrating that cyclability and voltage hysteresis remain challenging. Full cell LIBs with metal oxide anodes have been matched to numerous typical cathodic chemistries, including $LiCoO_2$ [111] and $LiFePO_4$ [112, 113] and have achieved full

cell capacities of 360 mAh g^{-1} [113] to 400 mAh g^{-1} [111]. Despite exhibiting multiple improvements over graphitic anodes, metal oxide anodes originally had limited use due to the volume expansion and contraction experienced during a charge/discharge cycle. More recent work has shown that reduction in particle size and the incorporation of conductive and stabilizing elements (such as carbon coatings or CNTs) can dramatically reduce this effect [58, 59].

The morphology of multiple carbon nanotubes grown radially from a nanoparticle surface (known informally as carbon nanotube sea urchins) was described in a form most similar to the work presented here by H. Kim et al. [114] and within our lab by de La Verpilliere et al. [115]. Sea urchins are formed from bi-metallic cores containing catalyst and non-catalyst metals, in this case iron and aluminum respectively. Within the nanoparticle core, islands of reduced metal exist within an aluminum or iron/aluminum alloy matrix. These catalyst sites grow CNTs (as seen in Figure 2.3a) and can be present in tens and even hundreds across the surface of a given core particle.

The sea urchin-like morphology has been presented in other studies as well using various core compositions. Carbon cores have been synthesized by several studies, including Chuang et al. [116] who created mesoporous carbon particles seeded with iron catalyst particles. Kuo et al. [117] also used mesoporous carbon cores but seeded them with platinum particles for use as a fuel cell catalyst. Bozlar et al. [118] grew CNTs on micrometre-sized alumina particles using ferrocene as the catalyst. They determined that adding as little as 0.15 wt% of this material to a polymer increased its thermal conductivity by 130%. Other core materials include nickel-aluminum [119], copper oxide-aluminum [120], boron in combination with aluminum, silicon, lanthanum, yttrium, or gadolinium [121], stainless steel [122], and silica [123].

While the sea urchin morphology has not previously been tested in LIBs, similar CNT-metal oxide morphologies have been reported for this application, particularly for anodes. Collections of metal oxide subunits such as nanoparticles and nanorods mixed with CNTs have proven to be effective anodes. Jia et al. [107] synthesized Fe_3O_4 crystals coated in carbon and mixed with CNTs (Figure 2.3b). With this material they achieved a reversible capacity of 994 mAh g^{-1} at 0.16 C, and were able to construct the anode without a binder (e.g. polyvinylidene difluoride, PVDF). In fact, they found that the material's performance improved when no binder was used. Note that the "C" notation is a method of representing charge rate with respect to the cell's total capacity. It represents the number of times the cell is charged in one hour (e.g. 2 C means the cell is brought from empty to full in 30 minutes). Ban et al. [50] created a material comprised of Fe_3O_4 nanorods on a single-walled CNT web that did not require a binder (Figure 2.3c). They reported excellent cyclability and a capacity of over 1000 mAh g^{-1} at 1 C. The material also performed well at high current rates, exhibiting a capacity of 600 mAh g^{-1} at 10 C. Yang et al. [59] synthesized $ZnFe_2O_4$

particles from zinc nitrate and iron sulphate (Figure 2.3d). Their material consisted of agglomerates of primary particles 10-50 nm in diameter mixed with CNTs. They achieved a capacity of 1278 mAh g^{-1} after 200 cycles at 0.16 C, and scanning electron microscopy (SEM) images show the CNTs prevent pulverization of the material from cycling compared to pure $ZnFe_2O_4$.

Material morphologies have also been reported that contain metal oxides mixed with CNTs to form larger structural units such as spheres or polyhedra. SnO_2 spheres (Figure 2.3e) were synthesized by Choi et al. [108] both with and without the encapsulation of CNTs. They were able to modulate the porosity by including (and later decomposing) smaller polystyrene spheres. They determined that the material with the highest capacity and longest cycle life consisted of porous spheres with CNTs. Similarly, Sun et al. [58] synthesized micrometre-sized spherical agglomerates of MnO mixed with CNTs. Without the inclusion of CNTs, the pure MnO experienced a decrease of approximately 50% in capacity over 100 cycles (600 to 300 mAh g^{-1}), yet performance was stabilized when CNTs were included (from 700 mAh g^{-1} to 600 mAh g^{-1}). Co_3O_4 polyhedra particles were synthesized by Huang et al. [109] by depositing cobalt ions onto CNTs, then stimulating cobalt deposition to grow larger particles, often encapsulating multiple CNTs (Figure 2.3f). They were able to achieve a reversible capacity of 813 mAh g^{-1} at a charging rate of 0.12 C and 514 mAh g^{-1} at 1.94 C. Ru et al. [124] synthesized large (tens of micrometres) $ZnCo_2O_4$ polyhedra from zinc and cobalt nitrate solutions, and mixed them with CNTs (Figure 2.3g). The material's capacity was stable when CNTs were included but continuously decreased when pure $ZnCo_2O_4$ was used. They reported a capacity of 865 mAh g^{-1} after 150 cycles at 0.12 C, compared to approximately 530 mAh g^{-1} for the same conditions when CNTs were not included. The electrochemical performance of the preceding materials is summarized in Table 2.1.

Rather than multiple CNTs anchored to a given metal oxide particle, anode materials which are comprised of CNTs coated in metal oxide nanoparticles have also been synthesized (Figure 2.3h). This has been done using iron [56], manganese [110, 125, 126], tin [127, 128], zinc [129], and nickel [130]. Bimetallic particles have also been used, including iron and manganese [131], iron and cobalt [132], manganese and cobalt [133], and manganese with zinc [134]. In comparison to the anode materials examined above, a faster and more scalable synthesis approach is presented in Chapter 5. The hierarchical CNT-metal oxide anode product can be fabricated in approximately five seconds from inexpensive and readily-available precursors and shows promising electrochemical performance.

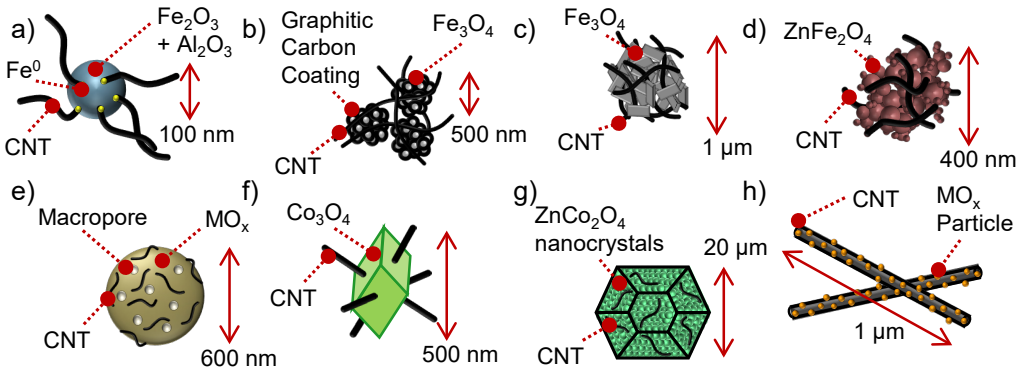

Fig. 2.3 Previously synthesized hybrid CNT architectures for energy storage, where (a) is the existing "sea urchin" morphology [114, 115], (b) Fe_3O_4 crystals coated in carbon and mixed with CNTs [107], (c) Fe_3O_4 nanorods embedded in a CNT web [50], (d) $ZnFe_2O_4$ particles agglomerated with CNTs [59], (e) CNTs encapsulated in porous or nonporous SnO_2 or MnO spheres [58, 108], (f) Co_3O_4 polyhedra grown on a CNT network [109], (g) $ZnCo_2O_4$ nanocrystals assembled into polyhedra and mixed with CNTs [124], and (h) CNTs decorated with metal oxide nanoparticles [56, 110, 125–134]

Table 2.1 Electrochemical performance of CNT sea urchin-like materials

Label (Figure 2.3)	Metal Oxide	Capacity (mAh g^{-1})	Charge Rate (C Rate)	Reference
a	Fe_2O_3, Al_2O_3	N/A	N/A	[114, 115]
b	Fe_3O_4	994	0.16	[107]
c	Fe_3O_4	1000 600	1 10	[50]
d	$ZnFe_2O_4$	1278	0.16	[59]
e	SnO_2 MnO	1108 600	1.3 0.22	[108] [58]
f	Co_3O_4	813 514	0.12 1.94	[109]
g	$ZnCo_2O_4$	865	0.12	[124]

2.4 High Throughput CNT Growth from Plasma Processes

Plasma-based synthesis of CNTs is a broad field. To organize the literature, several classifications can be applied. These include (1) the heat input method, and more specifically, the type of plasma generation method used, (2) the CNT growth method (substrate versus floating catalyst), (3) catalyst composition, (4) carbon precursor, and (5) the presence of sulphur. In relation to the research conducted here, previous studies can be categorized using a Venn diagram (Figure 2.4) with categories encompassing RF or microwave plasma, similar carbon/catalyst precursors to those used here (i.e. iron and/or sulphur), and floating catalyst work. The first group to be examined is that which employs RF or microwave plasmas alongside many of the same reactants used here, but does not function using a floating catalyst (region I in Figure 2.4). It is here that substrate growth is classified. Various substrate and catalyst materials have been investigated including silicon substrates with iron catalyst particles [135, 136], as is common with substrate-based CNT synthesis. Watanabe et al. [24] used a plethora of catalyst materials deposited on a metal plate. They examined the effects of nickel, iron, cobalt, molybdenum, and lanthanum hexaboride as catalysts, and determined that nickel was the most effective because of its high activity and low CNT defect rate. Combining nickel with the other catalysts increased the activity of these materials. CNTs have also been grown on profiled silicon substrates without the use of a catalyst [29]. Malesevic et al. [137] used acetylene with a nickel catalyst to grow CNTs and carbon nanowalls on a substrate simultaneously. Nickel substrates were also used by Weng et al. [138] in conjunction with aluminum. In comparison to iron and aluminum substrates, the authors were able to grow CNTs at a lower temperature using nickel (500°C versus 550°C). As discussed previously, growth can be slow due to limitations of gaseous carbon diffusion and catalyst deactivation [139]. Removal of the CNTs from the substrate as well as integration of the CNTs into the desired material can prove challenging. As such, growth of CNTs on substrates is not seen as a viable method for scaled-up, high throughput production.

The second division of literature to be explored is that which uses reactants which are similar to those used in this study, as well as a floating catalyst (region II in Figure 2.4). Where these studies differ from the study presented here is in the heat addition method: RF or microwave plasmas are not used. Instead, other plasma mechanisms such as arc discharge have been commonly used with floating catalysts. Arc discharge processes often include other potentially unwanted products in addition to CNTs. Okuno et al. [64] used iron and nickel catalysts along with carbon black in arc discharge plasma to form "stacked cup" CNTs and nano-necklaces. Also with a nickel catalyst, Choi et al. [140] noted an excessive amount of metal present in their

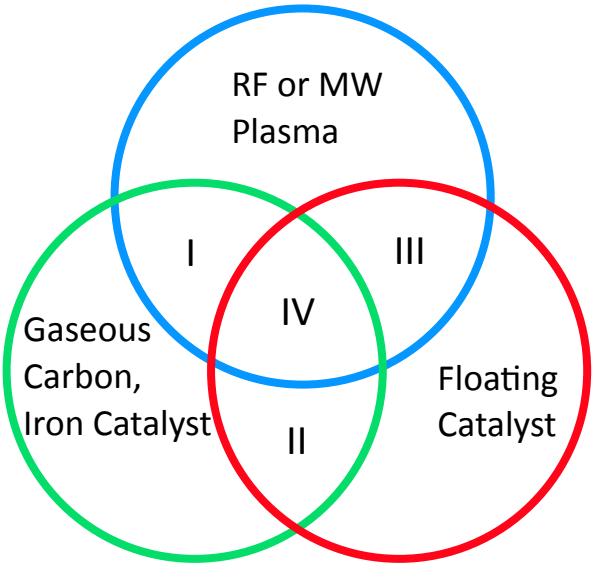

Fig. 2.4 Venn diagram of features used in plasma production of CNTs

CNT product. As would be expected, they determined that more CNTs are produced in a hydrogen environment compared to an argon environment. Arc discharge plasma has also been used without a catalyst by employing electrodes comprised of materials needed for CNT synthesis such as graphite or diamond powder [141, 142].

Previous studies also exist which use RF or microwave plasmas for floating catalyst CNT production, although the precursors are often different from those used in this work (region III in Figure 2.4). Studies have created models of carbon black with a nickel catalyst in RF plasma [143, 144] which have been compared to experiments with similar conditions [61]. Shahverdi and Soucy [65] examined the effects of adding counterflow ammonia injection and determined that it increased the nitrogen content of the CNTs by as much as one order of magnitude. Morphological changes to the CNTs were also observed such as the presence of onion-like and planar carbon structures. Like hydrogen, ammonia is also a known etching gas and can increase the purity and quality of the CNTs [29]. Kim et al. [63] were able to produce a carbonaceous product at a rate of 100 g h^{-1} which had a SWNT content of 40 wt% using yttrium oxide or cerium oxide in a mixture of nickel and cobalt as catalysts. Similarly, other studies [145–148] also used nickel, cobalt, and yttrium oxide catalysts. Hekmat-Ardakan et al. [148] noted that an increase in sulphur content improved the structural quality of the CNTs. They suggest that the sulphur reacts with the yttrium to form Y_2S_3, which is an exothermic reaction and hence more energy is present which can be used for CNT formation. Despite this claim, the formation of Y_2S_3 is likely not be the dominating reason as to why sulphur is beneficial in CNT production. Because these reactants have been subjected to temperatures of several thousand Kelvin in the plasma, it seems unlikely that a small amount of additional heat released from an

exothermic reaction would be significant enough to affect the CNT production rate or quality. Indeed, in their study the rate of heat release from Y_2S_3 formation is ~ 5000 times lower than the power input from their plasma. Similar techniques have also been used to synthesize materials other than CNTs, such as boron nitride nanotubes [149].

The studies listed above all have some relevance and similarity in relation to the work to be conducted here, but each differs in at least one way. The most relevant studies are those located in the centre of the Venn diagram (region IV), and feature similar precursors to this work in addition to RF or microwawe plasma in a floating catalyst process. Smiljanic et al. [150] used ethylene as the carbon precursor and ferrocene as the catalyst precursor with a microwave plasma. While their experiments were conducted in an argon atmosphere, they too note that the addition of hydrogen is important for the growth of CNTs. Downstream of the plasma system was a tube furnace, maintained at 1300 K, which prevents large temperature gradients they claim may contribute to amorphous carbon formation. They produced SWNTs with diameters between 0.9 and 1.5 nm, and bundles of nanotubes with diameters of approximately 20 nm which were at least 3 μm long.

Also using a microwave plasma, Zajíčková et al. [151] used methane and iron pentacarbonyl in an argon and hydrogen atmosphere to synthesize iron oxide nanoparticles and CNTs. The iron oxide particles were faceted Fe_3O_4 and γ-Fe_2O_3 particles which formed chain-like structures. At higher plasma power, CNTs with diameters between 8 and 20 nm were also observed. Moreover, Kim et al. [139] used toluene in conjunction with ferrocene in argon-hydrogen RF plasma. Their work is an extension of experiments that used carbon black, and they suspect that a liquid carbon source would improve the purity of the CNT product. They note a strong preference for the formation of SWNTs, and suggest this may be due to smaller catalyst particles compared to other studies (3 to 4 nm versus >10 nm). The purity of the CNT material is estimated between 50 to 60 wt%, with 30 wt% being attributed to the metal catalyst and other constituents which were not readily oxidized. The authors examined the effects of sulphur content on the CNT product, noting that a small amount of sulphur results in SWNTs along with a large fraction of amorphous carbon. Increases in the sulphur content improve the purity and promote growth of larger diameter SWNTs and MWNTs. The diameter distribution of the CNTs also becomes smaller when more sulphur is used.

2.5 Objectives

As the greater aim of this work has been to develop plasma-based processes which are able to produce multiple CNT products using cost-effective materials and in conditions

which could be effectively scaled-up to economically-relevant quantities, several specific objectives can be defined. These objectives are as follows:

1. Design and develop a microwave plasma system that operates in a stable and continuous manner

2. Develop simple, inexpensive, and minimally-invasive method for quantification of plasma properties such as temperature and electron density

3. Produce CNT-metal oxide active material for LIB anodes

4. Develop process for fast, highly concentrated mass production of CNTs

The first objective is to develop the plasma system in such a way that it is able to operate in a stable, repeatable manner, can operate nearly indefinitely, and can accommodate a wide range of gas mixtures and precursors. Specifically, the propensity for the plasma to damage its reactor tube must be minimized to the point where a given reactor tube can be used for weeks or months. Furthermore, background particle generation, often caused by excessive heating of a component, must be reduced below the critical value where it prevents homogeneous nucleation of catalyst nanoparticles. This should correspond to a background particle concentration of at most two orders of magnitude less than the concentration of catalyst particles on their own, and should be less than 10^5 cm^{-3}. If possible, the background particle concentration should be reduced even further to below 10^3 cm^{-3}.

Following development of the plasma system itself, its properties must be quantified to obtain a more complete understanding of its capabilities and potential uses. As the two most important descriptors of a plasma are its temperature and electron density, they must be determined. In particular, the temperature of a plasma will have an effect on which materials can and cannot be vaporized in appreciable quantities, and a detailed quantification of the plasma can serve as the starting point for any aerosol or process models that will be developed in the future. While techniques exist to measure these properties, they can typically be classified within several categories: techniques that employ large, expensive high-end equipment, those that are only viable for certain plasmas (a particular pressure range or gas composition), or those that involve a large amount of modeling and processing time. It would therefore be more useful to develop a method for quantifying the plasma, particularly its temperature, that is viable for any plasma composition or pressure and that does not require large, specialized equipment or extensive modeling. A simple, portable method should be developed that can be applied to any given plasma and involves as little high-end research equipment as possible.

The plasma system will be used to demonstrate production of several CNT-based materials, the first being a CNT-metal oxide anode material for use in LIBs. To

accomplish this, a powder feeder should be developed that can supply solid metal precursor material to the plasma. The resulting core nanoparticles should then be combined with hydrogen and a carbon source to grow CNTs from the cores. Most cores should grow multiple CNTs to maximize the effects of the conductive network they provide. The resulting CNT-metal oxide material should exhibit good stability at high charge and discharge rates, high long-term cycle stability, and should possess a specific capacity higher than the current industry standard of 372 mAh g^{-1} (graphite).

The second major application of the plasma system is the fast and highly-concentrated production of CNTs. The primary objective of this section of work is to grow CNTs to long lengths at high number concentrations, largely by creating conditions similar to those found in the Windle process (i.e. gas composition and process flow rates). Catalyst particle production must be quantified and various carbon precursors and injection strategies must be examined to determine the most effective setup. Finally, the temperature profile downstream of the plasma must be designed such that it is conducive to fast, high-density CNT growth and perhaps even aerogel formation.

In working towards these objectives, plasma processes can be demonstrated as effective means for producing a multitude of CNT-based materials useful in a wide range of the next generation of materials in a continuous, scalable, and economically-viable manner.

Chapter 3

Design and Optimization of Plasma System

3.1 Introduction

3.1.1 Context

This section explores the phenomena and behaviour of microwave plasma as well as the design and development steps taken to produce a setup that is capable of satisfying the objectives presented in the previous chapter. In particular, the operating principle is discussed along with the influence of various gas properties and the resultant effects on plasma deportment.

Practical considerations are also discussed, including a method for starting the system, as are methods of stabilizing and centralizing the plasma within the reactor tube and the corresponding material selection for these components. Finally, methods for introduction of solid powdered precursors are discussed and the optimal design of such a powder feeder is presented. By the end of this chapter it should be clear that objective (1) has been met. Specifically, the plasma system has been designed and commissioned in such a way that it is capable of producing various CNT-related materials in a continuous, stable, and repeatable manner.

3.1.2 Microwave Plasma Operating Principle

The unit used for this work is a Sairem GMP 60K surface wave microwave plasma system. The term "surface wave" indicates that energy is supplied by sending microwaves through a waveguide which intersects with the reactor tube. A standing wave is created in the microwave cavity and ideally an antinode will exist near the centre of the reactor tube, maximizing power absorption by the plasma. Importantly, the microwaves themselves are not directly responsible for ionization of the plasma gas. From Planck's

equation where energy is related to frequency via Planck's constant ($E = hf$), the energy of microwave photons at a frequency of 2.45 GHz is 1.01×10^{-5} eV: far too low for ionization, which requires on the order of 10 eV for most common gases. Hence, the microwaves are not able to ionize the gas on their own. Despite the fact that the microwaves have no effect on the neutral gas molecules or atoms, they will have a strong effect on charged particles. As the electromagnetic field oscillates, charged particles gain energy as they are forced back and forth. While ions are relatively unresponsive to these oscillations due to their large mass, electrons are easily accelerated. These electrons, which do have sufficient energy to ionize neutral species, collide with other particles and liberate additional charges. The newly-freed electrons are then able to collide with additional particles and a cascade effect is produced. Therefore, the fundamental operating principle of surface wave microwave plasma (as depicted in Figure 3.1) is that microwave energy is transferred to free electrons which then transfer their energy to neutral species via collisions which results in additional ionization and heating of all species [69, 152].

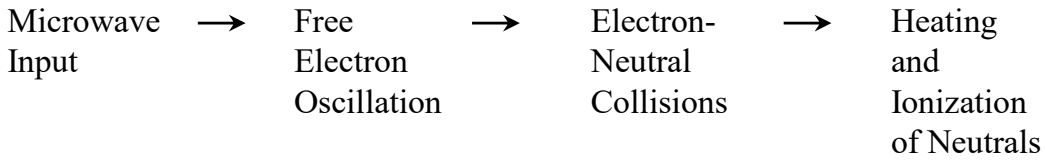

Fig. 3.1 Plasma ignition mechanism

3.2 Experimental Setup

The general experimental setup for the plasma system is shown in Figure 3.2. The power supply (not shown) energizes the magnetron which produces the microwave field. Microwaves are directed through a rectangular cavity which contains several wave conditioning elements in addition to the waveguide and reactor tube. The goal of the microwave cavity is to produce a standing microwave field with an amplitude maximum located inside the reactor tube. The conditioning elements needed to accomplish this include a sliding short circuit at the end of the cavity. It contains an aluminum plate whose axial position can be adjusted and acts as the boundary to the microwave resonant cavity. Also included is a three-stub tuner which contains three copper rods that can be lowered into the microwave field. These rods distort the microwave field and can be used not only to maximize the microwave power at the reactor tube, but also to minimize the microwave power reflected back to the magnetron. The reactor tube itself is oriented perpendicular to the microwave cavity, and plasma formation will occur at the intersection of the cavity with the reactor

tube. The ceramics comprising the reactor tube such as quartz and alumina have low dielectric constants and are therefore transparent to the microwave energy. The waveguide is also fitted with two components which surround and hold the reactor tube, known as chimneys. These chimneys contain any additional microwave energy that may be emitted by the plasma during operation. Both chimneys are typically at least 20 cm long since plasmas operated under vacuum can often occupy large volumes. However, atmospheric pressure plasmas are significantly smaller and the use of long chimneys is often unnecessary. Customized short chimneys (∼5 cm) were often used for this work and have been shown to effectively contain any potential microwave leaks (less than 1 mW cm^{-2} as per health and safety guidelines). For this work using atmospheric pressure and low flow rates (<10 standard litres per minute, SLPM), the plasma exists entirely inside the bounds of the waveguide and chimneys.

Support features of the plasma system include water cooling supplied by a chiller for the power supply, magnetron, three-stub tuner, and waveguide. Water is provided in a parallel circuit with approximately 3 litres per minute (LPM) flowing through the power supply and magnetron, and another 2.5 LPM flowing through the three-stub tuner and waveguide. Cooling air is also used to maintain the temperature of the chimneys and reactor tube. A supply of air at 5 bar is provided to the upper and lower chimneys and corresponds to a flow rate of approximately 150 LPM split equally between chimneys.

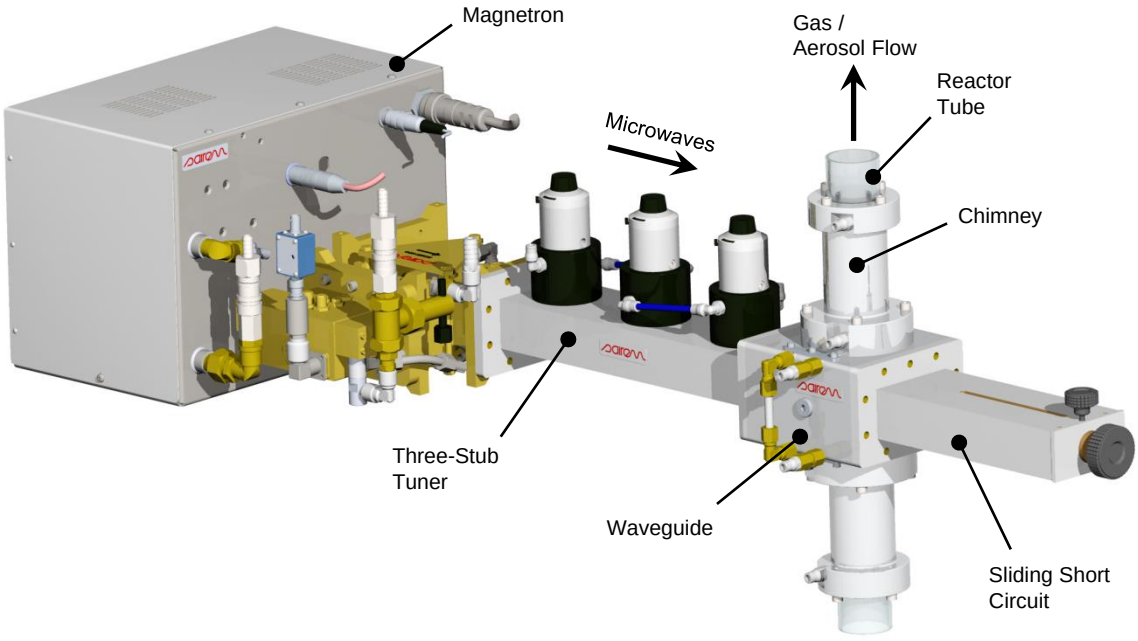

Fig. 3.2 Microwave plasma system (solid model files courtesy of Sairem)

3.3 Plasma Start-up

In most cases, application of microwave energy to the reactor tube is not sufficient by itself to stimulate plasma generation. As discussed above, microwave photons possess energies that are five to six orders of magnitude too low to ionize the gas molecules directly. Rather, free electrons must already be present so they can be accelerated by the microwave field to energies sufficient for gas ionization in the event they collide with other particles. The question then becomes how to provide free electrons to the system in a quantity sufficient to initiate an electron cascade.

A common method of starting a microwave plasma system is to insert an electrically-isolated metal wire or rod into the microwave field. The sharp curvature of the tip of the rod concentrates the electromagnetic field to the point where electrons are able to overcome their workfunction and are liberated from the surface. As the metal is present in the system in this case (and may temporarily become very hot), contamination of the system during startup is likely.

An alternative approach is to produce an electric arc independently from the microwave field. This can be accomplished using a device such as a handheld tesla coil (Electro-Technic Products, model BD-10A) which can produce voltages up to 50 kV. Arcs from this tesla coil can span several centimetres, and if argon is used the arcs can extend to tens of centimetres down the reactor tube. In this way, the tesla coil can be applied to the exit of the reactor tube where no contamination is possible yet the plasma can still be ignited. In fact, if a section of the reactor tube exists which is sufficiently far from any other conductors (a length of approximately 20 cm in the case of this system), the tesla coil can be touched to the outside of the reactor tube and the plasma is still able to ignite. This can be useful since the reactor tube can be sealed or connected to other equipment and does not need to be open for ignition to be possible.

While this mechanism could be used to ignite plasmas of any gas composition, argon is the easiest to ignite. Therefore the procedure for ignition of this plasma system that has been deemed the simplest and most reliable is to first flush the reactor tube with argon, then apply microwave power and a tesla coil spark. Once the plasma has been ignited the gas can be replaced with the desired mixture for the particular experiment.

3.4 Plasma Behaviour

3.4.1 Effects of Gas Composition on Plasma Formation

Despite the fact that many common and inert gases behave similarly under normal conditions, their behaviour while ionized as a plasma can vary dramatically, as can

their effects on the surrounding equipment. Gas properties such as ionization energy, breakdown potential (i.e. the ease of a plasma to be ignited), thermal conductivity, skin depth, microwave absorption, and chemical reactivity are discussed with relevance to the plasma's startup behaviour, steady-state behaviour, and interaction with other species or materials that may be present. Each of these properties are examined in greater detail below.

Ionization energy: The ionization energy of a gas corresponds to the amount of energy required to liberate an electron from its host atom. If electrons can be liberated sufficiently quickly before recombination, a plasma can be sustained. Among all the elements in the periodic table, the non-metals - particularly the gases - have the highest ionization energies. The elements with the highest ionization energies are those in the top right of the table - light elements with nearly complete electron shells. Light elements possess valence electrons close to their nuclei and have fewer complete electron shells below their valence shell. As a result, the attractive force between the valence electrons and atomic nucleus is strong and largely unshielded. The highest first ionization energy is that of helium (24.6 eV), followed by neon (21.6 eV). For comparison, the element with the lowest ionization energy is caesium at only 3.9 eV. As electron excitation is a type of latent heat, more energy will be required to produce plasmas from gases with higher ionization energies. An initial conclusion may therefore be that practically speaking, helium is the most difficult gas to ionize; however, this is not the case. A gas's ability to be ionized is in fact dependent on more than just its ionization energy as is explored in the following material properties. In fact, the amount of power required specifically for ionization is relatively small. Using helium with a flow rate of 5 SLPM and an approximate ionization fraction of 0.1%, only 8 W are required. Despite the low power consumption, ionization energy has a large influence on the plasma's electron density. From the Saha equation in section 1.4.1, the ionization energy is contained in an exponential term and thus variations in this property can alter the electron density by orders of magnitude for a given temperature. Therefore, ionization energy on its own is not a significant source of energy consumption nor is it a practical limitation for plasma generation, though it does significantly affect the plasma's electron density.

Breakdown potential: One method of determining the propensity of a gas to undergo macroscopic electrical breakdown is from how easily a spark can be generated in the gas across two electrodes. Paschen's law can be used to determine this breakdown voltage for a particular pressure (P) and electrode spacing (d), and curves for several candidate gases are displayed in Figure 3.3 (using coefficients from Lieberman and Lichtenberg [153]). For high Pd values it is in fact helium that possesses the lowest breakdown voltage, followed by neon. This is an interesting result considering these two gases also possess the highest ionization energies. The explanation for this

counter-intuitive phenomenon is that other metastable electron energy states exist within the neutral atoms, and in the case of helium and neon, these metastable states are near the ionization energy. As a result, a small number of atoms can be easily ionized and their liberated electrons then initiate the cascade of collisions leading to breakdown. Conversely, nitrogen exhibits a high breakdown voltage, making it difficult to start the plasma system. Also note that these trends apply for high pressure or large electrode spacing, whereas the trends are entirely reversed at low pressure or a small electrode spacing. The distinction must be made that Paschen's law applies to direct current voltages and cannot be quantitatively be applied to this microwave-based system. Modifications exist for conditions such as alternating current [154] or small electrode spacing [155]. Still, Paschen's law gives qualitative insight into the breakdown characteristics of various gases and can still be useful for development of the setup used in this work.

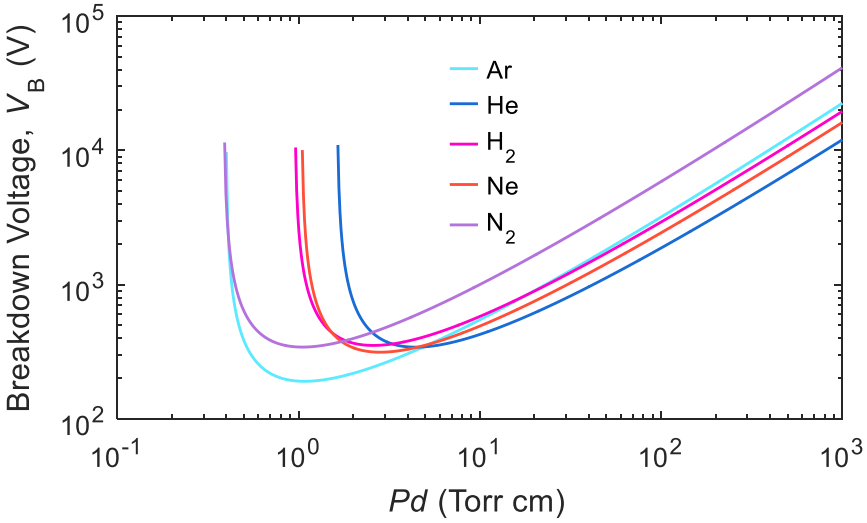

Fig. 3.3 Paschen curves for various potential plasma gases

Thermal conductivity: The thermal conductivity of a gas has a large influence on the components in close proximity to the plasma and heated gas. A high thermal conductivity can be detrimental for several reasons. First, the gas transfers heat very effectively to the quartz reactor tube (and any other components nearby such as an injection torch). This heating can be severe and may result in accumulated wear on the tube surface or complete crack failure. Secondly, since the gas conducts its heat easily, it is also difficult to maintain energy in the flow downstream of the plasma. Ideally, the plasma and its byproducts are very hot but the equipment containing the plasma is relatively cool. Highly conductive gases produce the opposite effect: excessive heating of the reactor tube, yet poor retention of heat in the gas downstream since the energy is conducted away too quickly. Hydrogen and helium have extremely high thermal conductivities (180.5 mW K^{-1} m^{-1} and 151.3 mW K^{-1} m^{-1} respectively) in comparison

to other gases such as nitrogen (25.8 mW K^{-1} m^{-1}) or argon (17.7 mW K^{-1} m^{-1}). Unfortunately, these gases (particularly hydrogen) are useful for CNT production as discussed in future chapters.

A second property influenced by thermal conductivity is the plasma size. As conductive gases transmit heat to adjacent atoms more readily, and as the temperature of the adjacent atoms increases, so too does their likelihood of ionization (recall from the Saha equation that ionization fraction scales with temperature). Therefore, conductive gases occupy larger volumes than non conductive gases. In this work, the contrast between helium and argon is exemplary, since the former exists as a diffuse plasma (up to $\sim$ 30 mm in diameter) that often occupies the majority of the tube cross-section whereas the latter exists as thin, unstable filaments <3 mm in diameter. For comparison, the reactor tube inner diameters used in this work range from 22 mm to 46 mm. Details about plasma size and shape are discussed in section 3.4.2.

Skin depth: As plasmas contain positive ions and their corresponding free electrons, they are inherently electrically conductive. Like any conductor, exposure to electromagnetic fields results in movement of these charges which in turn produces a screening effect whereby the electromagnetic field is not able to penetrate beyond a certain distance into the conductive medium. The characteristic penetration distance of an oscillating electromagnetic field is known as the skin depth (L_s) and can be determined from:

$$L_s = c\sqrt{\frac{\varepsilon_0 m_e}{e^2 N_e}}, \tag{3.1}$$

where c is the speed of light, ε_0 is the permittivity of free space, m_e is the electron mass, e is the electron charge, and N_e is electron density. Note that the skin depth is independent of gas properties and is only influenced by electron density. Furthermore, this equation neglects the translational motion (thermal energy) of the electrons. Using a typical electron density value for an atmospheric pressure microwave plasma of $N_e = 3 \times 10^{20}$ m^{-3} [69], the skin depth is approximately 0.31 mm. This indicates that the microwave energy powering the plasma is only active on the outer layer of the plasma. Given that the scale of the skin depth is that of hundreds of micrometres to single millimetres, yet the plasma itself has a length scale of centimetres, energy must be able to to permeate farther into the plasma, beyond the skin depth. Specifically, the high translational energy of the electrons allows them to penetrate deeper into the plasma and sustain it, and it is for this reason that this type of plasma is known as "collisionally-dominated" since the majority of its volume is powered purely from collisions with free electrons in the relative absence of an external field. Had the electron density been lower ($\sim 10^{17}$ m^{-3} for the plasmas considered here), the skin

depth would approach the plasma length scale and the microwave field would therefore be capable of permeating the entire plasma volume.

Microwave absorption: At a given electromagnetic input frequency, some plasmas are more suited to power absorption than others. Since the plasmas considered here are collisionally-dominated, particularly by electron-neutral interactions, the power absorbed by the plasma normalized by volume and electric field strength can be determined from Leins et al. [69] as:

$$\frac{p}{VE^2} = \frac{N_e}{N_c}\varepsilon_0\omega\frac{\nu_{en}/\omega}{1+\left(\nu_{en}/\omega\right)^2}. \tag{3.2}$$

Here, p is absorbed power, V is volume, E is electric field strength, N_e is electron density, N_c is cutoff density, ε_0 is vacuum permittivity, ν_{en} is the collision frequency between electrons and neutrals, and ω is the microwave angular frequency ($\omega = 2\pi f$, where f is 2.45 GHz). The cutoff density is equal to $N_c = \varepsilon_0 m_e \omega^2/e^2$ where m_e is electron mass and e is electron charge. The electron neutral collision frequency can also be expanded as $\nu_{en} = N_0 u < \sigma_{en} >$, where N_0 is neutral particle density, u is relative electon-neutral velocity, and $< \sigma_{en} >$ is the electron-neutral collision cross-section. Also from Leins et al. [69], each of these constituent variables can be explored further to identify the behaviour of the collision frequency. The neutral particle density can be determined simply from the ideal gas law (assuming the charge fraction is small), $N_0 = P/k_b/T_{gas}$, where P is pressure, k_b is Boltzmann's constant, and T_{gas} is gas temperature. The electron-neutral velocity can be determined by examining both the velocity of the neutral particles and that of the electrons. The most probable (thermal) velocity of a population of particles is equal to:

$$u_{th} = \sqrt{\frac{2k_bT}{m}}, \tag{3.3}$$

where m is particle mass. As an example, given a temperature of 5000 K, the neutral particle velocity of an argon atom is 1.44×10^3 m s^{-1} and the electron velocity is 3.89×10^5 m s^{-1}. Clearly, due to the electron's smaller mass, its velocity is much higher than that of the heavy neutral atoms; therefore, the relative velocity between these two species can be simplified as the velocity of only the electrons. Combining the above results gives the complete equation describing the electron-neutral collision frequency:

$$\nu_{en} = \frac{P}{T_{gas}}\sqrt{\frac{2T_e}{k_bm_e}} < \sigma_{en} > . \tag{3.4}$$

Note that T_{gas} and T_e are gas/neutral and electron temperature respectively. Next, it is helpful to examine the power density equation (3.2). Taking the derivative with respect

to ν_{en} gives:

$$\frac{\partial \frac{p}{VE^2}}{\partial \nu_{en}} = \frac{N_e}{N_c}\varepsilon_0 \frac{1-\left(\nu_{en}/\omega\right)^2}{\left(1+\left(\nu_{en}/\omega\right)^2\right)^2}. \tag{3.5}$$

The positive root of this equation (i.e. the maximum power density) is achieved when $\nu_{en}/\omega = 1$. In other words, the highest power absorption or "best tuned" plasma will be that which has an electron-neutral collision frequency equal to that of the microwave angular frequency.

Chemical activity: The chemical activity of the plasma gas is important largely because it can be damaging to the reactor tube and any other nearby components. Fortunately, inert gases are most commonly used, including nitrogen, argon, and helium. Depending on the properties discussed above (particularly thermal conductivity), inert gases can still be damaging to equipment; however, they do not pose any risk of damage via chemical mechanisms. Conversely, reactive gases such as oxygen and hydrogen can have detrimental chemical effects. Most of the materials used near the plasma are oxides (i.e. quartz, alumina, etc.) and as these are already oxidized, they do not readily react with oxygen in the plasma. A non-oxide that has been used in this work is boron nitride, which is only stable in oxidizing environments up to approximately 800°C despite its impressive stability in inert environments in excess of 2000°C. Therefore, when appreciable quantities of oxygen are used such as with an air plasma, boron nitride components should be avoided.

Conversely, hydrogen is a reducing agent and will readily react with oxides. Some such as alumina are resistant to reduction from hydrogen although others, such as quartz, easily react with hydrogen and this can result in severe damage to the tube within seconds. If hydrogen is to be used, quartz components should be avoided or the plasma should be constrained in such a way that it is not able to contact the quartz.

3.4.2 Experimental Observations of Plasma Behaviour

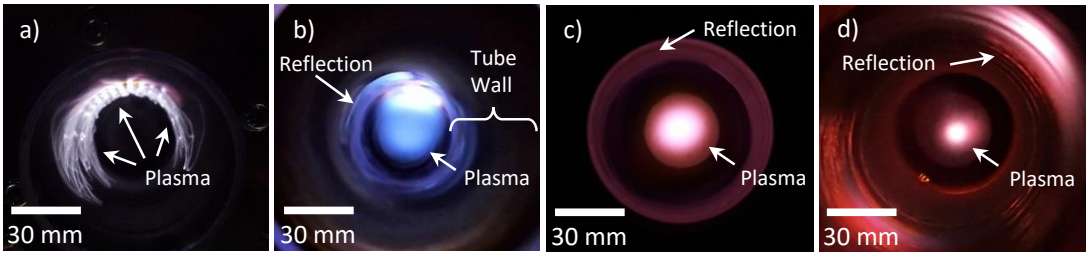

Fig. 3.4 Axial views of 50 mm OD tube containing various plasma gases including (a) argon, (b) helium, (c) nitrogen, and (d) nitrogen with ~16% hydrogen. Flow rates for these conditions are between 4 and 6 SLPM with absorbed microwave power between 1.0 and 1.5 kW.

Experimentally, the effects of the aforementioned properties can be observed. Behaviour of several common plasma gases are described below.

Argon: In comparison to the other gases listed here, the behaviour of argon is markedly unique, and is displayed in Figure 3.4a. Argon (as well as the heavier noble gases) forms thin, unstable filaments of plasma that adhere to the reactor tube wall. This is most likely explained by the low thermal conductivity of argon and other heavy noble gases. As they are not able to conduct heat to adjacent gas molecules, it is difficult to maintain temperatures suitable for ionization beyond the immediate region of a thin filament. Its propensity to adhere to the reactor tube wall rather than to exist in the middle of the tube cross-section may also be due to its low thermal conductivity - and therefore its ability to ionize the adjacent gas. The gas near a solid surface will have a low velocity given the existence of a boundary layer, and this likely makes it easier for the filaments to form there. Fortunately, the low conductivity and reactivity of argon also means that despite the fact that it exists in close proximity to the reactor tube, damage is nearly non-existent. It is only in the instance when filaments are relatively stable and do not move across the tube surface that the tube will slowly be etched by the argon plasma. Overall, argon is the simplest plasma gas to use and the most forgiving regarding equipment longevity.

Helium: In contrast to argon, helium has a very high thermal conductivity and will also readily ionize due to the metastable electron states that exist near its ionization energy. As a result, helium forms much larger, spatially diffuse plasmas, like that visible in Figure 3.4b. Helium may also form multiple plasma modes at once, often located on opposing sides of the reactor tube. Heating of the reactor tube can be severe due to the higher thermal conductivity and also because its large volume makes it difficult to constrain. As a result, the plasma is almost always in contact with at least one location of the reactor tube as is evident in Figure 3.4b. If helium is to be used, the plasma must be constrained very well and all adjacent equipment must be stable at high temperatures and resistant to thermal shock.

Nitrogen: Nitrogen behaves similarly to helium, although from an experimental perspective it is more forgiving. With lower thermal conductivity than helium, it is less damaging to the reactor tube and tends to form slightly smaller plasmas that can be manipulated using gas flow patterns to produce a stable, centrally-located plasma such as that in Figure 3.4c. Nevertheless, prolonged contact between the nitrogen plasma and the reactor tube can cause etching or fractures. Detailed discussion of plasma stabilization to prevent these failure mechanisms is presented in section 3.5.

Nitrogen-Hydrogen Mixture: Hydrogen is a strong reducing agent and is necessary for many CNT growth processes and ideally, a large hydrogen fraction could be included in the plasma gas. Unfortunately, hydrogen is a very difficult gas to use in plasmas and must be mixed with other species such as nitrogen. Despite its

high thermal conductivity, the addition of hydrogen to a nitrogen plasma causes the diameter of the plasma to decrease - a counter-intuitive trend given that plasma size tends to scale with thermal conductivity. An example of the diameter reduction is shown in Figure 3.4d. While a standard nitrogen plasma produced using this system may have a diameter of 10-15 mm, addition of approximately 30% hydrogen will result in the plasma decreasing to a diameter of <3 mm. Moreover, hydrogen requires a very high input power to be sustained and as a result, the power density of the nitrogen-hydrogen plasma is extremely high, although it only occupies a small portion of the tube cross-section.

Given it has the highest thermal conductivity of any gas commonly used in plasma work, hydrogen readily conducts its heat to the reactor tube and any other nearby components. Additionally, its reducing properties mean that it will react with many oxides including quartz. As a result, the presence of hydrogen in a plasma can not only cause failure from melting or thermal shock but also chemical failure by reacting with the reactor tube and converting it to its reduced form, the results of which are covered in section 3.6.1. Note as well that both the excessive heating and chemical reactivity can become problematic even if the plasma is well constrained in the centre of the tube with no plasma directly contacting the tube. Even the gas adjacent to the plasma can contain sufficient energy to damage the reactor tube, and as such, reactor tube coatings may be necessary and the upper limit for microwave power is dictated by the reactor geometry, particularly the diameter of the tube. This phenomenon is explained in more detail in section 3.5.3.

3.4.3 Operating Pressure

While plasmas are produced over many orders of magnitude of pressure ranging from several pascals [78] to more than 100 bar [98], this work is conducted at atmospheric pressure. Significant cost and complexity are incurred for continuous processes which do not proceed at atmospheric pressure. Additionally, plasma generation above atmospheric pressure is difficult. This is because the decreased mean free path makes sustained ionization challenging since recombination occurs quickly and over short distances. Conversely, plasma generation under vacuum is easily achievable; however, the increased mean free path results in a decrease in energy density. Low pressure plasmas also tend to be farther from thermal equilibrium since their gas temperature is much lower than their electron temperature and their thermal conductivity is also reduced when compared to an atmospheric pressure plasma. These factors reduce the plasma's ability to transfer heat to precursors and vaporize material effectively. For these reasons, an atmospheric pressure plasma system is the most suitable choice for a continuous material synthesis process.

3.5 Plasma Stabilization

Atmospheric pressure microwave plasmas are naturally unstable and will tend to "cling" to a solid surface rather than remain isolated in the centre of a given space. Consequently, the proximity of the plasma to the surface (typically the reactor tube wall) results in extreme heating and failure via multiple mechanisms including cracking, melting, or chemical reactions. These failure mechanisms are discussed in detail in section 3.6.1. It is imperative that the plasma system be developed in such a way that the plasma is able to exist in the centre of the reactor tube cross-section and does not contact the reactor tube. A central, stable plasma will subject the reactor tube to minimal thermal loads, resulting in a long operational tube life and negligible contaminating background particle production. Several plasma stabilization designs have been constructed and tested and their results are presented in the following section.

3.5.1 Mechanical Stirring System

The mechanical stirring system is intended to increase the gas velocity near the walls of the reactor tube. Since plasma formation is more difficult in high-velocity regions, formation near the walls is discouraged and the plasma will instead favour the centre of the tube. The system is shown in Figure 3.5a. The paddles of the stirring system are located upstream of the plasma, meaning that the gas must maintain its circumferential velocity until it reaches the plasma region for the design to be effective and successful. A simplified scenario takes the velocity profile of the gas as it leaves the stirring system and models the velocity decay over time. Using the volumetric flow rate, this decay time can then be converted into an axial travel distance through the reactor tube. As a starting point, the circumferential component of the Navier-Stokes equation in cylindrical coordinates can be used, and several simplifying assumptions can be applied. These assumptions are that (1) the system is at steady-state, (2) the gas is nitrogen at 600 K, (3) the initial gas velocity profile matches that of the paddles, (4) there is zero velocity at the tube wall, (5) there is zero circumferential velocity on the tube axis, (6) the system is circumferentially symmetric, (7) there is no radial velocity, and (8) there are no circumferential acceleration or pressure terms. With these assumptions, the Navier-Stokes equation reduces to:

$$\rho \frac{\partial u_\theta}{\partial t} = \mu \left[\frac{1}{r} \frac{\partial}{\partial r} \left(r \frac{\partial u_\theta}{\partial r} \right) - \frac{u_\theta}{r} \right]. \tag{3.6}$$

Here, u_θ is circumferential velocity, t is time, ρ is density, and r is radius. This equation was then input into a partial differential equation (PDE) solver in Matlab. The boundary conditions are $u_\theta = 0$ at $r = 0$ and at $r = r_{\text{out}}$ (the inner radius of the

reactor tube). Additionally, the initial condition is that the velocity profile matches that of the paddles (i.e. increases linearly with radius) between the tube axis and the paddle radius, and is a decreasing linear function between the paddles and tube wall:

$$u_\theta = \omega_{\text{pad}} r, \quad \text{for } 0 < r < r_{\text{pad}}, \tag{3.7}$$

$$u_\theta = \omega_{\text{pad}} r_{\text{pad}} \frac{r - r_{\text{out}}}{r_{\text{pad}} - r_{\text{out}}}, \quad \text{for } r_{\text{pad}} < r < r_{\text{out}}. \tag{3.8}$$

Here, ω_{pad} is the angular velocity of the paddles and r_{pad} is the outer radius of the paddles. The circumferential velocity profile from the solution to this PDE as a function of time and radius is shown in Figure 3.5b. Similarly, the velocity profile as a function of radius at multiple time steps is shown in Figure 3.5c. As expected, the peak of the velocity profile reduces in magnitude over time and moves towards the radius equidistant from the zero-velocity boundary conditions. From the volumetric flow rate and the inner diameter of the tube, the velocity profile as a function of time can be converted to a profile as a function of axial distance from the paddles (z direction), as long as the scenario is simplified so as not to include the parabolic flow profile of fully-developed flow:

$$L = u_z t = \frac{Q}{A} t = \frac{Q}{\pi r_{\text{out}}^2} t. \tag{3.9}$$

Here, L is axial distance from the paddles, Q is volumetric flow rate, and A is cross-sectional area. These distances are also shown in Figure 3.5c. This information can be used to determine whether the mechanical stirring mechanism is viable and if so, the proximity of the stirring paddles to the plasma can also be determined to maintain sufficient gas swirl. Under these conditions, the peak velocity is approximately 0.3 m s^{-1} and quickly decays below 0.1 m s^{-1} in less than one second (corresponding to an axial travel of approximately 10 cm at the example flow rate of 5 SLPM). Importantly, the Reynolds number in the tube at this flow rate is approximately 120, meaning the flow should be laminar and any swirl imparted to the gas from the paddles will not be immediately disrupted by turbulence. Experimentally, this amount of vorticity produced from the paddles was still not able to stabilize the plasma and unfortunately the rotational speed of the paddles presents a limitation. It was not possible to fit a motor which was able to spin the paddles any faster, while still maintaining an appropriate gas seal. Instead, other solutions to increase gas velocity and vorticity have been explored and are discussed below.

Part of the issue with the mechanical stirring mechanism is that the paddles must be located relatively far from the plasma, so preservation of the vorticity is difficult. The shaft and paddles themselves are fabricated from stainless steel which has a reasonably high operating temperature window. However, since the vapour pressure of metals

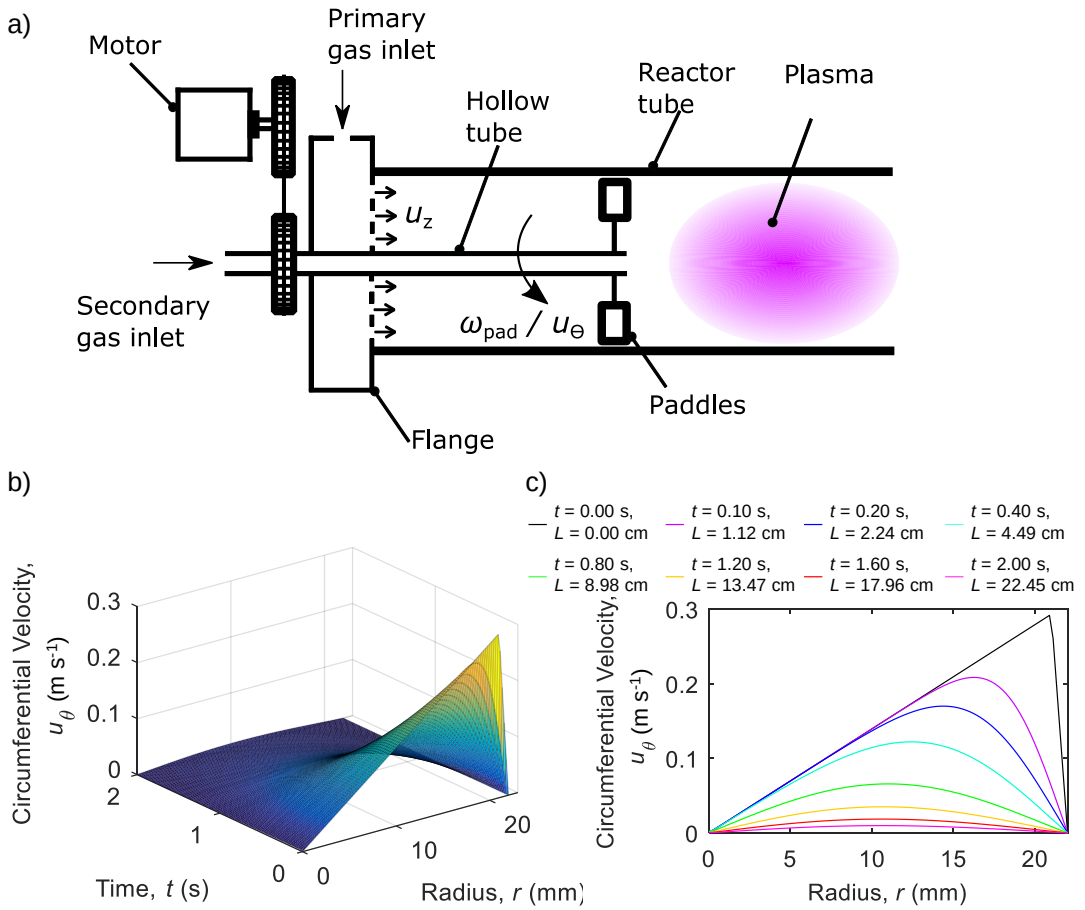

Fig. 3.5 (a) Mechanical stirring mechanism schematic, (b) surface plot of circumferential velocity (u_θ) as a function of both time and radius, and (c) circumferential velocity (u_θ) as a function of radius at various time steps, which have also been converted to axial distance past paddles given a flow rate of 5 SLPM

is higher than most ceramics, they tend to produce nanoparticles as they are heated which can contaminate the process. This is particularly troubling for the applications presented here since the primary component of stainless steel is iron which is an excellent catalyst for CNT growth, thus bringing into question whether the resultant CNTs would have been grown from contaminating particles or intentional catalyst particles. A second but more immediate concern is that closer to the plasma, very high microwave field strengths are present. These fields cause additional heating of materials with high or infinite dielectric strengths, and can often result in arcing as well as melting of metal components. It is conceivable that a ceramic shaft and paddles could be constructed but this would be challenging to fabricate and as mentioned above, the maximum velocity that can be produced is still rather low since it is limited by the motor speed and torque. Therefore, inducing vorticity using fluid flow rather than mechanical means has been pursued.

3.5.2 Axial Flow Torch

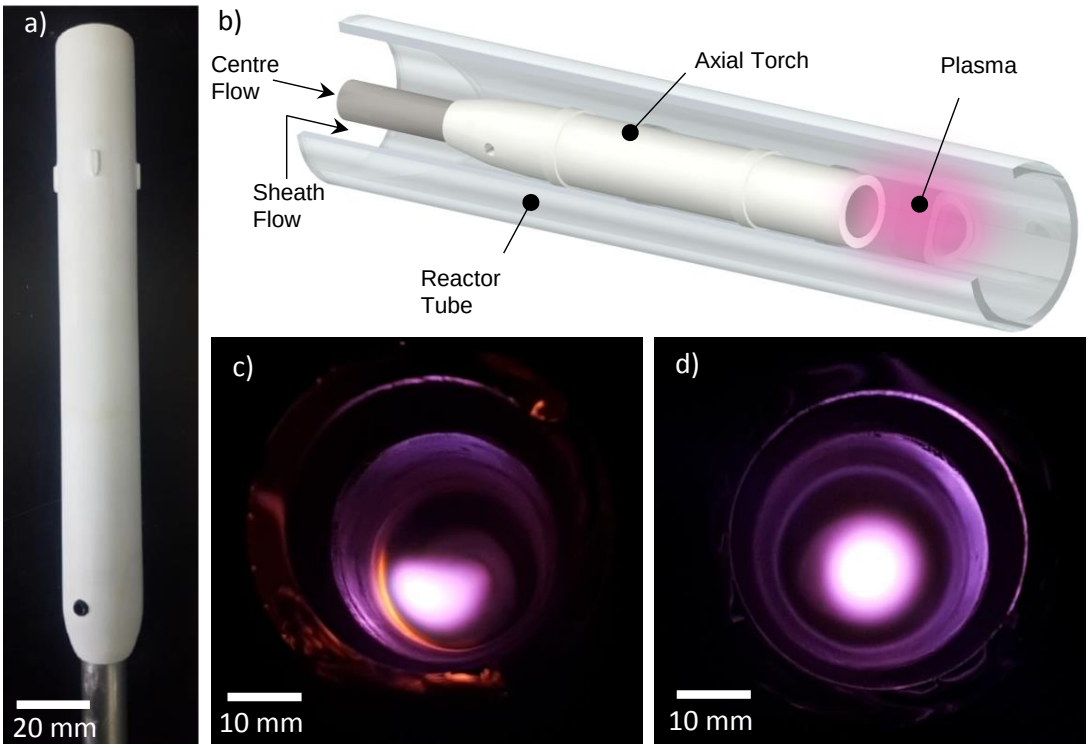

Fig. 3.6 (a) Side view of boron nitride axial flow torch, (b) schematic of axial flow torch in quartz reactor tube, (c) axial view of nitrogen plasma without torch, and (d) axial view of nitrogen plasma with torch

As stated in the mechanical stirring section, a high gas velocity near the tube wall is necessary to discourage plasma formation in that region. Instead, the high velocity forces the plasma to exist near the centre of the tube where it is farther away from any surfaces that may be damaged. A component referred to here as the axial flow torch has been designed to accomplish this task. This torch is able to be placed much closer to the plasma than the stirring system could be, and this ensures the plasma is exposed to the high sheath velocity before it decays farther along the reactor tube.

The torch is effectively a hollow cylinder (pictured in Figure 3.6a and b), and gas flows can be passed through the centre of the torch or in the annular sheath region between the torch and the tube wall. If a sufficiently high sheath flow rate is used relative to the central flow rate, the fast-moving sheath gas will discourage plasma formation and instead force the plasma to the central flow. The axial velocity through the annular sheath region can be determined using the following equation:

$$u = \frac{Q}{A} = \frac{Q}{\frac{\pi}{4}\left(d_{\text{out}}^2 - d_{\text{in}}^2\right)}, \tag{3.10}$$

where d_{out} and d_{in} are the diameter of the quartz tube wall and torch diameter, respectively. Using a quartz tube inner diameter of 23.5 mm and a torch diameter of 21.2 mm, along with a flow rate of 8 SLPM at 600 K, the face velocity of the sheath gas is 3.63 m s^{-1}. Note that this is an order of magnitude higher than the maximum velocity achieved by the mechanical stirring system.

The axial torch design has been successful, and is able to produce stable, central plasmas for sheath flow rates as low as 4 SLPM. In this case, the central flow should be at most 1.5 SLPM, and ideally 1.0 SLPM or lower. The difference in plasma behaviour is evident when comparing Figure 3.6c and d, where the former displays typical unstable plasma behaviour. Note the lack of axial plasma symmetry and the strong heating of the quartz tube wall. Conversely, the use of the torch stabilizes the plasma in the centre of the tube and eliminates excessive quartz tube heating. Since all components are relatively cool with no plasma/wall contact, contaminating background particle production is negligible and can often be below 10^3 cm^{-3}. For comparison, this particle concentration is approximately one order of magnitude lower than those found in ambient air and four to five orders of magnitude lower than the concentrations of particles produced in the processes described in this work.

3.5.3 Swirl Torch

While the axial torch proved to be a robust and successful design that was used for much of the work presented here, it did possess some limitations. In particular, heat loss from the plasma to the reactor tube wall is significant when hydrogen is present. This heat loss is detrimental for two reasons: the reactor tube may fail from excessive heating despite no direct contact with the plasma, and the temperature of the gas downstream of the plasma may be too low for CNT growth processes. The natural conclusion is simply to increase the diameter of the reactor tube so there is larger separation between the plasma and tube wall, yet this will not be successful. Increasing the reactor tube diameter would also result in a larger sheath region between tube wall and torch, thereby decreasing the velocity of the stabilizing sheath flow and the torch will no longer effectively centralize the plasma. Similarly, the diameter of the axial torch cannot be increased along with the tube diameter to maintain the original sheath velocity since this would result in the plasma stabilizing on the boundary of the sheath flow, though no longer in the centre of the tube. As such, the distance between plasma and tube wall will still be small. It is for these reasons that at atmospheric pressure, there is an upper limit to the reactor tube diameter that can support stable and central plasma using an axial flow torch. From experimental observation using flow rates <10 SLPM, this limit likely corresponds to a reactor tube inner diameter of $\sim$30 mm.

As discussed with the mechanical stirring system in section 3.5.1, vorticity is another useful tool for plasma stabilization. Nevertheless, a design would be required

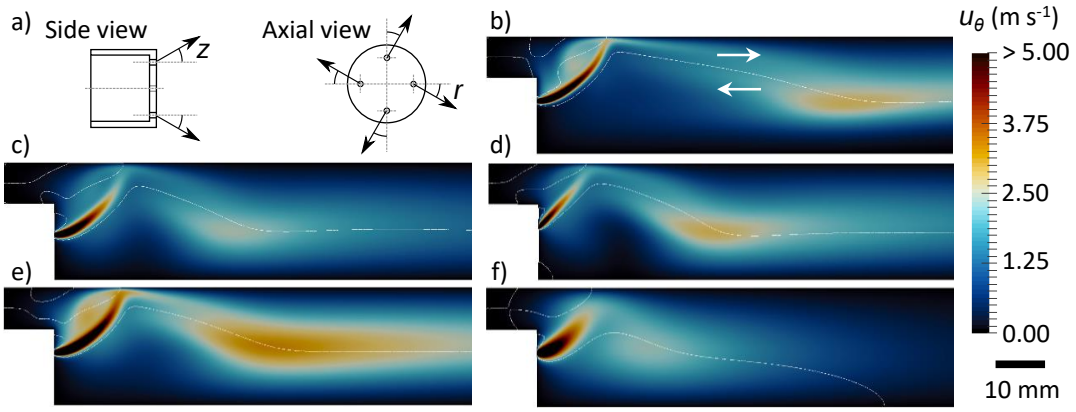

Fig. 3.7 Axisymmetric CFD models (computed by Filip Gökstorp) for gas flow produced by swirl torch in half cross section of reactor tube. The schematics in (a) define the angles z and r relative to the axial and radial vectors, respectively. In the CFD simulations, the reactor tube axis is the bottom edge of the images and the torch head is in the bottom left corner. Nominal conditions include an exit velocity of 15.9 m s^{-1}, a nominal injection hole pitch circle diameter of 20 mm, and a kinematic viscosity of 1.24×10^{-4} m^2 s (nitrogen at 1000 K). Conditions include (b) holes angled with $z = 45°$ and $r = 90°$, (c) $z = 45°$, $r = 90°$, and a pitch circle diameter of 16 mm, (d) $z = 45°$ and $r = 45°$, (e) $z = 45°$, $r = 90°$, and an exit velocity of 21.2 m s^{-1}, and (f) $z = 45°$, $r = 90°$, with the kinematic viscosity of 8.28×10^{-4} m^2 s (hydrogen at 1000 K)

that can generate more vorticity (higher circumferential velocities) than the mechanical stirring system and is also able to exist closer to the plasma. A cylindrical ceramic component similar to the axial torch was conceived to accomplish this. Where this torch differs from the axial torch is that its end is not fully open. Instead, several small angled holes are drilled so vorticity can be generated as the gas exits the torch. These holes can be angled both relative to the reactor tube axis (i.e. $z = 0°$ when aligned with the tube axis) and relative to the radial vector (i.e. $r = 0°$ when aligned radially outwards). Both angles are shown schematically in Figure 3.7a. A computational fluid dynamics (CFD) study performed by Filip Gökstorp explored the effects of variations in geometry and gas parameters on the flow in the tube, and the results are displayed in Figure 3.7, where the circumferential velocity profiles are shown. The white contours show lines of zero axial velocity, i.e. the boundaries between forward-flowing gas and recirculation zones. In these cases, the gas near the tube wall (upper boundary) is moving forward and the gas near the tube axis (lower boundary) is recirculating, as indicated by the arrows in Figure 3.7b. The torch is located in the bottom left corner of the visualizations.

Note that this is a two dimensional axisymmetric model, meaning that an integer number of holes cannot be represented on the torch tip. Instead, one hole is represented which possesses the same gas exit velocity as would be seen with four holes in reality (nominally corresponding to 3 SLPM through four holes of diameter 1 mm; 15.9

m s^{-1}). The hole is positioned on a pitch circle diameter of 20 mm and the gas viscosity is that of nitrogen at 1000 K. It should be noted that a consequence of the model being axisymmetric is that while the gas exit velocity is correct, the total flow rate is higher than it would be in reality. The result is that the momentum of the flow is higher than it would be in reality and therefore flow patterns such as swirl will persist farther downstream. Nevertheless, the relevance of these two dimensional simulations is found in the comparison between geometries. They offer a straightforward method for screening torch tip designs since the relative amount of gas swirl and its relative position in the reactor tube can be compared and contrasted. The ideal flow is one that maintains a large amount of swirl over a larger portion of the reactor tube.

Figure 3.7b employs the geometry that was used in the final design, which has the holes angled at 45° from the tube axis ($z = 45°$) and perpendicular to the radial vector (i.e. along the circumferential vector, $r = 90°$). The injection streamline is clearly visible and is seen to impinge on the wall relatively close to the torch tip. From here, the gas continues to move down the axis of the tube at which point a zone of strong swirl (large circumferential velocity) is observed, which also happens to be located on the boundary of recirculation. It is believed that it is this recirculation in combination with the high circumferential velocity that is ultimately responsible for the plasma stabilization. The circumferential velocity should therefore be maximized and if possible, the length of this high-swirl region should be extended along the tube axis to reduce the dependence on torch position.

Figure 3.7c shows the effects of decreasing the pitch circle diameter of the injection holes from 20 mm to 16 mm. In this case, the magnitude of swirl as well as its persistence along the tube axis are decreased which will reduce the torch's ability to centralize the plasma and will also mean the torch will need to be positioned more precisely in relation to the plasma. Figure 3.7d has the injection holes angled with $z = 45°$ and $r = 45°$ which also decreases the length of the swirl region, although its magnitude is likely acceptable. Figure 3.7e increases the gas exit velocity to 21.2 m s^{-1}, corresponding to 4 SLPM rather than 3 SLPM. A strong and lengthened swirl region is produced, meaning that larger flow rates are likely to stabilize the plasma effectively, as expected. Finally, Figure 3.7f reproduces the condition from Figure 3.7b but the kinematic viscosity has been replaced with that of hydrogen which is $\sim$6.7 times higher than the value used for nitrogen in the preceding simulations. It is clear that the magnitude of swirl decreased and the region of maximum swirl moves significantly closer to the torch. Also noteworthy is the fact that the recirculation zone is fully visible in this case, whereas it extends beyond the field of view for the low viscosity cases. With this increased viscosity it appears that plasma stabilization will be more difficult. While operating at 100% hydrogen is not likely, this trend may be indicative for instances where hydrogen is added to a nitrogen plasma.

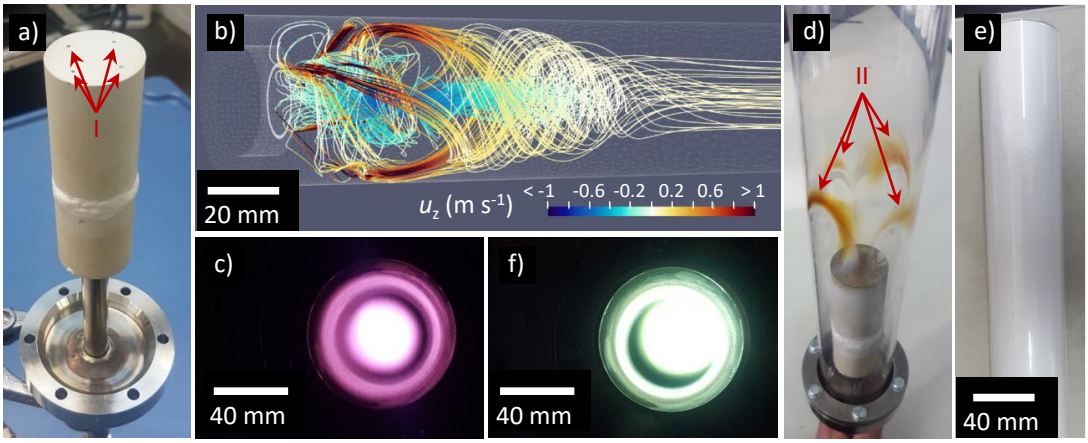

Fig. 3.8 (a) Perspective view of swirl torch including four angled gas injection holes, (b) 3D CFD flow visualization including colour traces of axial velocity, u_z (right is positive), (c) axial view of nitrogen plasma using swirl torch, (d) quartz tube damage from nitrogen-hydrogen mixture, (e) quartz tube with boron nitride powder coating on inner surface, and (f) nitrogen plasma immediately after application of boron nitride coating

The final design consisted of the geometry used in Figure 3.7b ($z = 45°$ and $r = 90°$). The torch itself is shown in Figure 3.8a where the injection holes are also marked (I). The torch is mounted on a stainless steel rod and its position relative to the plasma can be varied, similar to the axial torch. A three dimensional CFD model of the final condition was also provided by Filip Gökstorp (Figure 3.8b) and again shows the axial velocity (u_z), clearly demonstrating the recirculation pattern along the tube axis. If the plasma is positioned in this zone, it will be stable and centralized. An axial view of such a plasma (nitrogen) is shown in Figure 3.8c.

The swirl torch has been proven to stabilize plasmas using flow rates as low as 3 SLPM. The ability to operate with a low flow rate is important since this corresponds to a long residence time - a critical feature for CNT growth. The swirl torch should in theory also be capable of handling higher hydrogen fractions than the axial torch since there is a larger separation between plasma and tube wall. In practice however, a secondary effect has been observed when hydrogen is included in the plasma. Despite the fact that the plasma itself is far from the tube wall, the four gas jets from the torch are still sufficiently hot to incite hydrogen-quartz reactions. The effects are displayed in Figure 3.8d where four damaged regions from the gas impinging on the reactor tube are visible (II). A simple solution to counteract this effect is to apply a thin coating to the reactor tube that will not react with the hydrogen. A boron nitride spray was applied to the tube (Figure 3.8e) and this immediately resolved the issue. Using a fresh boron nitride coating, the plasma must be operated for several minutes before starting a production process since any loose boron nitride is vaporized in the plasma (Figure 3.8f). This results in contaminating particle production, although as the plasma

returns to its normal color and particle production ceases, the system is again pure and ready for use. When stable, background particle concentrations equivalent to those from the axial torch are observed (often $<10^3$ cm^{-3}). In this configuration, the system can be operated indefinitely with at least 50% hydrogen, with no apparent damage to the torch or reactor tube.

3.6 Material Selection

Selection of materials for the plasma system can be challenging since the materials must satisfy many criteria simultaneously and are often subjected to extreme conditions. The two components that are subjected to the highest stresses and wear are the reactor tube and plasma torch. Since these components are exposed to the microwave field, they must be transparent to microwaves, and must withstand the high temperatures produced during plasma generation. Ceramics are an obvious choice in this case. Relevant properties of several ceramics are shown in Table 3.1. Among the materials listed are quartz and alumina, which are inexpensive and readily available, but are too hard to be machined with standard tools. Several other ceramics which can be machined have also been included such as Macor and Duratec, in addition to more specialized materials such as boron nitride and Shapal.

The three most important properties of the ceramic components used in the plasma system are their maximum working temperature, thermal shock resistance, and chemical stability. The stability of the ceramic at high temperatures is vital since the plasma itself is several thousand degrees and components nearby may reach temperatures well above 1000°C. It is for this reason that quartz as well as Macor and Duratec are unfavourable: their maximum working temperatures may be acceptable for some low energy or non-thermally conductive plasmas, but in other cases the conditions can easily exceed these operational limits. Nevertheless, these materials (particularly quartz) do have their uses, as will be discussed further in this section.

Thermal shock resistance is equally as important as maximum working temperature. Unlike a furnace, the plasma can be started nearly instantaneously, resulting in extremely high heating rates for nearby components (potentially in excess of 100 K s^{-1}). As a result of the brittle nature of many ceramics, the build-up of thermal stresses from the rapid heating can result in cracking and fracture failure. While thermal shock resistance is not an independent material property, it can be deduced from the combination of material strength, thermal expansion coefficient, thermal conductivity, and manufacturing method. As the component is heated, internal stresses may accumulate but these are reduced if the material has a low thermal expansion coefficient or a high thermal conductivity - allowing the material to reach thermal equilibrium more quickly. A high ultimate strength also allows the material to withstand larger stresses

(thermal or otherwise). However, in practice, given the high stiffness of ceramics and the dramatic increases in stress caused by even small cracks, ultimate strength is often not a good indicator of material resilience. Among the materials in Table 3.1, those with low thermal expansion coefficients have the highest resistance to thermal shock. Boron nitride, Shapal, and quartz are all very resilient in this category. Note that quartz has a very low thermal conductivity, but since its thermal expansion coefficient is so low (an order of magnitude lower than Shapal and even half that of boron nitride) it is still able to survive high heating or cooling rates. Both boron nitride and Shapal have very high thermal conductivities (nearly two orders of magnitude higher than all other ceramics here except alumina), making them ideal for applications with fast temperature changes. Moreover, since boron nitride is formed simply by compressing its powdered form and is not sintered, thermal stress can also be relieved as the particles are still able to move a small amount relative to one another. For these reasons, it is effectively impossible to damage a boron nitride component from thermal shock.

Also important is the material's behaviour in the microwave field. While many ceramics can broadly be described as being transparent to microwaves, none are perfectly transparent. Instead, they may absorb microwave energy, causing unnecessary heating and may also modify the mircowave field in the waveguide, making plasma generation more difficult. A property that describes the interaction of the ceramic with electromagnetic waves is the dielectric constant. As is evident from Table 3.1, the dielectric constant of all listed ceramics is similar. Alumina does exhibit a slightly higher value but in practice this is insignificant. All materials are sufficiently transparent to this microwave frequency that plasma generation is not greatly affected. In contrast, water has a dielectric constant of approximately 80 and a perfect conductor will have a dielectric constant of infinity so in fact, all the listed ceramics are highly transparent to microwaves. It is important to note that dielectric constant often increases with temperature [156–158] which can lead to increased microwave absorption, a runaway heating effect, and cessation of plasma generation. This phenomenon is noted in Chapter 6.

3.6.1 Reactor Tube

The two materials to be considered for the reactor tube are alumina and quartz, as the other ceramics are prohibitively expensive and may not be sufficiently strong to act as a reactor tube. Both are examined below.

Alumina: Alumina is able to operate up to a high temperature of roughly 1700°C which is helpful when processes require a large amount of power and consequently generate significant heat. Alumina is also very chemically inert and is not noticeably reduced in the presence of hydrogen. Despite its advantages, the severe limitation of alumina reactor tubes is their vulnerability to thermal shock. Plasma systems operate

Table 3.1 Material properties of various ceramics considered for plasma system components [159–162]

Material	Quartz	Alumina	Macor	Duratec	Boron Nitride	Shapal
Composition	SiO_2	Al_2O_3	SiO_2 MgO Al_2O_3 K_2O B_2O_3 F	Ca_2SiO_4	BN	AlN BN
Thermal Conductivity (W m^{-1} K^{-1})	1.46	26-35	1.46	0.49	78-130	100
Maximum Temperature (°C)	1100	1700	1000	1000	>2000	1900
Thermal Expansion Coefficient ($K^{-1} \times 10^{-6}$)	0.54	8.0	12.3	6.6	1.0	5.2
Dielectric Constant	3.8	9.0-10.1	5.64	2.4-5.4	4.0	6.8
Machinable (Y/N)	N	N	Y	Y	Y	Y

in such a way that their ignition is nearly instantaneous which causes extreme thermal gradients. In this work to date, it has not been possible to reliably operate any plasma using alumina tubes aside from argon at low power since the tubes crack upon start-up, as shown by (I) in Figure 3.9a. One exception to this is very small diameter reactor tubes (3-6 mm OD). These tubes are small enough that the plasma is in contact with the entire inner surface of the reactor tube, reducing the risk of thermal inhomogeneity that normally results in cracking. Despite the more even heating, the proximity of the plasma to the reactor tube means that heating is severe for gases other than argon. Using nitrogen, which itself is not particularly conductive, heating of the tube becomes so severe (likely beyond 1500°C) that the alumina softens and deforms, such as with (II) in Figure 3.9b. This process causes small fractures in the tube that are likely to cause complete failure the next time the tube is used. The inclusion of even a few percent hydrogen exacerbates this heating problem further. Therefore, while multiple configurations for alumina reactor tubes have been explored and are discussed in

Chapter 6, none have been deemed satisfactorily robust under the conditions required for the CNT synthesis processes.

Quartz: Conversely, quartz is commonly used in plasma processes since its low thermal expansion coefficient makes it resistant to thermal shock, and most plasma diagnostics and spectroscopy measurements are performed using quartz due to its optical transparency. The drawbacks of quartz include its relatively low temperature limit and the fact that it is easily reduced in the presence of hydrogen. Excessive heating can be caused by plasma adhering to the tube wall, and this results in etching of the quartz to form the white marks labeled (III) in Figure 3.9c, and in some cases softening or melting as with (IV). Small cracks may also form such as those in (V) in Figure 3.9d and reduction from hydrogen is apparent in (VI) where the tube wall has turned yellow and brown (as the quartz is reduced then later oxidizes back to less crystalline forms of SiO_2). Excessive heating can be mitigated by increasing the tube diameter so the gap between wall and plasma is larger, which in turn reduces the amount of heat conducted to the walls (though as discussed in section 3.5, care must be taken to ensure the gas flow pattern is conducive to a stable, central plasma for tubes with large diameters). Reactivity with hydrogen can be partially mitigated by ensuring the plasma does not directly touch the wall; however, in some instances such as with the swirl torch, the high-velocity hydrogen impinging on the tube wall can still react with the quartz despite the fact that it is not in an ionized state. In this case, a thin boron nitride coating was applied to the inner surface of the tube. The coating shields the quartz from reduction and as a secondary function, also helps distribute heat more evenly around the tube since its thermal conductivity is much higher than that of quartz. Ultimately, the most robust and versatile reactor tubes are quartz (in conjunction with an injection torch) which are in some cases coated with boron nitride powder depending on the plasma gas composition. In this way, the plasma system can be run nearly indefinitely and the tube may only need to be replaced on a time scale of weeks or months. For highly optimized systems, the tube lifetime may be unlimited.

3.6.2 Plasma Torch

As the torch designs used in this work are bespoke, they must be fabricated from machinable ceramics. This makes alumina and quartz infeasible since specialized diamond-tipped tools are required for machining of these materials. Instead, four machinable ceramics have been tested, namely Macor, Duratec, boron nitride, and Shapal. Each is discussed in detail below.

Macor and Duratec: Macor is the most widely available machinable ceramic and is comprised of a mixture of oxides (primarily SiO_2). Unfortunately, its low thermal conductivity and high expansion coefficient make it susceptible to thermal shock. Similarly, Duratec, which is composed of calcium silicate, is typically used

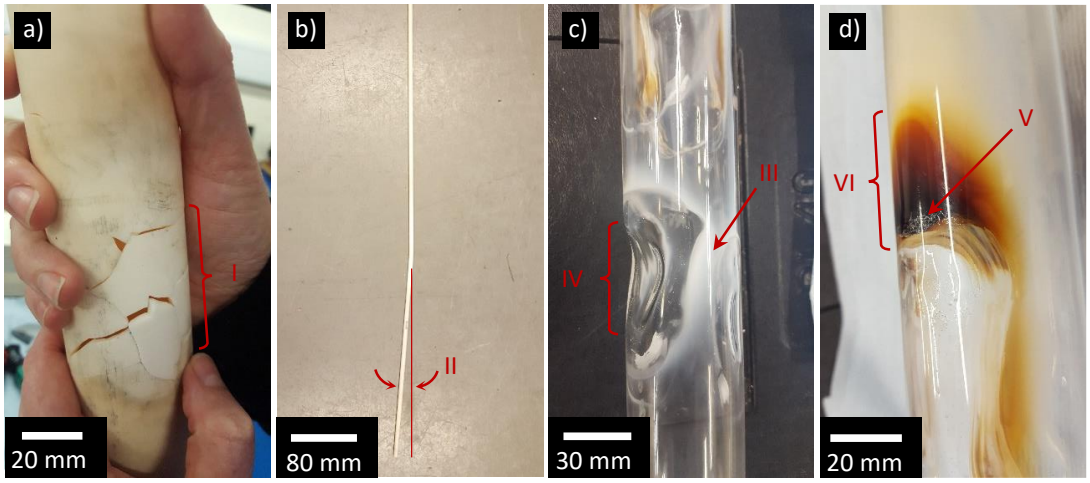

Fig. 3.9 Failure mechanisms of reactor tubes including (a) cracked 50 mm OD alumina, (b) softened and bent 6 mm OD alumina, (c) etched and softened 50 mm OD quartz, and (d) 50 mm OD quartz with small fractures and chemically reduced region from hydrogen exposure

for thermal insulation given its extremely low conductivity. Both Macor and Duratec have maximum usage temperatures of 1000°C which may be suitable for plasma gases which have low thermal conductivities but is not sufficient for more conductive plasmas such as those including hydrogen. In practice, robust torches have not been fabricated from either Macor or Duratec. Plasma start-up has caused shock fractures and steady operation has overheated the materials to the point where they melt. Therefore, it was necessary to pursue more high performance ceramics for the torch construction.

Boron Nitride: In general, nitrides are excellent choices for plasma applications where extreme temperature gradients and high temperatures may be encountered. Boron nitride has a high thermal conductivity and very low expansion coefficient. It is for this reason that it is very resistant to thermal shock. Moreover, in inert environments, boron nitride possesses a very high maximum use temperature which is helpful for conductive plasmas such as helium or hydrogen which readily transfer heat to the torch. Boron nitride is typically fabricated by pressing its powdered form into large blocks from which smaller pieces can be cut and machined. As a result, pure boron nitride tends to be very soft, and can be scratched or broken easily. In fact, the Knoop hardness of pressed boron nitride is 39 MPa [163] which is lower than that of keratin, the protein that comprises hair and nails ($\sim$ 150 MPa) [164]. For comparison, the Knoop hardness of alumina is 20.6 GPa [159]. Given its chalky consistency, it is not possible to bond or cement pure boron nitride components. Nevertheless, the axial torch fabricated from boron nitride proved highly successful and has withstood at least 100 hours of operation and at least as many thermal cycles. This torch has never failed from shock and only exhibits a small amount of wear on its tip from occasional plasma contact.

Shapal: Contrary to pure boron nitride, Shapal (consisting of a mixture of boron nitride and aluminum nitride) exhibits substantial hardness and is much less prone to scratching or chipping, yet can still be machined with standard tools. The increased hardness also means that small or detailed features can be machined and will not wear or change shape over time. Shapal also shares the high thermal conductivity and maximum use temperature characteristic of boron nitride. The vortex torch fabricated from Shapal has performed well, with no signs of wear or stress from thermal shock or excessive temperature. Shapal is highly recommended for plasma applications.

3.7 Powder Feeder

One of the major advantages of a plasma-based process is that precursors can be introduced in ways that would not be possible if a traditional furnace is used. Traditionally, precursors must be introduced either as a vapour or in solution, meaning that the choice of precursor material is limited by vapour pressure and solubility. However, as the plasma can achieve temperatures of several thousand degrees (significantly higher than a furnace), solid precursors can be used which are directly vaporized in the plasma. Therefore, coarse powders which are inexpensive and readily available are viable options. These powders could include elemental metals, metal oxides, sulphur, or silicon, all of which have been tested as part of this work. In this work only elemental metal powders have been implemented for material production.

Many commercial powder feeders exist but nearly all have mass throughputs that are far too high for the lab-scale work presented here. This work requires several tens of milligrams per minute yet the feeders available on the market process hundreds of milligrams per minute to several grams per minute, or even more. It was therefore necessary to explore other options and to conduct some or all of the development in-house.

3.7.1 Fluidized Bed Feeder

The first concept considered was a fluidized bed feeder. In this design, powder rests on a plate containing small holes through which a gas is passed. The upward flow of the gas "fluidizes" the powder, and some of the powder is carried up with the gas and out of the feeder. The limitation of this style of feeder is that the feed rate is linked to gas flow rate which can affect the behaviour of the plasma. Moreover, dense powders (such as the elemental metals used here) have high settling velocities meaning that they cannot be carried any significant horizontal distance before settling out of the flow.

For low Reynolds numbers, the settling velocity of a particle can be determined from:

$$u_{\mathrm{t}} = \frac{\rho_{\mathrm{b}} d^2 g}{18\mu}, \tag{3.11}$$

where u_{t} is terminal or settling velocity, ρ_{b} is bulk density, d is diameter, and μ is dynamic viscosity. For a 60 μm aluminum particle in air, the settling velocity is approximately 0.29 m s^{-1}, meaning that any horizontal sections of tubing must be extremely short to ensure acceptable powder penetration. As a secondary problem, a powder mixture of iron and aluminum has been used for this work; however, the lower density of aluminum means that it is fluidized more effectively than iron and the ratio passed to the remainder of the process is unknown. In conclusion, a fluidized bed design was determined not to be feasible for this project and given the high densities and settling velocities of powders used here, gravity fed systems were explored as alternatives.

3.7.2 Orifice Feeder

The simplest version of a metered gravity fed powder feeder consists of powder flowing through a small hole of known diameter. One practical example of this feeding mechanism is an hour glass. The powder flow through an orifice can be characterized using an empirical relation known as the Beverloo equation:

$$\dot{m} = C_{\mathrm{bev}} \rho_{\mathrm{b}} g^{\frac{1}{2}} \left(d_{\mathrm{o}} - k_{\mathrm{bev}} d_{\mathrm{p}}\right)^{\frac{5}{2}}, \tag{3.12}$$

where $\dot{m}$ is the mass throughput of powder, ρ_{b} is the bulk material density, g is acceleration from gravity, d_{o} is orifice diameter, d_{p} is particle diameter, and C_{bev} and k_{bev} are dimensionless constants. Given the $\left(d_{\mathrm{o}} - k_{\mathrm{bev}} d_{\mathrm{p}}\right)$ term, it is clear that the Beverloo equation predicts cessation of powder flow when the particle diameter approaches the orifice diameter. This is to be expected since several particles nearly the size of the orifice would be able to jam the flow of material. The Beverloo equation is normally quoted as being valid for orifice diameters down to six times the particle diameter [165]. For particles with diameters of approximately 60 μm (like those used in this work), this corresponds to a minimum orifice diameter of 0.360 mm, or 14.17 thousandths of an inch. Using a bulk density of 5000 kg m^{-3} (a mixture of iron and aluminum) and C_{bev} and k_{bev} values of 0.60 [166] and 1.5 [167] respectively (midpoints of their respective ranges used), the mass flow rate of powder for this orifice size is 675 mg min^{-1}. This value represents the minimum mass throughput possible with this particular powder and feeder design, and is in fact still too large for the applications considered in this work where a rate of several tens of milligrams per minute is ideal.

Beyond the ultimate limitation of feed rate is the problem of powder not flowing effectively on its own. This phenomenon is mild to moderate for metal powders but severe for non-metal powders such as metal oxides, silicon, or sulphur, which will almost never exit an orifice this size using gravity alone. A vibration motor (eccentric weight on a small DC motor) was fitted to the side of the orifice to induce powder flow. While this was successful for a short period of time, it was also found that small orifices (even those larger than six particle diameters) were prone to clogging which stops the feed process entirely. This was the case even for relatively fluid elemental metal powders. It is therefore necessary to use a feeder based on a different mechanism.

3.7.3 Rotating Feeder

A commercial rotating powder feeder unit was found whose minimum feed rate was close to the rates needed for this process. The feeder, shown in Figure 3.10a, consists of a cylindrical hopper in which powder for dispensation is stored. An adjustable motor is situated on top of the hopper and a rotating shaft protrudes down to the bottom of the hopper. Fitted to the end of the shaft (I) is a cone-shaped component with a spiral profile on its underside. This component, shown in green, is depicted in Figure 3.10b along with its operating principle. As the cone rotates, powder is accumulated by the spiral and guided towards a large ($\sim$10 mm) central hole in the bottom plate. Initial tests of this feeder showed that while the average feed rate near the lower limit of the feeder was appropriate for this work (tens of milligrams per minute), at rates below several hundred milligrams per minute the delivery was very unsteady. This was caused by two factors: if large clumps of powder are present, they are able to pass through the feeder and even if the powder is well-dispersed, it accumulates around the edge of the hole and a large amount will suddenly fall through. As a result, the process will not be steady, and additionally, large powder clumps do not have sufficient surface area to be properly vaporized during their short residence time through the plasma. Two sets of modifications have been designed to accurately control the feed rate of the powder and ensure that clumping and agglomeration is kept to a minimum.

The ideal modifications are (1) decrease the gap between the cone and bottom plate so that the maximum height the powder can build up before falling into the central hole is minimal, and (2) reduce the diameter of the hole to decrease the circumference where powder is able to build up. The resulting concept and operating principle is shown in Figure 3.10c, while the bespoke components are displayed in Figure 3.10d. The spiral profile on the cone (II) has been modified to match a broad conical profile on the bottom plate (III) which rests on the powder feeder outlet (IV), and the plate hole has been reduced from 10 mm to 3 mm. The smaller hole circumference ensures that less powder is able to accumulate immediately beside the hole and the raised profile of the bottom plate ensures that the height the powder is able to accumulate (up

to the underside of the rotating cone) is also reduced. As such, very little powder is in a position to fall through the hole at any given time. In matching the spiral profile to the raised bottom plate, any powder clumps are crushed before passing through the hole. This design resulted in an effective feeder for elemental metal powders with good flowability. The flowability of a powder can be quantified using the Hausner ratio, which represents the ratio of tapped density to bulk density [168]. Low ratios ($<\sim 1.15$) correspond to free-flowing powders and high ratios ($>\sim 1.15$) correspond to powders that clump and agglomerate [168]. Metal powders tend to be free-flowing and in the case of iron, a Hausner ratio of approximately 1.05 was measured [169].

The feeder developed in this thesis was able to repeatedly deliver steady flow rates of iron and aluminum powder as low as 10 mg min^{-1}, yet could still supply several hundred milligrams per minute at maximum speed. Despite these successes, this design exhibited limitations, particularly for powders with poor flowability such as metal oxides (e.g. iron oxide which has a Hausner ratio of 1.2 to 1.3 [170]), sulphur, or silicon. Although the feeder design does not allow large clumps of powder to pass through, powders which are very susceptible to clumping will instead compact between the bottom plate and rotating cone, which will often stop the powder feed entirely. Therefore, for consistent feeding of clumping and poorly flowing powders, another design was required which did not cause compaction.

To this end, two additional modifications were implemented and the resultant feeding mechanism is shown in Figure 3.10e. The spiral profile on the cone was replaced with angled fins (Figure 3.10f, component V) and the bottom plate containing a single hole was replaced with a fine copper mesh (VI) supported with a steel plate containing many large holes (VII), both of which are placed on top of the outlet (VIII). In this way, the powder is forced down by the fins and broken up as it passes through the mesh, yet rotation of these fins does not cause compaction. Given the low flowability of the oxides, very little material naturally falls through the copper mesh unless forced to do so by the rotating fins. Secondly, the large agglomerated chunks of powder are broken up as they pass through the mesh, improving vaporization in the plasma. While the agglomerating tendency of the powder is not completely eliminated, agglomerates entering the plasma now have at most the diameter of the copper mesh spacing ($\sim$0.5 mm) and this represents a significant improvement. It should also be noted that powders with good flowability cannot be used with the mesh/fin configuration since the powder easily falls through the mesh by itself. Therefore, a powder feeder configuration must be selected based on the type of powder in question: non-clumping or agglomerating powders such as elemental metals should use the spiral cone configuration whereas powders prone to agglomeration through water/humidity absorption, static charging, or mechanical locking should use the mesh/fin configuration. Between the two designs presented here, a wide range of

powder compositions can be introduced into the plasma in an accurate and repeatable manner between rates of approximately 10 mg min^{-1} to several hundred milligrams per minute.

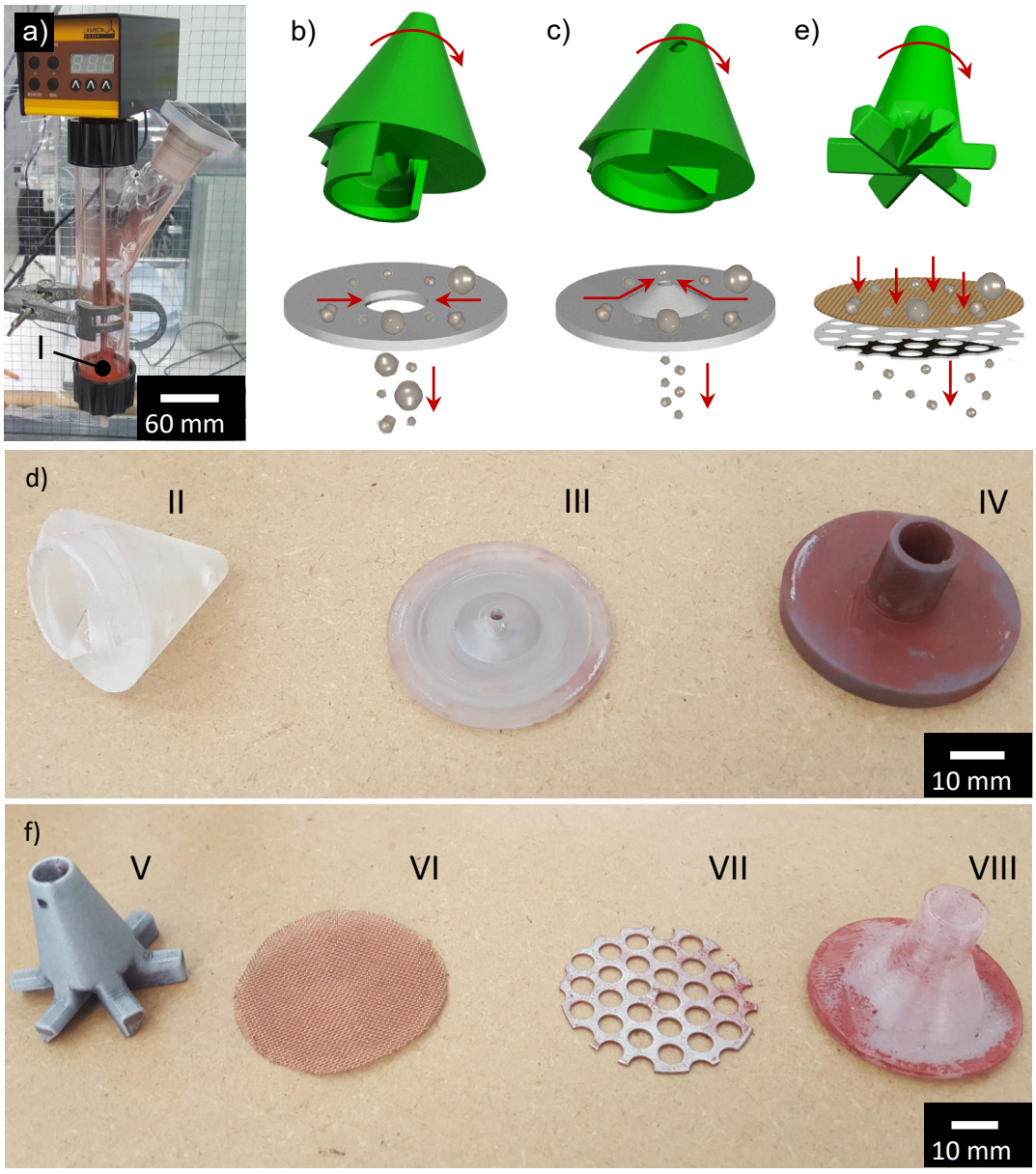

Fig. 3.10 (a) Commercial powder feeder, (b) standard components and feeding mechanism, (c) feeding mechanism of improved spiral cone and raised base profile with (d) corresponding fabricated parts, (e) feeding mechanism for fin cone and mesh plate with (f) corresponding components

3.8 Conclusions

This chapter has outlined the principles of microwave plasma operation as well as behaviours of various gases at atmospheric pressure. It has also discussed developments pertaining to plasma stability, equipment longevity, and precursor introduction. In particular, it has been noted that the microwave field is not directly responsible for igniting the plasma, and free electrons must already be present to initiate an ionization cascade from electron-neutral collisions. A handheld tesla coil is used to provide the free electrons and an argon atmosphere provides the most favourable conditions for ignition. After the plasma has been ignited, the gas mixture can be changed.

A wide range in plasma behaviour has been observed for different gases and this also results in a range of effects on the surrounding equipment. Argon exists as unstable filaments which adhere to the reactor tube wall. Conversely, nitrogen and helium plasmas exist as spheres or ellipsoids which also have a propensity for adhering to the reactor tube wall but can be centralized if the appropriate gas flow patterns are created.

Thermal conductivity of the plasma gas is a particularly important characteristic for plasmas since it influences not only its shape but also its effects on the surrounding equipment. A higher thermal conductivity corresponds to a spatially larger plasma since adjacent atoms are more easily heated to temperatures conducive to ionization. A higher thermal conductivity also means that the plasma is more likely to damage the reactor tube and it becomes increasingly important that the plasma is stable and centralized. The inclusion of hydrogen not only increases thermal conductivity but the plasma also becomes a strong reducing agent which can severely damage a quartz reactor tube.

Several mechanisms have been developed to stabilize the plasma. Mechanically-driven paddles were first installed to induce vorticity into the gas flow but this was unsuccessful for two reasons: the maximum vorticity was not sufficient to stabilize the plasma and the fact that the paddles had to be mounted some distance away from the plasma meant that the vorticity was even lower by the time the swirling gas reached the plasma region. Ceramic torches were then developed, with the first being the "axial flow torch" which relied on the generation of a high velocity sheath region to prevent plasma formation too close to the tube wall. This design was highly effective at stabilizing and centralizing the plasma and was used for a large portion of the work presented here. Despite its success, the axial flow torch must be used in small diameter tubes, meaning that when the gas's thermal conductivity is high, heating of the reactor tube can be severe even if the plasma is not directly touching the wall. To prevent this, another torch was developed. This "swirl torch" imparted vorticity to the gas and could not only generate much higher swirl than the paddles but could also be mounted

much closer to the plasma. The swirl torch allows a larger diameter tube to be used which in turn reduces heating. As a result, plasmas with higher conductivity (i.e. larger hydrogen fractions) can be used.

After optimization of the plasma system, precursor introduction was also developed in the form of a powder feeder. Several designs were tested including a fluidized bed, orifice feeder, and a positive displacement rotational feeder. The commercial rotating feeder was deemed the most viable but in its standard configuration it was not able to deliver powder at a steady rate for low throughput. Design modifications were made to the key components of the feeder, resulting in a system which is able to deliver steady and repeatable quantities of powder even at mass throughputs as low as 10 mg min^{-1} for powders with both good and poor flowabilities.

With the designs presented here, objective (1) pertaining to the development of continuous and stable operation of the plasma system has been met. The system is now able to operate nearly indefinitely in a continuous, stable, and repeatable manner and is able to handle a variety of gas mixtures. Accumulating tube damage has been greatly reduced and in many cases totally eliminated, and because the plasma does not contact any solid surfaces, the particle generation is low (often lower than the ambient concentration in the lab). Its ability to accept and vaporize a variety of precursors including solid powders has also been realized. The system is now ready to be used for production of CNT materials, although it is helpful to quantify the system to better understand its limits and provide starting information for any models that may be developed in the future. The following chapter therefore deals with determination of plasma properties, particularly its temperature and electron density.

Chapter 4

Measurement of Plasma Temperature and Electron Density

4.1 Introduction

This chapter addresses objective (2) and presents a method of measuring plasma temperature and electron density using commonly available and inexpensive equipment, and that does not require complex or time consuming post-processing. This is accomplished through introduction of rubidium into the plasma for OES measurements. While more accurate techniques undoubtedly exist, this method may be more widely applicable as it can be performed for <£1000 and data analysis is simple. Results from this study can be used to confirm that the plasma is indeed suitable for vaporization of the chosen precursor materials and this data could be a key starting point for future aerosol models on materials synthesis using similar plasma processes.

4.2 Experimental Setup

A simple 3D schematic of the experimental setup is displayed in Figure 4.1a, and a more detailed configuration is presented in Figure 4.1b. Plasma is generated using the axial flow torch when nitrogen or hydrogen are used (BOC, 99.998% and 99.999% respectively); however, the torch is not necessary for operation with argon (BOC, 99.998%). Generally, a central gas flow of approximately 1 SLPM is used, along with a sheath gas flow of between 3 and 8 SLPM.

Rubidium is introduced using atomization and subsequent drying of a dilute aqueous RbCl (Sigma Aldrich, 99.8%) solution with a concentration of approximately 2 mg mL^{-1}. A piezo atomizer is used to generate a mist which is then passed through a desiccant dryer to remove the water, resulting in an aerosol of RbCl particles. The RbCl aerosol is introduced into the plasma through the central torch flow.

Spectroscopic measurements were taken using a collection lens mounted in front of the optical access port on the side of the waveguide, as seen in both Figure 4.1a and b. A collection filter is used in conjunction with a 50 μm optical fibre to pass light into either an Oceanoptics 2000+ or Oceanoptics 4000 spectrometer with ranges of 190 to 890 nm and 345 to 1040 nm respectively, and a resolution of 1.5 to 2.3 nm. Note as well that the response of the optical fibre and spectrometers is not uniform across the collected wavelengths, so calibration must be performed using a known white light source.

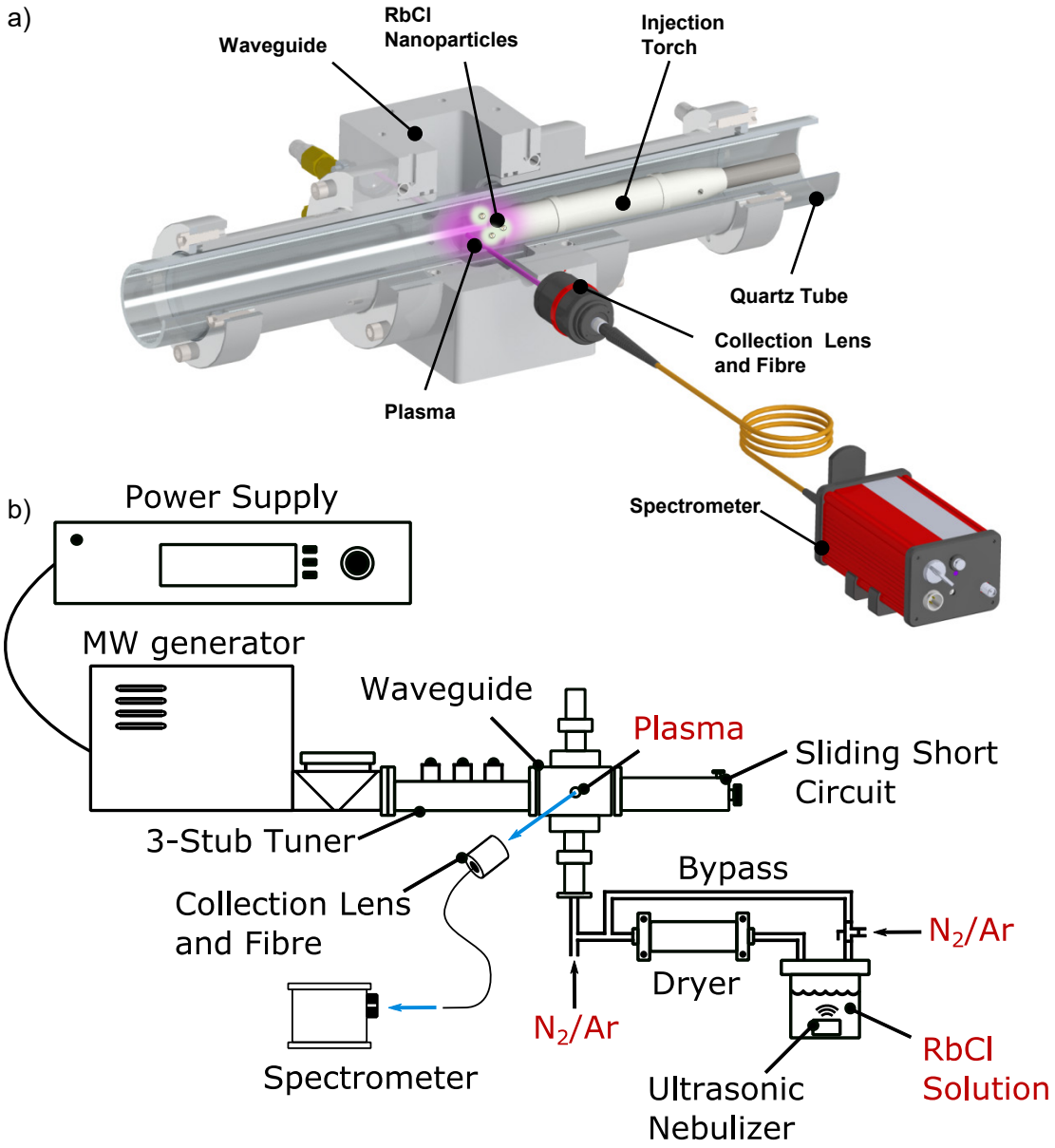

Fig. 4.1 (a) 3D schematic of rubidium chloride introduction and emission spectrum data collection, and (b) experimental setup for production of RbCl particles and subsequent introduction to plasma

4.3 Methods

4.3.1 The Boltzmann Plot Method

The Boltzmann plot method is a well established technique for calculating the excitation temperature of a plasma by examining the relative population densities of various electron energy states and correlating them to a temperature. An important criterion for the validity of the Boltzmann plot method is that the plasma is in local thermodynamic equilibrium (LTE). From Ohno et al. [101], if the LTE condition is satisfied, the intensity of light (I) emitted upon de-excitation from an upper energy state (i) to a lower energy state (j) can be related to the energy of the upper state (E_i) through the following equation:

$$\frac{I_{ij}\lambda_{ij}}{A_{ij}g_i} = \frac{hcN}{4\pi G(T_\mathrm{exc})}\exp\left(-\frac{E_i}{k_\mathrm{b}T_\mathrm{exc}}\right). \tag{4.1}$$

Here, λ_{ij} is the wavelength of light emitted from de-excitation, A_{ij} is the probability of the ij transition (Einstein constant), g is excitation degeneracy, h is Planck's constant, c is the speed of light in a vacuum, N is the total number concentration of the particular charge state, k_b is Boltzmann's constant, T_exc is excitation temperature, and G is the product of internal partition functions of the particular charge state, i.e. $G(T_\mathrm{exc}) = \sum_i g_i \exp\left(-\frac{E_i}{k_\mathrm{b}T_\mathrm{exc}}\right)$. Equation 4.1 can be linearized by taking the natural logarithm to yield the relation used in the Boltzmann plot method [101]:

$$\ln\left(\frac{I_{ij}\lambda_{ij}}{A_{ij}g_i}\right) = -\frac{E_i}{k_\mathrm{b}T_\mathrm{exc}} + \ln\left(\frac{hcN}{4\pi G(T_\mathrm{exc})}\right). \tag{4.2}$$

Boltzmann plots can then be constructed by plotting $\ln\left(\frac{I_{ij}\lambda_{ij}}{A_{ij}g_i}\right)$ against the upper energy level of the transition E_i. Excitation temperature can be extracted from the linear regression line since the slope is equal to $-\frac{1}{k_\mathrm{b}T_\mathrm{exc}}$.

4.3.2 Electron Density Estimation from Saha Equation

Electron density gives an indication of the degree of ionization within a plasma. In general, plasmas containing easily ionized species, as well as those at high temperature or high pressure, will exhibit the largest electron densities. While methods exist which can directly measure electron density and have been discussed in Chapter 2, it was not feasible to perform these techniques with the equipment available. In particular, Stark broadening can be used although this requires a high-end spectrometer since the width of the emission line in question is critical. While more affordable spectrometers like those used here still give good intensity response, the line widths are not particularly

accurate since their resolution is wider than the typical emission line width. Instead, an estimation of electron density can be made that does not require quantification of line widths at all. The estimation is based on the assumptions that the plasma is in LTE and only singly-charged ions exist. The Saha equation as presented in Equation 1.1 in Chapter 1 is:

$$\frac{N_{k+1}}{N_k} = \frac{2}{N_e}\left(\frac{2\pi m_e k_b T_{exc}}{h^2}\right)^{\frac{3}{2}} \frac{G_{k+1}}{G_k} \exp\left(-\frac{E_{\infty,k+1} - E_{\infty,k}}{k_b T_{exc}}\right), \tag{4.3}$$

k can be taken as 0 to produce only neutral (N_0) and singly charged (N_1) atoms and molecules. The assumption can also be made that $G_1 \approx G_0$. The G values may vary by a factor of two or three, yet this is negligible in comparison to the rest of equation 4.3 which can vary by many orders of magnitude. The ion concentration of a given species x then becomes:

$$N_{1,x} = 2\frac{N_{0,x}}{N_e}\left(\frac{2\pi m_e k_b T_{exc}}{h^2}\right)^{\frac{3}{2}} \exp\left(-\frac{E_{\infty,1,x}}{k_b T_{exc}}\right). \tag{4.4}$$

The total number density of atoms, molecules, and ions of all species can be determined from the ideal gas law ($N = P/k_b/T_{exc}$). The neutral portion of a given species can be determined by subtracting the ion density of that species from the product of the total particle concentration and the atomic fraction of the species in question: $N_{0,x} = NF_x - N_{1,x}$. Since only singly-charged ions are present at these temperatures, to preserve charge equilibrium, the electron density must be equal to the sum of ion densities of all species:

$$N_e = \sum_x N_{1,x}. \tag{4.5}$$

4.4 Emission Spectra

Given that LTE atmospheric pressure microwave plasmas have temperatures of several thousand degrees, they are sufficiently energetic to produce singly charged positive ions, yet even these charged atoms will account for $\ll 1\%$ of the total population in the case of most gases. Further, a negligible number of atoms will have higher charge states (i.e. +2 or more). Therefore, for atmospheric pressure microwave plasmas, the emission spectrum should be dominated by excited neutral atoms with a small presence of singly-charged ions.

In many cases, the Boltzmann plot method has been used with emission lines from the plasma gas itself [67, 70, 78, 90–93]. This requires a monatomic gas since these express much simpler electron transitions than molecular gases because the latter is also subject to rotational and vibrational motion. As a comparison to the new proposed

technique explored in this chapter, argon has also been used for the Boltzmann plot method.

At this point it is important to clarify the phenomenon of electron transitions and their corresponding light emission. Figure 4.2a shows schematic representations of electron transitions for argon and rubidium. For a given charge state, the electron energy is bounded by the ground state (E_{gr}) and the ionization energy (E_∞). Light emission occurs during de-excitation of an electron as it moves from a high energy state (E_i) to a lower energy state (E_j). In doing so, a photon of wavelength (λ_{ij}) is released. Importantly, while the energy differences (and therefore emitted wavelength of the argon and rubidium transitions) may be similar, they do not necessarily occur between similar energy levels within the atom, as depicted in Figure 4.2a. In particular, all recorded argon transitions have upper state energies (E_i) of at least 13 eV whereas rubidium transitions have E_i values typically around 2-3 eV.

The emission spectrum of argon is displayed in Figure 4.2b. The strongest emission lines are the neutral (Ar_0) lines situated in the near-infrared. The spectrum exhibits narrow peak profiles as is typical for monatomic gases. Additional smaller Ar_0 lines are seen in the near-ultraviolet (UV) between 400 and 450 nm as shown in the inset plot of Figure 4.2b. An ionized Ar_+ line is also observed in the inset at 335 nm. Note that another line is present in the spectrum at 589 nm, and this can likely be attributed to sodium impurities in the quartz. As only pure argon was present in the plasma at this time, trace quantities of sodium are likely being liberated and excited by the argon plasma as its filaments move across the quartz tube surface. Other studies have noted the same phenomenon and work has even been conducted to measure plasma gas temperature via van der Waals broadening from this emission line [81].

In contrast to the sharp, distinct peaks of argon, nitrogen plasma exhibits a series of broad humps across the visible range, as shown in blue in Figure 4.2c. The first three peaks between 350 and 500 nm are ionic emission lines whereas the remaining humps between 500 and 900 nm are neutral molecular and atomic nitrogen lines. Evidently, it is impossible to visually distinguish individual emission lines from the broad humps, and consequently the Boltzmann plot cannot be used on nitrogen gas, although a variation of the Boltzmann plot method can be employed to determine vibrational temperature using tabulated Franck-Condon factors [93]. This technique is beyond the scope of the work presented here. This is inconvenient since many of the processes developed in this work use nitrogen as a major carrier gas constituent. Therefore, quantification of nitrogen plasma temperature must be performed indirectly via a tracer species, in this case rubidium. As a group I element, rubidium possesses a single electron in its outer shell, resulting in a simple and well-characterized emission spectrum that can be easily interpreted even with an inexpensive spectrometer.

The changes in emission spectrum from rubidium addition are displayed in Figure 4.2c and d. Figure 4.2c shows the entire emission spectrum where most notably the two largest Rb_0 emission lines are visible at 780 and 795 nm. The sodium emission line is also visible for larger Rb flows. Since the nitrogen plasma does not contact the quartz tube, it is unlikely that the sodium originates from the same place as it would when argon is used. Instead, sodium likely exists as an impurity in either the RbCl or water in which it is dissolved. Figure 4.2d also shows the emission spectra of nitrogen and rubidium but focuses on the high-energy wavelengths where additional smaller rubidium lines are visible. In particular, several ionized Rb_+ lines as well as another sodium line are seen in the UV.

In addition to the appearance of Rb emission lines, a noteworthy feature of these spectra is the fact that the nitrogen emission decreases as more Rb is introduced. The nitrogen profile is hardly recognizable for the larger Rb input of 0.8 SLPM. Importantly, this indicates that it may no longer be appropriate to describe this plasma as a "nitrogen plasma" and instead, it likely consists predominantly of Rb ionization. Unfortunately, it was determined that high Rb concentrations such as that used to produce the green spectrum in Figure 4.2c and d were necessary to observe many of the low-intensity emission lines necessary for accurate results from the Boltzmann plot. Therefore, while this technique cannot technically be described as non-invasive since it does still alter the behaviour of the plasma, it can still be deemed minimally-invasive since probes or sensors are not inserted into the system and the plasma's fundamental operation is unchanged. As described above, techniques such as this are favourable for characterization of relatively high temperature plasmas like those used here, and still present considerable advantages over physical measurement techniques.

While nitrogen is used as the primary carrier gas for the majority of this work, hydrogen is a vital component as well, given its function as a reducing agent and ability to create favourable conditions for CNT growth. The effects of hydrogen addition to the nitrogen plasma were also investigated and the resulting emission spectra are displayed in Figure 4.2e and f. In comparison to the standard nitrogen plasma spectrum, addition of 12.2% (1.0 SLPM) hydrogen results in a decrease in the nitrogen emission spectrum. Also visible are the characteristic atomic hydrogen alpha, beta, and gamma lines at 656, 486, and 434 nm respectively. Similar to the nitrogen-only case, addition of rubidium to the nitrogen-hydrogen mixture causes a dramatic change in the spectrum with the characteristic nitrogen and hydrogen lines disappearing almost entirely.

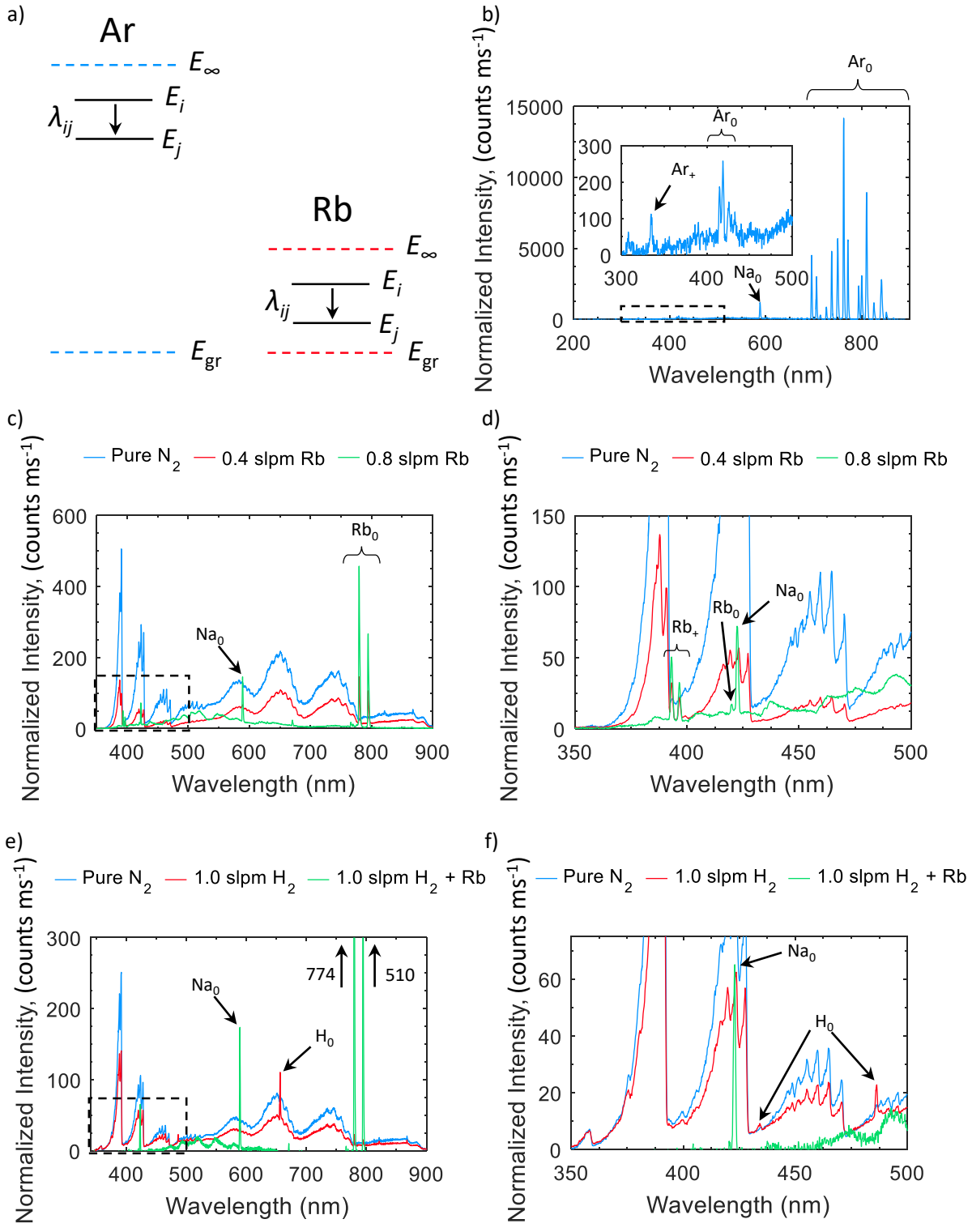

Fig. 4.2 Schematic of electron transitions (a) as well as plasma emission spectra including (b) pure argon where the inset shows low intensity lines contained in the dotted box, (c) nitrogen with various quantities of rubidium, (d) high-energy portion of nitrogen-rubidium spectra, (e) nitrogen with hydrogen and rubidium, and (f) high-energy portion of nitrogen-hydrogen spectra

4.5 Excitation Temperature

Extraction of the peak intensities from the emission spectra in Figure 4.2 have then been used to create Boltzmann plots and subsequently determine the excitation temperature of their respective plasmas. Intensities were measured based on peak area. In instances where peaks overlapped but could still be resolved, peak area was taken to be double the area of the peak's non-overlapped side, i.e. assuming a symmetric peak. In cases where multiple emission lines should be present but could not be resolved within a single peak, these lines were excluded from the Boltzmann plot. The Boltzmann plot for argon is displayed in Figure 4.3a, with the line data shown in Table 4.1. Given the high ionization energy of argon, the upper state of many of its given electron transitions are situated at high energies (between 13 and 15 eV). It is immediately obvious that while many lines can be extracted from the argon spectrum, many do not fall on what should be a linear profile with respect to their emission intensity versus upper transition level energy. As a result, uncertainty exists in the temperature calculation. Relatively large uncertainties in the Boltzmann plot have been reported previously [101]. The argon filament instability can be neglected as a significant source of this uncertainty since the relative intensities of the emission lines are stable and repeatable despite the variations in absolute intensity. Secondly, it is conceivable that much of the spread in the data originates from the poor signal-to-noise ratio of some of the low intensity lines such as those in the UV portion of the spectrum. This is false however, since many of the lines which disagree strongly with the slope in Figure 4.3c are the most intense in the recorded spectrum, possessing excellent signal to noise ratios. The most likely cause for the deviation from theory is that the plasma is not in perfect equilibrium, and this hypothesis is verified and discussed in section 4.6.3 below. Nevertheless, the excitation temperature of the argon plasma in this instance was determined to be 7118 K. Despite the uncertainty, this is within the range of other studies on argon microwave plasmas which commonly possess temperatures between 5000 and 6000 K [71, 106], but may vary between 4000 and 14 000 K [70, 88].

In contrast to the large uncertainty in slope and therefore excitation temperature of argon, the Boltzmann plot from the Rb-N_2 plasma shows good grouping and a reliable slope, as seen in Figure 4.3b, with line data presented in Table 4.2. While there are fewer emission lines when compared to argon, the rubidium lines express a highly linear trend, and in this case the temperature was determined to be lower than that from the argon plasma, at 6390 K. This agrees closely with Leins et al. [69] who used very similar equipment and conditions and calculated a maximum excitation temperature of 5800 K.

The effects of hydrogen addition to the nitrogen plasma were also explored, and the corresponding Boltzmann plots are shown in Figure 4.3c. Under these particular

Table 4.1 Properties for argon transitions used in Boltzmann plot [171]

λ_{ij} (nm)	Transition	g_i	A_{ij} (s^{-1})	E_i (eV)
667.73	$4P_{1/2} \rightarrow 4S_{3/2}$	1	2.36×10^5	13.480
687.13	$4D_{1/2} \rightarrow 4P_{1/2}$	3	2.78×10^6	14.711
696.54	$4P_{1/2} \rightarrow 4S_{3/2}$	3	6.40×10^6	13.328
703.03	$6S_{3/2} \rightarrow 4P_{5/2}$	5	2.67×10^6	14.839
706.72	$4P_{3/2} \rightarrow 4S_{3/2}$	5	3.80×10^6	13.302
714.70	$4P_{3/2} \rightarrow 4S_{3/2}$	3	6.30×10^5	13.283
727.29	$4P_{1/2} \rightarrow 4S_{3/2}$	3	1.83×10^6	13.328
738.40	$4P_{3/2} \rightarrow 4S_{3/2}$	5	8.50×10^6	13.302
763.51	$4P_{3/2} \rightarrow 4S_{3/2}$	5	2.45×10^7	13.172
794.82	$4P_{3/2} \rightarrow 4S_{1/2}$	3	1.86×10^7	13.283
826.45	$4P_{1/2} \rightarrow 4S_{1/2}$	3	1.53×10^7	13.328
852.14	$4P_{3/2} \rightarrow 4S_{1/2}$	3	1.39×10^7	13.283
866.79	$4P_{3/2} \rightarrow 4S_{1/2}$	3	2.43×10^6	13.153

Table 4.2 Properties for rubidium transitions used in Boltzmann plot [171]

λ_{ij} (nm)	Transition	g_i	A_{ij} (s^{-1})	E_i (eV)
620.63	$6D_{3/2} \rightarrow 5P_{1/2}$	4	2.95×10^6	3.557
629.83	$6D_{5/2} \rightarrow 5P_{3/2}$	6	3.71×10^6	3.557
740.82	$7S_{1/2} \rightarrow 5P_{3/2}$	2	3.87×10^6	3.262
761.89	$5D_{3/2} \rightarrow 5P_{1/2}$	4	2.12×10^6	3.186
775.77	$5D_{5/2} \rightarrow 5P_{3/2}$	6	4.35×10^6	3.187
780.03	$5P_{3/2} \rightarrow 5S_{1/2}$	4	3.81×10^7	1.589
794.76	$5P_{1/2} \rightarrow 5S_{1/2}$	2	3.61×10^7	1.559

conditions, the nitrogen-only case was found to have a temperature of 5417 K. The addition of both 0.5 and 1.0 SLPM hydrogen (6.5 and 12.2% respectively) showed remarkably similar results, decreasing the temperature to between 4200 and 4300 K. The effect of hydrogen decreasing the plasma temperature has also been noted by Bings et al. [71], although interestingly Jovicevic et al. [106] found that introduction of 2.7% hydrogen increased excitation temperature along the axis of the plasma. It is interesting that in this case, the temperature does not vary when the hydrogen fraction is doubled.

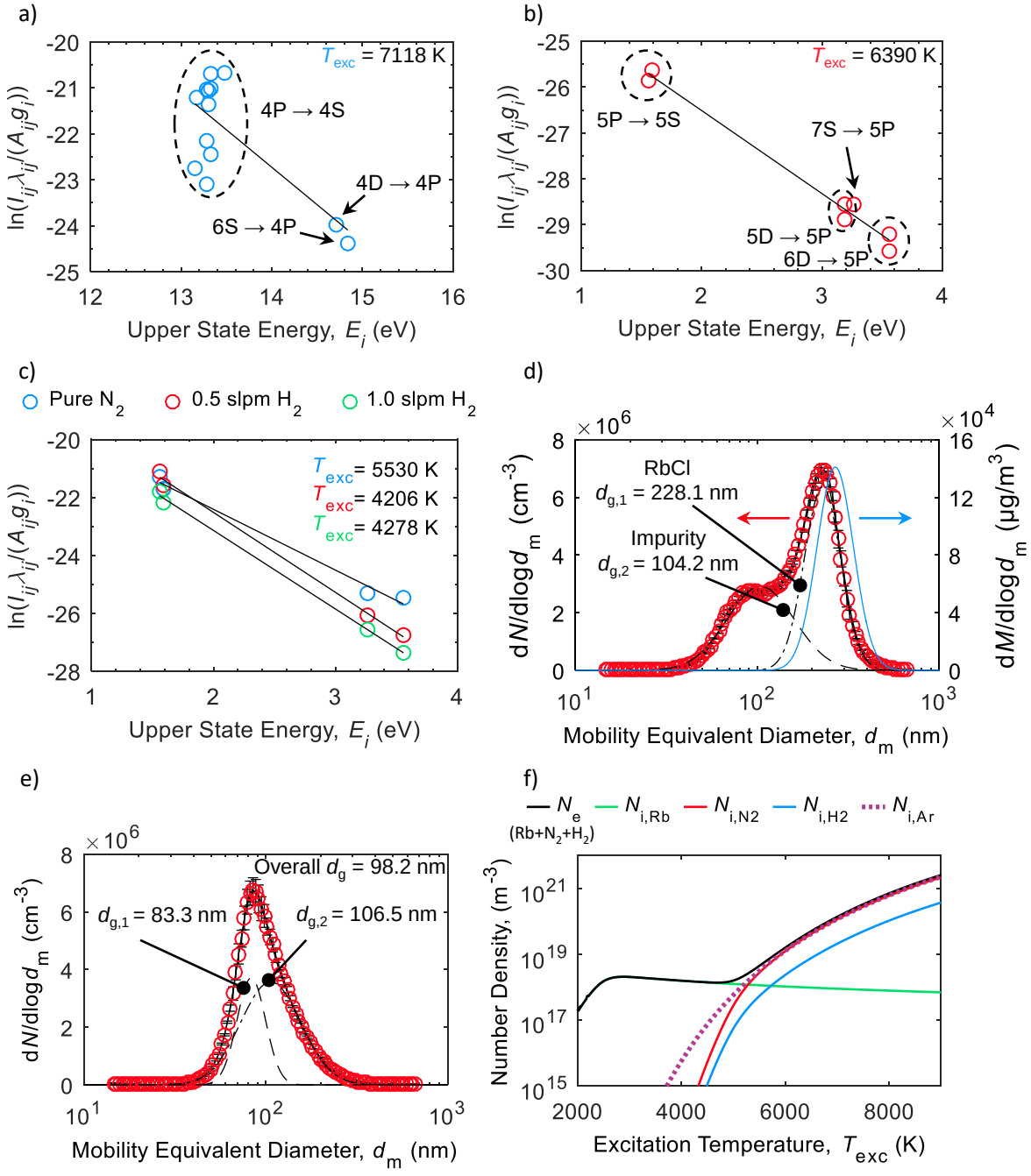

Fig. 4.3 Bolzmann plots for (a) Ar, (b) N_2, and (c) N_2 with various H_2 flow rates. Also shown are SMPS size distributions for (d) RbCl solution and (e) purified water. Both are comprised of three scans and error bars represent one standard deviation. (f) presents electron and ion densities for Ar as well as N_2-H_2-Rb plasmas

4.6 Electron Density

4.6.1 Rubidium Characterization

Determination of electron density requires that the relative abundances of each species is quantified. This is simple for gases since their atomic concentrations can be determined as long as the temperature, pressure, and flow rate are known. Calculation of the atomic concentration of rubidium is more complex but can begin by quantifying the RbCl aerosol size distribution. This can be measured using a scanning mobility particle spectrometer (SMPS), which sweeps though a range of electrical mobilities (a property that can be related to particle size or "mobility-equivalent diameter"). Contained in the SMPS is a differential mobility analyzer (DMA) which allows a narrow (nearly monodisperse) particle size range to pass though at a given time, and the corresponding concentration is measured using a condensation particle counter (CPC). Scanning through the range of the DMA results in a size distribution of the incident aerosol. A more detailed explanation of the SMPS and the operating conditions used for this work are presented in Appendix A.

A representative size distribution using an RbCl concentration of 2 mg mL^{-1} is displayed in Figure 4.3d. Here, d_m is mobility-equivalent diameter and $dN/d\log d_m$ represents the number concentration of a particular size bin, normalized by bin width. The data has been fit with the summation of two lognormal distributions. The larger distribution possesses a geometric mean diameter (d_g), geometric standard deviation (σ_g), and total concentration of 228.1 nm, 1.26, and 1.61×10^6 particles per cm^3 respectively. The smaller distribution contains a d_g, σ_g, and total concentration of 104.2 nm, 1.53, and 1.35×10^6 cm^{-3} respectively. The fact that the two distributions are visibly distinct indicates that two species are likely present after drying. The larger is likely to be RbCl particles; however, the smaller peak could be composed of other impurities in the water such as sodium or potassium salts. To confirm this, size distributions were also recorded from atomized water that did not contain RbCl and this is shown in Figure 4.3e. Despite the fact that the water should ideally be pure and therefore no particles should exist after the drying step, impurities do exist and are the cause of the smaller peak in Figure 4.3d. This is common for spray drying processes and is known as "residue after drying". The impurity size distribution in Figure 4.3e was also fit with two lognormal distributions since its skew results in a poor fit from a single distribution. This impurity size distribution has an overall d_g similar to the small peak in Figure 4.3d (98.2 nm compared to 104.2 nm), although in this case the impurity-only sample contained a higher total concentration of particles than the small peak in Figure 4.3d: 2.21×10^6 cm^{-3} versus 1.35×10^6 cm^{-3}. This is inconsequential however, since number concentration of aerosols can commonly vary by an order of magnitude or more. The similar diameter between the two impurity peaks is

more reliable and is the useful metric for proving this hypothesis. The reasonable conclusion based on these plots is that the RbCl particles can be represented by the larger lognormal distribution only.

The total atomic concentration of rubidium can be determined by first calculating the mass concentration of the RbCl aerosol from a size distribution such as that in Figure 4.3d. The mass distribution can be calculated by computing the mass of a particle in each size bin then multiplying this by the number concentration in each bin, as follows [172]:

$$\left(\frac{\mathrm{d}M}{\mathrm{dlog}d_\mathrm{m}}\right) = \rho_\mathrm{b}\left(\frac{\pi}{6}{d_\mathrm{m}}^3\right)\left(\frac{\mathrm{d}N}{\mathrm{dlog}d_\mathrm{m}}\right) . \tag{4.6}$$

Here, $\mathrm{d}M/\mathrm{dlog}d_\mathrm{m}$ is the mass concentration of each bin, normalized by bin width and ρ_b is the bulk density of RbCl (2.80 g cm^{-3}). The bulk density will be a good approximation since the particles are compact. The total mass concentration (M_RbCl) can then be determined by multiplying each bin by the bin width and summing over all bins:

$$M_\mathrm{RbCl} = \sum\left(\frac{\mathrm{d}M}{\mathrm{dlog}d_\mathrm{m}}\right)\left(\mathrm{dlog}d_\mathrm{m}\right) . \tag{4.7}$$

The atomic concentration of rubidium in the gas at ambient conditions (N_Rb) can be calculated from the total mass concentration of RbCl by accounting for the mass fraction of rubidium in the salt molecule:

$$N_\mathrm{Rb} = M_\mathrm{RbCl}N_\mathrm{a}\frac{M_\mathrm{m,Rb}}{M_\mathrm{m,Rb}+M_\mathrm{m,Cl}} , \tag{4.8}$$

where N_a is Avogadro's number, and $M_\mathrm{m,Rb}$ and $M_\mathrm{m,Cl}$ are the molar masses of rubidium and chlorine respectively. In the case of the size distribution in Figure 4.3d, the total RbCl concentration was calculated by considering only the larger lognormal distribution possessing a d_g of 228.1 nm (which constitutes ~90% of the total aerosol mass). The mass distribution is also shown in Figure 4.3d in blue, and the total RbCl mass concentration at standard conditions is 35 562 μg m^{-3}. The atomic Rb concentration is 1.77×10^{20} m^{-3} before mixing with additional gas and entering the plasma. This represents an atomic fraction of rubidium of approximately one atom in a million relative to the nitrogen carrier gas entering the plasma.

4.6.2 Electron Density from Saha Equation

The system of equations in section 4.3.2 pertaining to the Saha equation was solved iteratively in Matlab, and the resulting plot of electron (and ion) density as a function of excitation temperature is displayed in Figure 4.3f. Argon is represented by the

dotted purple line, and its electron/ion density at the excitation temperature determined previously of 7162 K is 1.46×10^{20} m^{-3}. This corresponds to a charge fraction of 1.42×10^{-4}. This is slightly lower than the range of Choi et al. [70] who determined the electron density of their argon microplasma to be $6.5 - 7.4 \times 10^{20}$ m^{-3}.

The electron density for the N_2-H_2-Rb plasma was also determined for the case in Figure 4.3c where 1.0 SLPM H_2 is used. The multiple species present in the plasma produce a more complex electron density profile as seen with the black line in Figure 4.3f. The low ionization energy of rubidium (4.18 eV) means that a large fraction is ionized even at low temperatures. By comparison, the much higher ionization energies of nitrogen and hydrogen ($\sim$15.5 eV) cause extremely low ion concentrations to be present below 5000 K. Therefore, for lower temperatures, the free electrons originate almost exclusively from the rubidium. In this case, rubidium ionization increases until 2900 K at which point nearly the entire population of rubidium will be ionized, and the electron density is limited by the concentration of rubidium atoms in the plasma. The electron density in this regime peaks at 2900 K at 2.08×10^{18} m^{-3} and gradually decreases as temperature decreases due to expansion from the ideal gas law. Above 5000 K, the ion and electron densities from nitrogen and hydrogen become appreciable and at 5300 K the same number of nitrogen atoms are ionized as rubidium atoms, at 1.20×10^{18} m^{-3} for each species. For temperatures above 5300 K, the electron density is dominated by nitrogen and hydrogen ionization.

Note that while nearly all of the rubidium is ionized, only two Rb_+ lines were observed (394 and 397 nm), and these were relatively low intensity in comparison to the Rb_0 lines. This is because like argon (shown schematically in Figure 4.2a), Rb_+ lines are associated with de-excitation from high energy states (>19 eV). So while the plasma is sufficiently hot to nearly fully ionize the rubidium, it is not hot enough to promote a significant proportion of Rb_+ electrons to energy levels where they are able to de-excite and emit light. Therefore, the majority of the emission spectrum is still associated with Rb_0.

From the Boltzmann plot in Figure 4.3c, the excitation temperature of the plasma using 1.0 SLPM H_2 of 4278 K corresponds to an electron density of 1.48×10^{18} m^{-3}. Likewise, the overall charge fraction of this plasma is 8.62×10^{-7} although >99% of these electrons originate from the rubidium. Given that the charge fraction of nitrogen at this temperature is 4.06×10^{-10} and is similar for hydrogen, it is not likely that the plasma would be sustainable at such a low temperature without the presence of the rubidium. Conversely, when rubidium is added to a pure nitrogen plasma such as that in Figure 4.3b, the majority of the ionization pertains to the nitrogen rather than the rubidium at temperatures typical for this MW system. Its excitation temperature of 6390 K corresponds to an electron density of 3.88×10^{19} m^{-3} and a nitrogen charge fraction of 3.29×10^{-5}. The electron density and ionization fraction from nitrogen

reported here are slightly lower than those observed by Leins et al. [69] whose values were approximately 1×10^{20} m^{-3} and 1×10^{-4}, respectively. This is largely due to the fact that they used air rather than nitrogen, and the ionization energy of O_2 as well as the NO_2 that forms at high temperature are both lower than that for nitrogen, causing more electrons to be liberated. For further comparison, these results are similar to if not slightly lower than other atmospheric pressure microwave plasmas [67, 87]. In general, microwave plasmas exhibit electron densities several orders of magnitude higher than those from lower energy density plasmas such as dielectric barrier discharge [173] or those at low pressure [78]. Conversely, plasmas with higher energy densities such as arc discharge or RF induction often possess electron densities several orders of magnitude higher than those from microwave systems [76, 92, 101].

4.6.3 Validity of Assumptions and Interpretation of Results

The validity of the above calculations can be determined using excitation temperature and electron density. The overarching assumption of the Boltzmann plot method and Saha equation are that the plasma is in LTE. There are in fact two tiers of LTE - that known as partial LTE as well as complete LTE. The former is an easier condition to satisfy and is characterized by at least some electron states being in equilibrium. By extension, the Boltzmann plot method and Saha equation can still be used, although these may incur some additional uncertainty relative to a plasma in complete LTE. Naturally, complete LTE implies that all electron states behave in accordance with the Saha equation. The plasmas examined here must be checked for the condition of LTE, and must be in at least partial equilibrium for the above results to be valid and meaningful. Griem [174] presented a criterion for partial LTE, which provides a minimum electron density as a function of excitation temperature. The partial LTE criterion is:

$$N_e \geq 7.4 \times 10^{24} \frac{z^7}{n^{\frac{17}{2}}} \sqrt{\frac{k_b T_{exc}}{E_H}}, \tag{4.9}$$

where N_e is in m^{-3}, z is the effective charge acting on a given electron (i.e. $z = 1$ for a neutral atom and $z = 2$ for a singly-charged ion), n is the principal quantum number of the upper electron energy state, and E_H is the Rydberg constant. The temperature should be input in Kelvin and E_H should be in joules. The minimum electron densities to satisfy partial LTE are presented in Table 4.3. For multi-species plasmas, a minimum electron density was determined with respect to each species' lowest n value (i.e. the most conservative N_e requirement for each species). The electron density of the argon plasma is more than an order of magnitude larger than the minimum value required for partial LTE, but the conclusions that can be extracted from the N_2-Rb and N_2-H_2-Rb plasmas are more nuanced. In both of these cases, the calculated electron densities are

sufficiently large for rubidium to be in partial LTE but not large enough for nitrogen or hydrogen to be in partial LTE. Fortunately, the Boltzmann plots that have been constructed in this work use argon and rubidium, both of which are shown to be in partial LTE. Also note that the minimum required electron density for partial LTE is strongly inversely correlated with n. Consequently, even if transitions at the lowest energy states of nitrogen and hydrogen are not in partial LTE, many of their electrons at higher energy states will be. In particular, the nitrogen and hydrogen transitions from $n = 5$ or higher will be in partial LTE at 4278 K and those with $n = 4$ and higher will be in partial LTE at 6390 K. Next, the condition of complete LTE can be verified, and this criterion is also presented by Griem [174]:

$$N_e \geq 9.2 \times 10^{23} z^7 \left(\frac{E_{ij}}{E_H}\right)^3 \sqrt{\frac{k_b T_{exc}}{E_H}}. \tag{4.10}$$

N_e is still in m^{-3} and E_{ij} is the largest transition energy considered, in joules. For argon, the largest transition energy used for the Boltzmann plot is the $4P_{1/2} \rightarrow 4S_{3/2}$ transition at 668 nm. Similarly, the largest transition used in any rubidium-containing plasmas is the $6D_{3/2} \rightarrow 5P_{1/2}$ transition at 621 nm. For nitrogen and hydrogen, neither of which are used directly in a Boltzmann plot, transitions at 388 and 434 nm were used, respectively. In all cases, the observed electron densities are lower than the critical density for complete LTE. Therefore, as suspected, the plasmas examined here are not in complete LTE.

Table 4.3 Electron density in comparison to criteria for partial and complete LTE

T_{exc} (K)	Species	n	N_e (m^{-3})	$N_{e,LTE}$ Partial (m^{-3})	$N_{e,LTE}$ Complete (m^{-3})
7118	Ar	4	1.46×10^{20}	1.20×10^{19}	4.97×10^{20}
6390	N_2	3	3.88×10^{19}	1.31×10^{20}	2.41×10^{21}
6390	Rb	5	3.88×10^{19}	1.70×10^{18}	1.89×10^{21}
4278	N_2	3	1.48×10^{18}	1.07×10^{20}	1.96×10^{21}
4278	H_2	3	1.48×10^{18}	1.07×10^{20}	1.40×10^{21}
4278	Rb	5	1.48×10^{18}	1.39×10^{18}	4.79×10^{20}

The fact that the plasma is not in perfect equilibrium may explain the behaviour of the Boltzmann plots. Particularly evident in the case of argon is the fact that the agreement with the theoretically-linear trend is mediocre. The higher-energy electron states in a plasma can stay at equilibrium at the lowest electron densities, and with increasing electron density the lower energy states will begin to assume equilibrium as well (hence the inverse dependence on n in the partial LTE criterion) [174–176]. It is likely no coincidence then, that the data points pertaining to the 4P→4S transitions exhibit the worst agreement. These are the lowest energy transitions and will therefore

be the most difficult states to hold in equilibrium. Fortunately, much of this work is motivated by nitrogen and hydrogen plasmas which exhibit stronger correlations to their respective linear trendlines.

Since the temperatures of all species are equal in complete LTE, the excitation temperature is equal to both the electron temperature and the gas temperature (i.e. translational, rotational, and vibrational). Conversely, while not in LTE, the excitation temperature lies between the electron and gas temperatures and therefore represents a lower bound to electron temperature and an upper bound to gas temperature. The most relevant temperature to materials synthesis is likely the gas temperature since this will provide the majority of the energy/heat transfer to the precursors. While this technique is not capable of measuring gas temperature directly, comparisons can be made against other studies that have accomplished this with more expensive equipment or complex models. Leins et al. [69] used a similar microwave plasma system and calculated similar temperatures and electron densities to those observed here. Their plasma is also likely to possess a similar gas temperature to the one used in this work. They compared the emission spectrum of OH radical rotation to modeled spectra and found the gas temperature to be approximately 3000 K with a maximum of 3600 K. This is 50-60% of their measured excitation temperature, and while this may appear to be a large difference, in the scope of plasmas this is still relatively close. T_{gas} versus T_{exc} differences of at least an order of magnitude and perhaps several orders of magnitude are possible. It is reasonable to assume that the plasma system used for this work behaves in a similar manner and will also possess a gas temperature of approximately 3000 K. Importantly, this resembles the vaporization temperature of iron - the least volatile precursor used in processes developed in the following chapters. As such, the system should be capable of vaporizing all precursors including iron powder, provided the particles have sufficient residence time in the plasma for heat transfer to occur.

Another phenomenon that must be addressed is the cumulative nature of the collected emission spectra. While the collection lens was focused at the centre of the plasma, light emitted along the line of sight of the lens can still be collected, and as a result, spectral information is gathered not only from the plasma centre as intended but also from its near and far peripheries. An Abel transform could be used to deconvolute this signal to provide emission intensity as a function of radius. The Abel transformation was not used for this work because it introduces additional uncertainty and has been shown to have a minimal effect on peak plasma temperature (100-200 K) for a comparable plasma system [69]. That said, an opportunity for future work is to collect spectra from various locations in the plasma so a temperature profile can be constructed. This would also have the benefit of improving the repeatability of the measurements since movements of the plasma relative to the collection lens can result

in variations in the temperature values. A spatial map would guarantee that all regions of the plasma are observed.

As discussed in Chapter 2, group I elements have previously been observed to affect plasma temperature [71, 106], and therefore the results may not be perfectly representative of the plasma when rubidium (or another group I element) is not present. Moreover, due to the lower ionization energy of these elements relative to common plasma gases, the plasma, at low temperature, can be considered a predominantly rubidium plasma since its ion concentration will be orders of magnitude higher than that of the other gases. This phenomenon is evident both from the significant change in emission spectrum after rubidium addition, as well as from the calculated ion concentrations of rubidium versus nitrogen or hydrogen. Since the presence of rubidium distinctly alters the behaviour of its host plasma, OES using group I elements should be considered a "minimally-invasive" technique. Nevertheless, elements such as rubidium with relatively high principal quantum numbers are more likely to be in at least partial LTE and could allow measurement techniques such as the Boltzmann plot method to be used in a wider range of conditions, particularly at lower temperatures, than would be possible from smaller atoms.

4.7 Conclusions

This chapter has presented a quantitative study to determine plasma temperature and electron density. Rubidium was introduced as aerosolized RbCl particles to nitrogen and nitrogen-hydrogen plasmas and emission spectra were recorded. Peak intensities were extracted from the spectra and Boltzmann plots were constructed whose regression slope can be linked to excitation temperature. The nitrogen plasma was found to have an excitation temperature between 5500 and 6400 K, and the addition of hydrogen reduced the temperature by approximately 1300 K. The same technique was applied to pure argon without rubidium and its excitation temperature was determined to be 7118 K.

Electron densities for these plasmas were then estimated using the Saha equation. The nitrogen-rubidium plasma had an electron density as high as 3.88×10^{19} m^{-3} whereas when hydrogen was present, the electron density reduced to 1.47×10^{18} m^{-3}. Further, nearly all electrons in the latter case originate from the rubidium since the higher ionization energies of nitrogen and hydrogen produce very low charge fractions below 5000 K. Naturally, the higher temperature of the argon plasma corresponded to a higher electron density, at 1.46×10^{20} m^{-3}. Using criteria established by Griem [174] to verify whether or not the plasmas are in partial or complete LTE, it was determined that argon and rubidium were in partial LTE. It was also determined that nitrogen and hydrogen were not entirely in partial LTE but their higher energy electron states

likely were. In all cases the plasmas did not meet the complete LTE criterion. This is a sensible conclusion since linear agreement with the Boltzmann plot (particularly in the case of argon) is not ideal. Imperfect agreement with the linear theoretical fit likely comes from the fact that electrons in low energy states, such as those making the 4P→4S transitions for argon, require the highest electron densities to achieve equilibrium. Since the plasma is not in perfect equilibrium, its gas temperature will be slightly lower than its excitation temperature. Previous work [69] on a similar system has indicated that the gas temperature is 50-60% of the excitation temperature. In this case, the plasma's gas temperature is likely ∼3000 K which should be sufficient to vaporize adequate amounts of the precursors used in the processes developed in the next chapters.

The objective of this chapter has been to develop a simple, inexpensive, and minimally-invasive method for quantifying plasma temperature and electron density of a range of plasmas. By seeding the plasma with rubidium and recording data with a small, simple, and inexpensive spectrometer whereby the total equipment cost is <£1000, this objective (objective (2) as defined in Chapter 2) has demonstrably been met. Nevertheless, several details must be considered before applying this technique. It is likely that the presence of rubidium may alter the temperature and corresponding electron density, and may even become the dominant ionized species at low temperature. Further, since the plasmas have been determined to be in partial LTE, the Boltzmann plot can be used but may incur some additional uncertainty in comparison to a complete LTE case. The uncertainty is most likely associated with the electrons in lower energy states. These results can be implemented in the future in aerosol models that will provide a more detailed understanding of the forthcoming synthesis processes and will aid in optimizing the performance of the final materials.

Chapter 5

CNT-Metal Oxide Li-ion Battery Anode Material

5.1 Introduction

While the hierarchical structures discussed in section 2.3 (Chapter 2) have shown great benefit as LIB anode materials, many of the approaches are not scalable, using expensive or prefabricated materials with complex, time consuming, multi-step processes. The process developed in this chapter exploits the high temperature of the microwave plasma system so that inexpensive and readily available raw materials (iron and aluminum powder) can be used. This process is also fast and results in a complete synthesis time of roughly five seconds. The final material has hierarchical structure consisting of core iron and aluminum oxide nanoparticles encapsulated with a carbon coating and multiple CNTs grown from its surface. The highly conductive carbon coatings and CNTs negate the need for post process conductive additives during anode assembly.

This work shows for the first time how materials synthesized from bulk industrial powders in a fast, simple, and scalable plasma-based process can be used as high capacity anodes, and in doing so, satisfies objective (3). The resulting plasma-synthesized metal oxide materials are characterized using on-line techniques that give real-time morphology metrics of the synthesized materials, allowing for real-time process optimization. The resulting anodic materials are collected, processed and analysed within half-cell devices to determine the cycling capability of the synthesized materials.

5.1.1 Experimental Setup

The mechanisms of this process are shown in Figure 5.1a with a more detailed schematic of the experimental setup in Figure 5.1b. For this work, a 30 mm O.D.

reactor tube was used (500 mm length, 23.5 mm I.D.) along with the axial flow torch. A nitrogen flow of 9 SLPM is used as the carrier gas in the plasma (BOC, 99.998% purity).

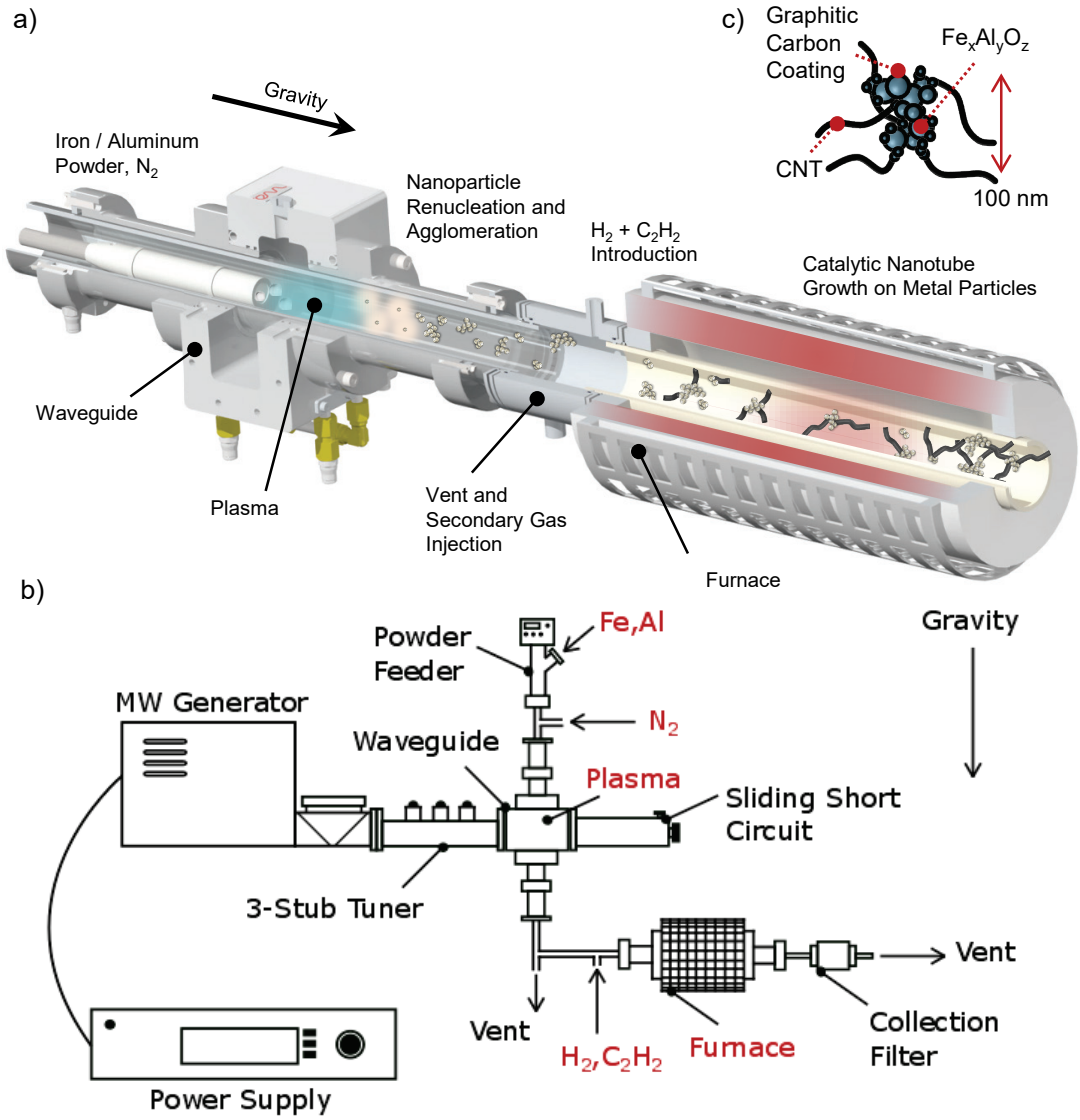

Fig. 5.1 (a) Mechanisms for synthesis of CNT-metal oxide anode material, (b) detailed experimental setup, and (c) schematic of final material

The powder feeder discussed in Chapter 3 (nominally the Lambda Doser, Lambda Laboratory Instruments, and modified with customized parts for lower and more consistent throughput) is connected to the inlet of the work tube. Powder is delivered to the plasma system in the form of elemental metals (i.e. iron and aluminum: Goodfellow, max 60 μm, 99.0% and 99.9% purity respectively) at a rate of approximately 30 mg min^{-1}.

Downstream of the plasma, the material is passed into a tube furnace (alumina tube, 500 mm total length, 300 mm heated section, 30 mm O.D., 23 mm I.D.) at 830°C.

A total flow rate of 1.7 SLPM is sent through the furnace of which approximately 1.5 SLPM is gas from the plasma (remainder of plasma gas vented to extraction), 200 sccm is hydrogen (BOC, 99.999%), and a small amount (10 – 20 sccm) is acetylene (BOC, 98.5%). CNTs and a carbonaceous coating are grown on the core particles in the furnace during the residence time of approximately 1.5 seconds. The material is then collected on polytetrafluoroethylene (PTFE) filters.

As the relatively large elemental metal powder particles ($\sim$60 μm) are fed into the plasma, they are vaporized from the extremely high temperature. Downstream of the plasma where the temperature begins to decrease, supersaturation of the metal vapours is reached, and homogeneous nucleation of metal nanoparticles occurs. The particles increase in size from surface growth and agglomerate into fractal-like agglomerates with mobility-equivalent diameters between approximately 20 nm and 200 nm.

As the particles enter the growth furnace, CNTs are grown from catalyst sites of reduced, elemental iron present on the core particles' surfaces and a graphitic carbon coating is formed on the larger primary particles. Multiple CNTs can be grown radially from each particle, resulting in the "sea urchin-like" morphology, such as that shown in Figure 5.1c. Finally, an ex-situ oxidation step is performed to complete the synthesis process.

5.1.2 Material Morphology

The hierarchical structure of the metal oxide-CNT material is shown in Figure 5.2a. Metal oxide primary particles (iron and aluminum) on the order of nanometres to tens of nanometres comprise larger fractal-like agglomerates particles (I) which are several tens to several hundreds of nanometres across. Primary particles are coated with graphitic carbon (II) and catalyse CNT growth (III). These can often be seen trapped within the CNT (IV), separate from their host agglomerate as depicted in Figure 5.2b (microscopy details in Appendix A). The agglomerate particles and CNTs agglomerate further as they deposit on the collection filter, resulting in a final material formed of a continuous matrix of metal oxide particles and CNTs as shown in Figure 5.2c. The carbonaceous coating on the particles shown in Figure 5.2d increases the short-range thermal and electrical conductivity of the material (i.e. between primary particles of a given agglomerate). The multilayer graphitic structure is shown to encapsulate most primary particles providing intra-agglomerate conductivity. The CNTs that grow from the fractal agglomerate surface (example cross-section shown in Figure 5.2e) are $\sim$10s micrometres long and allow contact between agglomerate particles for inter-agglomerate conduction. Carbonaceous components in anodes including coatings and CNTs have repeatedly been shown to increase conductivity and improve battery performance [177]. As a result, anode construction is simplified since no conductive additive is necessary. In addition, carbon conformally bonded

to the metal oxide provides more efficient electron conduction compared with an externally-mixed conductive additive such as super P (since the super P conducts electricity via point contact between the super P particles and metal oxide particles). Iron and aluminum serve as useful metals for this process since iron is a catalyst for CNT growth and multiple forms of iron oxide are excellent candidates for LIB anodes.

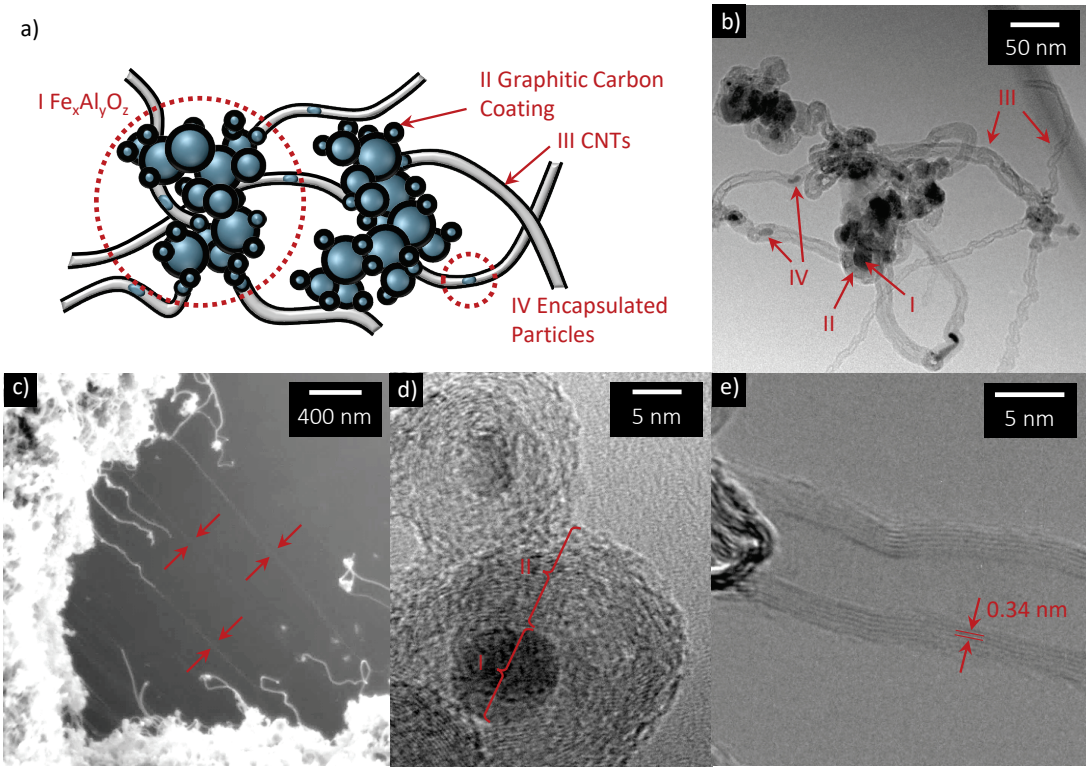

Fig. 5.2 Hierarchical metal oxide-CNT (a) material schematic and images including (b) TEM of individual agglomerate, (c) SEM of bulk material, (d) TEM of primary particle and carbon coating, and (e) single CNT cross-section. Additional images available in Appendix B.

5.2 Agglomerate Size Distribution

On-line scanning mobility particle spectrometer (SMPS) measurements of the agglomerate core particles measured at the exit of the plasma system as well as the cores after CNT growth in the furnace are presented in Figure 5.3a, and provide real-time size distribution data for the system. See Appendix A for details on SMPS measurements. The mobility diameter d_m represents the diameter of a sphere with the same drag as the measured irregular agglomerate particles. As in the previous chapter, the number concentration N is normalized by logarithmically-spaced size bin widths as $dN/(d\log d_m)$. The increase in particle size due to the growth of CNTs is represented by the shift in the geometric mean diameter (d_g) from 41 nm for agglomerated core particles to 157 nm after CNT growth. Both distributions are best fit with the sum of

two lognormal distributions since skew and additional features such as the small peak on the left side of the core particle distribution cannot be properly captured using a single lognormal distribution.

The measurement and counting of each particle within the distribution (>10^6 particles measured per scan) gives detailed statistical information not readily available from microscopy. The geometric standard deviation (σ_g) of the particles is 1.87 and 1.94 before and after growth, and given more time would decrease according to theoretical and other experimental predictions ($\sigma_g \sim 1.4$) for gas-phase nanoparticles undergoing agglomeration [178]. Particles continue to agglomerate and are lost to the wall by thermophoretic and diffusive forces to the reactor walls during the growth stage. The reactor number concentration of particles reduced from 2.18×10^8 cm^{-3} before and 6.66×10^7 cm^{-3} after the furnace, respectively.

5.2.1 Mass Mobility Relation and Primary Particle Size

While size-based particle information contributes to a partial understanding of morphology, further details can be gleaned by combining size data with mass measurements. The relation between the mobility-equivalent diameter and mass for agglomerates has the form:

$$m = C_m d_m^{D_m}. \tag{5.1}$$

Here, m is particle mass, C_m is a constant prefactor, and D_m is the mass-mobility exponent. For a spherical particle (i.e. a liquid droplet) D_m is 3, thus the particle's mass scales with diameter cubed and C_m is a function of the bulk material density, $m = (\rho_b \pi/6) d_m^3$. For a two dimensional object such as a sheet (i.e. graphene), the mass mobility exponent will be 2 and for a one-dimensional object (CNT) D_m will be 1. Fractal-like agglomerates such as those produced here (as in most non-coalescing aerosol processes) possess mass-mobility exponents between 2 and 3 since they grow in three dimensions but do not completely fill a given spherical volume. Mass-mobility exponents where $D_m \to 3$ represent compact agglomerates, whereas when $D_m \to 2$, the agglomerates contain more branching and open space, increasing the exposed surface area as depicted in Figure 5.3b.

The individual particle masses and mobility diameters were measured in series at the plasma exit, and the mass-mobility relation is plotted in Figure 5.3c to provide structural information of the core particles (information on measurement of particle mass using a centrifugal particle mass analyzer (CPMA) is discussed in Appendix A). The power-law fit to the particles measured at many different mobility diameters results in a $D_m = 2.31$. These results are similar to flame-synthesized oxide particles such as zirconium oxide [179] and silica [180] as well as metals from spark discharge

synthesis including gold [181] and copper [182]. Further, mass-mobility measurements of agglomerate particles can also be used to estimate the diameter of primary particles within an agglomerate as well as the number of primaries per agglomerate. Primary particles may be of particular importance since this functional unit dictates the surface area to volume ratio of the active material. Smaller particles will have most of their mass within several nanometres of the surface which can facilitate lithiation and delithiation processes (and should be less susceptible to pulverization). However, smaller primary particles may also be more prone to solid electrolyte interphase (SEI) formation as their higher specific surface area provides more opportunity for electrolyte breakdown [183]. Primary particle diameter can be estimated using the formulas developed by Eggersdorfer et al. [179]:

$$d_{\mathrm{pp}} = \left(\frac{\pi k_a}{6v} d_{\mathrm{m}}^{2D_\alpha} \right)^{\frac{1}{2D_\alpha - 3}}, \tag{5.2}$$

and similarly, the number of primary particles per agglomerate can be determined from:

$$N_{\mathrm{pp}} = \frac{6V}{\pi d_{\mathrm{pp}}^3}. \tag{5.3}$$

d_{pp} is the average primary particle diameter, d_{m} is mobility-equivalent diameter, N_{pp} is the average number of primary particles per agglomerate, k_a and D_α are empirically-determined constants, and V is the solid volume of the agglomerate, equal to:

$$V = \frac{m}{\rho_{\mathrm{b}}}, \tag{5.4}$$

where m is particle mass and ρ_{b} is the particle's bulk density. k_a and D_α were determined by Eggersdorfer et al. [179] as 1.0 and 1.07 respectively from work with ZrO_2 agglomerates, while assuming a well-mixed primary particle sample and minimal primary particle shielding within the agglomerate (i.e. all particles are exposed to the surrounding gas). The average primary particle diameter and number per agglomerate can be used in conjunction with the agglomerate size distribution to calculate the population-averaged primary particle diameter as follows:

$$\bar{d_{\mathrm{pp}}} = \frac{\sum \left(\frac{\mathrm{d}N}{\mathrm{dlog}d_{\mathrm{m}}} \right) (\mathrm{dlog}d_{\mathrm{m}}) N_{\mathrm{pp}} d_{\mathrm{pp}}}{\sum \left(\frac{\mathrm{d}N}{\mathrm{dlog}d_{\mathrm{m}}} \right) (\mathrm{dlog}d_{\mathrm{m}}) N_{\mathrm{pp}}}. \tag{5.5}$$

Figure 5.3d shows that the metal oxide agglomerates synthesized from the plasma system contain primary particles of diameter ranging from approximately $d_{\mathrm{pp}} = 9$

to 19 nm, with a small positive correlation between mobility diameter and primary particle diameter. Differences in primary particle diameters result from unique time-temperature profiles of the primary particles in the reactor. Higher concentration of metal vapour results in saturation at higher temperatures, thus allowing coalescing growth from coagulation. The increase in primary particle number with agglomerate size is shown in Figure 5.3e, whereby approximately nine particles are contained in a 30 nm agglomerate and increases to several hundred particles within a 200 nm agglomerate. The agglomerate size, surface area and primary particle numbers can be measured in real time from the process and monitored relative to the influence on the rates of lithium diffusion and SEI formation. The mean population primary particle diameter was 13.4 nm for those conditions that resulted in the best battery performance measured in this study.

The distribution of primary particle size as measured from transmission electron microscopy (TEM) is shown in Figure 5.3f. Statistical analysis of the primary particle size distribution from TEM resulted in an average primary particle diameter of 11.28 ± 6.85 nm which agrees well with the results of the aerosol-based method. As such, estimation of primary particle size and number through the aerosol-based method is a desirable alternative to TEM since it is a statistically robust method in which $\sim 10^6$ particles are measured and represented by each data point.

The total mass production of material was determined from the combined SMPS and CPMA measurement. To accomplish this, the mass distribution is first determined by multiplying the number-based size distribution by the particle mass-mobility function. This is similar to the calculation in section 4.6.1 [172] which determined the mass concentration of rubidium, however in this case since the particles are fractal-like instead of spherical the effective density is used in place of the bulk density:

$$\frac{\mathrm{d}M}{\mathrm{dlog}d_\mathrm{m}} = m\left(\frac{\mathrm{d}N}{\mathrm{dlog}d_\mathrm{m}}\right) = C_\mathrm{m} d_\mathrm{m}^{D_\mathrm{m}}\left(\frac{\mathrm{d}N}{\mathrm{dlog}d_\mathrm{m}}\right). \tag{5.6}$$

Total mass concentration M can be calculated by summing the distribution:

$$M = \sum \frac{\mathrm{d}M}{\mathrm{dlog}d_\mathrm{m}}\left(\mathrm{dlog}d_\mathrm{m}\right) = \sum C_\mathrm{m} d_\mathrm{m}^{D_\mathrm{m}} \frac{\mathrm{d}N}{\mathrm{dlog}d_\mathrm{m}}\left(\mathrm{dlog}d_\mathrm{m}\right). \tag{5.7}$$

Using the prefactor and mass-mobility exponent from Figure 5.3c of 1.12×10^{-5} fg nm$^{-2.31}$ and 2.31 respectively, the total mass concentration is 30.73 mg m^{-3}. Given the total flow rate of gas through the plasma system of 9 SLPM, the production rate of cores in this study's configuration is 16.6 mg h^{-1} (and approximately 33 mg h^{-1} for cores and CNTs given that the core mass fraction is $\sim$50 %). While material yield was not optimized for this study, optimizations that increase the powder feed through the plasma and reduce deposition losses on the tube walls would allow orders of magnitude higher

production. If 50% of the plasma power used in this work is dedicated to heating and vaporizing the powder mixture from room temperature to the vaporization point of iron (>2861°C), the theoretical upper limit to mass throughput is 1.15 kg h^{-1}. This indicates that even a lab-scale plasma system is capable of impressive production rates.

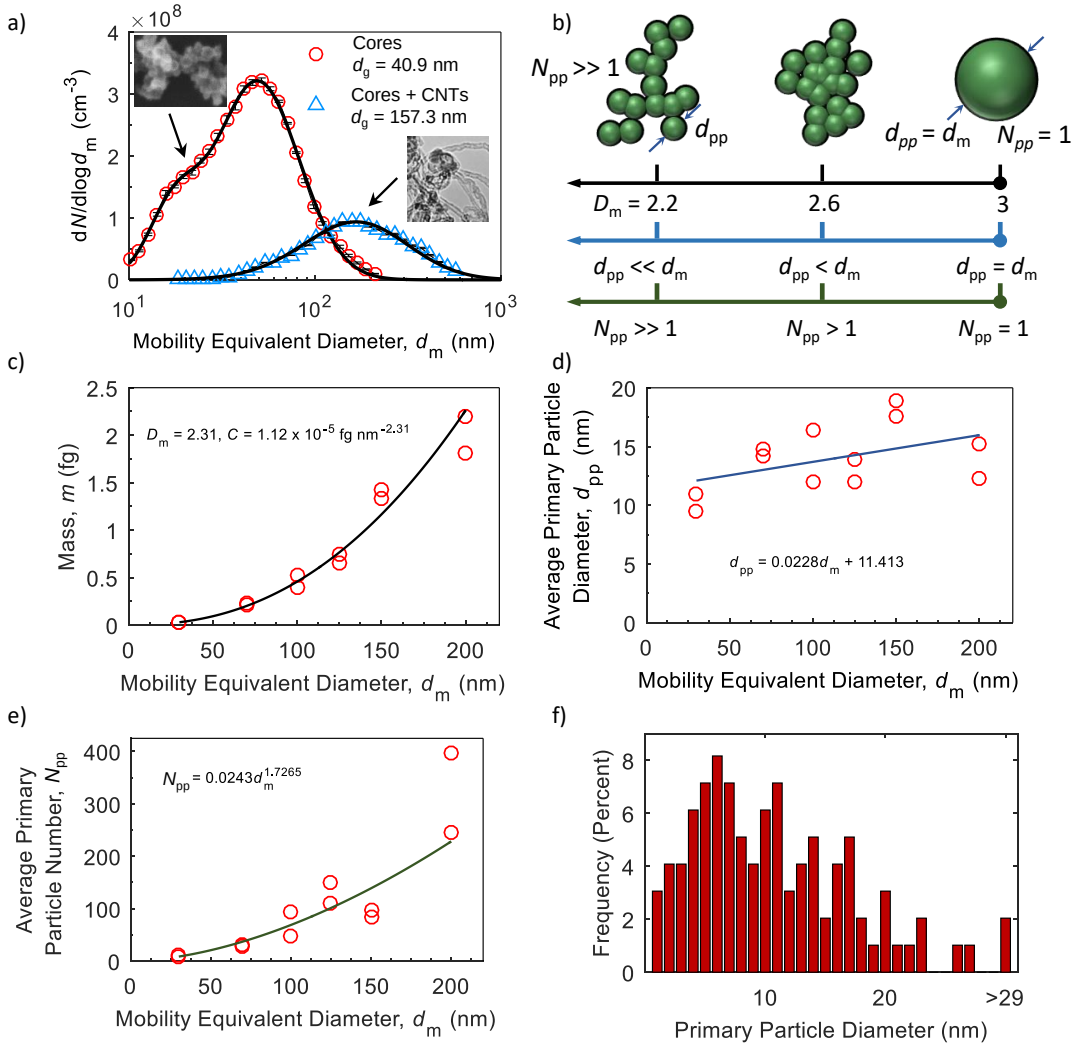

Fig. 5.3 (a) SMPS scans of core particles after plasma and cores plus CNTs after growth. Five scans were performed for each condition. Error bars represent one standard deviation, (b) schematic of particles associated with various mass-mobility exponents, (c) mass-mobility relation for metal oxide core particles, (d) average primary particle diameter, (e) average primary particle number per agglomerate, and (f) histogram of primary particle size from TEM

5.2.2 CNT Characterization

From TEM, it is evident that there is a range in CNT diameter, as shown in Figure 5.2b. On average, the CNTs have a diameter of 7.75 ± 2.74 nm with six to seven walls (see Appendix B for additional statistics on CNTs and primary particles). A single

CNT cross-section is displayed in Figure 5.2e where the expected wall spacing of 0.34 nm [184] is clearly visible. CNTs were predominantly observed growing from particles 6 nm and smaller. These particles often detached themselves from their host agglomerate and were ultimately contained within the CNT growing from them. This phenomenon is demonstrated in Figure 5.2b. Particles larger than 6 nm were often coated in layers of carbon (see Figure 5.2d), most of which is crystalline although some amorphous carbon is present as well.

Raman spectra excited at 638 nm for material produced from elemental powder is shown in Figure 5.4a. The G/D ratio is approximately 1.8. The majority of the signal from the D peak is likely due to any amorphous carbon coating the larger primary particles. A radial breathing mode (RBM) at 191.7 cm^{-1} is also visible, indicating the presence of at least a few SWNTs. From the Kataura plot in Figure 5.4b, properties of SWNTs can be determined from the RBMs. The excitement energy of 1.943 eV from the 638 nm laser can be intersected with the RBM wavenumber which shows that the peak corresponds to metallic CNTs. While other SWNTs may exist which are not resonant with the 638 nm laser (see Appendix A), the fact that these SWNTs are metallic means they will be good conductors between metal oxide cores. Given the non-discreet resonance curve of SWNTs to a given laser wavelength, as well as the continued uncertainty in the coefficients used to convert between wavenumber and diameter [185, 186], it is not feasible to match RBM peaks to specific data points/chiralities on the Kataura plot. Nevertheless, a diameter range can be extracted for these CNTs; the metallic CNTs have diameters between 1.21 and 1.39 nm.

5.2.3 Core Particle Composition and CNT Mass Fraction

As an anode in an LIB, the metal oxide particles undergo a conversion reaction as they are charged and discharged with lithium ions. This global reaction for the lithium conversion reaction process is $M_xO_y + 2ye^- + 2yLi^+ \rightleftharpoons xM^0 + yLi_2O$, where M represents a transition metal, in this case iron. To maximize energy density of metal oxide materials, a high oxygen content is required. For aluminum, the most thermodynamically stable oxide is alumina, Al_2O_3, whereas multiple stable oxidation states exist for iron, including FeO (1 O : 1 Fe), Fe_3O_4 (1.33 O : 1 Fe), and Fe_2O_3 (1.5 O : 1 Fe).

Sample oxidation was studied using several methods. Concurrent oxygen gas (0-15 sccm) injection with the nitrogen in the plasma (in-situ oxidation) showed insufficient oxidation of metals and increases in oxygen concentration competed with CNT growth. Decoupled CNT growth and core oxidation proved more effective, achieving near full oxidation of the metallic components. Plasma-produced unoxidized core particles with CNTs were collected. The resulting powder was then placed in an oxidation furnace at 300°C for one hour for ex-situ annealing. Figure 5.4c displays

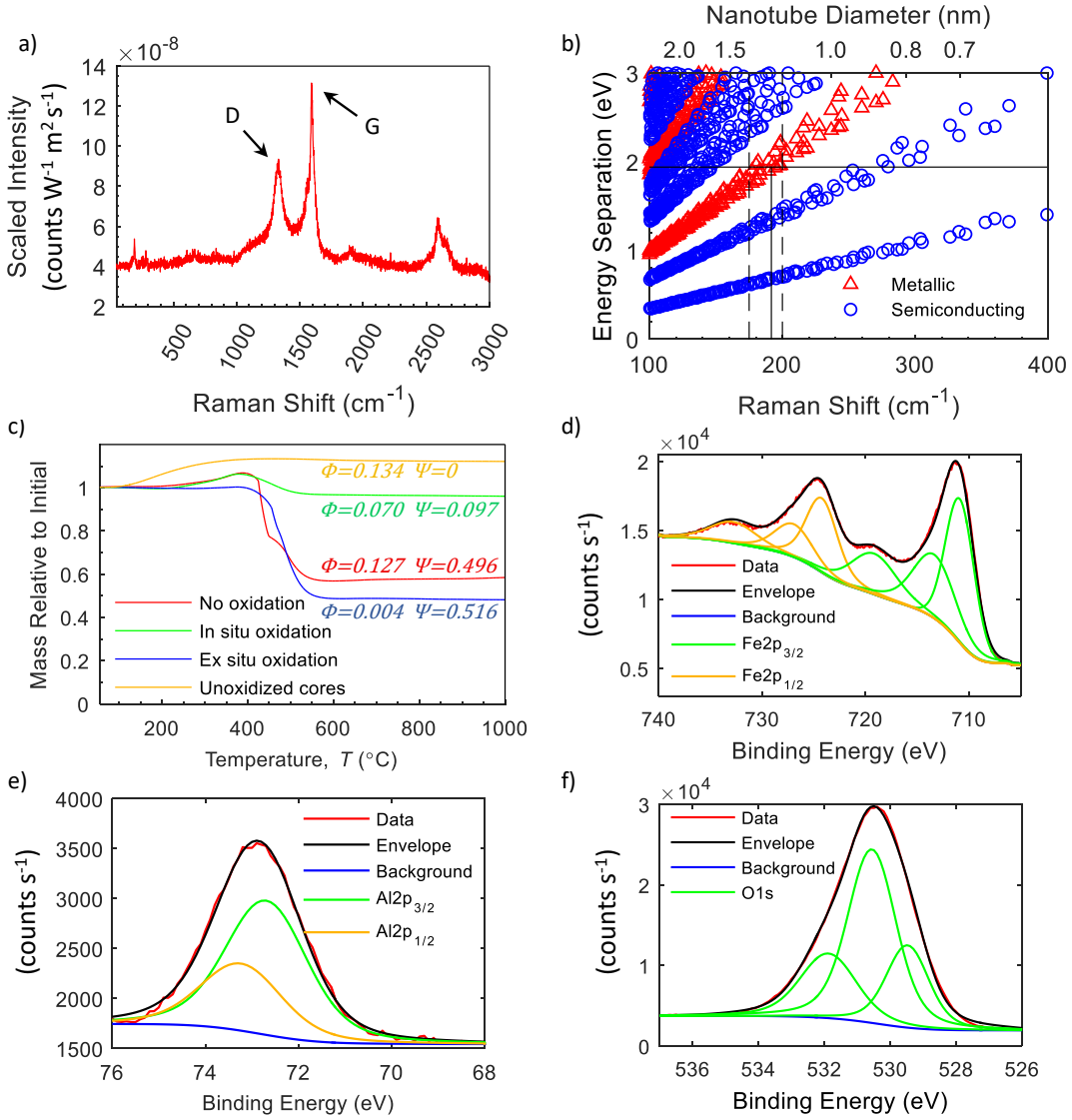

Fig. 5.4 (a) Raman spectrum of CNT/metal oxide composite material, (b) Kataura plot using RBM from Raman, (c) TGA of metal oxides and CNTs with various process modifications, where Φ is the uptake mass of oxygen during TGA relative to the initial metal oxide mass and Ψ is the mass fraction of CNTs to total product mass, and finally XPS data and curve fit for (d) iron, (e) aluminum, and (f) oxygen.

thermogravimetric analysis (TGA) characterizations of the material before and after oxidation, including in-situ oxidation and a base-case analysis using only unoxidized core particles without CNT growth. Φ represents the uptake mass of oxygen during TGA relative to the initial metal oxide mass and Ψ represents the mass fraction of CNTs to total product mass. The unoxidized cores demonstrate that oxidation is completed at a lower temperature than the start of carbon combustion, so these two processes can be correctly independently quantified from TGA. Figure 5.4c demonstrates that the unoxidized core-only (no CNTs) material appears to gain a higher percentage of mass

during TGA than other samples, but in absolute terms the increased oxidation of solely the metal is determined accounting for the non-metal fraction of material.

It is evident that without any added oxygen, the "no oxidation" and unoxidized core samples show the largest increase in mass during TGA with Φ equal to 0.127 and 0.134, respectively. When an oxidation step is included, the material is seen to uptake less oxygen during TGA. In-situ oxidation (15 sccm O_2 added to plasma) did improve core oxidation ($\Phi = 0.070$); however there is a dramatic decrease in CNT mass fraction as well ($\Psi = 0.097$). Since oxygen is required for core oxidation but a lack of oxygen is necessary for CNT growth, oxygen must be added subsequent to the CNT growth. The separation of CNT growth and core oxidation steps resulted in material that is optimized for this application: highly oxidized metal for maximum energy storage capacity and a substantial carbonaceous coating and CNT network for high conductivity and thus improved cell stability. This highlights the potential for continuous production of oxidized core particles ($\Phi = 0.004$) without adversely affecting the CNTs.

This conclusion is supported by a thermodynamic equilibrium model (compiled and run by Cen Zhang) of metal and metal oxide particle formation, shown Appendix C. Metal precursors were input in the same molar ratios observed here, along with nitrogen as the carrier gas and a small amount of oxygen which may enter the system as a leak or on the metal particles' surface. The molar ratio of these components is 18 000 N : 10 Fe : 5 Al : 1 O. Given that this is an equilibrium rather than kinetic model, the results indicate the final products after an infinite amount of time and do not account for reaction rates. Still, given that the plasma is highly energetic, reactions are likely to proceed quickly, meaning that the chemical composition of the products is likely to be similar to that determined with the equilibrium model.

Given the molar ratios above, the model dictates that liquid iron will be the first species to nucleate downstream of the plasma, followed by liquid aluminum and solid Al_2O_3. Importantly, all except a trace amount of the contaminating oxygen exists in aluminum compounds, such that the iron should still exist as reduced metal ideal for CNT growth. Further, complete oxidation of the iron for optimal energy storage would therefore be difficult since all the aluminum must first be oxidized; however, as shown above, increased oxygen fractions inhibit CNT growth. Therefore, the use of an ex-situ core oxidation step is justified since it allows iron oxidation to proceed to completion but will not adversely affect CNT growth.

X-ray Photoelectron Spectroscopy (XPS) shown in Figure 5.4d-f of iron, aluminum, and oxygen, respectively, confirm the presence of oxides. Particularly, the iron is well-oxidized as shown by the spectra from 707-709 eV, indicating that elemental iron is not present [187]. Moreover, the peak at 711.0 eV is characteristic of Fe^{3+}, an ionic state which is present in both Fe_2O_3 and Fe_3O_4 [188]. The satellite peak at 719.6 eV

is also characteristic of Fe^{3+}, particularly Fe_2O_3, and the peaks from the Fe $2p_{1/2}$ orbital located at 724.4 and 733.2 eV support the claim that the iron is nearly fully oxidized [189]. The additional width of both the primary $2p_{3/2}$ and $2p_{1/2}$ profiles (best fit with second peaks at 713.7 and 727.3 eV respectively) may indicate the presence of Fe^{2+}, likely in the form of Fe_3O_4, since the other Fe^{2+} oxide, FeO, is unstable below 575°C [190]. The oxygen 1s scan is best fit with peaks at 529.5, 530.6, and 531.9 eV - typical values for metal oxides [188, 191, 192]. It therefore seems likely that the iron in these particles is primarily in the form of Fe_2O_3 since the profile best matches the fully oxidized Fe^{3+} state while some portion of Fe_3O_4 exists as well (attributed to the weaker evidence of Fe^{2+}). Aluminum scans show a profile best fit with two peaks, located at 72.7 and 73.4 eV. These are most likely associated with Al_2O_3 [193]. Aluminum is a very reactive metal and will certainly form an oxide on its surface during annealing. As a result, the presence of Al_2O_3 is highly probable even at room temperatures. This oxide layer is self-limiting so it is conceivable that some elemental aluminum exists below the surface. However, since the primary particles are small (d_{pp} < 20 nm), it is likely that the oxide can penetrate the majority of the particle volume.

5.2.4 Electrochemical Performance

Figure 5.5a shows the discharge-charge voltage profiles for the first two cycles where the characteristic voltage plateau for iron oxide around 0.75 V is observed [194–197]. The capacity was calculated based on the mass fraction of metal oxide (48.4% of the total mass i.e. $\Psi = 0.516$ according to the TGA). The first discharge capacity is approximately 1610 mAh g^{-1} and the reversible charge capacity is approximately 870 mAh g^{-1}. Given that the metal oxide is comprised of both iron and aluminum oxide (approximately 75% of the metal oxide mass is attributed to iron oxide given a 2 Fe : 1 Al molar ratio), the capacity could be scaled further to present results on the basis of iron oxide mass. In this case, the resulting capacity is somewhat higher than iron oxide's theoretical capacity of around 1000 mAh g^{-1}. It is not likely that aluminum is contributing to the storage capacity of the material since it is well-oxidized and most of the aluminum will exist as aluminum oxide (which will only be reduced at a voltage higher than the cycling voltage of this cell), particularly on the particle surface as discussed in the preceding XPS results. Instead, any additional capacity beyond that of iron oxide is likely due to the carbonaceous coating present on many of the larger metal oxide particles. Additionally, the CNTs themselves may also be contributing some storage potential and this effect has been demonstrated previously [57]. In addition to the reduction plateau around 0.75 V (corresponding to Li insertion into Fe_2O_3 and Li_2O formation) a sloped delithiation curve (reoxidation of iron metal, Fe^0 to Fe^{3+}) is also seen between 1.5 and 2.0 V. This can also be observed using the cyclic voltammetry (CV) plot in Appendix B, where these redox reactions

manifest themselves as increased current (again at 0.75 V and between 1.5 and 2.0 V). Therefore, although the overall capacity of this material may be a combination of storage mechanisms from multiple components, the majority of the capacity is indeed related to the iron oxide. The primary function of the CNTs is to act as conductive pathways between the metal oxide particles and as a result, no conductive additive is necessary. This simplifies the anode construction process since only two components are now required.

In fact, the idea that the carbon coating and CNTs improve electrical conductivity is corroborated upon observation of Figure 5.5b and c. Figure 5.5b shows a Nyquist plot from electrochemical impedance spectroscopy (EIS) data for the metal oxide material with carbon coating and CNTs grown in-situ from the particle surfaces at various cycles ranging from 1 to 200. Conversely, Figure 5.5c shows EIS data for the same metal oxide cores, but rather than in-situ carbon growth, the cores were mixed ex-situ with pre-fabricated CNTs. Experimental details for cycling and EIS are presented in Appendix A. The semicircle in the Nyquist plot is related to charge transfer resistance in the electrode layer. Because mass loadings were identical in both electrodes, the smaller semicircular profile seen for the in-situ carbon growth indicate better electron conduction compared with the ex-situ metal oxide and CNT mixture electrode. With increasing cycles, both electrodes show decreasing charge transfer resistance. The in-situ mixture shows little variation in charge transfer resistance up to 200$^{\text{th}}$ cycle, but the ex-situ mixture shows an abrupt increase in charge transfer resistance at the 200$^{\text{th}}$ cycle. The conclusion can therefore be made that the in-situ CNT growth directly from the agglomerate surface and carbon coating growth presented in this process produces a material with improved electrical conductivity when compared to externally mixing a conductive additive.

For a rate of 1 C on the rate-varying coin cell, a reversible specific capacity of around 500 mAh g^{-1} could be achieved (Figure 5.5d). For higher rates up to 14 C a drop in capacity was observed, which could be due to poor ion conduction at these high current densities or non-ideal contact between the individual CNTs resulting in less active material participating in the reaction. This could be improved by calendering the electrodes. The fluctuation in capacity between the lower rates could be explained by temperature fluctuations during the electrochemical measurement. Despite what may have been imperfect contact, capacity recovery at lower rates after cycling at higher rates is excellent, with the material performing equal to or better than the initial cycles up to 1 C. For long-term behaviour testing, measurements were recorded at 2.7 C for 400 cycles (Appendix B). The capacity increases over time from what could be due to inactive material becoming exposed from the repeated volume change during the cycling. Electrolyte additives such as fluoroethylene carbonate (FEC) may be able to improve the cell's reversibility.

The overall performance of the metal oxide-CNT material demonstrates long-term stability and robust capacity recovery at high rates. The synthesis process itself is highly attractive for high production rates since it is simple, inexpensive, continuous, and fast. Multiple opportunities for optimization include further calendaring, electrolyte optimization, and pre-lithiation that could further improve the performance of this anode material. The unique hierarchical architecture, strong battery performance metrics and high-throughput production result in a holistically attractive material for LIB anodes.

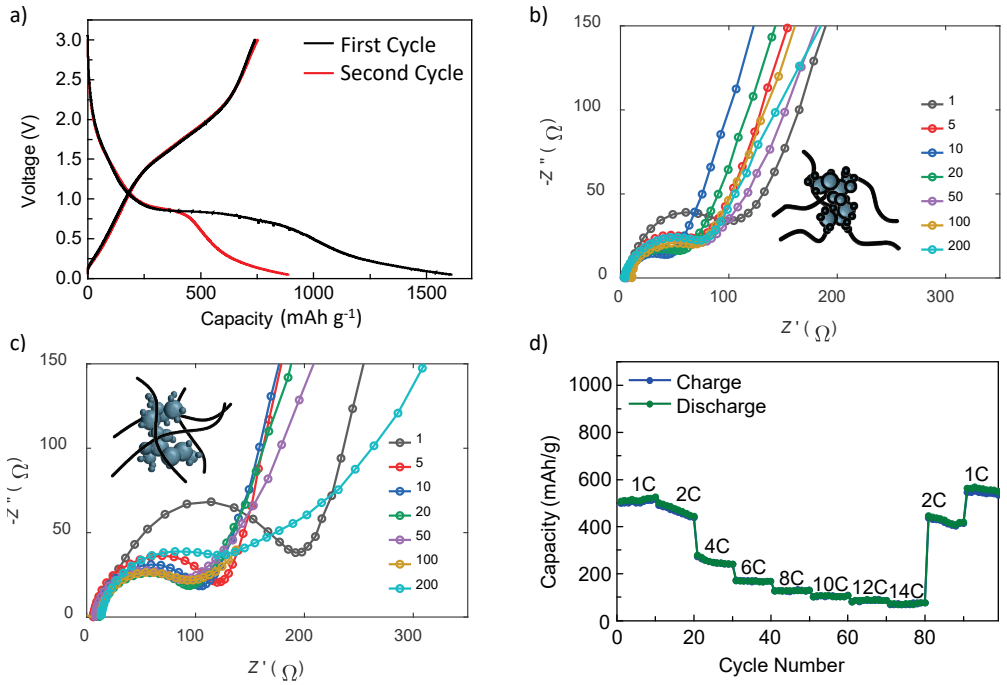

Fig. 5.5 (a) First and second discharge and charge casted electrodes at 0.1 C, (b) electrochemical impedance spectra for metal oxide particles with CNTs grown in-situ after various cycles, (c) electrochemical impedance spectra for metal oxide particles externally mixed with pre-fabricated CNTs after various cycles, and (d) specific capacities for rates from 1-14 C

5.3 Conclusions

A plasma-based process for fast, facile, and inexpensive synthesis of a metal oxide–carbon nanotube composite active material for conversion anodes in lithium ion cells has been presented, and thus satisfies objective (3) as defined in Chapter 2. Largely due to the exceptionally high temperature of the plasma, the active material can be synthesized in a matter of seconds using inexpensive and readily available raw precursor materials. These unique features, along with the high energy density of the plasma system, make the process easily scalable and industrially relevant. The

resulting composite material is formed of hierarchical structures beginning with metal oxide primary particles which agglomerate while suspended in the gas phase to form larger metal oxide agglomerates. CNTs are then grown from the primary particles within the agglomerates (while a carbonaceous coating is also formed on many of the primary particles) and the CNT/metal oxide particles are collected as a powder. The carbonaceous coating increases the short-range (intra-agglomerate) thermal and electrical conductivity while the CNTs enhance the long-range (inter-agglomerate) conductivity. An ex-situ annealing step was performed to ensure the metal was fully oxidized. The mass-mobility exponent of the agglomerate particles was determined to be 2.31, indicating an open agglomerate structure for lithium ion diffusion. The primary particles within the agglomerate were characterized with on-line aerosol methods allowing for real-time optimization. The primary particle diameter scaled with agglomerate diameter and the population-averaged primary particle diameter was 13.4 nm, which agrees well with the 11.28 ± 6.85 nm from TEM analysis. The final material displayed a reversible capacity of 870 mAh g^{-1} on a metal oxide mass basis. If scaled for the mass of iron oxide, the capacity exceeds the theoretical capacity of iron oxide, meaning that other components of this material, most likely the carbon coating or CNTs, contribute to energy storage as well. Long-term cycling showed that capacity increased which could be due to SEI formation. This could be mitigated by further calendaring. The material shows resistance to degradation from high rate cycling and robust recovery. This work demonstrates that high performance anodes can be synthesized from this remarkably fast, simple, and scalable continuous throughput process.

Chapter 6

High Throughput Production of CNTs

6.1 Introduction

This chapter addresses objective (4) and focuses on the developments towards creating a process capable of continuous, high mass throughput production of CNTs. Given the high energy density of the plasma, it is hoped that a process based on this technology will be capable of higher production rates than would be possible with either batch and/or furnace-based synthesis. Further, were this process to be optimized with additional future work, it may be capable of growing CNTs of sufficient lengths and number concentrations to induce aerogel formation, making it the first plasma-based process to achieve this. While an aerogel has not been produced in this work to date, significant developments have been made regarding the optimal conditions which would be most likely to do so. This chapter examines the mechanisms responsible for fast, high throughput CNT growth and aerogel formation, and explores in detail multiple experimental configurations that have been tested to best replicate these conditions.

6.1.1 High-Throughput CNT Growth Mechanisms

To achieve high mass throughput CNT synthesis, it is imperative that the phenomena, mechanisms, and conditions that result in efficient CNT growth are understood. Specifically, CNT growth speed must be as fast as possible and the catalyst nanoparticles must be a size and chemistry conducive for CNT nucleation. Much of this information can be gleaned from the Windle process since aerogel formation requires very fast CNT growth speed and high spatial density. The Windle process is therefore an excellent model on which to base this novel plasma process, and aerogel formation is an enticing albeit ambitious goal.

In the Windle process (shown schematically in Figure 1.1), iron and sulphur precursors (typically ferrocene and thiophene) are introduced as vapours into the furnace. These molecules decompose around 450°C and 800°C respectively [34] and Fe/S nanoparticles nucleate. Some CNT growth occurs here as the temperature increases between the inlet of the reactor and the hotzone. However, at the hottest point of the furnace (∼1300°C), the saturation vapour pressure of iron and sulphur are sufficiently high that the nanoparticles are vaporized and CNT growth stops completely. As the material passes beyond the hotzone of the furnace and the temperature begins to decrease again, the saturation pressures of iron and sulphur decrease to their current partial pressures, and catalyst nanoparticles once again nucleate. Note that since the particles that nucleate before the hotzone are subsequently vaporized, their input size distribution is irrelevant and instead it is only the total mass concentration of precursor material that is of interest for high-throughput processes such as aerogel formation [36].

Though no CNT growth occurs at the hottest point of the furnace, an important part of the process is observed here - the carbon precursor is "cracked" and forms pyrolytic compounds which have been shown to grow CNTs much more effectively than the raw precursors such as methane [26, 27]. These compounds are typically C_2 molecules and it is believed that the double or triple bond present in these molecules or radicals is responsible for the rapid CNT growth [26, 27]. New research also indicates that silica particles contained in the reactor tube catalyse this carbon conversion process [198]. After the pyrolytic compounds have formed and the catalyst particles have renucleated, CNT growth proceeds at a much higher rate. Given sufficient number concentration [47] and CNT length, aerogel formation is likely.

The relatively high temperature of the furnace, therefore, serves two functions: providing an environment suitable for hydrocarbon cracking and pyrolytic compound formation, as well as converting the catalyst material into nanoparticles of the appropriate size and number concentration for efficient and widespread CNT growth. In a sense, the plasma system assumes the role of the hottest section of the furnace since its primary function is precursor vaporization. It possesses a much smaller thermal entry length due to its high energy density, and as a result the precursor breakdown and vaporization phases occur rapidly and in a small volume. This is a major factor contributing to the ability of a relatively small plasma system to produce large amounts of material. It is worth noting however, that the carbon source must still be cracked so it must be introduced strategically to ensure it reaches sufficient temperature for CNT growth to proceed.

The ideal temperature profile of the plasma-based CNT growth process is displayed in Figure 6.1. Precursors are vaporized in the hot plasma region at several thousand degrees ($T_{\text{gas}} \sim 2700$°C [69]). As they exit the plasma they cool quickly and

significantly, and this stimulates catalyst nucleation at a temperature in the range of 1200-1400°C depending on the mass concentration (partial pressure) of the catalyst material. Carbon should then be introduced so the growth process can begin.

Several temperature profiles may be observed for the CNT growth region. If the reactor tube is simply left exposed, its temperature will decrease rapidly and there may not be sufficient residence time at temperatures conducive for fast CNT growth (>∼800°C). Ideally, the reactor tube would simply be insulated to preserve the heat of the process and reduce the severity of the temperature gradient. For the immediate experiments however, the greatest control possible is preferred to ensure the highest chance of success and so a small tube furnace is added downstream of the plasma. The active temperature control within the furnace provides the best control and repeatability of the growth environment, and following adequate understanding of the process, the furnace may be removed and replaced with passive temperature control (insulation). Even still, the use of a small growth furnace is not detrimental to the concept of this process. A much smaller unit can be used compared to the furnaces required for the Windle process since the incoming gas has already been heated from the plasma and it may not need to achieve such high temperatures (the furnace is no longer responsible for precursor vaporization). The addition of a small furnace is common for plasma processes and has been employed in previous CNT synthesis [150].

For this process to be the most effective, three criteria must be met. First, carbon must be introduced in such a way that it is allowed to crack into pyrolytic compounds before the CNT growth region, yet must not decompose to such a degree that soot is formed. This is one of the main functions of the hydrogen carrier gas - suppressing soot formation in favour of conversion to more reactive pyrolytic compounds. In an inert atmosphere, soot formation from methane is appreciable above 500°C and nearly complete by 1000°C [199], yet in the presence of hydrogen, methane is stable well beyond 1000°C. It is at these high temperatures that the pyrolytic compounds are able to form. Secondly, the decreasing temperature profile after catalyst nucleation should be shallow and ideally monotonic since there will be no way to re-heat the gas when a growth furnace is not used. Finally, catalyst particles must possess the correct size and chemistry for effective CNT growth. This not only means that precursors must be introduced at the correct rates, but also that any contamination (such as particles generated from plasma contact with the torch or tube) is minimized since these particles can alter catalyst chemistry and act as heterogeneous nucleation sites, leading to undesirable catalyst size distributions.

6.1.2 Experimental Setup

The mechanisms of the high-throughput CNT production process are shown in Figure 6.2. Several configurations have been explored for this section of work but the

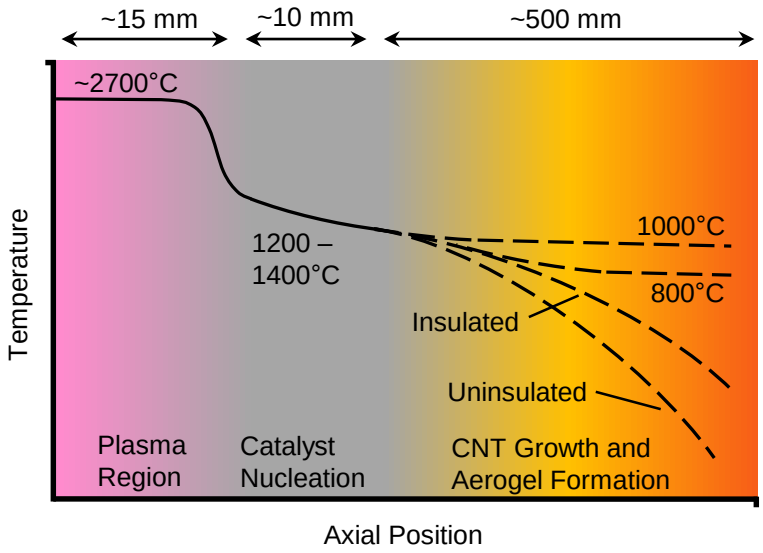

Fig. 6.1 Idealized temperature profile for high-throughput plasma production of CNTs. Several options are shown for the growth phase including fixed temperatures from active heating and controlled gradients from insulated versus non-insulated reactor tubes

general setup is discussed here. In most cases, the axial flow torch was used along with a 30 mm O.D. quartz reactor tube (23.5 mm I.D.). The major carrier gas was either nitrogen (BOC, 99.998% purity) or helium (BOC, 99.996% purity), and some fraction of hydrogen (BOC, 99.999%) was also included. While the energy for the process would ideally be supplied entirely by the plasma system, the downstream temperature gradient and CNT growth temperature are sensitive parameters, so to preserve the highest level of control, these preliminary experiments were conducted with a small tube furnace fitted to the outlet of the plasma system, maintained at a temperature between 800 and 1000°C. Note that unwanted nitrogen doping of the CNTs is not likely in this setup. CNT growth will occur at temperatures similar to traditional floating catalyst CVD processes and at these conditions, N_2 is too stable to react appreciably with the CNTs. When CVD doping is desired, ammonia or nitrogen-containing hydrocarbons are typically included [200–204], though this has not been a focus of the work presented here.

While solid catalyst precursors could be used as has been demonstrated in Chapter 5, initial tests for this process were conducted with the more traditional ferrocene and thiophene. This was done to maximize repeatability between tests and comparability to the furnace process. Ferrocene (Acros Organics, 98%) was sublimed in a heated vessel at approximately 95°C and the vapour was introduced through the central flow of the plasma torch. Thiophene (Alfa Aesar, 99%) was placed in an ice bath (0°C) and its vapour was also introduced in the central torch flow.

Carbon was introduced via three broad methods, each of which are discussed in detail in the following sections. The carbon source has been injected in the plasma

sheath flow as well as radially through a flange mating the plasma system to a growth furnace. Finally, carbon has also been introduced using a counterflow injector passing through the growth furnace.

As the ferrocene and thiophene approach the plasma they first decompose, liberating their respective iron and sulphur atoms. Nanoparticles may temporarily nucleate from these atoms, but this is short-lived since all the precursor material is vaporized as it passes through the plasma. Upon exiting the plasma the catalyst nanoparticles renucleate, similar to the metal oxide particles in the previous chapter. These particles then mix with the carbon precursor and pass into the growth furnace. CNT length increases as they continue through the furnace, and if length and number concentration are sufficiently high, aerogel formation may occur. Samples are collected on PTFE filters mounted at the exit of the tube furnace.

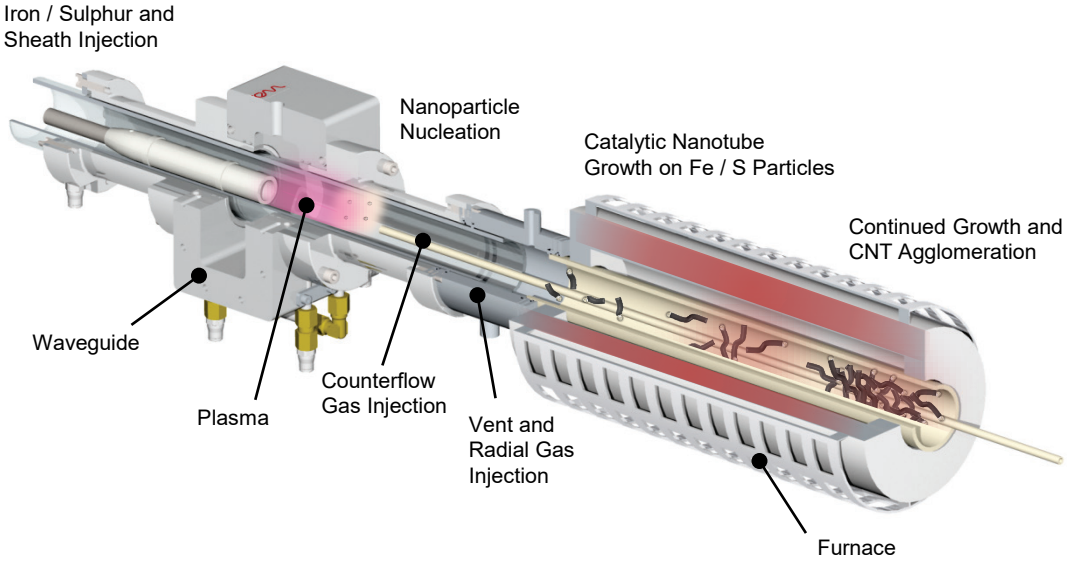

Fig. 6.2 Mechanisms for high-throughput CNT synthesis

6.2 Configuration 1: Plasma Beyond Torch Tip with Separate Reactor Tubes

While the overall setup has been presented in the previous section, several variations have been tested in an effort to configure the system in such a way that it satisfies all the requirements for high-throughput CNT production (i.e. catalyst particles of the appropriate size and chemistry, pyrolytic carbon availability, shallow downstream temperature gradient). These variations focus primarily on two main features: the plasma configuration and the carbon injection method.

The first configuration is the standard use of the axial flow torch, in which the plasma exists beyond the tip of the torch, as shown in Figure 6.3. In this way, the plasma is isolated from any solid components such as the reactor tube or torch itself, and this produces a system largely free from contaminants (as discussed in Chapter 3). This configuration is also capable of handling moderate fractions of hydrogen - up to ∼25% when mixed with nitrogen. However, a minimum flow rate of approximately 4 SLPM is required to maintain plasma stability. Ideally, the total flow rate in the process (and especially that through the growth furnace) would be lower than this, at perhaps 1 to 2 SLPM. The lower flow rate serves two purposes: it concentrates the reagents in a smaller volume of gas which encourages CNT agglomeration and potentially aerogel formation, and also allows for longer residence times for CNT growth which correlates to longer CNTs and higher mass throughput.

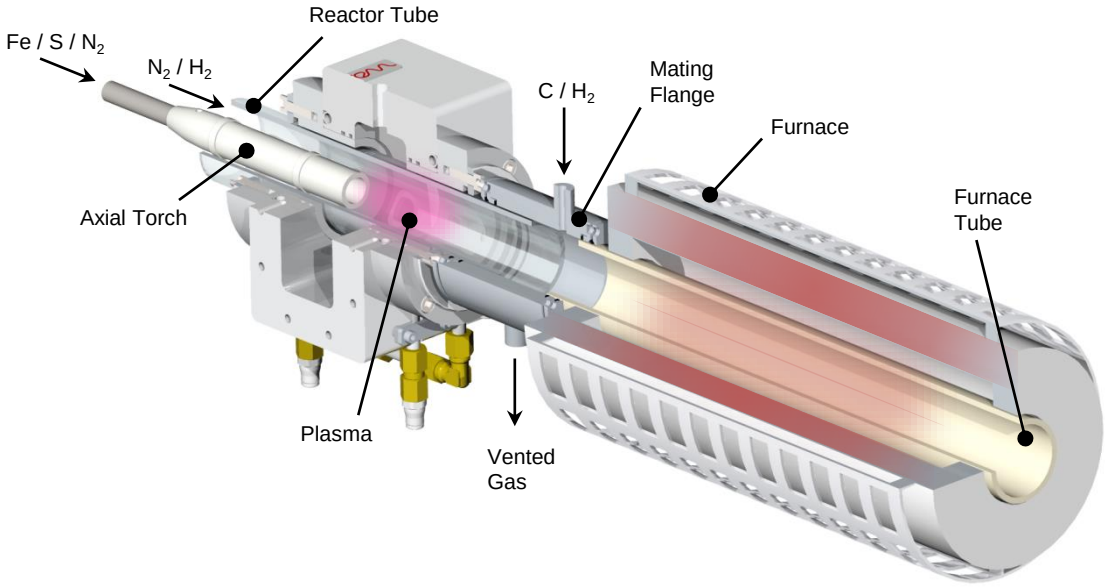

Fig. 6.3 Configuration 1 featuring predominantly nitrogen plasma beyond axial torch and separate reactor and furnace tubes connected with a mating flange. Using the flange, gas can be vented and carbon and hydrogen can be introduced

This configuration employs separate reactor and furnace tubes, and these are mated together using a flange that also allows for gas to be exhausted and additional gas such as hydrogen or the carbon precursor to be injected. The ability to vent excess gas from the plasma allows for independent control over furnace flow rate and potentially longer growth times. The disadvantage of the inclusion of the mating flange is that heat losses are significant, particularly when gas is vented since this gas carries with it much of the process heat. As a result, the gas entering the furnace must be reheated to the growth temperature and it is therefore likely that this configuration would always require at least a small furnace rather than the ideal passive/insulative temperature control.

Regarding carbon sources, it is important to note that the high stability of methane requires that it reach at least 1200°C to be cracked into the C_2 compounds ideal for CNT growth. As a result, methane is not an ideal candidate using radial injection since it is not likely that it will attain this temperature. The relatively high heat losses of the flange along with the maximum temperature of the small tube furnace of 1000°C show that while the conditions are still favourable for CNT growth, conversion of methane to pyrolytic compounds is not likely using radial injection. Therefore, acetylene was used in this configuration since it is far less stable and will react at lower temperatures. It should also be noted that inclusion of the carbon source as a sheath gas is impossible in this configuration since passing the carbon precursor near or directly through the plasma can result in significant decomposition to soot, and this extinguishes the plasma.

Characterization of the material produced from this configuration began with catalyst particle size distributions, and one such example is displayed in Figure 6.4a. This was done using approximately 12% hydrogen in nitrogen, with a ferrocene carrier gas flow rate of 100 sccm. The data is well-fit using a single lognormal distribution possessing a mean diameter of 16.8 nm and a total concentration of 1.38×10^8 cm^{-3}. These values are encouraging for high throughput CNT growth since this concentration is high compared to the maximum concentration that is stable without significant agglomeration for timescales on the order of seconds. The mean diameter is also reasonable for MWNT growth. In addition, distributions such as this have already successfully produced high CNT yields in the Windle process, with 15 nm particles being the greatest promoters of CNT growth [36].

After venting flow to maximize growth time and with the addition of 10 sccm of acetylene, the size distribution in Figure 6.4b was recorded. This distribution is noteworthy since it is distinctly bimodal. Two lognormal distributions were used to fit the data, with one distribution showing a mean diameter (12.7 nm) similar to the catalyst particles themselves. The fact that a peak similar to the catalyst particles is still visible implies that many of these particles were either entirely coated with graphitic or amorphous carbon before CNT growth could occur, or they were not active to begin with. The more likely phenomenon is the latter since the quantity of carbon introduced is low and is unlikely to overwhelm the catalysts. The second distribution had a larger mean diameter and this likely represents the CNT growth. It must be noted that the sizes presented represent mobility-equivalent diameter and therefore do not directly represent CNT length. Kim et al. [205] examined the relation between CNT length and mobility-equivalent diameter. With their relation, the peak of this distribution of slightly below 30 nm would correspond to a length of less than 100 nm (assuming 15 nm CNT diameter) and the largest CNTs measured here with mobility-equivalent diameters of 80-90 nm would have lengths between 350 and 500 nm.

SEM images of this material are shown in Figure 6.4c and d, in which CNTs are visible. Indeed, many particles are present which did not grow CNTs, and these are responsible for the left-hand peak in Figure 6.4b. As a result, the CNT product is relatively impure. Typical CNT length is seen to be several hundred nanometres, with several CNTs indicated with the red lines. There is therefore reasonable agreement with the CNT length to mobility-equivalent diameter relation determined by Kim et al. [205]. This length must be increased for the mass throughput of the process to be improved, but this is certainly possible since the CNT length in the Windle process is estimated to be at least 100 μm [6].

Despite the presence of many inactive catalyst particles, the crystalline purity of the CNTs themselves is high according to the Raman spectrum in Figure 6.4e. This sample shows a G/D ratio of well over 20, a strong 2D peak at 2633 cm^{-1}, and multiple RBMs. Given the presence of the RBMs and the high G/D ratio, a substantial number of SWNTs are likely present, although these will be too thin to be seen in the SEM. The RBMs are all located at wavenumbers higher than 230 cm^{-1}, meaning their corresponding CNTs are all 1 nm or less in diameter and examination of a Kataura plot such as that in Figure 5.4b (Chapter 5) indicates these SWNTs are likely to be metallic.

One distinct reason these CNTs are shorter than those observed in previous growth processes is that in this case, no sulphur was added. Despite being a known catalyst poison at moderate to high concentrations, sulphur is believed to increase the speed of CNT growth in the Windle process and has long been established as a vital additive for the success of the process [34].

This initial configuration has provided promising preliminary results for high-throughput CNT production. The catalyst particle size and number concentrations are ideal; CNTs have been produced even without inclusion of sulphur, and the contaminating background particle concentration is low ($< 10^3$ cm^{-3}). However, significant heat is lost through the mating flange, resulting in an undesirable (i.e. non-monatonic) temperature profile. The next iteration of this plasma-based process examined the effects of including sulphur to increase CNT growth rate, and aimed to improve the temperature profile by reducing heat loss between the plasma and growth furnace. In doing so, the process is less dependent on active temperature control for the growth portion. Conservation of process heat is particularly important with the inclusion of hydrogen since its high thermal conductivity allows it to readily dissipate process heat to the surroundings. The presence of hydrogen is crucial for high-throughput CNT growth and its concentration should be maximized for this work.

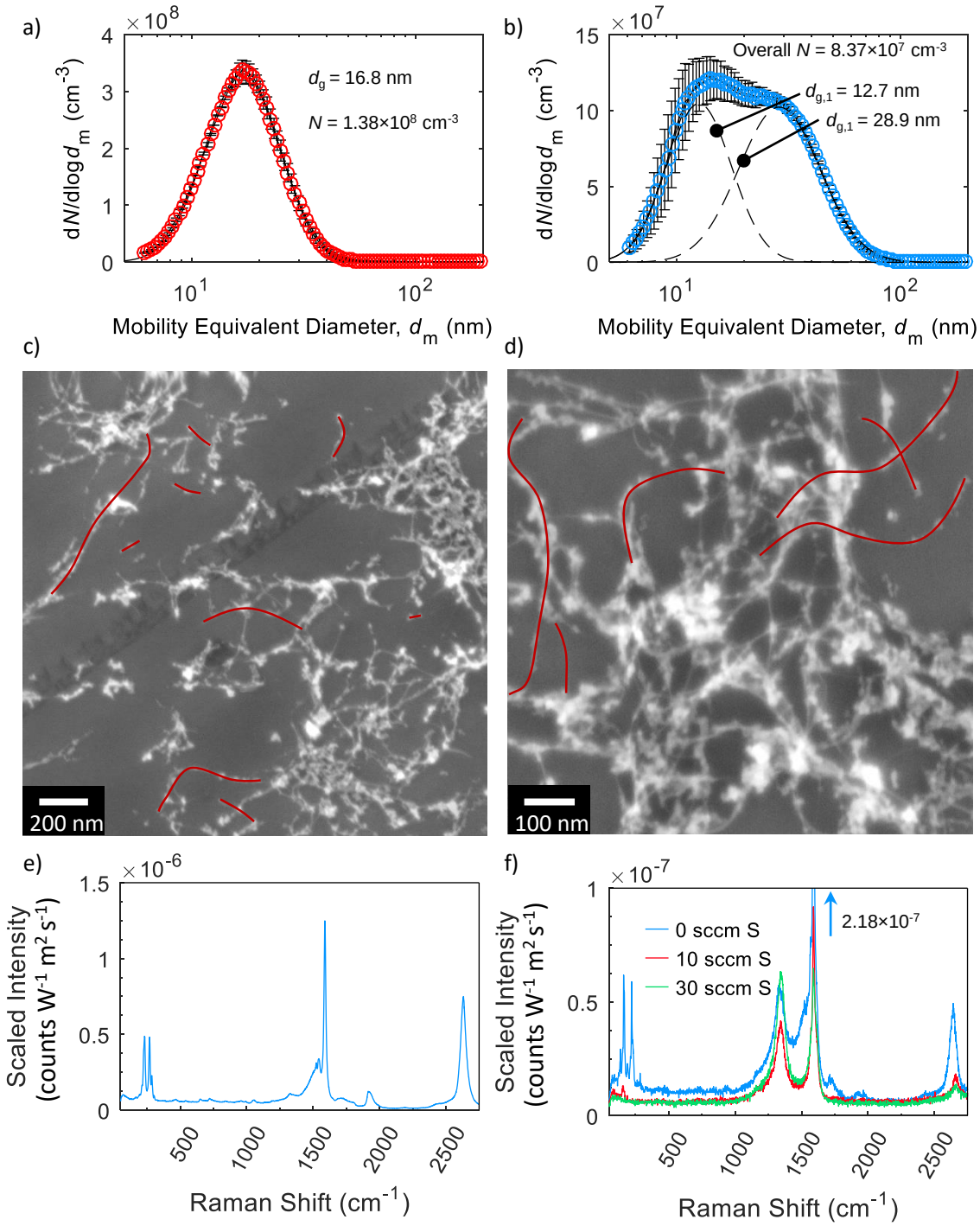

Fig. 6.4 (a) Catalyst particle size distribution from plasma beyond torch. Data is an average of two scans and a lognormal fit was applied with $\sigma_g = 1.47$, (b) CNT size distribution after growth in configuration 1, as an average of three scans. Fit applied with two lognormal distributions with $\sigma_{g1} = 1.40$ and $\sigma_{g2} = 1.51$, and error bars represent one standard deviation. SEM images of material produced in configuration 1 at (c) low and (d) high magnification with several individual CNTs indicated in red, (e) Raman spectrum from CNTs grown with configuration 1, and (f) Raman spectra from CNTs grown from configuration 2 with various quantities of sulphur added to the catalyst mixture

6.3 Configuration 2: Plasma Beyond Torch Tip with Single Reactor Tube

The second process configuration (visible in Figure 6.5) replaces the separate reactor tubes and mating flange with a single reactor tube for both the plasma and furnace. In doing so, heat losses can be minimized and the temperature profile will decrease less rapidly since heat is no longer lost through the thermally conductive metal mating flange. Further, the furnace can now be mounted closer to the plasma exit, allowing the temperature to remain sufficiently high for optimal CNT growth. Unfortunately, with a single reactor tube there is no opportunity to vent any process gas and the entire volume must pass through the growth furnace, decreasing growth time.

Regarding carbon injection, a counterflow method is used through the furnace. The carbon source is preheated as it passes through the furnace and the injection location can be easily varied by moving the probe axially. In this way, the carbon can be introduced at the optimal temperature for CNT growth. The probe can be positioned upstream of the furnace and close to the plasma exit where temperatures can easily exceed 1200°C, and methane is converted in appreciable quantities to the C_2 compounds favourable for CNT growth. As such, methane should be used for this configuration since it is the more ideal precursor for a large-scale process, in addition to the fact that these elevated temperatures would cause immediate decomposition of acetylene into soot.

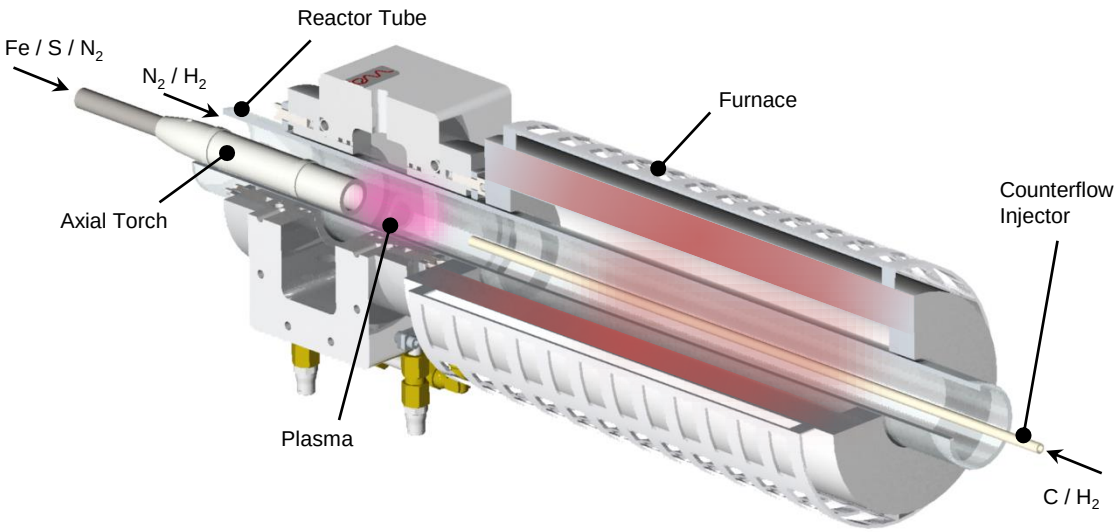

Fig. 6.5 Configuration 2 featuring a single reactor tube, plasma (predominantly nitrogen) situated beyond the axial torch, and counterflow carbon and hydrogen injection

Despite the shorter growth time, CNTs have been successfully synthesized from this configuration as well, and the Raman spectrum from one of these samples is shown in blue in Figure 6.4f. Like the CNTs grown from configuration 1, RBMs are visible - indicating the presence of SWNTs - although in this case, the G/D ratio is lower at approximately 3.8 based on peak height. The larger D peak relative to the G peak indicates that more defects are present and these could be in the form of defects in the CNT lattice, or as other graphitic or amorphous carbon present on the catalyst particles.

Next, the effects of sulphur were examined. Thiophene was introduced with the ferrocene into the plasma as a vapour in nitrogen. The Raman spectra for 10 sccm and 30 sccm of this thiophene-in-nitrogen flow are presented in Figure 6.4f. By comparison, the standard Windle process at this scale uses approximately 60 sccm for a thiophene flow. Here, using only 10 sccm, the RBMs are seen to disappear almost entirely, and the G/D ratio is reduced to around 2. Increases in sulphur content in the Windle process have been shown to produce CNTs with more walls [34], so the fact that fewer SWNTs are present (smaller RBM signal) is not surprising; however, this effect is prominent considering the modest sulphur input. Further, using 30 sccm of thiophene vapour, the resulting material appears to be low quality carbon since no RBMs are visible and the G/D ratio is almost exactly 1. So while the presence of a G peak indicates there is still some ordered carbon present, many defects must also be present.

The ability of the sulphur to inhibit CNT growth much more easily in this system than a conventional furnace may be because the hydrogen fraction in the process is much lower (12% compared to nearly 100%). Where the sulphur would normally react with the hydrogen to produce H_2S, it may be less likely to do so with less hydrogen present and therefore will precipitate on the particles [34]. In this way, much more sulphur may be present on the particles for a given thiophene mass flow rate. To counteract this, the hydrogen fraction could be increased, allowing more sulphur to convert to H_2S and only a small amount to condense with the iron to form the catalyst particles. With the current plasma configuration in which the plasma is situated beyond the tip of the axial flow torch, hydrogen fractions of at most 25% are achievable for long-term operation. At higher hydrogen fractions, the heat conducted to the tube walls can cause failure even if the plasma is well-centralized. So while configuration 2 improves the temperature profile from configuration 1 and maintains its ideal catalyst size distribution and low contaminating background particle concentration, it is not able to provide the correct catalyst chemistry. Given the lack of a vent, the growth time is short. The ability to operate with increased hydrogen fractions, as well as a lower total flow rate for longer growth times, would benefit the process and are the aims of the next configuration.

6.4 Configuration 3: Plasma in Torch with Single Reactor Tube

In an effort to reduce the overall flow rate, the third configuration moves the axial torch towards the plasma so that the plasma exists within the central channel of the torch, as shown in Figure 6.6. Given the low reactivity of boron nitride and its high melting point, it is able to maintain contact with the plasma without significant damage. In this configuration, the plasma is already in contact with the inner surface of the boron nitride torch and does not need to be stabilized with high gas flows. The overall flow rate can be reduced to 1 SLPM or lower. Moreover, the ability of the torch to tolerate severe heating means that higher hydrogen fractions are possible (up to $\sim$80%) and the balance gas can be switched from nitrogen to helium. The use of helium as the balance gas (when less than 100% hydrogen is used) has been shown to be more conducive to high throughput CNT production and aerogel formation than other inerts [38], but has been avoided in the previous two configurations because helium is difficult to stabilize using the axial torch in its standard layout. Naturally, the extreme heating of the torch results in high concentrations of contaminating particles, often 10^7 cm^{-3}. This concentration is approaching that of the catalysts themselves, which are at most only one order of magnitude more numerous.

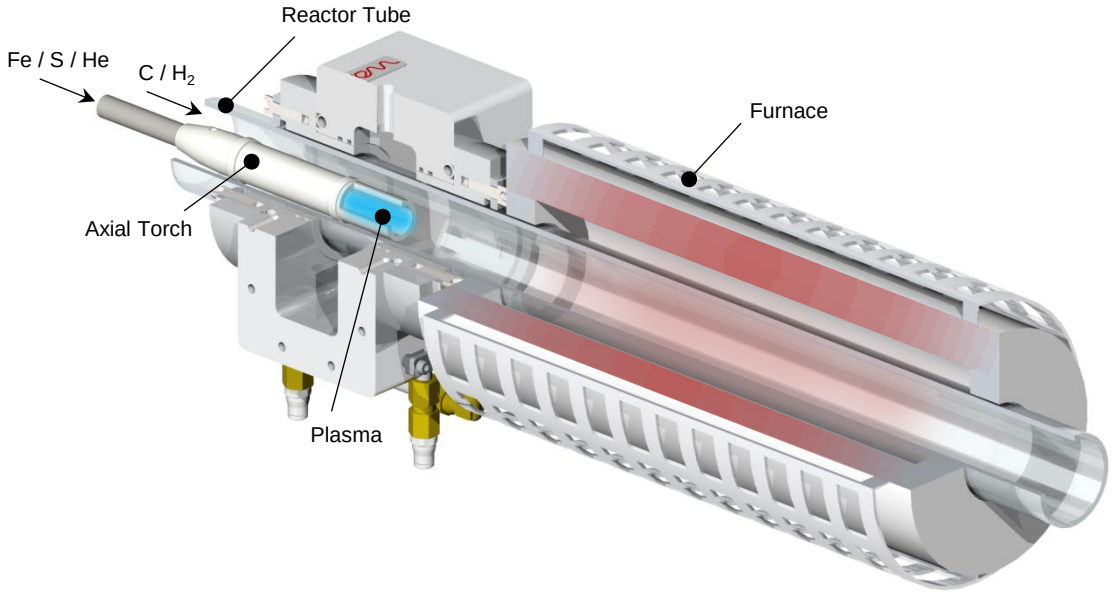

Fig. 6.6 Configuration 3 featuring single reactor tube, sheath injection of carbon and hydrogen, and plasma (helium/hydrogen) situated inside axial torch

In theory, since the torch now acts as a physical barrier between the central torch flow and the sheath flow, the carbon source (in this case, methane) can be introduced in the sheath flow where it will mix with the other carrier gases at the tip of the torch.

Here, the torch tip aligns with the plasma exit. This simplifies the setup since no counterflow injection is needed yet the methane can still be heated to the point where it forms pyrolytic compounds. Despite this, long-term synthesis will not allow carbon introduction through the sheath flow. In this configuration, the torch is heated strongly by the plasma, and even though most of the sheath flow remains sufficiently cool to prevent soot formation, a small amount of methane contacting the hot torch does decompose and a soot layer is formed on the torch. Since soot is an excellent absorber of many wavelengths including microwaves, the soot absorbs the incident microwaves and the plasma is quickly extinguished.

A secondary issue is also caused by the strong heating of the torch (labelled as I in the axial view, Figure 6.7a). In general the dielectric constant of a ceramic increases with temperature [156–158], meaning that it will absorb more microwave energy which in turn causes additional heating and a positive feedback loop is established. The plasma is seen to be intense and bright initially, but as the torch temperature increases the plasma becomes faint and later extinguishes, making continuous operation of this configuration impossible.

Finally, it has also been observed that under low total flow rates ($\sim$1 SLPM), high torch heating, and a predominantly hydrogen atmosphere, the axial temperature profile is steep despite the use of a single reactor tube. At the exit of the chimney ($\sim$20 cm downstream) the effluent gas is less than 600°C. While configuration 3 presents several considerable advantages over the previous setups such as its ability to operate with very high hydrogen fractions and very low flow rates, its high contaminant generation and unstable plasma make it unsuitable for CNT production. It was determined that a more radical configuration would be necessary for satisfying all the conditions for high-throughput CNT synthesis. In particular, it appeared as though it may be necessary to further decrease the separation between plasma and growth furnace to preserve as much heat as possible.

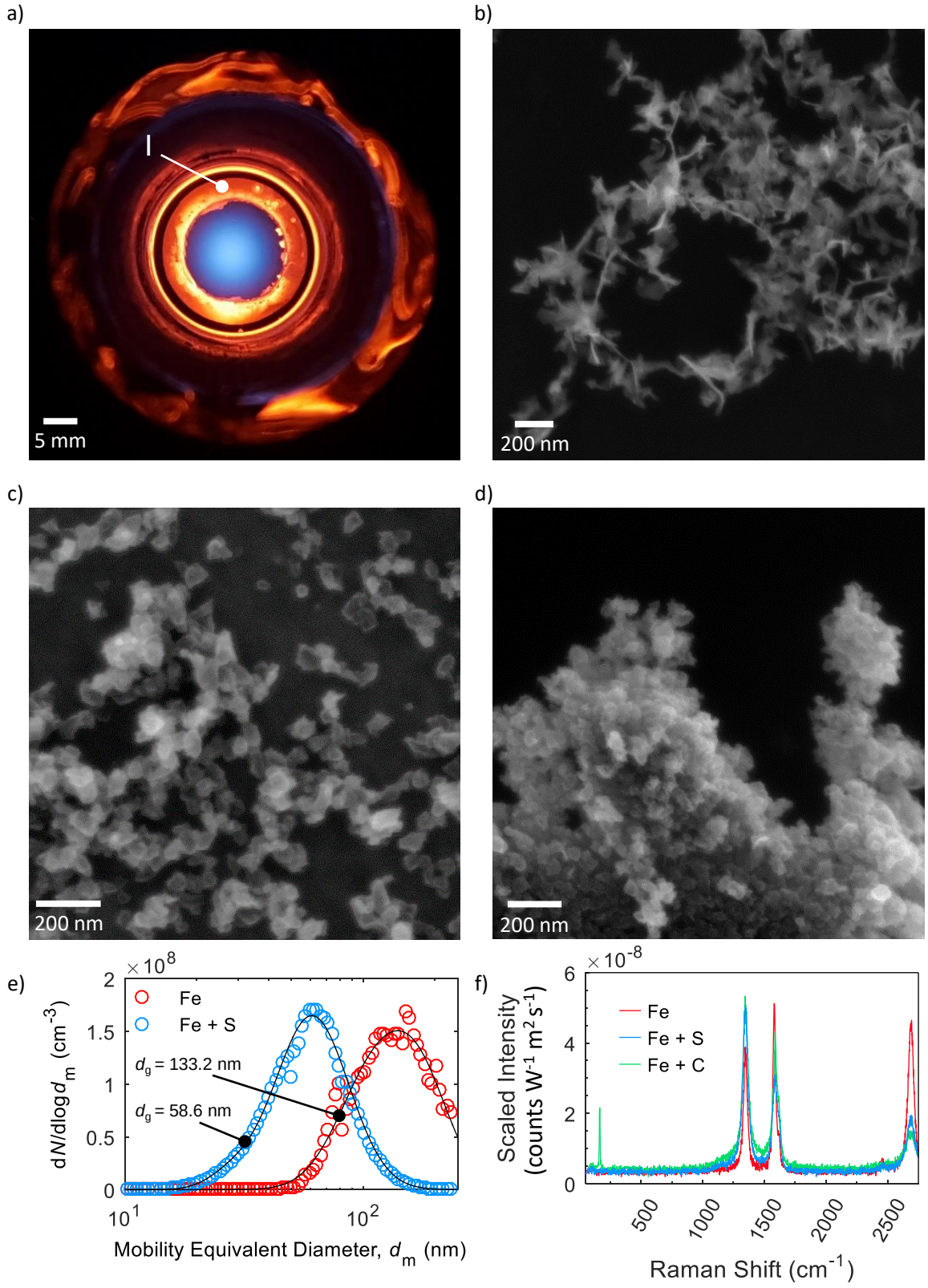

Fig. 6.7 (a) on-axis view of configuration 3 where torch (I) and reactor tube are strongly heated by He/H_2 plasma, SEM images of catalyst material produced from configuration 4 using (b) only ferrocene, (c) ferrocene and elemental sulphur, and (d) ferrocene and acetylene, (e) size distributions of catalyst material from iron and iron with sulphur. Fits applied with two lognormal distributions each; $\sigma_{g1} = 1.44$, $\sigma_{g2} = 1.33$ for Fe and $\sigma_{g1} = 1.26$, $\sigma_{g2} = 1.43$ for Fe + S. (f) Raman spectra of catalyst material with and without carbon addition.

6.5 Configuration 4: Plasma Jet Directly into Furnace

The fourth plasma configuration is radically different from the preceding setups and features a much smaller plasma tube (6 mm O.D.) that extends beyond the waveguide and chimneys and protrudes into the furnace, as pictured in Figure 6.8. The motivation behind the reduction in tube diameter is to increase the gas velocity and create a jet of plasma into the furnace. The proximity of the jet to the furnace and CNT growth region guarantees a smooth and monotonic temperature profile, making it highly likely that the process would also be successful with a simple insulated CNT growth zone. Argon was used for the plasma gas in this instance, since its low thermal conductivity allows it to exist near the thin alumina reactor tube without excessively heating it or subjecting it to thermal shock. Plasma gas flow rates less than 1 SLPM are possible with this configuration.

Counterflow carbon injection is once again required here since there is no opportunity for radial injection and it is not feasible to pass the carbon directly through the plasma. Moreover, the hydrogen must also be added in this counterflow stream because even as much as 3-4% hydrogen in the argon causes the plasma tube to heat to such a degree that the alumina softens or melts. And while it is possible to create a plasma jet in the furnace under a pure argon atmosphere, the addition of hydrogen into the furnace volume results in contraction of the jet to the point where it does not protrude from the reactor tube, and once again the claim that the temperature profile is monotonic becomes dubious.

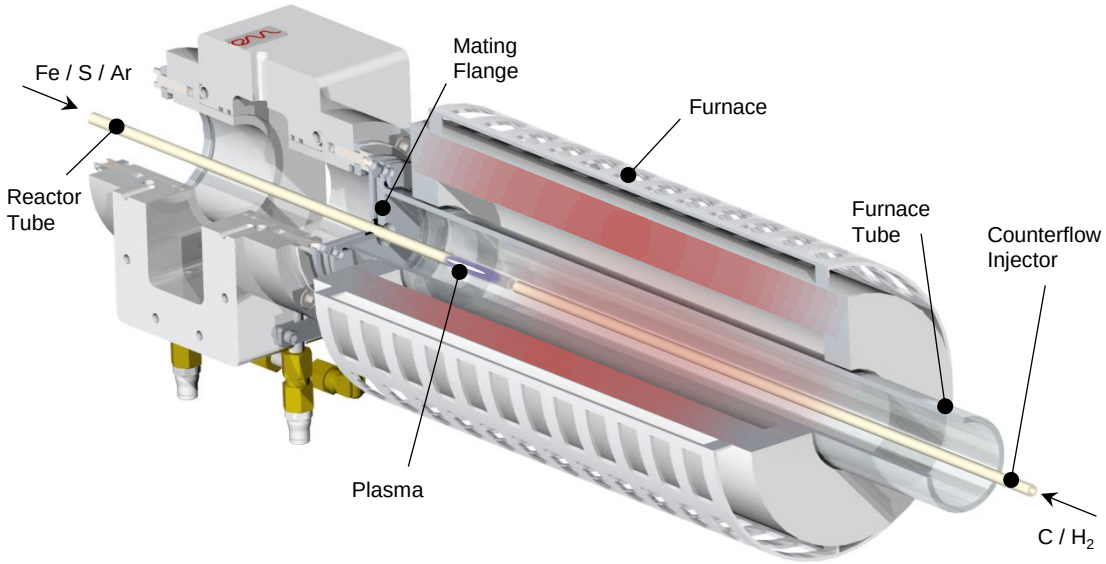

Fig. 6.8 Configuration 4 featuring thin reactor tube producing argon plasma jet inside growth furnace. Carbon and hydrogen introduced via counterflow injection.

It was also immediately obvious that the close contact between the plasma and reactor tube caused significant background particle generation. Particle generation from tubes is a known issue (in fact it is one of the main reasons that metal tubes are not used in many aerosol processes including the Windle process) and tubes are typically "baked" at high temperature for several hours before use to ensure that the majority of the particles have been removed. In this case, the 6 mm plasma tubes were baked at 1400°C for one day before being installed in the system. Prior to baking, the tubes produced a background particle concentration of approximately 3×10^7 cm^{-3}, yet after the baking process this concentration is reduced to approximately 5×10^3 cm^{-3} - nearly a four order of magnitude reduction and certainly acceptable for use without noticeable contamination.

Experiments were then conducted to characterize the catalyst particles produced by this configuration, first using ferrocene and thiophene as is typical. However, as thiophene was introduced to the plasma, the jet was immediately observed to reduce in length and within several minutes the plasma would extinguish. One proposed reason for this is that the carbon contained in the thiophene molecule is deposited on the tube wall upon decomposition and absorbs microwaves. This is likely since this deposition can be seen visually and can be removed by passing air through the plasma tube and supplying microwaves (without plasma). The carbon absorbs enough energy that it heats to the point where the deposited soot will react with the oxygen and the tube wall is cleaned, at which point plasma generation is once again possible.

Using the vapour pressure curves for ferrocene [206] and thiophene [207] at their respective temperatures of 95°C and 0°C, in addition to a thiophene carrier flow rate of approximately half that of the ferrocene carrier, thiophene brings approximately 70% more carbon into the system than does ferrocene. Interestingly however, this accumulation of carbon extinguishing the plasma is not an issue when only ferrocene is used. It is not known why solid carbon accumulation in the reactor tube is problematic for thiophene but not ferrocene. One possibility is that the higher mobility of the comparatively lighter thiophene molecules allows them to deposit more easily on the tube walls. In any case, thiophene was replaced with elemental sulphur (Acros Organics, 99.5%), placed in a heated vessel similar to that for ferrocene, and set at 80°C. In this way, precursors could be introduced into the plasma almost indefinitely.

SEM images of synthesized materials are presented in Figure 6.7b to d, where Figure 6.7b displays the resultant material after passing only ferrocene through the plasma, Figure 6.7c presents material from the addition of both ferrocene and sulphur, and Figure 6.7d displays material from ferrocene addition with acetylene. The material from ferrocene alone in Figure 6.7b appears somewhat unusual since it has not formed agglomerates from spherical primary particles as would be expected, but instead has formed what appears to be jagged flakes and filaments. Naturally, particles of

this morphology are not likely to be suitable for CNT growth, although some CNTs may be present here since the ferrocene molecule does contain carbon and would be capable of producing a small number of CNTs. In fact, growth of CNTs using only ferrocene has been documented previously [208, 209]. When sulphur is added to this mixture, the resultant particles are much more spherical although the particles are 50 to 60 nm - too large for the CNTs from most high-throughput or self-assembling processes. This is a marked difference when compared to Figure 6.7b, particularly when considering that the vapour pressure of elemental sulphur at 80°C (at most several tens of Pascals) [210] is much lower than that of thiophene at 0°C ($\sim$2600 Pa) [207]. Again, it appears that with particle formation occurring in the absence of hydrogen, all of the sulphur is forced to condense on the particle phase and large (primary) particles result. Importantly then, the ideal sulphur input scales not just relative to the ferrocene input, but also with the hydrogen fraction of the plasma gas. Lower hydrogen fractions will require a lower sulphur input to prevent excessive accumulation in the catalysts.

The size distributions of catalysts both with and without the inclusion of sulphur are shown in Figure 6.7e. Note that while the mean size of the iron-only distribution is more than twice that of the iron and sulphur distribution, it is likely caused by the open and highly branched morphology of the former. In other words, these particles are likely to possess a low mass-mobility exponent (D_{m}), in which case the distribution would actually contain a fairly small mass concentration despite the large mobility-equivalent diameters of the particles. The mean iron-sulphur diameter of 59 nm is similar to the average primary particle diameter observed in the SEM, indicating that many of these particles have not agglomerated at the time of measurement and only appear to have agglomerated once collected on the filter. The total number concentrations of the iron-only and iron-sulphur distributions are similar (6.90×10^7 cm^{-3} and 6.72×10^7 cm^{-3} respectively), so it appears that the sulphur does not undergo homogeneous nucleation and instead condenses on the pre-existing iron-based particles. This is contradictory to Hoecker et al. [36] who found that sulphur induces iron nucleation and results in higher catalyst number concentrations. It is possible that the much lower residence time in the plasma compared to the hot zone of a furnace (in addition to the plasma's higher temperature gradients) may inhibit the chemistry required for sulphur-induced nucleation to occur. Further experiments would be necessary to confirm this. Finally, the SEM image in Figure 6.7d displays the resultant material from ferrocene through the plasma, later mixing with acetylene in the growth furnace. While this may produce occasional CNTs, the product is unsurprisingly comprised mostly of what appears to be amorphous carbon.

Raman spectra of these samples are shown in Figure 6.7f. The spectrum pertaining to the iron-only case has a G/D ratio that is slightly larger than one and also displays a large 2D peak. Therefore, the conclusion is that much of the carbon present in the

ferrocene molecule has been retained on the particles exiting the plasma. Moreover, the filaments observed in the SEM could be short CNTs or possibly graphene sheets. Similar to the results for configuration 2, the addition of sulphur here is seen to decrease the apparent quality of the carbonaceous material as evidenced by the reduction of the 2D peak and decrease of G/D ratio to below 1. The inclusion of carbon for CNT growth with the iron-only catalyst also results in a large amount of disordered carbon according to the large D peak, although an RBM is visible indicating occasional CNTs have been grown successfully. Nevertheless, it is clear that the conditions in configuration 4 are not conducive for CNT growth. As the growth furnace and conditions have not changed in any significant way, the catalyst particle production must be unfavourable, especially given the unusual material in the iron-only case.

Despite the low overall flow rates attainable with configuration 4, its low background particle concentration, and what should in theory be an ideal temperature profile for catalyst nucleation and CNT growth, it is worth considering why the small diameter plasma tube has been unsuccessful thus far. While a plasma jet into the growth furnace is possible with pure argon, it becomes increasingly difficult to maintain this jet as additional species are introduced. When hydrogen is added to the growth furnace using the counterflow injector, the plasma is no longer able to protrude from the reactor tube and will terminate at the tube exit. Second, while the addition of catalyst precursors such as ferrocene and sulphur don't extinguish the plasma, they do reduce its length within the reactor tube. Third, it has also been observed that despite its thin profile, heat losses from the mating flange can impede plasma formation beyond this point. So while the growth furnace contains approximately 50% H_2 in this configuration, the catalyst particle formation occurs in the reactor tube which is a 100% Ar environment. It would be more ideal, particularly when sulphur is included, to form the particles in some fraction of hydrogen as this more closely resembles the traditional Windle process. While the iron and aluminum catalyst particles in Chapter 5 also form without hydrogen present, the precursor used is elemental powder rather than ferrocene which contains ten carbon atoms for every iron atom. The inclusion of hydrogen may therefore be more important here to suppress soot formation which is not a concern when the powders were used. Further, the lack of hydrogen and likely presence of trace amounts of oxygen or water vapour may cause oxidation of the catalysts. Given the lower mass throughput of catalyst compared to iron/aluminum cores (and what would probably be comparable traces of oxygen and water vapour), this oxidation could be more complete and therefore more of an issue here. In summary, it may be helpful to position the reactor tube end closer to the waveguide centreline so a jet can still be created even during length contraction of the plasma. Catalyst particles could then be formed with hydrogen present. This was the primary goal for configuration 5.

6.6 Configuration 5: Plasma Jet in Continuous Reactor Tube

The fifth configuration is designed to support the existence of a plasma jet in a wider range of conditions, specifically with hydrogen present in the growth furnace and precursors passing through the plasma. It provides somewhat of a compromise between the plasma jet in configuration 4 and the more traditional setups such as configuration 1. Shown in Figure 6.9, the plasma reactor tube producing the jet is housed in a larger tube directly passing to the furnace. The hope is that with the jet closer to the microwave source, it will be less prone to contraction from hydrogen or catalyst precursor addition and moreover, heat will not be lost through conduction to the mating flange as with configuration 4. The diameter of the alumina tube housing the plasma has also been further reduced, from 6 mm to 3 mm in an effort to further increase the gas velocity and the plasma's propensity to form a jet. It is now also possible to inject the carbon source as a sheath gas similar to configuration 3 since the thin tube does not heat to the same degree as the axial torch in configuration 3, and therefore methane breakdown and soot deposition are considerably reduced.

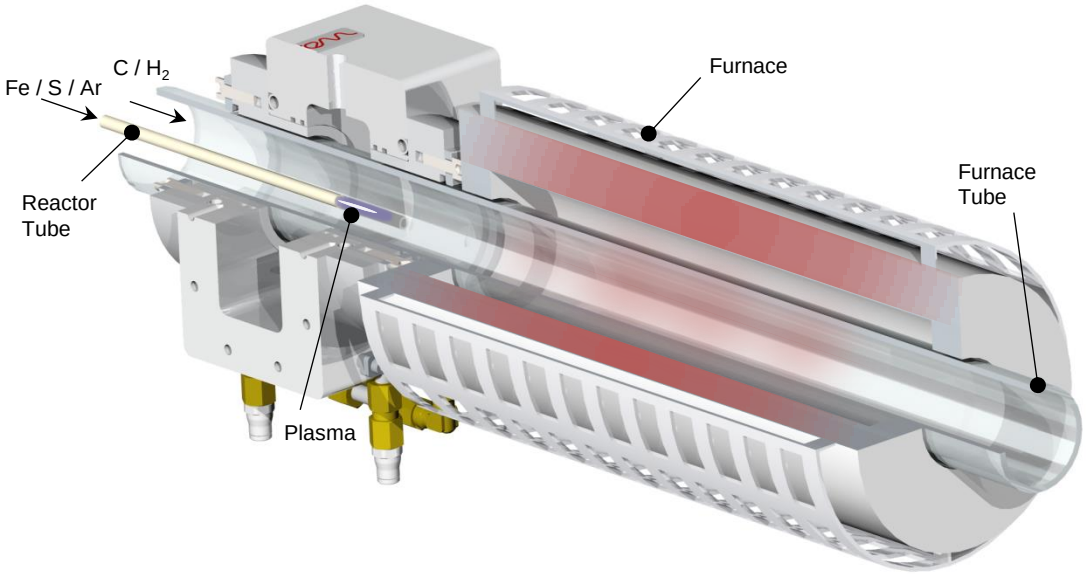

Fig. 6.9 Configuration 5 featuring 3 mm reactor tube and argon plasma jet situated inside larger furnace tube. Carbon and hydrogen injected as sheath gases.

Using this configuration, it is possible to maintain a small (<1 cm) argon plasma jet when hydrogen is present in the furnace tube and while precursors are passed through the plasma. Conversely, the total particle concentration emitted from the plasma is low in this configuration ($< 1 \times 10^6$ cm^{-3}) and also appears to be somewhat unsteady. This is exemplified in Figure 6.10a which depicts the total concentration output from

the plasma over time using a CPC. At the 50 s mark, ferrocene was introduced into the system which should produce several orders of magnitude more particles, yet in this case the concentration never exceeds 7×10^5 cm^{-3}. Moreover, this concentration is only transient and the value soon decreases back towards that of the background. The conclusion is then that penetration of the ferrocene and its constituent atoms is not effective in this configuration.

To eliminate the chance of contamination and in this case early deposition of the iron caused by the carbon within the ferrocene, the iron precursor was replaced by a hot wire particle generator [211]. This type of particle generator simply features a resistively-heated wire, in this case of iron, with a gas flow across it to remove the nascent particles. The peak size and number concentration (and therefore the mass concentration) of the iron particles can be controlled with the temperature of the wire, and this is normally accomplished by varying the current through the wire. Since iron is readily oxidized, hydrogen must be included in the gas flow to ensure the wire does not oxidize and break. As discussed previously, hydrogen exhibits a much higher thermal conductivity than other carrier gases (argon in this case) so the convective cooling on the wire is improved. As a result, the temperature of the wire, and thus its outgoing particle distribution is also dependent on the hydrogen fraction in the carrier gas. This phenomenon is shown in Figure 6.10b which presents size distributions using approximately 9% and 17% H_2 in Ar. Note that this increase in hydrogen fraction results in the mean diameter decreasing to 56% of its previous value (42.9 nm to 24.1 nm). The quantity of iron sent to the plasma is therefore controllable over a large range of mass throughputs.

Unfortunately, the requirements of the hot wire generator do not agree well with the requirements of the plasma system. As discussed for configuration 4, the inclusion of even very modest amounts of hydrogen (<4%) are sufficient to cause significant heating of the plasma tube and possibly even its catastrophic failure. Attempts were made to operate the generator using 2% H_2. However, this was not sufficient to prevent oxidation and failure of the wire within minutes. As a result, it does not appear that any overlap of hydrogen fraction exists which is suitable for the hot wire generator and this plasma configuration simultaneously. Moreover, even during the time the generator was able to function, particle generation from the plasma appeared similar to that from ferrocene. Once again, very few particles are produced by the plasma so the conclusion can be made that it is not solely the ferrocene's carbon that is responsible for the questionable catalyst production from configurations using thin plasma tubes. Instead, precursor material is likely lost to the tube walls. Three mechanisms could be responsible for this wall loss: diffusion, charging, and thermophoresis. Each of these phenomena are examined here.

Diffusion via Brownian motion is ubiquitous for aerosol samples and losses to tube walls occurs continuously. Classical diffusion theory [212] dictates that the penetration efficiency through a given length of tube is dependent only on the volumetric flow rate. Penetration is not dependent on tube diameter so there is no reason the thin tubes would have higher diffusion losses than any other reactor tube. Instead, ions or particles may be lost from space charging effects. This phenomenon occurs when many charges are present in a given volume, and can also be common when non-conducting tubes are used. Both of these criteria are met for the reactor tube since alumina is an insulator and the plasma has a high concentration of charges. Given the thin cross section of the reactor tube, the electrostatic forces may be large and could be responsible for particle deposition on the tube walls and a significant decrease in number concentration. Finally, themophoresis may also cause the high particles losses, and this is an effect which is certainly stronger given the small tube cross section. With a large temperature gradient such as that existing between the hot plasma and relatively cool tube wall, particles experience more energetic atomic collisions from the hot side and a net force is created towards the cold side. In this case, this force will result in deposition on the tube wall. The thermophoretic force is a function of the temperature gradient and no doubt an extremely large gradient exists in the reactor tube. It could be as high as several thousand Kelvin per millimetre. For comparison, dedicated thermophoretic sampling devices employ temperature gradients up to 100 to 200 K mm^{-1}. Therefore it seems highly likely that thermophoresis is causing the majority of the iron mass to be deposited on the walls. Further, if the particles manage to evaporate before they contact the tube wall, the iron vapour may still be lost to the wall since the wall temperature is well below the iron's melting point and the iron would remain here upon contact.

Given these findings, it appears that the use of a thin reactor tube to house the plasma and create a jet for efficient linkage of the catalyst nucleation and CNT growth stages exhibits limitations that outweigh its ability to produce a favourable temperature profile. Precursor penetration of the plasma is limited both for ferrocene and thiophene, and the material that is produced does not possess the correct morphology and number concentration for optimal high-throughput CNT production. It is clear that temperature gradients within the plasma region must not be too severe, and it is likely helpful if hydrogen is present during not only the CNT growth phase, but also the catalyst formation phase (either to suppress soot formation upon catalyst decomposition or prevent catalyst oxidation). A configuration is required which reduces the plasma-to-wall temperature gradients and can accommodate higher hydrogen fractions.

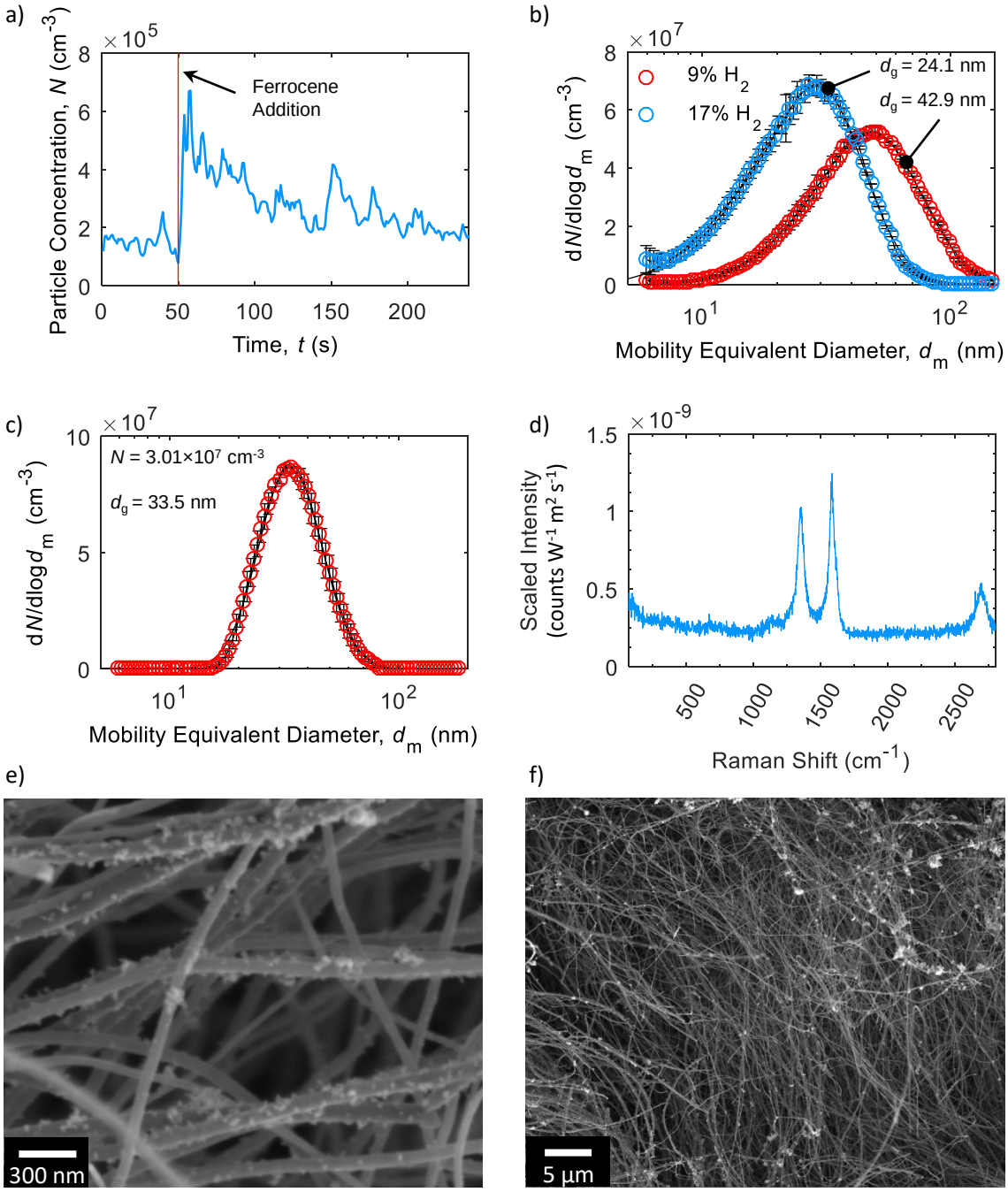

Fig. 6.10 (a) Total particle concentration over time for output of configuration 5 including discrete addition of ferrocene, and (b) size distributions of particles produced from hot wire generator at two hydrogen fractions. Data fit with two lognormal distributions each; $\sigma_{g1} = 1.68$, $\sigma_{g2} = 1.49$ for low H_2 and $\sigma_{g1} = 1.73$, $\sigma_{g2} = 1.45$ for high H_2. (c) catalyst particles from ferrocene and thiophene using swirl torch (configuration 6) fit with single lognormal distribution with $\sigma_g = 1.37$. All SMPS distributions are averages of two scans each and error bars represent one standard deviation. Characterization of material from configuration 6 including (d) Raman spectrum (average of two scans) and SEM with (e) high magnification and (f) low magnification.

6.7 Configuration 6: Swirl Torch with Single Reactor Tube

As discussed previously, the inclusion of hydrogen results in more severe heating of the reactor tube. Unfortunately, it has also been shown above that hydrogen is required for catalyst particle formation and has long been documented as a critical component in high CNT growth rate processes such as aerogel formation. The axial torch is able to accommodate hydrogen fractions of up to $\sim$25% for continuous operation, whereas the thin reactor tube producing a plasma jet is only able to handle 3-4% before failure. In both instances, even if the plasma is not directly contacting the tube wall, its proximity unfortunately still allows heat to conduct from the plasma to the tube wall. It is therefore apparent that a configuration is required that allows for larger separation between the plasma and the tube wall. As such, the swirl torch was designed and implemented. Detailed discussion of the swirl torch design is presented in Chapter 3, and a more complete schematic is shown in Figure 6.11.

Since the swirl torch allows the use of more thermally conductive gas mixtures, helium can be introduced in place of nitrogen. Again, the use of helium as the balance carrier gas alongside hydrogen has been seen to allow aerogel formation at lower hydrogen fractions than if another inert such as nitrogen or argon is used [38], and so helium should be chosen over other inerts when permissible. The maximum hydrogen fraction is also higher than previous configurations for steady-state operation, at around 50%. Unlike configuration 3 which was able to operate with 80% hydrogen in helium but is not stable over time, the swirl torch configuration is able to operate indefinitely without the plasma extinguishing or tube damage being incurred. Plasmas produced using the swirl torch are also stable down to approximately 3 SLPM which is slightly lower than the axial torch. Moreover, contaminating background particle concentrations are very low - often $\sim 10^2$ cm^{-3} - even at high H_2 fractions. An additional advantage is that since the reactor tube inner diameter has been increased from 23.5 mm (axial torch) to $\sim$46.5 mm, the swirl torch allows residence times nearly four times longer than are achievable from the axial torch for a given flow rate. Finally, since much of the gas injected using the swirl torch moves along the reactor tube wall and does not pass directly through the plasma, the carbon source (methane) could now be included in the front-end gas mixture which is advantageous because it simplifies the setup yet still ensures adequate heating/cracking into pyrolytic compounds.

An example SMPS scan of catalyst particles performed by Liron Issman is presented in Figure 6.10c. The mean particle diameter of 33.5 nm is more suitable for CNT growth than the larger (and sometimes fractal) particles produced using the plasma jet. The total number concentration is still somewhat low here at 3.01×10^7 cm^{-3} although this is likely due at least in part to the lower ferrocene pot temperature of 88°C. CNTs

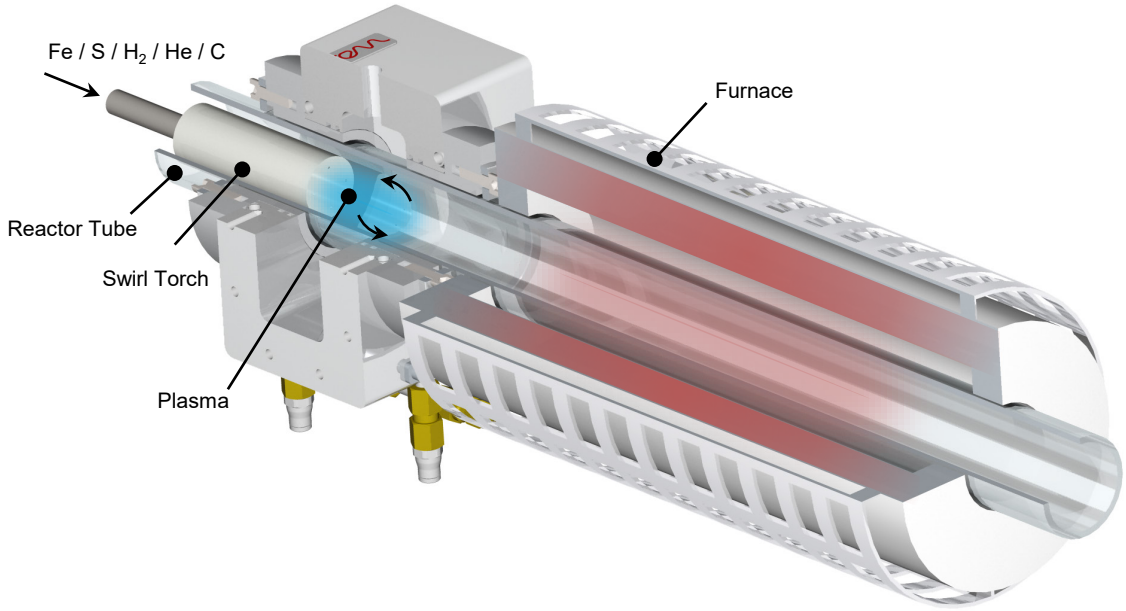

Fig. 6.11 Configuration 6 featuring a single reactor tube, plasma (helium/hydrogen) constrained using swirl torch, and front-end carbon injection

have successfully been synthesized using this configuration (experiment conducted by Liron Issman), and with higher abundance than any other configuration. The Raman spectrum is presented in Figure 6.10d, which indicates a clear CNT signal, albeit with a relatively high number of defects (large D peak). The CNTs themselves are pictured in the SEM images in Figure 6.10e and f. The image in Figure 6.10e is at high magnification and shows plentiful CNTs with large diameters around 50 nm. Smaller catalyst particles can be seen adhering to the CNT surfaces. The high abundance of CNTs is made even more apparent in Figure 6.10f which shows the same material at low magnification. Of particular interest is the length of the CNTs, which can be seen regularly reaching tens of micrometres. It should be noted that these CNTs were collected from material that was at one point attached to the tube wall but had detached during the experimental run. Therefore, this material would have been exposed to the growth conditions for longer than would have been possible had the CNTs been strictly suspended as an aerosol. Nevertheless, it seems clear that highly favourable growth conditions have been created with configuration 6 and the floating catalysts should be capable of substantial CNT growth as well.

Further optimization may include varying the iron and sulphur input to reduce the mean catalyst diameter and increase number concentration. Since the precursors are injected through the swirling jets, much of the material passes through the periphery of the plasma rather than directly through its centre. As a result, this precursor material is subjected to lower temperatures and temporal temperature gradients than it would have been had it passed directly through the plasma. More severe temporal temperature gradients, which can be linked to nucleation of smaller and more numerous catalyst

particles, would be observed if the precursor material was injected along the reactor tube axis directly through the plasma, perhaps using a thin injection line situated along the centre of the torch. This should ensure more homogeneous vaporization as well. At this point, it is possible that given some small process modifications, a spinnable aerogel could be synthesized using the plasma process.

6.8 Conclusions

This chapter has presented progress towards high mass throughput production of CNTs using the plasma system. The process requirements have included the ability to operate nearly indefinitely, the highest hydrogen fraction possible, low contaminating background particle production, flow rates of at most several litres per minute, and a smooth (ideally monatonic) downstream temperature profile. A summary of the advantages and disadvantages of each tested configuration is presented in Table 6.1. The first configuration featured the axial torch along with radial acetylene injection before the growth furnace. The particle size distribution was suitable for high throughput CNT growth (small mean diameter and high number concentration), and while high quality CNTs were synthesized, they were most often short. Further, many of the catalyst particles did not produce CNTs. The greatest limitation of this configuration is that significant heat is lost from the mating flange and gas vent, therefore making this process infeasible without the growth furnace.

The second configuration attempted to reduce heat loss post-plasma by removing the mating flange and instead using a single reactor tube for both the plasma and furnace. As a result, the growth time was reduced as all process gas was forced to pass through the furnace. Nevertheless, CNTs were synthesized in this configuration as well using counterflow injection of methane. The addition of modest flow rates of sulphur (thiophene) demonstrated that CNT quality degrades quickly with increasing sulphur content, likely because the relatively low hydrogen fraction forces most of the sulphur to condense on the catalyst particles rather than form H_2S.

The third configuration attempted to increase the hydrogen fraction by positioning the plasma inside the axial torch which can withstand the extreme heating caused by hydrogen plasmas. While a hydrogen fraction of 80% could be achieved at the very low total flow rate of 1 SLPM, the increasing dielectric constant of the torch prevented this configuration from being used in steady-state CNT production. Further, continuous contact of the plasma and torch resulted in high contaminant particle production that would have ultimately resulted in an impure final product.

The fourth configuration replaced the axial torch and 30 mm reactor tube with a much smaller 6 mm tube which protruded into the growth furnace to make the transition from particle nucleation to CNT growth as smooth as possible. A substantial

Table 6.1 Summary of high-throughput process configurations

Configuration	Advantages	Disadvantages
1	Catalyst $N = 10^8$ cm^{-3} Catalyst $d_g = 17$ nm High residence time Good long-term stability	H_2 fraction up to 25% Non-monatonic T profile
2	Catalyst $N = 10^8$ cm^{-3} Catalyst $d_g = 17$ nm Monatonic T profile Good long-term stability	H_2 fraction up to 25% Low residence time
3	H_2 fraction up to 80% High residence time	Many contaminating particles Poor long-term stability
4	50% H_2 fraction for growth High residence time	No H_2 for catalyst formation Non-monatonic T profile Catalyst $N = 10^7$ cm^{-3} Catalyst $d_g > 59$ nm Poor long-term stability
5	50% H_2 fraction for growth High residence time	No H_2 for catalyst formation Non-monatonic T profile Catalyst $N = 10^5$ cm^{-3} Poor long-term stability
6	H_2 fraction up to 50% Compatible with He Monatonic T profile Moderate residence time Good long-term stability	Catalyst $N = 10^7$ cm^{-3} Catalyst $d_g = 34$ nm

jet was achievable in pure argon but when hydrogen or precursors were introduced, the plasma contracted and the jet was not sustainable. Background particle concentration was several orders of magnitude lower than that from catalyst particles, although thiophene had to be replaced with elemental sulphur because accumulation of carbon in the reactor tube caused the plasma to extinguish. Nucleation of catalyst particles in the pure argon atmosphere resulted in an unusual flaked morphology using just ferrocene and large (50-60 nm) spherical particles when sulphur was included. In both cases, the number concentration and morphology was not suitable for CNT production.

Configuration 5 also employed a plasma jet but was positioned closer to the waveguide and placed within a larger tube directly connecting the furnace to the plasma. Once again, the catalyst particle number concentration was low and was not

found to be stable over time. It is suspected that this could be due to thermophoretic or electrostatic losses in the small diameter plasma tube. Ferrocene was replaced with a hot iron wire particle generator. However, it was not compatible with the plasma system since it required a higher hydrogen fraction than the plasma was able to accommodate.

The sixth and final configuration replaced the small cross-section reactor tube with a much larger 50 mm tube fitted with the swirl torch, allowing residence times that are nearly four times longer than are possible using the axial torch. Importantly, this configuration is actually capable of having the carbon introduced through the front of the reactor, simplifying the setup and allowing excellent preheating of the methane without hindering operation of the plasma itself. This design produces very low background particle concentrations and is capable of operating indefinitely at higher hydrogen fractions than are possible with any other configuration (at least 50% H_2). Initial tests have indicated that the catalyst particle size distribution is more suitable than those from the plasma jet since the mean diameter is substantially smaller ($\sim$30 nm compared to >50 nm), however total particle concentration remains somewhat low so far (3×10^7 cm^{-3}) and is a point for improvement. CNTs have been synthesized in high abundance and while defects are present, the CNTs are regularly at least tens of micrometres in length. Given that the swirl torch requires a relatively low flow rate, produces little contamination, contains a shallow and monatonic temperature gradient between the plasma and growth region, supports a highly reducing environment, and has been directly observed to produce long and numerous CNTs, objective (4) regarding developments of plasma-based high-throughput CNT synthesis has been met.

Chapter 7

Conclusions

The aims of this thesis have been to develop and characterize a microwave plasma system and to use this system to produce useful carbon nanotube materials in a cost-effective, scalable, and economically-relevant manner. The plasma system has been designed and constructed in such a way that it can: accommodate multiple gas mixtures including a significant fraction of hydrogen, operate nearly indefinitely without incurring damage to any of its components, and produce minimal contaminating background particles whose concentrations are several orders of magnitude lower than the intended catalyst distributions. Plasma stabilization is best accomplished using either an axial flow torch or swirl torch, which have been shown to effectively stabilize and centralize plasmas containing nitrogen, helium, and hydrogen. An analysis of materials for use with the plasma indicated that the torches should be fabricated from a material with a high melting point and high thermal shock resistance, and should be machinable. This work confirmed that boron nitride or a boron nitride-aluminum nitride composite are ideal for this application. This work also confirmed that the reactor tube should be comprised of quartz since it is inexpensive and also exhibits high thermal shock resistance. The quartz may require a boron nitride spray coating to prevent chemical damage from hydrogen. A rotational powder feeder was also developed that is capable of delivering accurate mass throughputs, and can accommodate powders spanning a wide range of flowability. These developments produced a versatile and robust system that can be adapted to produce multiple CNT products.

The plasma itself was also quantified regarding its temperature and electron density through an OES technique that involves introducing aerosolized rubidium as a tracer species. The Boltzmann plot method was used to determine the plasma's excitation temperature, and found it to be typical of atmospheric pressure microwave systems, ranging from approximately 4000 to 7000 K depending on the gas composition. Argon produced the highest temperature ($\sim$7000 K) and nitrogen was somewhat cooler ($\sim$6000 K). Addition of hydrogen to the nitrogen plasma further reduced its excitation

temperature to approximately 4300 K which is representative of the plasmas used for materials synthesis here. Electron densities were determined from the Saha equation, resulting in densities that ranged between 10^{18} and 10^{20} m^{-3}. Given these densities, it was determined that argon and rubidium were in partial local thermodynamic equilibrium, as were the higher energy states of nitrogen and hydrogen. No species were in complete LTE. This likely also explains the behaviour of the Boltzmann plot data since some points (particularly the low energy transitions of argon) do not display a good correlation with the linear fit. This method of temperature estimation is attractive since it can be performed for <£1000 and does not require any complex models or time-intensive post-processing.

The plasma system was then used to synthesize a metal oxide-CNT hybrid material for use in LIB anodes. Elemental iron and aluminum powders were used as the precursors for the core material and acetylene was used to grow the CNTs. The ability to use these raw materials in conjunction with the short process time of several seconds makes this process an appealing method by which to produce such materials since most anodes are currently synthesized using prefabricated materials and slow, multi-step techniques. This material displayed good long-term stability and capacity recovery after high rate cycling, and possessed a specific capacity higher than that of the current industry standard. Much of the material's stability is due to the presence of CNTs and a carbonaceous coating which improve the thermal and electrical conductivity, negating the need for a conductive additive during cell construction.

The plasma system was also incorporated into a method for high-throughput production of CNTs. Multiple configurations were tested in an effort to satisfy the challenging conditions most amenable to high spatial density growth of long CNTs. It was determined that the catalyst particles must nucleate in a hydrogen-rich environment to prevent excessive amounts of sulphur from accumulating on the particles, as well as to ensure the particles form as spheres ideal for CNT growth rather than as irregular agglomerates. The swirl torch is more suitable than the axial torch or plasma jet configurations since: its background concentration is low, it allows for long residence times, it can support helium operation and high hydrogen fractions (at least 50% H_2), and precursor penetration is good.

Beyond these advances, improvements can certainly be made to each of the three main bodies of work presented here, giving ample opportunity for future work. Regarding the plasma diagnostics, temperature measurement through another technique - even if it requires more specialized equipment - would be useful for quantifying the accuracy of the presented method. Direct measurement of gas temperature would also be useful since it is likely the most meaningful quantity with regard to the plasma's ability to vaporize precursor materials. Additionally, direct measurement of electron density from a technique such as Stark broadening would provide additional insight

on the plasma's proximity to local thermodynamic equilibrium. Finally, a temperature map of the plasma could provide a more complete and robust quantification of its temperature and electron density.

Potential improvements to the anode material include optimization of the CNT fraction since there exists an inherent trade-off between the material's conductivity (high CNT fraction) and its capacity (low CNT fraction). Other core materials could also be used such as those which express high volumetric capacity rather than high mass-based capacity. Refractory metals such as tungsten may be suitable for this. The plasma's high temperature places it in a unique position to explore vaporization and renucleation processes using these highly stable metals.

CNT synthesis must also be optimized using the swirl torch. Variations in gas composition, as well as precursor input rates, will be imperative for increasing CNT length and abundance. Further optimizations of the gas flow pattern (perhaps through additional CFD modeling) could allow even lower flow rates to be stable, leading to additional increases in residence time in the growth zone. Additional work should be conducted to determine the ideal method for carbon injection, so that enough of the reactive carbon species are present alongside the particles for rapid and efficient CNT growth. As recent work has indicated that quartz particles from the reactor tube may actively accelerate this carbon activation, deliberate inclusion of quartz for this purpose could offer an additional pathway to increase yield and growth rate.

The hope is that both the work presented here, along with its potential insight (given future work and further developments) can contribute to making the remarkable properties and considerable performance of CNTs globally impactful. Indeed, this work has been the catalyst for a multi-million pound scale-up project and has already garnered significant enthusiasm beyond the University of Cambridge. This body of work has demonstrated that complex, multifunctional CNT-based materials can be synthesized quickly and inexpensively and these attributes could facilitate making the final materials affordable and widely-available. As a result, the next generation of nanomaterials can be adopted in many fields of science and technology, maximizing their positive impacts on society.

References

[1] Sumio Iijima. Helical microtubules of graphitic carbon. *Nature*, 354:56–58, 1991. ISSN 0028-0836. doi: 10.1038/350055a0.

[2] Naoyuki Matsumoto, Azusa Oshima, Sachiko Ishizawa, Guohai Chen, Kenji Hata, and Don N. Futaba. One millimeter per minute growth rates for single wall carbon nanotube forests enabled by porous metal substrates. *RSC Advances*, 8(14):7810–7817, 2018. ISSN 20462069. doi: 10.1039/c7ra13093g. URL http://dx.doi.org/10.1039/C7RA13093G.

[3] A. A. Puretzky, D. B. Geohegan, S. Jesse, I. N. Ivanov, and G. Eres. In situ measurements and modeling of carbon nanotube array growth kinetics during chemical vapor deposition. *Applied Physics A: Materials Science and Processing*, 81(2):223–240, 2005. ISSN 09478396. doi: 10.1007/s00339-005-3256-7.

[4] L. X. Zheng, M. J. O'Connell, S. K. Doorn, X. Z. Liao, Y. H. Zhao, E. A. Akhadov, M. A. Hoffbauer, B. J. Roop, Q. X. Jia, R. C. Dye, D. E. Peterson, S. M. Huang, J. Liu, and Y. T. Zhu. Ultralong single-wall carbon nanotubes. *Nature Materials*, 3(10):673–676, 2004. ISSN 1476-1122. doi: 10.1038/nmat1216.

[5] Guohai Chen, Robert C. Davis, Hiroe Kimura, Shunsuke Sakurai, Motoo Yumura, Don N. Futaba, and Kenji Hata. The relationship between the growth rate and the lifetime in carbon nanotube synthesis. *Nanoscale*, 7 (19):8873–8878, 2015. ISSN 20403372. doi: 10.1039/c5nr01125f. URL http://dx.doi.org/10.1039/c5nr01125f.

[6] Alan Windle, Adam Boies, and Fiona Smail. Direct spinning of CNT fibres: past, present and future scale up. *Carbon*, 152:218–232, 2019. ISSN 00086223. doi: 10.1016/j.carbon.2019.05.024. URL https://doi.org/10.1016/j.carbon.2019.05.024.

[7] Rufan Zhang, Yingying Zhang, Qiang Zhang, Huanhuan Xie, Weizhong Qian, and Fei Wei. Growth of half-meter long carbon nanotubes based on Schulz-Flory distribution. *ACS Nano*, 7(7):6156–6161, 2013. ISSN 19360851. doi: 10.1021/nn401995z.

[8] Michael F L De Volder, Sameh H Tawfick, Ray H Baughman, and A John Hart. Carbon nanotubes: present and future commercial applications - Supplemental Information. *Science*, 339(6119):535–539, 2013. ISSN 1095-9203. doi: 10.1126/science.1222453. URL http://www.ncbi.nlm.nih.gov/pubmed/23372006.

[9] Shuchen Zhang, Lixing Kang, Xiao Wang, Lianming Tong, Liangwei Yang, Zequn Wang, Kuo Qi, Shibin Deng, Qingwen Li, Xuedong Bai, Feng Ding, and Jin Zhang. Arrays of horizontal carbon nanotubes of controlled chirality grown

using designed catalysts. *Nature*, 543(7644):234–238, 2017. ISSN 14764687. doi: 10.1038/nature21051.

[10] B. Q. Wei, R. Vajtai, and P. M. Ajayan. Reliability and current carrying capacity of carbon nanotubes. *Applied Physics Letters*, 79(8):1172–1174, 2001. ISSN 00036951. doi: 10.1063/1.1396632.

[11] Jean-Christophe Charlier, Xavier Blase, and Stephan Roche. Electronic and transport properties of nanotubes. *Rev. Mod. Phys.*, 79:677–732, May 2007. doi: 10.1103/RevModPhys.79.677. URL https://link.aps.org/doi/10.1103/RevModPhys.79.677.

[12] P. Kim, L. Shi, A. Majumdar, and P. L. McEuen. Thermal transport measurements of individual multiwalled nanotubes. *Physical Review Letters*, 87(21): 215502, oct 2001. ISSN 0031-9007. doi: 10.1103/PhysRevLett.87.215502. URL https://link.aps.org/doi/10.1103/PhysRevLett.87.215502.

[13] Eric Pop, David Mann, Qian Wang, Kenneth Goodson, and Hongjie Dai. Thermal conductance of an individual single-wall carbon nanotube above room temperature. *Nano Letters*, 6(1):96–100, 2006. ISSN 15306984. doi: 10.1021/nl052145f.

[14] Wen-Tai Hong and Nyan-Hwa Tai. Investigations on the thermal conductivity of composites reinforced with carbon nanotubes. In *Diamond*, pages 1577–1581, 2008. doi: 10.1016/j.diamond.2008.03.037.

[15] Saion Sinha, Saimir Barjami, Germano Iannacchione, Alexander Schwab, and George Muench. Off-axis thermal properties of carbon nanotube films. *Journal of Nanoparticle Research*, 7(6):651–657, 2005. ISSN 13880764. doi: 10.1007/s11051-005-8382-9.

[16] Steven L. Mielke, Diego Troya, Sulin Zhang, Je Luen Li, Shaoping Xiao, Roberto Car, Rodney S. Ruoff, George C. Schatz, and Ted Belytschko. The role of vacancy defects and holes in the fracture of carbon nanotubes. *Chemical Physics Letters*, 390(4-6):413–420, 2004. ISSN 00092614. doi: 10.1016/j.cplett.2004.04.054.

[17] Traian Dumitrică, Ted Belytscko, and Boris I. Yakobson. Bond-breaking bifurcation states in carbon nanotube fracture. *Journal of Chemical Physics*, 118(21):9485–9488, 2003. ISSN 00219606. doi: 10.1063/1.1577540.

[18] Diego Troya, Steven L. Mielke, and George C. Schatz. Carbon nanotube fracture - Differences between quantum mechanical mechanisms and those of empirical potentials. *Chemical Physics Letters*, 382(1-2):133–141, 2003. ISSN 00092614. doi: 10.1016/j.cplett.2003.10.068.

[19] Shigenobu Ogata and Yoji Shibutani. Ideal tensile strength and band gap of single-walled carbon nanotubes. *Physical Review B - Condensed Matter and Materials Physics*, 68(16):1–4, 2003. ISSN 1550235X. doi: 10.1103/PhysRevB.68.165409.

[20] T. Ozaki, Y. Iwasa, and T. Mitani. Stiffness of single-walled carbon nanotubes under large strain. *Physical Review Letters*, 84(8):1712–1715, 2000. ISSN 10797114. doi: 10.1103/PhysRevLett.84.1712.

[21] Akira Takakura, Ko Beppu, Taishi Nishihara, Akihito Fukui, Takahiro Kozeki, Takahiro Namazu, Yuhei Miyauchi, and Kenichiro Itami. Strength of carbon nanotubes depends on their chemical structures. *Nature Communications*, 10 (1):1–7, 2019. ISSN 2041-1723. doi: 10.1038/s41467-019-10959-7. URL http://dx.doi.org/10.1038/s41467-019-10959-7.

[22] Michele Meo and Marco Rossi. Prediction of Young's modulus of single wall carbon nanotubes by molecular-mechanics based finite element modelling. *Composites Science and Technology*, 66(11-12):1597–1605, 2006. ISSN 02663538. doi: 10.1016/j.compscitech.2005.11.015.

[23] M. Yu, O. Lourie, M. Dyer, K. Moloni, T. Kelly, and R. Ruoff. Strength and Breaking Mechanism of Multiwalled Carbon Nanotubes Under Tensile Load. *Science*, 287(5453):637–640, 2000. ISSN 00368075. doi: 10.1126/science.287.5453.637.

[24] Takayuki Watanabe, Takahiro Notoya, Takamasa Ishigaki, Hiroyuki Kuwano, Hideki Tanaka, and Yusuke Moriyoshi. Growth mechanism for carbon nanotubes in a plasma evaporation process. *Thin Solid Films*, 506-507:263–267, 2006. doi: 10.1016/j.tsf.2005.08.289.

[25] Maoshuai He, Shuchen Zhang, Qianru Wu, Han Xue, Benwu Xin, Dan Wang, and Jin Zhang. Designing catalysts for chirality-selective synthesis of single-walled carbon nanotubes: Past success and future opportunity. *Advanced Materials*, 1800805:1800805, 2018. ISSN 09359648. doi: 10.1002/adma.201800805. URL http://doi.wiley.com/10.1002/adma.201800805.

[26] Gyula Eres, Anika A. Kinkhabwala, Hongtao Cui, David B. Geohegan, Alexandar A. Puretzky, and Douglas H. Lowndes. Molecular beam-controlled nucleation and growth of vertically aligned single-wall carbon nanotube arrays. *Journal of Physical Chemistry B*, 109(35):16684–16694, 2005. ISSN 15206106. doi: 10.1021/jp051531i.

[27] G. Zhong, S. Hofmann, F. Yan, H. Telg, J. H. Warner, D. Eder, C. Thomsen, W. I. Milne, and J. Robertson. Acetylene: A key growth precursor for single-walled carbon nanotube forests. *Journal of Physical Chemistry C*, 113(40):17321–17325, 2009. ISSN 19327447. doi: 10.1021/jp905134b.

[28] P. Chen, H.-B. Zhang, G.-D. Lin, Q. Hong, and K.R. Tsai. Growth of carbon nanotubes by catalytic decomposition of ch4 or co on a nimgo catalyst. *Carbon*, 35(10):1495 – 1501, 1997. ISSN 0008-6223. doi: https://doi.org/10.1016/S0008-6223(97)00100-0. URL http://www.sciencedirect.com/science/article/pii/S0008622397001000.

[29] Erik C. Neyts, Kostya Ostrikov, Mahendra K. Sunkara, and Annemie Bogaerts. Plasma catalysis: Synergistic effects at the nanoscale. *Chemical Reviews*, 115 (24):13408–13446, 2015. doi: 10.1021/acs.chemrev.5b00362.

[30] Michaël F.L. De Volder, Sameh Tawfick, Sei Jin Park, and A. John Hart. Corrugated carbon nanotube microstructures with geometrically tunable compliance. *ACS Nano*, 5(9):7310–7317, 2011. ISSN 19360851. doi: 10.1021/nn202156q.

[31] Sameh Tawfick, Michael De Volder, and A. John Hart. Structurally programmed capillary folding of carbon nanotube assemblies. *Langmuir*, 27(10):6389–6394, 2011. ISSN 07437463. doi: 10.1021/la200635g.

[32] Thang Q. Tran, Robert J. Headrick, E. Amram Bengio, Sandar Myo Myint, Hamed Khoshnevis, Vida Jamali, Hai M. Duong, and Matteo Pasquali. Purification and dissolution of carbon nanotube fibers spun from the floating catalyst method. *ACS Applied Materials and Interfaces*, 9(42):37112–37119, 2017. ISSN 19448252. doi: 10.1021/acsami.7b09287.

[33] Ya-Li Li, Ian a Kinloch, and Alan H Windle. Direct spinning of carbon nanotube fibers from chemical vapor deposition synthesis. *Science (New York, N.Y.)*, 304: 276–278, apr 2004. doi: 10.1126/science.1094982.

[34] Lee Weller, Fiona R. Smail, James A. Elliott, Alan H. Windle, Adam M. Boies, and Simone Hochgreb. Mapping the parameter space for direct-spun carbon nanotube aerogels. *Carbon*, 146:789–812, 2019. ISSN 00086223. doi: 10.1016/j.carbon.2019.01.091. URL https://doi.org/10.1016/j.carbon.2019.01.091.

[35] Bartolomé Mas, Belén Alemán, Ignacio Dopico, Ignacio Martin-Bragado, Teresa Naranjo, Emilio M. Pérez, and Juan J. Vilatela. Group 16 elements control the synthesis of continuous fibers of carbon nanotubes. *Carbon*, 101: 458–464, 2016. ISSN 00086223. doi: 10.1016/j.carbon.2016.02.005.

[36] Christian Hoecker, Fiona Smail, Martin Pick, Lee Weller, and Adam M. Boies. The dependence of CNT aerogel synthesis on sulfur-driven catalyst nucleation processes and a critical catalyst particle mass concentration. *Scientific Reports*, 7(1):1–11, 2017. ISSN 20452322. doi: 10.1038/s41598-017-14775-1. URL http://dx.doi.org/10.1038/s41598-017-14775-1.

[37] D. R. Poirier, Hongbin Yin, Mikio Suzuki, and Toshihiko Emi. Interfacial properties of dilute Fe-O-S melts on alumina substrates. *ISIJ International*, 38 (3):229–238, 2008. ISSN 0915-1559. doi: 10.2355/isijinternational.38.229.

[38] T S Gspann, F R Smail, and A H Windle. Spinning of carbon nanotube fibres using the floating catalyst high temperature route : purity issues and the critical role of sulphur. *Faraday Discussions*, 173:47–65, 2014. doi: 10.1039/C4FD00066H.

[39] Ignacio Martin-Gullon, José Vera, Juan A Conesa, José L González, and César Merino. Differences between carbon nanofibers produced using Fe and Ni catalysts in a floating catalyst reactor. *Carbon*, 44:1572–1580, 2006. doi: 10.1016/j.carbon.2005.12.027.

[40] Kun-Hong Lee, Sung-Hyun Lee, Junbeom Park, Hye-Rim Kim, and Jaegeun Lee. Synthesis of high-quality carbon nanotube fibers by controlling the effects of sulfur on the catalyst agglomeration during the direct spinning process. *RSC Adv.*, 5:41894–41900, 2015. ISSN 2046-2069. doi: 10.1039/C5RA04691B. URL http://pubs.rsc.org/en/Content/ArticleLanding/2015/RA/C5RA04691B.

[41] R.M. Sundaram and A.H. Windle. Effect of carbon precursors on the structure and properties of continuously spun carbon nanotube fibers. *Science of Advanced Materials*, 7(4):643–653, 2015.

[42] Yue-Ying Fan, Adam Kaufmann, Alexander Mukasyan, and Arvind Varma. Single-and multi-wall carbon nanotubes produced using the floating catalyst method: Synthesis, purification and hydrogen up-take. *Carbon*, 44:2160–2170, 2006. doi: 10.1016/j.carbon.2006.03.009.

[43] Marcelo Motta, Ya-Li Li, Ian Kinloch, and Alan Windle. Mechanical properties of continuously spun fibers of carbon nanotubes. 5(8):1529–1533, 2005. doi: 10.1021/nl050634+.

[44] Marcelo Motta, Ian Kinloch, Anna Moisala, Venugoplan Premnath, Martin Pick, and Alan Windle. The parameter space for the direct spinning of fibres and films of carbon nanotubes. *Physica E*, 37:40–43, 2007. doi: 10.1016/j.physe.2006.07.005.

[45] Devin Conroy, Anna Moisala, Silvana Cardoso, Alan Windle, and John Davidson. Carbon nanotube reactor: Ferrocene decomposition, iron particle growth, nanotube aggregation and scale-up. *Chemical Engineering Science*, 65(10): 2965–2977, may 2010. doi: 10.1016/j.ces.2010.01.019.

[46] Víctor Reguero, Bele Alema, and Juan Joseilatela. Controlling carbon nanotube type in macroscopic fibers synthesized by the direct spinning process. *Chemistry of Materials*, 26:3550–3557, 2014. doi: 10.1021/cm501187x.

[47] Adam M. Boies, Christian Hoecker, Ajinkya Bhalerao, Nikolaos Kateris, Jean de La Verpilliere, Brian Graves, and Fiona Smail. Agglomeration dynamics of 1D materials: Gas-phase collision rates of nanotubes and nanorods. *Small*, 1900520:1–10, 2019. ISSN 1613-6810. doi: 10.1002/smll.201900520. URL https://onlinelibrary.wiley.com/doi/abs/10.1002/smll.201900520.

[48] Wei Xu, Yun Chen, Hang Zhan, and Jian Nong Wang. High-strength carbon nanotube film from improving alignment and densification. *Nano Letters*, 16 (2):946–952, 2016. ISSN 15306992. doi: 10.1021/acs.nanolett.5b03863.

[49] Juan J. Vilatela and Alan H. Windle. Yarn-like carbon nanotube fibers. *Advanced Materials*, 22(44):4959–4963, 2010. ISSN 09359648. doi: 10.1002/adma.201002131.

[50] Chunmei Ban, Zhuangchun Wu, Dane T. Gillaspie, Le Chen, Yanfa Yan, Jeffrey L. Blackburn, and Anne C. Dillon. Nanostructured fe3o4/swnt electrode: Binder-free and high-rate li-ion anode. *Advanced Materials*, 22(20):E145–E149, 2010. doi: 10.1002/adma.200904285. URL https://onlinelibrary.wiley.com/doi/abs/10.1002/adma.200904285.

[51] Liming Dai, Dong Wook Chang, Jong Beom Baek, and Wen Lu. Carbon nanomaterials for advanced energy conversion and storage. *Small*, 8(8):1130–1166, 2012. ISSN 16136810. doi: 10.1002/smll.201101594.

[52] Andreas R. Köhler, Claudia Som, Aasgeir Helland, and Fadri Gottschalk. Studying the potential release of carbon nanotubes throughout the application life cycle. *Journal of Cleaner Production*, 16(8-9):927–937, 2008. ISSN 09596526. doi: 10.1016/j.jclepro.2007.04.007.

[53] Jia Chen. Analysis of moore's law on intel processors. In Limin Jia, Zhigang Liu, Yong Qin, Minghua Zhao, and Lijun Diao, editors, *Proceedings of the 2013 International Conference on Electrical and Information Technologies for Rail Transportation (EITRT2013)-Volume II*, pages 391–400, Berlin, Heidelberg, 2014. Springer Berlin Heidelberg. ISBN 978-3-642-53751-6.

[54] L. Xiu. Time moore: Exploiting moore's law from the perspective of time. *IEEE Solid-State Circuits Magazine*, 11(1):39–55, winter 2019. ISSN 1943-0582. doi: 10.1109/MSSC.2018.2882285.

[55] Gage Hills, Christian Lau, Andrew Wright, Samuel Fuller, Mindy D. Bishop, Tathagata Srimani, Pritpal Kanhaiya, Rebecca Ho, Aya Amer, Yosi Stein, Denis Murphy, Arvind, Anantha Chandrakasan, and Max M. Shulaker. Modern microprocessor built from complementary carbon nanotube transistors. *Nature*, 572(7771):595–602, 2019. ISSN 0028-0836. doi: 10.1038/s41586-019-1493-8. URL http://www.nature.com/articles/s41586-019-1493-8.

[56] Cao Guan, Jilei Liu, Yadong Wang, Lu Mao, Zhanxi Fan, Zexiang Shen, Hua Zhang, and John Wang. Iron oxide-decorated carbon for supercapacitor anodes with ultrahigh energy density and outstanding cycling stability. *ACS Nano*, 9 (5):5198–5207, 2015. doi: 10.1021/acsnano.5b00582. URL https://doi.org/10.1021/acsnano.5b00582. PMID: 25868870.

[57] Abdul-Rahman O. Raji, Rodrigo Villegas Salvatierra, Nam Dong Kim, Xiujun Fan, Yilun Li, Gladys A. L. Silva, Junwei Sha, and James M. Tour. Lithium batteries with nearly maximum metal storage. *ACS Nano*, 11(6):6362–6369, 2017. doi: 10.1021/acsnano.7b02731. URL https://doi.org/10.1021/acsnano.7b02731. PMID: 28511004.

[58] Xiaofei Sun, Youlong Xu, Ding Peng, Guogang Chen, Xiaoyu Zheng, Rui Zhang, and Long Li. The composite sphere of manganese oxide and carbon nanotubes as a prospective anode material for lithium-ion batteries. *Journal of Power Sources*, 255:163–169, 06 2014. doi: 10.1016/j.jpowsour.2013.12.106.

[59] Tianbo Yang, Wanxi Zhang, Linlin Li, Bo Jin, En Mei Jin, Sang Mun Jeong, and Qing Jiang. In-situ synthesized znfe2o4 firmly anchored to the surface of mwcnts as a long-life anode material with high lithium storage performance. *Applied Surface Science*, 425, 07 2017. doi: 10.1016/j.apsusc.2017.07.152.

[60] T. Guo, P. Nikolaev, A. Thess, D. T. Colbert, and R.E. Smalley. Catalytic growth of single-walled nanotubes by laser vaporization. *Chemical Physics Letters*, 243(September):49–54, 1995. ISSN 00092614. doi: 10.1016/0009-2614(95)00825-O.

[61] S A Esfarjani, J Mostaghimi, K S Kim, A Shahverdi, and G Soucy. Radio frequency thermal plasma: The cutting edge technology in production of single-walled carbon nanotubes. *Journal of Thermal Science and Technology*, 6(2): 307–322, 2011. doi: 10.1299/Jtst.6.307.

[62] SC Snyder, GD Lassahn, and JD Grandy. Direct determination of gas velocity and gas temperature in an atmospheric-pressure argon–hydrogen plasma jet. *Journal of Quantitative Spectroscopy and Radiative Transfer*, 107(2):217–225, 2007.

[63] Keun Su Kim, Ala Moradian, Javad Mostaghimi, Yasaman Alinejad, Ali Shahverdi, Benoit Simard, and Gervais Soucy. Synthesis of single-walled carbon nanotubes by induction thermal plasma. *Nano Research*, 2(10):800–817, 2009. doi: 10.1007/s12274-009-9085-9.

[64] Hanako Okuno, Eusebiu Grivei, Frédéric Fabry, Thomas M. Gruenberger, José Gonzalez-Aguilar, Andreï Palnichenko, Laurent Fulcheri, Nicolas Probst, and Jean-Christophe Charlier. Synthesis of carbon nanotubes and nano-necklaces by thermal plasma process. *Carbon*, 42:2543–2549, jan 2004. doi: 10.1016/j.carbon.2004.05.037. URL http://www.scopus.com/inward/record.url?eid=2-s2.0-4043163391{&}partnerID=tZOtx3y1.

[65] Ali Shahverdi and G. Soucy. Counter-current ammonia injection flow during synthesis of single-walled carbon nanotubes by induction thermal plasma. *Chemical Engineering Science*, 104:389–398, 2013. doi: 10.1016/j.ces.2013.09.036. URL http://dx.doi.org/10.1016/j.ces.2013.09.036.

[66] Jun-Ho Seo and Bong-Guen Hong. Thermal plasma synthesis of nano-sized powders. *Nuclear Engineering and Technology*, 44(1):9–20, 2012.

[67] Zihao Ouyang, Vijay Surla, Tae Seung Cho, and David N Ruzic. Characterization of an atmospheric-pressure helium plasma generated by 2.45-ghz microwave power. *IEEE Transactions on Plasma Science*, 40(12):3476–3481, 2012.

[68] Dimitrios Karabourniotis. Excitation temperatures in the ionizing plasma of high-pressure mercury discharges. *Applied Physics Letters*, 83(26):5395–5397, 2003. doi: 10.1063/1.1636819. URL https://doi.org/10.1063/1.1636819.

[69] M Leins, M Walker, A Schulz, U Schumacher, and U Stroth. Spectroscopic investigation of a microwave-generated atmospheric pressure plasma torch. *Contributions to Plasma Physics*, 52(7):615–628, 2012.

[70] J Choi, IS Eom, SJ Kim, YW Kwon, HM Joh, BS Jeong, and TH Chung. Characterization of a microwave-excited atmospheric-pressure argon plasma jet using two-parallel-wires transmission line resonator. *Physics of Plasmas*, 24(9): 093516, 2017.

[71] NH Bings, M Olschewski, and JAC Broekaert. Two-dimensional spatially resolved excitation and rotational temperatures as well as electron number density measurements in capacitively coupled microwave plasmas using argon, nitrogen and air as working gases by spectroscopic methods. *Spectrochimica Acta Part B: Atomic Spectroscopy*, 52(13):1965–1981, 1997.

[72] Takaya Oshita, Hiroaki Kawano, Toshihiro Takamatsu, Hidekazu Miyahara, and Akitoshi Okino. Temperature controllable atmospheric plasma source. *IEEE Transactions on Plasma Science*, 43(6):1987–1992, 2015.

[73] Yuri Noma, Jai Hyuk Choi, Takaaki Tomai, and Kazuo Terashima. Gas-temperature-dependent generation of cryoplasma jet under atmospheric pressure. *Applied Physics Letters*, 93(10):101503, 2008.

[74] E. Kroupp, D. Osin, A. Starobinets, V. Fisher, V. Bernshtam, L. Weingarten, Y. Maron, I. Uschmann, E. Förster, A. Fisher, M.E. Cuneo, C. Deeney, and J.L. Giuliani. Ion temperature and hydrodynamic-energy measurements in a z-pinch plasma at stagnation. *Physical Review Letters*, 107(10), 2011. doi: 10.1103/PhysRevLett.107.105001. URL https://www.scopus.com/inward/record.uri?eid=2-s2.0-80052235791&doi=10.1103%2fPhysRevLett.107.105001&partnerID=40&md5=1187f5aab7e02407534387cdcc343700. cited By 29.

[75] V E Moiseenko, V V Nemov, O Ågren, S V Kasilov, and I E Garkusha. Fast ion motion in the plasma part of a stellarator-mirror fission–fusion hybrid. *Plasma Physics and Controlled Fusion*, 58(6):064005, may 2016. doi: 10.1088/0741-3335/58/6/064005. URL https://doi.org/10.1088%2F0741-3335%2F58%2F6%2F064005.

[76] SP Kuo, E Koretzky, and RJ Vidmar. Temperature measurement of an atmospheric-pressure plasma torch. *Review of scientific instruments*, 70(7): 3032–3034, 1999.

[77] JH Kim, YH Kim, YH Choi, W Choe, JJ Choi, and YS Hwang. Optical measurements of gas temperatures in atmospheric pressure rf cold plasmas. *Surface and Coatings technology*, 171(1-3):211–215, 2003.

[78] AW Khan, F Jan, A Saeed, M Zaka-ul Islam, M Abrar, NAD Khattak, and M Zakaullah. Comparative study of electron temperature and excitation temperature in a magnetic pole enhanced-inductively coupled argon plasma. *Current Applied Physics*, 13(7):1241–1246, 2013.

[79] Chuan-Jie Chen and Shou-Zhe Li. Spectroscopic measurement of plasma gas temperature of the atmospheric-pressure microwave induced nitrogen plasma torch. *Plasma Sources Science and Technology*, 24(3):035017, 2015.

[80] J Muñoz, MS Dimitrijević, C Yubero, and MD Calzada. Using the van der waals broadening of spectral atomic lines to measure the gas temperature of an argon–helium microwave plasma at atmospheric pressure. *Spectrochimica Acta Part B: Atomic Spectroscopy*, 64(2):167–172, 2009.

[81] C Yubero, MC García, M Varo, and P Martínez. Gas temperature determination in microwave discharges at atmospheric pressure by using different optical emission spectroscopy techniques. *Spectrochimica Acta Part B: Atomic Spectroscopy*, 90:61–67, 2013.

[82] Sven Hofmann, AFH Van Gessel, Tiny Verreycken, and P Bruggeman. Power dissipation, gas temperatures and electron densities of cold atmospheric pressure helium and argon rf plasma jets. *Plasma Sources Science and Technology*, 20 (6):065010, 2011.

[83] T Verreycken, AFH Van Gessel, A Pageau, and P Bruggeman. Validation of gas temperature measurements by oes in an atmospheric air glow discharge with water electrode using rayleigh scattering. *Plasma Sources Science and Technology*, 20(2):024002, 2011.

[84] Ji Hun Kim, Yoon Ho Choi, and YS Hwang. Electron density and temperature measurement method by using emission spectroscopy in atmospheric pressure nonequilibrium nitrogen plasmas. *Physics of plasmas*, 13(9):093501, 2006.

[85] M Baeva, K Rackow, MM Becker, J Ehlbeck, and D Loffhagen. Characterization of atmospheric pressure microwave plasma in n2/o2/h2o gas mixtures. *Topic C9, 30th ICPIG, Belfast, Northern Ireland UK*, 2011.

[86] Davide Mariotti, Yoshiki Shimizu, Takeshi Sasaki, and Naoto Koshizaki. Gas temperature and electron temperature measurements by emission spectroscopy for an atmospheric microplasma. *Journal of applied physics*, 101(1):013307, 2007.

[87] Hojoong Sun, Jungwun Lee, Seong-kyun Im, and Moon Soo Bak. Optical emission spectroscopic studies on atmospheric electrodeless microwave plasma in carbon dioxide–hydrogen mixture. *IEEE Transactions on Plasma Science*, 45(12):3154–3159, 2017.

[88] Xi-Ming Zhu, Wen-Cong Chen, and Yi-Kang Pu. Gas temperature, electron density and electron temperature measurement in a microwave excited microplasma. *Journal of Physics D: Applied Physics*, 41(10):105212, 2008.

[89] Julien Lam, Vincent Motto-Ros, Dimitri Misiak, Christophe Dujardin, Gilles Ledoux, and David Amans. Investigation of local thermodynamic equilibrium in laser-induced plasmas: measurements of rotational and excitation temperatures at long time scales. *Spectrochimica Acta Part B: Atomic Spectroscopy*, 101: 86–92, 2014.

[90] Shuai Zhang, Wenchun Wang, Li Jia, Zhijie Liu, Yang Yang, and Leyang Dai. Rotational, vibrational, and excitation temperatures in bipolar nanosecond-pulsed diffuse dielectric-barrier-discharge plasma at atmospheric pressure. *IEEE Transactions on Plasma Science*, 41(2):350–354, 2013.

[91] G. Shanmugavelayutham, V. Selvarajan, P.V.A. Padmanabhan, K.P. Sreekumar, and N.K. Joshi. Effect of powder loading on the excitation temperature of a plasma jet in dc thermal plasma spray torch. *Current Applied Physics*, 7(2):186 – 192, 2007. ISSN 1567-1739. doi: https://doi.org/10.1016/j.cap.2006.03.003. URL http://www.sciencedirect.com/science/article/pii/S1567173906000927.

[92] S Yugeswaran and V Selvarajan. Excitation temperature and electron number density behavior of atmospheric pressure dc argon plasma jet during spheroidization of nickel. *Vacuum*, 83(5):841–847, 2009.

[93] F. Iza and J. A. Hopwood. Rotational, vibrational, and excitation temperatures of a microwave-frequency microplasma. *IEEE Transactions on Plasma Science*, 32(2):498–504, April 2004. ISSN 0093-3813. doi: 10.1109/TPS.2004.826145.

[94] M.M. Rahman and M.W. Blades. Atmospheric pressure, radio frequency, parallel plate capacitively coupled plasma—excitation temperatures and analytical figures of merit. *Spectrochimica Acta Part B: Atomic Spectroscopy*, 52(13):1983 – 1993, 1997. ISSN 0584-8547. doi: https://doi.org/10.1016/S0584-8547(97)00080-3. URL http://www.sciencedirect.com/science/article/pii/S0584854797000803.

[95] Robert I. McCrindle and Cornelius J. Rademeyer. Excitation temperature and analytical parameters for an ethanol-loaded inductively coupled plasma atomic emission spectrometer. *J. Anal. At. Spectrom.*, 10:399–404, 1995. doi: 10.1039/JA9951000399. URL http://dx.doi.org/10.1039/JA9951000399.

[96] Shinobu Mukasa, Shinfuku Nomura, Hiromichi Toyota, Tsunehiro Maehara, Fumiaki Abe, and Ayato Kawashima. Temperature distributions of radio-frequency plasma in water by spectroscopic analysis. *Journal of Applied Physics*, 106(11):113302, 2009. doi: 10.1063/1.3264671. URL https://doi.org/10.1063/1.3264671.

[97] Yoshiaki Hattori, Shinobu Mukasa, Hiromichi Toyota, Toru Inoue, and Shinfuku Nomura. Continuous synthesis of magnesium-hydroxide, zinc-oxide, and silver nanoparticles by microwave plasma in water. *Materials Chemistry and Physics - MATER CHEM PHYS*, 131, 12 2011. doi: 10.1016/j.matchemphys.2011.09.068.

[98] Jacob Zalach and Steffen Franke. Iterative boltzmann plot method for temperature and pressure determination in a xenon high pressure discharge lamp. *Journal of Applied Physics*, 113, 01 2013. doi: 10.1063/1.4788701.

[99] Guilherme Luiz Scheffler and Dirce Pozebon. Effect of n2 on the emission profile and excitation temperature in axially viewed plasma-icp oes. *J. Anal. At. Spectrom.*, 30:468–478, 2015. doi: 10.1039/C4JA00431K. URL http://dx.doi.org/10.1039/C4JA00431K.

[100] Seyedeh Zahra Mortazavi, Parviz Parvin, Ali Reyhani, Ahmad Nozad Golikand, and Soghra Mirershadi. Effect of laser wavelength at ir (1064 nm) and uv (193 nm) on the structural formation of palladium nanoparticles in deionized water. *The Journal of Physical Chemistry C*, 115(12):5049–5057, 2011. doi: 10.1021/jp1091224. URL https://doi.org/10.1021/jp1091224.

[101] Noriyasu Ohno, M Abdur Razzak, Hiroshi Ukai, Shuichi Takamura, and Yoshihiko Uesugi. Validity of electron temperature measurement by using boltzmann plot method in radio frequency inductive discharge in the atmospheric pressure range. *Plasma and fusion research*, 1:028–028, 2006.

[102] Lee Weller, Robert J Bettles, Paul Siddons, Charles S Adams, and Ifan G Hughes. Absolute absorption on the rubidium d1 line including resonant dipole–dipole interactions. *Journal of Physics B: Atomic, Molecular and Optical Physics*, 44(19):195006, 2011.

[103] James Keaveney, Charles S. Adams, and Ifan G. Hughes. Elecsus: Extension to arbitrary geometry magneto-optics. *Computer Physics Communications*, 224:311 – 324, 2018. ISSN 0010-4655. doi: https://doi.org/10.1016/j.cpc.2017.12.001. URL http://www.sciencedirect.com/science/article/pii/S0010465517304009.

[104] Mark A. Zentile, James Keaveney, Lee Weller, Daniel J. Whiting, Charles S. Adams, and Ifan G. Hughes. Elecsus: A program to calculate the electric susceptibility of an atomic ensemble. *Computer Physics Communications*, 189:162 – 174, 2015. ISSN 0010-4655. doi: https://doi.org/10.1016/j.cpc.2014.11.023. URL http://www.sciencedirect.com/science/article/pii/S001046551400407X.

[105] Paul Siddons, Charles S Adams, Chang Ge, and Ifan G Hughes. Absolute absorption on rubidium d lines: Comparison between theory and experiment. *Journal of Physics B: Atomic, Molecular and Optical Physics*, 41(15):155004, 2008.

[106] S Jovicevic, M Ivkovic, and N Konjevic. Parametric study of an atmospheric pressure microwave-induced plasma of the mini mip torch — ii. two-dimensional spatially resolved excitation temperature measurements. *Spectrochimica Acta Part B: Atomic Spectroscopy*, 56(12):2419 – 2428, 2001. ISSN 0584-8547. doi: https://doi.org/10.1016/S0584-8547(01)00305-6. URL http://www.sciencedirect.com/science/article/pii/S0584854701003056.

[107] Xilai Jia, Zheng Chen, Xia Cui, Yiting Peng, Xiaolei Wang, Ge Wang, Fei Wei, and Yunfeng Lu. Building robust architectures of carbon and metal oxide nanocrystals toward high-performance anodes for lithium-ion batteries. *ACS Nano*, 6(11):9911–9919, 2012. doi: 10.1021/nn303478e. URL https://doi.org/10.1021/nn303478e. PMID: 23046380.

[108] Seung Ho Choi, Jong-Heun Lee, and Yun Chan Kang. Perforated metal oxide–carbon nanotube composite microspheres with enhanced lithium-ion storage properties. *ACS Nano*, 9(10):10173–10185, 2015. doi: 10.1021/acsnano.5b03822. URL https://doi.org/10.1021/acsnano.5b03822. PMID: 26355350.

[109] Gang Huang, Feifei Zhang, Xinchuan Du, Yuling Qin, Dongming Yin, and Limin Wang. Metal organic frameworks route to in situ insertion of multi-walled carbon nanotubes in co3o4 polyhedra as anode materials for lithium-ion batteries. *ACS Nano*, 9(2):1592–1599, 2015. doi: 10.1021/nn506252u. URL https://doi.org/10.1021/nn506252u. PMID: 25629650.

[110] Jie Yue, Xin Gu, Xiaolei Jiang, Liang Chen, Nana Wang, Jian Yang, and Xiaojian Ma. Coaxial manganese dioxide@n-doped carbon nanotubes as superior anodes for lithium ion batteries. *Electrochimica Acta*, 182, 09 2015. doi: 10.1016/j.electacta.2015.09.150.

[111] Liu-Yang Sun, Lie Yang, Jing Li, Narayan R.L., and Xiaohui Ning. Superior full-cell cycling and rate performance achieved by carbon coated hollow fe3o4 nanoellipsoids for lithium ion battery. *Electrochimica Acta*, 288, 09 2018. doi: 10.1016/j.electacta.2018.08.060.

[112] Ultralong mno@c nanowires with internal voids anchored between graphene as a robust high performance anode for flexible li-ion battery. *Electrochimica Acta*, 296:276 – 282, 2019. ISSN 0013-4686. doi: https://doi.org/10.1016/j.electacta.2018.09.199. URL http://www.sciencedirect.com/science/article/pii/S0013468618322096.

[113] Weiqin Li, Cuihua An, Huinan Guo, Junli Sun, Mengying Wang, Yunwei Li, Lifang Jiao, and Yijing Wang. In situ synthesis of 1d mesoporous mno@c nanorods for high performance li-ion batteries. *ACS Sustainable Chemistry & Engineering*, 7(1):139–146, 2019. doi: 10.1021/acssuschemeng.8b01782. URL https://doi.org/10.1021/acssuschemeng.8b01782.

[114] S H. Kim, C Wang, and M R. Zachariah. Aerosol formation of sea-urchin-like nanostructures of carbon nanotubes on bimetallic nanocomposite particles. *Journal of Nanoparticle Research*, 13:139–146, 01 2010. doi: 10.1007/s11051-010-0011-6.

[115] Jean de La Verpilliere, Sarah Jessl, Khuzaimah Saeed, Caterina Ducati, Michael De Volder, and Adam Meyer Boies. Continuous flow chemical vapour deposition of carbon nanotube sea urchins. 04 2018. doi: 10.17863/CAM.23217.

[116] Chih-ming Chuang, Sahendra P Sharma, Jyh-ming Ting, Hong-ping Lin, Hsisheng Teng, and Cheng-Wei Huang. Preparation of sea urchin-like carbons by growing one-dimensional nanocarbon on mesoporous carbons. *Diamond and Related Materials*, 17:606–610, 2008. doi: 10.1016/j.diamond.2007.12.005.

[117] Ping-lin Kuo, Chun-han Hsu, Wan-ting Li, Jing-yi Jhan, and Wei-fu Chen. Sea urchin-like mesoporous carbon material grown with carbon nanotubes as a cathode catalyst support for fuel cells. *Journal of Power Sources*, 195(24): 7983–7990, 2010. doi: 10.1016/j.jpowsour.2010.06.048. URL http://dx.doi.org/10.1016/j.jpowsour.2010.06.048.

[118] By Michael Bozlar, Delong He, Jinbo Bai, Yann Chalopin, Natalio Mingo, and Sebastian Volz. Carbon nanotube microarchitectures for enhanced thermal conduction at ultralow mass fraction in polymer composites. *Advanced Materials*, 22:1654–1658, 2010. doi: 10.1002/adma.200901955.

[119] Whi Dong, Ji Young, Dong Geun, Hyung Woo, Suck Won, Hyun Seol, and Soo H Kim. Tailoring the carbon nanostructures grown on the surface of

Ni – Al bimetallic nanoparticles in the gas phase. *Journal of Colloid And Interface Science*, 362(2):261–266, 2011. doi: 10.1016/j.jcis.2011.06.043. URL http://dx.doi.org/10.1016/j.jcis.2011.06.043.

[120] Ji Hoon, Sang Beom, Min Goo, Dae Hyun, Kyung Tae, Hae Moon, Hyung Woo, Jong Man, and Soo Hyung. Flash-ignitable nanoenergetic materials with tunable underwater explosion reactivity : The role of sea urchin-like carbon nanotubes. *Combustion and Flame*, 162(4):1448–1454, 2015. doi: 10.1016/j.combustflame.2014.11.011. URL http://dx.doi.org/10.1016/j.combustflame.2014.11.011.

[121] Fumio Kokai, Akira Koshio, Keita Kobayashi, and Hiroshi Deno. Formation of nanocarbon and composite materials by laser vaporization of graphite and eleven metals. *SPIE*, 6879 68791F-1, 2008. doi: 10.1117/12.761065.

[122] Xuan Hoa Nguyen, Yang Bok Lee, Choong Hyun Lee, and Dae-soon Lim. Synthesis of sea urchin-like particles of carbon nanotubes directly grown on stainless steel cores and their effect on the mechanical properties of polymer composites. *Carbon*, 48(10):2910–2916, 2010. doi: 10.1016/j.carbon.2010.04.027. URL http://dx.doi.org/10.1016/j.carbon.2010.04.027.

[123] Yuanzhe Piao, Kwangjin An, Jaeyun Kim, Taekyung Yu, and Taeghwan Hyeon. Sea urchin shaped carbon nanostructured materials: Carbon nanotubes immobilized on hollow carbon spheres. *Journal of Materials Chemistry A*, 16:2984–2989, 2006. doi: 10.1039/b601684g.

[124] Qiang Ru, Xiong Song, Yudi Mo, Lingyun Guo, and Hou Xianhua. Carbon nanotubes modified for znco2o4 with a novel porous polyhedral structure as anodes for lithium ion batteries with improved performances. *Journal of Alloys and Compounds*, 654, 09 2015. doi: 10.1016/j.jallcom.2015.09.105.

[125] Fengliu Lou, Haitao Zhou, Trung Dung Tran, Marthe Emelie Melandso Buan, Fride Vullum-Bruer, Magnus Ronning, John Charles Walmsley, and De Chen. Coaxial carbon/metal oxide/aligned carbon nanotube arrays as high-performance anodes for lithium ion batteries. *ChemSusChem*, 7(5):1335–1346, 2014. doi: 10.1002/cssc.201300461. URL https://onlinelibrary.wiley.com/doi/abs/10.1002/cssc.201300461.

[126] Yong Li, Daixin Ye, Wen Liu, Bin Shi, Rui Guo, Haijuan Pei, and Jingying Xie. A three-dimensional core-shell nanostructured composite of polypyrrole wrapped mno(2)/reduced graphene oxide/carbon nanotube for high performance lithium ion batteries. *Journal of colloid and interface science*, 493:241—248, May 2017. ISSN 0021-9797. doi: 10.1016/j.jcis.2017.01.008. URL https://doi.org/10.1016/j.jcis.2017.01.008.

[127] Jianguo Ren, Junbing Yang, Ali Abouimrane, Dapeng Wang, and Khalil Amine. Sno2 nanocrystals deposited on multiwalled carbon nanotubes with superior stability as anode material for li-ion batteries. *Lancet*, 196, 10 2011. doi: 10.1016/j.jpowsour.2011.06.036.

[128] Jing Wang, Fang Fang, Tao Yuan, Junhe Yang, Liang Chen, Chi Yao, Shiyou Zheng, and Dalin Sun. Three-dimensional graphene/single-walled carbon nanotube aerogel anchored with sno2 nanoparticles for high performance lithium storage. *ACS Applied Materials & Interfaces*, 9(4):3544–3553, 2017. doi: 10.1021/acsami.6b10807. URL https://doi.org/10.1021/acsami.6b10807. PMID: 28060478.

[129] Hilal Köse, Şeyma Karaal, Ali Osman Aydın, and Hatem Akbulut. A facile synthesis of zinc oxide/multiwalled carbon nanotube nanocomposite lithium ion battery anodes by sol–gel method. *Journal of Power Sources*, 295:235 – 245, 2015. ISSN 0378-7753. doi: https://doi.org/10.1016/j.jpowsour.2015.06.135. URL http://www.sciencedirect.com/science/article/pii/S0378775315300227.

[130] Jian Wu, Wen-Jin Yin, Wei-Wei Liu, Pan Guo, Guobiao Liu, Xicuan Liu, Dongsheng Geng, Woon-Ming Lau, Hao Liu, and Li-Min Liu. High performance nio nanosheets anchored on three-dimensional nitrogen-doped carbon nanotubes as a binder-free anode for lithium ion batteries. *J. Mater. Chem. A*, 4:10940–10947, 2016. doi: 10.1039/C6TA03137D. URL http://dx.doi.org/10.1039/C6TA03137D.

[131] Shuoyu Li, Yuyi Liu, Peisheng Guo, and Chengxin Wang. Self-climbed amorphous carbon nanotubes filled with transition metal oxide nanoparticles for large rate and long lifespan anode materials in lithium ion batteries. *ACS Applied Materials & Interfaces*, 9(32):26818–26825, 2017. doi: 10.1021/acsami.7b06394. URL https://doi.org/10.1021/acsami.7b06394. PMID: 28745487.

[132] Lingyan Wang, Linhai Zhuo, Haiyang Cheng, Chao Zhang, and Fengyu Zhao. Porous carbon nanotubes decorated with nanosized cobalt ferrite as anode materials for high-performance lithium-ion batteries. *Journal of Power Sources*, 283:289 – 299, 2015. ISSN 0378-7753. doi: https://doi.org/10.1016/j.jpowsour.2015.02.138. URL http://www.sciencedirect.com/science/article/pii/S0378775315003845.

[133] Alessandro Palmieri, Raana Kashfi-Sadabad, Sajad Yazdani, Michael Pettes, and William E. Mustain. High performance bi-metallic manganese cobalt oxide/carbon nanotube li-ion battery anodes. *Electrochimica Acta*, 213:620 – 625, 2016. ISSN 0013-4686. doi: https://doi.org/10.1016/j.electacta.2016.07.147. URL http://www.sciencedirect.com/science/article/pii/S0013468616316656.

[134] Wei Yao, Jianguang Xu, Jia Wang, Juhua Luo, Qingle Shi, and Qi Zhang. Chemically integrated multiwalled carbon nanotubes/zinc manganate nanocrystals as ultralong-life anode materials for lithium-ion batteries. *ACS Sustainable Chemistry & Engineering*, 3(9):2170–2177, 2015. doi: 10.1021/acssuschemeng.5b00434. URL https://doi.org/10.1021/acssuschemeng.5b00434.

[135] Eun Ju Bae, Yo-Sep Min, Donghun Kang, Ju-Hye Ko, and Wanjun Park. Low-temperature growth of single-walled carbon nanotubes by plasma enhanced chemical vapor deposition. *Chemistry of Materials*, 17:5141–5145, oct 2005. doi: 10.1021/cm050889o. URL http://stacks.iop.org/1347-4065/44/i=4R/a=1581.

[136] Tomohiro Nozaki, Takuya Karatsu, Shinpei Yoshida, and Ken Okazaki. Parametric study for selective growth of single-walled carbon nanotubes in plasma enhanced chemical vapor deposition. *Japanese Journal of Applied Physics*, 50:1–6, 2011. doi: 10.1143/JJAP.50.01AF03.

[137] Alexander Malesevic, Sorin Vizireanu, Raymond Kemps, Annick Vanhulsel, Chris Van Haesendonck, and Gheorghe Dinescu. Combined growth of carbon nanotubes and carbon nanowalls by plasma-enhanced chemical vapor deposition. *Carbon*, 45:2932–2937, dec 2007. doi: 10.1016/j.carbon.2007.10.004. URL http://www.sciencedirect.com/science/article/pii/S000862230700509X.

[138] Cheng-Hui Weng, Chao-Shun Yang, Hsuan Lin, Chuen-Horng Tsai, and Keh-Chyang Leou. Low temperature synthesis of single-walled carbon nanotubes in an inductively coupled plasma Chemical Vapor Deposition System. *Journal of Nanoscience and Nanotechnology*, 8(5):2526–2533, may 2008. ISSN 15334880. doi: 10.1166/jnn.2008.535. URL http://www.scopus.com/inward/record.url?eid=2-s2.0-45849146993{&}partnerID=tZOtx3y1.

[139] Keun Su Kim, Christopher T. Kingston, Dean Ruth, Michael Barnes, and Benoit Simard. Synthesis of high quality single-walled carbon nanotubes with purity enhancement and diameter control by liquid precursor Ar-H2 plasma spraying. *Chemical Engineering Journal*, 250:331–341, 2014. doi: 10.1016/j.cej.2014.03.117. URL http://linkinghub.elsevier.com/retrieve/pii/S1385894714004173.

[140] Shinil Choi, Junseok Nam, Sookseok Choi, Chanmin Lee, Jongin Kim, and Sang Hee Hong. Synthesis of carbon nanotubes by decomposition of hydrocarbon using an arc-jet plasma. *2004 NSTI Nanotechnology Conference and Trade Show - NSTI Nanotech 2004*, 3:221–224, 2004. URL http://www.scopus.com/inward/record.url?eid=2-s2.0-6344237212{&}partnerID=tZOtx3y1.

[141] Joeoong Hahn, Soo Bong Heo, and Jung Sang Suh. Catalyst free synthesis of high-purity carbon nanotubes by thermal plasma jet. *Carbon*, 43(12):2618–2641, oct 2005. doi: 10.1016/j.carbon.2005.05.013. URL http://www.scopus.com/inward/record.url?eid=2-s2.0-23144459764{&}partnerID=tZOtx3y1.

[142] Abraham J. Fetterman, Yevgeny Raitses, and Michael Keidar. Enhanced ablation of small anodes in a carbon nanotube arc plasma. *Carbon*, 46(10):1322–1326, 2008. doi: 10.1016/j.carbon.2008.05.018.

[143] S A Esfarjani, Seth Dworkin, Javad Mostaghimi, Benoit Simard, Keun Su Kim, Gervais Soucy, and Ali Shahverdi. CFD simulation of single-walled carbon nanotube growth in an RF induction thermal plasma process. Number June, pages 1–12, 2011. ISBN 978-1-62410-147-2. doi: doi:10.2514/6.2011-3600. URL http://dx.doi.org/10.2514/6.2011-3600.

[144] S A Esfarjani, S B Dworkin, J Mostaghimi, K S Kim, C T Kingston, B Simard, and G Soucy. Detailed numerical simulation of single-walled carbon nanotube synthesis in a radio-frequency induction thermal plasma system. *Journal of Physics: Conference Series*, 406:1–10, 2012. doi: 10.1088/1742-6596/406/1/012011. URL http://stacks.iop.org/1742-6596/406/i=1/a=012011?key=crossref.651ce94590354edafd198ba0896cb991.

[145] Ali Shahverdi, Keun Su Kim, Yasaman Alinejad, and Gervais Soucy. Thermogravimetric analysis of single-walled carbon nanotubes synthesized by induction thermal plasma. *Journal of Nanoparticle Research*, 110(2):1079–1085, 2012. doi: 10.1007/s10973-011-2114-4.

[146] Ali Shahverdi, Keun Su Kim, Yasaman Alinejad, and Gervais Soucy. In situ purity enhancement/surface modification of single-walled carbon nanotubes synthesized by induction thermal plasma. *Journal of Nanoparticle Research*, 14(2):1–10, 2012. doi: 10.1007/s11051-011-0660-0.

[147] Y Alinejad, A Shahverdi, N Faucheux, and G Soucy. Synthesis of single-walled carbon nanotubes using induction thermal plasma technology with different catalysts: Thermodynamic and experimental studies. *Journal of Physics: Conference Series*, 406:1–10, 2012. doi: 10.1088/1742-6596/406/1/

012019. URL http://stacks.iop.org/1742-6596/406/i=1/a=012019?key=crossref.907b8738033d4e19c06aca907bc60a6a.

[148] Alireza Hekmat-Ardakan, Yasaman Alinejad, Ali Shahverdi, and Gervais Soucy. Experimental and thermochemical evaluation of induction thermal plasma grown single-walled carbon nanotube synthesized by commercial carbon blacks with different sulfur contents. *Thermochimica Acta*, 565:211–220, 2013. doi: 10.1016/j.tca.2013.04.035. URL http://dx.doi.org/10.1016/j.tca.2013.04.035.

[149] Keun Su Kim, Christopher T. Kingston, Amy Hrdina, Michael B. Jakubinek, Jingwen Guan, Mark Plunkett, and Benoit Simard. Hydrogen-catalyzed, pilot-scale production of small-diameter boron nitride nanotubes and their macroscopic assemblies. *ACS Nano*, 8(6):6211–6220, 2014. doi: 10.1021/nn501661p.

[150] O. Smiljanic, B. L. Stansfield, J. P. Dodelet, A. Serventi, and S. Désilets. Gas-phase synthesis of SWNT by an atmospheric pressure plasma jet. *Chemical Physics Letters*, 356:189–193, 2002. doi: 10.1016/S0009-2614(02)00132-X.

[151] Lenka Zajíčková, Petr Synek, Ondřej Jašek, Marek Eliáš, Bohumil David, Jiří Buršík, Naděžda Pizúrová, Renáta Hanzlíková, and Lukáš Lazar. Synthesis of carbon nanotubes and iron oxide nanoparticles in MW plasma torch with Fe(CO)5 in gas feed. *Applied Surface Science*, 255(10):5421–5424, 2009. doi: 10.1016/j.apsusc.2008.09.003.

[152] Krzysztof J. Jankowski and Edward Reszke. *Microwave induced plasma analytical spectrometry*. RSC Analytical Spectroscopy Series. The Royal Society of Chemistry, 2011. ISBN 978-1-84973-052-5. doi: 10.1039/9781849732147. URL http://dx.doi.org/10.1039/9781849732147.

[153] Michael A. Lieberman and Allan J. Lichtenberg. *Principles of Plasma Discharges and Materials Processing*. Wiley, 2005.

[154] Amanda Loveless and Allen Garner. Scaling laws for ac gas breakdown and implications for universality. *Physics of Plasmas*, 24:104501, 10 2017. doi: 10.1063/1.4998245.

[155] Amanda Loveless, Guodong Meng, Qi Ying, Feihong Wu, Kejing Wang, Y.H. Cheng, and Allen Garner. The transition to paschen's law for microscale gas breakdown at subatmospheric pressure. *Scientific Reports*, 9:5669, 04 2019. doi: 10.1038/s41598-019-42111-2.

[156] Haixue Yan, Chengen Li, Jiaguang Zhou, Weimin Zhu, Lianxin He, and Yuxin Song. A-site (MCe) substitution effects on the structures and properties of CaBi4Ti4O15 ceramics. *Japanese Journal of Applied Physics, Part 1: Regular Papers and Short Notes and Review Papers*, 39(11):6339–6342, 2000. ISSN 00214922. doi: 10.1143/JJAP.39.6339.

[157] M. Manikandan, K. Saravana Kumar, N. Aparnadevi, and C. Venkateswaran. Hopkinson effect and temperature-dependent dielectric properties of single domain SrFe12O19 particles. *Physica Status Solidi (A) Applications and Materials Science*, 212(10):2179–2185, 2015. ISSN 18626319. doi: 10.1002/pssa.201532229.

[158] Muhammad Usman, Cheng Hua Lee, Dung Shing Hung, Shang Fan Lee, Chih Chieh Wang, Tzuoo Tsair Luo, Li Zhao, Mau Kuen Wu, and Kuang Lieh

Lu. Intrinsic low dielectric behaviour of a highly thermally stable Sr-based metal-organic framework for interlayer dielectric materials. *Journal of Materials Chemistry C*, 2(19):3762–3768, 2014. ISSN 20507526. doi: 10.1039/c4tc00149d.

[159] GoodFellow. Ceramic - Properties (Datasheet), 2019. URL http://www.goodfellow.com/pdf/TAB601A.pdf.

[160] GoodFellow. Duratec machinable ceramic for engineering applications (Datasheet).

[161] Corning. Macor machinable glass ceramic for industrial applications (Datasheet), 2012.

[162] Goodfellow. Shapal Hi-M Soft Machinable Aluminium Nitride Ceramic (Datasheet). URL http://www.goodfellow-ceramics.com/corporate/pdf/shapal-hi-m-soft.pdf.

[163] Technical Products. Boron Nitride Grade AX05 Material Specifications.

[164] Guohua Wei, Bharat Bhushan, and Peter M. Torgerson. Nanomechanical characterization of human hair using nanoindentation and SEM. *Ultramicroscopy*, 105(1-4):248–266, 2005. ISSN 03043991. doi: 10.1016/j.ultramic.2005.06.033.

[165] R. M. Nedderman. Granular materials, discharge through orifices. *Atomization and Sprays*, g, 01 2006. doi: 10.1615/AtoZ.g.GRAMATDISTHRORI.

[166] W. A. Beverloo, H. A. Leniger, and J. Van de Velde. The flow of granular material through orifices. *Journal of Chemical Engineering Science*, 15:260–296, 1961.

[167] R. M. Nedderman and C. Laohakul. The thickness of the shear zone of flowing granular media. *Powder Technology*, 25:91–100, 1980.

[168] Usama M Attia, Andrew Fones, Ross Trepleton, Hugh Hamilton, Susan Davies, and David Wimpenny. HIPing of Pd-doped titanium components : A study of mechanical and corrosion properties properties. In *11th International Conference of Hot Isostatic Pressing*, number January, 2014.

[169] A Santomaso, P Lazzaro, and P Canu. Powder flowability and density ratios: The impact of granules packing. *Chemical Engineering Science*, 58(13):2857–2874, 2003. doi: 10.1016/S0009.

[170] Stefan Pfeiffer, Kevin Florio, Malgorzata Makowska, Dario Ferreira Sanchez, Helena Van Swygenhoven, Christos G. Aneziris, Konrad Wegener, and Thomas Graule. Iron oxide doped spray dried aluminum oxide granules for selective laser sintering and melting of ceramic parts. *Advanced Engineering Materials*, 21(6):1–14, 2019. ISSN 15272648. doi: 10.1002/adem.201801351.

[171] A. Kramida, Yu. Ralchenko, J. Reader, and and NIST ASD Team. NIST Atomic Spectra Database (ver. 5.6.1), [Online]. Available: `https://physics.nist.gov/asd` [2019, August 9]. National Institute of Standards and Technology, Gaithersburg, MD., 2018.

[172] Brian Mackenzie Graves, Charles Robert Koch, and Jason Scott Olfert. Morphology and volatility of particulate matter emitted from a gasoline direct injection engine fuelled on gasoline and ethanol blends. *Journal of Aerosol Science*, 105(February 2016):166–178, 2017. ISSN 0021-8502. doi: 10.1016/j.jaerosci.2016.10.013. URL http://dx.doi.org/10.1016/j.jaerosci.2016.10.013.

[173] Xin Pei Lu and Mounir Laroussi. Electron density and temperature measurement of an atmospheric pressure plasma by millimeter wave interferometer. *Applied Physics Letters*, 92(5):1–2, 2008. doi: 10.1063/1.2840194.

[174] Hans R Griem. Validity of local thermal equilibrium in plasma spectroscopy. *Physical Review*, 131(3):1170–1176, 1963.

[175] Takashi Fujimoto and R W P McWhirter. Validity criteria for local thermodynamic equilibrium in plasma spectroscopy. *Physical Review A*, 42(11): 6588–6592, 1990.

[176] M. Numano. Criteria for local thermodynamic equilibrium distributions of populations of excited atoms in a plasma. *Journal of Quantitative Spectroscopy and Radiative Transfer*, 43(4):311–317, 1990. ISSN 0022-4073. doi: 10.1016/0022-4073(90)90020-7.

[177] Qingtang Zhang, Zuolong Yu, Ping Du, and Ce Su. Carbon nanomaterials used as conductive additives in lithium ion batteries. *Recent Patents on Nanotechnology*, 4(2):100–110, 2010. ISSN 1872-2105/2212-4020. doi: 10.2174/187221010791208803. URL http://www.eurekaselect.com/node/93890/article.

[178] Srinivas Vemury and Sotiris E. Pratsinis. Self-preserving size distributions of agglomerates. *Journal of Aerosol Science*, 26(2):175 – 185, 1995. ISSN 0021-8502. doi: https://doi.org/10.1016/0021-8502(94)00103-6. URL http://www.sciencedirect.com/science/article/pii/0021850294001036.

[179] M.L. Eggersdorfer, A.J. Gröhn, C.M. Sorensen, P.H. McMurry, and Sotiris Pratsinis. Mass-mobility characterization of flame-made zro2 aerosols: Primary particle diameter & extent of aggregation. *Journal of colloid and interface science*, 387:12–23, 08 2012. doi: 10.1016/j.jcis.2012.07.078.

[180] Georgios A. Kelesidis, Florian M. Furrer, Karsten Wegner, and Sotiris E. Pratsinis. Impact of humidity on silica nanoparticle agglomerate morphology and size distribution. *Langmuir*, 34(29):8532–8541, 2018. doi: 10.1021/acs.langmuir.8b00576. URL https://doi.org/10.1021/acs.langmuir.8b00576. PMID: 29940739.

[181] C.R. Svensson, L. Ludvigsson, B.O. Meuller, M.L. Eggersdorfer, K. Deppert, M. Bohgard, J.H. Pagels, M.E. Messing, and J. Rissler. Characteristics of airborne gold aggregates generated by spark discharge and high temperature evaporation furnace: Mass–mobility relationship and surface area. *Journal of Aerosol Science*, 87:38 – 52, 2015. ISSN 0021-8502. doi: https://doi.org/10.1016/j.jaerosci.2015.05.004. URL http://www.sciencedirect.com/science/article/pii/S0021850215000713.

[182] Matthias Stein, Dennis Kiesler, and Frank Einar Kruis. Adjustment and online determination of primary particle size in transferred arc synthesis of copper nanoparticles. *Aerosol Science and Technology*, 47(11):1276–1284, 2013. doi: 10.1080/02786826.2013.835484. URL https://doi.org/10.1080/02786826.2013.835484.

[183] E. Peled and S. Menkin. Review—sei: Past, present and future. *Journal of The Electrochemical Society*, 164(7):A1703–A1719, 2017. doi: 10.1149/2.1441707jes. URL http://jes.ecsdl.org/content/164/7/A1703.abstract.

[184] Oxana V. Kharissova and Boris I. Kharisov. Variations of interlayer spacing in carbon nanotubes. *RSC Adv.*, 4:30807–30815, 2014. doi: 10.1039/C4RA04201H. URL http://dx.doi.org/10.1039/C4RA04201H.

[185] M.S. Dresselhaus, G. Dresselhaus, R. Saito, and A. Jorio. Raman spectroscopy of carbon nanotubes. *Physics Reports*, 409(2):47 – 99, 2005. ISSN 0370-1573. doi: https://doi.org/10.1016/j.physrep.2004.10.006. URL http://www.sciencedirect.com/science/article/pii/S0370157304004570.

[186] Christian Thomsen and Stephanie Reich. Raman scattering in carbon nanotubes. *Light Scattering in Solid IX*, 108:115 – 208, 2007. doi: 10.1007/978-3-540-34436-0_3.

[187] Hans Mathieu and Dieter Landolt. An investigation of thin oxide films thermally grown in situ on fe24cr and fe24cr11mo by auger electron spectroscopy and x-ray photoelectron spectroscopy. *Corrosion Science*, 26:547–559, 12 1986. doi: 10.1016/0010-938X(86)90022-3.

[188] A. P. Grosvenor, B. A. Kobe, M. C. Biesinger, and N. S. McIntyre. Investigation of multiplet splitting of fe 2p xps spectra and bonding in iron compounds. *Surface and Interface Analysis*, 36(12):1564–1574, 2004. doi: 10.1002/sia.1984. URL https://onlinelibrary.wiley.com/doi/abs/10.1002/sia.1984.

[189] D Wilson and M.A. Langell. Xps analysis of oleylamine/oleic acid capped fe3o4 nanoparticles as a function of temperature. *Applied Surface Science*, 303:6–13, 06 2014. doi: 10.1016/j.apsusc.2014.02.006.

[190] 25 - iron, ruthenium and osmium. In N.N. Greenwood and A. Earnshaw, editors, *Chemistry of the Elements (Second Edition)*, pages 1070 – 1112. Butterworth-Heinemann, Oxford, second edition edition, 1997. ISBN 978-0-7506-3365-9. doi: https://doi.org/10.1016/B978-0-7506-3365-9.50031-6. URL http://www.sciencedirect.com/science/article/pii/B9780750633659500316.

[191] Jean-Charles Dupin, Danielle Gonbeau, Philippe Vinatier, and Alain Levasseur. Systematic xps studies of metal oxides, hydroxides and peroxides. *Phys. Chem. Chem. Phys.*, 2:1319–1324, 2000. doi: 10.1039/A908800H. URL http://dx.doi.org/10.1039/A908800H.

[192] Toru Yamashita and Peter Hayes. Analysis of xps spectra of fe2+ and fe3+ ions in oxide materials. *Applied Surface Science*, 254(8):2441 – 2449, 2008. ISSN 0169-4332. doi: https://doi.org/10.1016/j.apsusc.2007.09.063. URL http://www.sciencedirect.com/science/article/pii/S0169433207013748.

[193] Tuguhiro TAGO, Noriyuki KATAOKA, Hiromi TANAKA, Kentaro KINOSHITA, and Satoru KISHIDA. Xps study from a clean surface of al2o3 single crystals. *Procedia Engineering*, 216:175 – 181, 2017. ISSN 1877-7058. doi: https://doi.org/10.1016/j.proeng.2018.02.081. URL http://www.sciencedirect.com/science/article/pii/S187770581733206X. ICMAT 2017 Symposium (M to Z).

[194] J. Chen, L. Xu, W. Li, and X. Gou. α-fe2o3 nanotubes in gas sensor and lithium-ion battery applications. *Advanced Materials*, 17(5):582–586, 2005. doi: 10.1002/adma.200401101. URL https://onlinelibrary.wiley.com/doi/abs/10.1002/adma.200401101.

[195] Yanna NuLi, Peng Zhang, Zaiping Guo, and Huakun Liu. Shape evolution of α-fe2o3 and its size-dependent electrochemical properties for lithium-ion batteries. *Journal of The Electrochemical Society*, 155(3):A196–A200, 2008. doi: 10.1149/1.2826278. URL http://jes.ecsdl.org/content/155/3/A196.abstract.

[196] Hyun Sik Kim, Yuanzhe Piao, Soon Hyung Kang, Taeghwan Hyeon, and Yung-Eun Sung. Uniform hematite nanocapsules based on an anode material for lithium ion batteries. *Electrochemistry Communications - ELECTROCHEM COMMUN*, 12:382–385, 03 2010. doi: 10.1016/j.elecom.2009.12.040.

[197] Bao Wang, Jun Song Chen, Hao Bin Wu, Zhiyu Wang, and Xiong Wen (David) Lou. Quasiemulsion-templated formation of α-fe2o3 hollow spheres with enhanced lithium storage properties. *Journal of the American Chemical Society*, 133(43):17146–17148, 2011. doi: 10.1021/ja208346s. URL https://doi.org/10.1021/ja208346s. PMID: 21977903.

[198] X. Rodiles, V. Reguero, M. Vila, B. Alemán, L. Arévalo, F. Fresno, V. A.de la Peña O'Shea, and J. J. Vilatela. Carbon nanotube synthesis and spinning as macroscopic fibers assisted by the ceramic reactor tube. *Scientific Reports*, 9 (1):2–11, 2019. ISSN 20452322. doi: 10.1038/s41598-019-45638-6.

[199] James R. Fincke, Raymond P. Anderson, Timothy A. Hyde, and Brent A. Detering. Plasma pyrolysis of methane to hydrogen and carbon black. *Industrial and Engineering Chemistry Research*, 41(6):1425–1435, 2002. ISSN 08885885. doi: 10.1021/ie010722e.

[200] V. Thirumal, A. Pandurangan, R. Jayavel, S.R. Krishnamoorthi, and R. Ilangovan. Synthesis of nitrogen doped coiled double walled carbon nanotubes by chemical vapor deposition method for supercapacitor applications. *Current Applied Physics*, 16(8):816 – 825, 2016. ISSN 1567-1739. doi: https://doi.org/10.1016/j.cap.2016.04.018. URL http://www.sciencedirect.com/science/article/pii/S1567173916300918.

[201] Edward N. Nxumalo, Vincent O. Nyamori, and Neil J. Coville. Cvd synthesis of nitrogen doped carbon nanotubes using ferrocene/aniline mixtures. *Journal of Organometallic Chemistry*, 693(17):2942 – 2948, 2008. ISSN 0022-328X. doi: https://doi.org/10.1016/j.jorganchem.2008.06.015. URL http://www.sciencedirect.com/science/article/pii/S0022328X0800363X.

[202] Zaiyong Mo, Shijun Liao, Yuying Zheng, and Zhiyong Fu. Preparation of nitrogen-doped carbon nanotube arrays and their catalysis towards cathodic oxygen reduction in acidic and alkaline media. *Carbon*, 50(7):2620 – 2627, 2012. ISSN 0008-6223. doi: https://doi.org/10.1016/j.carbon.2012.02.021. URL http://www.sciencedirect.com/science/article/pii/S000862231200142X.

[203] Tiva Sharifi, Florian Nitze, Hamid Reza Barzegar, Cheuk-Wai Tai, Marta Mazurkiewicz, Artur Malolepszy, Leszek Stobinski, and Thomas Wågberg. Nitrogen doped multi walled carbon nanotubes produced by cvd-correlating xps and raman spectroscopy for the study of nitrogen inclusion. *Carbon*, 50 (10):3535 – 3541, 2012. ISSN 0008-6223. doi: https://doi.org/10.1016/j.

carbon.2012.03.022. URL http://www.sciencedirect.com/science/article/pii/S0008622312002709.

[204] X.Y. Tao, X.B. Zhang, F.Y. Sun, J.P. Cheng, F. Liu, and Z.Q. Luo. Large-scale cvd synthesis of nitrogen-doped multi-walled carbon nanotubes with controllable nitrogen content on a coxmg1xmoo4 catalyst. *Diamond and Related Materials*, 16(3):425 – 430, 2007. ISSN 0925-9635. doi: https://doi.org/10.1016/j.diamond.2006.08.019. URL http://www.sciencedirect.com/science/article/pii/S0925963506002834.

[205] S. H. Kim, G. W. Mulholland, and M. R. Zachariah. Understanding ion-mobility and transport properties of aerosol nanowires. *Journal of Aerosol Science*, 38 (8):823–842, 2007. ISSN 00218502. doi: 10.1016/j.jaerosci.2007.06.003.

[206] Michal Fulem, Květoslav Růžička, Ctirad Červinka, Marisa A.A. Rocha, Luís M.N.B.F. Santos, and Robert F. Berg. Recommended vapor pressure and thermophysical data for ferrocene. *Journal of Chemical Thermodynamics*, 57:530–540, 2013. ISSN 00219614. doi: 10.1016/j.jct.2012.07.023.

[207] Francisco M. Juárez-Guerra, José Luis Rivera, Abel Zúñiga-Moreno, Luis A. Galicia-Luna, José Luis Rico, and Javier Lara. Molecular modeling of thiophene in the vapor-liquid equilibrium. *Separation Science and Technology*, 41(2): 261–281, 2006. ISSN 01496395. doi: 10.1080/01496390500446129.

[208] Amelia Barreiro, Silke Hampel, Mark H. Rümmeli, Christian Kramberger, Alexander Grüneis, Kati Biedermann, Albrecht Leonhardt, Thomas Gemming, Bernd Büchner, Adrian Bachtold, and Thomas Pichler. Thermal decomposition of ferrocene as a method for production of single-walled carbon nanotubes without additional carbon sources. *The Journal of Physical Chemistry B*, 110 (42):20973–20977, 2006. doi: 10.1021/jp0636571. URL https://doi.org/10.1021/jp0636571. PMID: 17048915.

[209] Kapil Moothi, Clarence S. Yah, Geoffrey S. Simate, Selby Maphutha, and Sunny Iyuke. Synthesis of large carbon nanotubes from ferrocene: The chemical vapour deposition technique. *Trends in Applied Sciences Research*, 6:1270–1279, 06 2011. doi: 10.3923/tasr.2011.1270.1279.

[210] Beat Meyer. Elemental sulfur. *Chemical Reviews*, 76(3):367–388, 1976. doi: 10.1021/cr60301a003. URL https://doi.org/10.1021/cr60301a003.

[211] Adam M. Boies, Pingyan Lei, Steven Calder, Weon Gyu Shin, and Steven L. Girshick. Hot-wire synthesis of gold nanoparticles. *Aerosol Science and Technology*, 45(5):654–663, 2011. ISSN 02786826. doi: 10.1080/02786826.2010.551145.

[212] P.G. Gormly and M. Kennedy. Diffusion from a Stream Flowing through a Cylindrical Tube. *Proceedings of the Royal Irish Academy. Section A: Mathematical and Physical Sciences*, 52:163–169, 1948. ISSN 00358975. URL http://www.jstor.org/stable/20488498.

[213] J. S. Olfert and Nick Collings. New method for particle mass classification - the couette centrifugal particle mass analyzer. *Journal of Aerosol Science - J AEROSOL SCI*, 36:1338–1352, 2005.

Appendix A

Details of Analytical Techniques and Instruments

A.1 Electron Microscopy

Both transmission electron microscopy (TEM) and scanning electron microscopy (SEM) were used to analyse the morphology of the CNT materials presented here. For TEM, the samples were prepared in dry conditions by spreading the samples as a powder onto 400 mesh copper grids with a holey carbon film (Agar Scientific). High-resolution TEM (HRTEM) images were obtained using a Tecnai F20 system at 200 kV with a high brightness field emission gun (FEG). TEM analysis was performed by Herme Baldovi. SEM samples were prepared on single crystal silicon substrates. Particles were either deposited with a thermophoretic sampler or by spreading filter-collected dry powder over the substrate, applying a drop of ethanol and air drying. SEM images were obtained using a Leo Variable pressure SEM with an accelerating voltage of 2.49 kV and a working distance of approximately 5 mm.

A.2 Particle Size Distribution

The size of nanoparticles is commonly quantified using a scanning mobility particle spectrometer (SMPS) which is comprised of a differential mobility analyzer (DMA) and condensation particle counter (CPC). Particles are first given an electric charge using a radioactive or x-ray charger and are then classified in the DMA by electrical mobility or more intuitively, their charge-to-drag ratio. Particles are passed through the annular region between two concentric cylinders while a negative voltage is applied to the inner cylinder. Positively charged particles are attracted to the inner cylinder but the rate at which they migrate towards this cylinder is limited by their aerodynamic

drag. Particles with the correct charge-to-drag ratio reach the inner cylinder exactly at its end and are "classified".

As the DMA sweeps through various electrical mobilities, the CPC counts the number of particles at each mobility setting. Mobility is then converted to a particle size (mobility-equivalent diameter) and a number-based particle size distribution can be created. For the majority of this work, a 3081 series DMA (TSI Inc.) and 3022A series CPC (TSI Inc.) were used. For samples containing small particles, the CPC was set to "high flow" mode (1.5 LPM) and the DMA sheath flow was 15 LPM, resulting in a resolution of 10 (i.e. the full width half maximum of the transfer function of the DMA was one tenth of its set point). At this flow condition, the size range of the SMPS is approximately 6 nm to 220 nm. If larger particles are to be measured, the CPC can be set to "low flow" mode (0.3 LPM) and the DMA sheath to 3 LPM, preserving the resolution of 10. This results in a size range of approximately 14 nm to 680 nm. In most cases a dilution ratio of 11 was used, although all presented results have been corrected for this ratio and represent the true volumetric number concentrations. Data sets are then fit with either a lognormal distribution or the summation of two lognormal distributions, and these can be expressed with the geometric mean, geometric standard deviation, and total particle concentration.

A.3 Particle Mass Measurements

Particle mass can be measured with a Centrifugal Particle Mass Analyzer (CPMA), which classifies particles by mass-to-charge ratio [213]. Similar to an SMPS, the CPMA can be stepped through various mass setpoints while a CPC measures the concentration at each mass. A number-based mass distribution can then be generated. Furthermore, if particles of a specific mobility equivalent diameter are preselected, a CPMA scan can give the mass of these particles. Performing this measurement at several sizes throughout the total particle distribution can allow the mass mobility relation to be created and the mass-mobility exponent can be extracted.

A.4 Raman Spectrometry

Raman spectra were collected on a Horiba Explora Plus using a 638 or 532 nm laser. While some radial breathing modes were observed, other single-walled CNT chiralities may also have been synthesized which are not resonant with a given wavelength (i.e. points that exist at a different y-axis position in Figure 5.4b in Chapter 5). In some cases Raman signals could only be recorded with one of the wavelengths because the other laser induced strong reflections off the material resulting in a broad background spectrum and it was not possible to resolve the CNT signal.

A.5 Electrochemical Tests of Half Coin Cells

The electrochemical properties of the compounds were evaluated in 2032 coin cells containing metallic lithium foils as cathodes (half-cells). For the anodes, a slurry was prepared containing 90 wt% active material composite and 10 wt% polyvinylidene difluoride (PVDF) binder in N-methyl-2-pyrrolidone (NMP). Since the active material already contained highly conductive CNTs, it was not necessary to introduce any other conductive additives to the slurry. The slurry was cast onto etched copper. The electrodes were dried first in air and then under vacuum at 60°C for 12 hours before being cut to size and weighed in an argon-filled glovebox. The typical loading was 0.5 mg cm^{-2}. 1.0 M $LiPF_6$ EC/EMC = 50/50 (v/v) electrolyte and Celgard separators were used in the coin cells. Galvanostatic cycling experiments at room temperature were carried out with Biologic VMP3 and Lanhe potentiostats/galvanostats. The cells were cycled in between 0.05-3 V and C rates from 0.1 to 14 C. Half cell construction and cycling were performed by Simon Engelke. Electrochemical impedance spectroscopy (1000 to 0.05 Hz, 5 mV amplitude) was conducted using Biologic VMP3 and was performed by Changshin Jo.

Appendix B

Additional CNT-Metal Oxide Characterization

B.1 Additional Material Characterization

Additional microscopy images of the metal oxide-CNT material are shown in Figure B.1. The TEM image in Figure B.1a displays a portion of an agglomerate as well as catalyst primary particles trapped within CNTs and separated from the host agglomerate. Figure B.1b and c show SEM and TEM images respectively of agglomerate particles after CNT growth. The histogram in Figure B.1d displays the size distribution of primary particles which are responsible for CNT growth. Note that the likelihood of a particle producing CNTs decreases beyond 3 nm whereas most primary particles produced are larger than this, as seen in Figure 5.3 in Chapter 5. The larger primary particles are instead often coated with graphitic carbon. Finally, Figure B.1e displays the diameter distribution of the CNTs. It is right skewed with a mode at 7 nm, resulting in an average CNT diameter of 7.75 ± 2.74 nm.

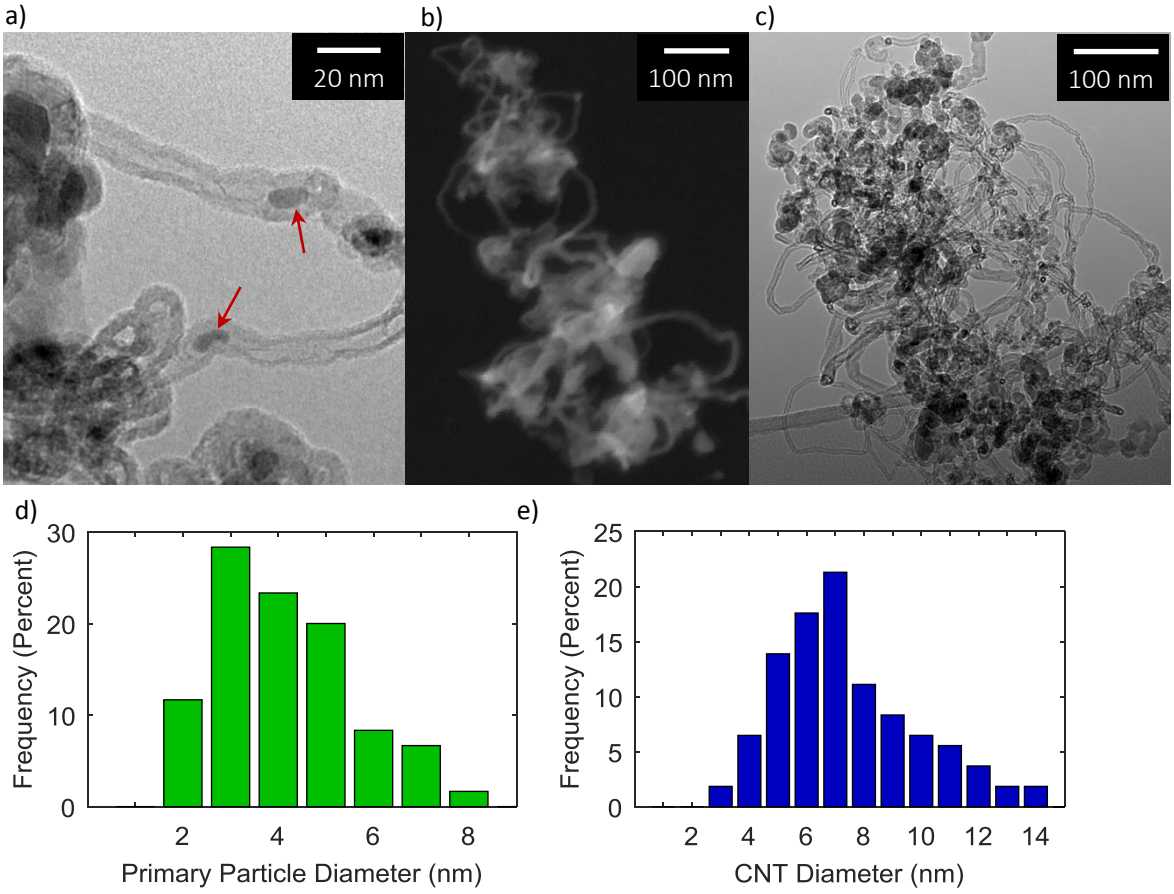

Fig. B.1 Additional images of material morphology including (a) TEM of a subsection of an agglomerate along with primary particles contained within CNTs, (b) SEM of agglomerate, and (c) TEM of large agglomerate. Panel (d) displays the primary particle size distribution of those responsible for CNT growth and (e) contains the distribution of CNT diameters

B.2 Additional Electrochemical Results

CV cycling was performed after the cell had been subjected to two cycles at 0.1 C. The CV data in Figure B.2a is in agreement with what has been reported for iron oxide nanoparticles elsewhere. A reduction peak around 0.75 V in the cathodic sweep (corresponding to Li insertion into Fe_2O_3 and Li_2O formation) can be observed as well as an oxidation peak around 2 V in the anodic sweep (Fe^{3+} to Fe^0). The three cycles have similar profiles, showing good repeatability.

Also shown is the long-term cycling in Figure B.2b. The capacity is relatively steady but does increase somewhat over time. This may be due to inactive material becoming exposed from the repeated volume change during the cycling. This is a nearly unavoidable phenomenon during the initial cycles of a cell. Coulombic efficiency remains near 100% for the entirety of the long term test. Many of the individual data points throughout this test were slightly higher than 100% (though

almost always less than 101%). This is likely simply due to measurement uncertainty. The several initial efficiencies near the beginning that are notably higher than 100% are the result of slightly higher discharge capacities and may be caused by irreversible reactions within the cell. These reactions are exhausted within a couple cycles at which point the cell behaves normally.

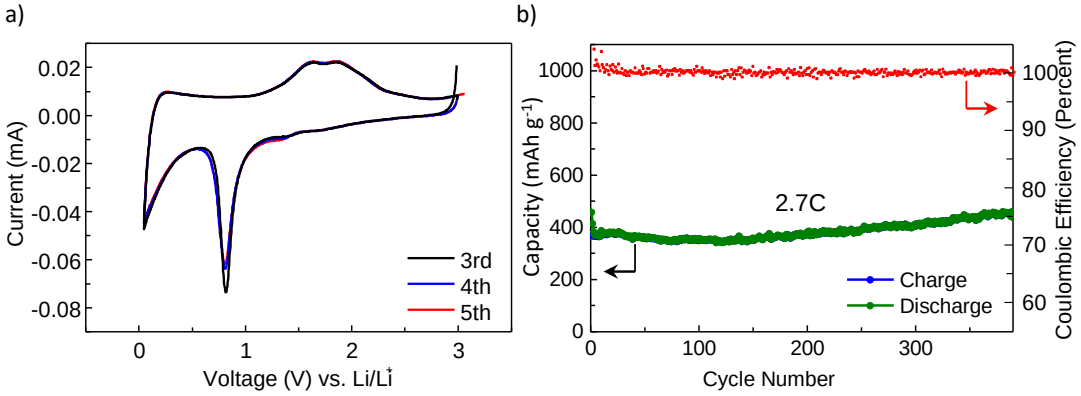

Fig. B.2 (a) cyclic voltammetry after two prior cycles and (b) long-term specific capacities for cycles at 2.7 C

Appendix C

Metal Oxide Thermal Equilibrium Model

To construct a model of the evolution of the metal oxide cores, nucleation of the particles must first be understood. This is important since the nucleating species and temperature will affect the aerosol behaviour. One method to identify this information is by using a Gibbs free energy minimization algorithm to simulate the compounds and phases present at thermal equilibrium for a given temperature. As this simulation predicts the results at thermal equilibrium, it does not produce any information regarding the kinetics of these reactions and phase changes. That is to say that if the species were left to react for an infinite time, their final states can be determined with this method. Of course, the precursor vaporization, nanoparticle nucleation, and subsequent core formation have certain timescales associated with them so there is a chance that the species will not have time to achieve the equilibrium states predicted by the model. However, a thermodynamic equilibrium model is still useful to determine the "direction" of the chemical reactions and phase changes, as well as the approximate temperatures where one can expect major changes to occur. Moreover, much of the synthesis process occurs at high temperature where reaction rates are fast. Gibbs free energy G is defined as:

$$G(T,P) = H(T,P) - TS(T,P). \tag{C.1}$$

Here, H is enthalpy, S is entropy, T is temperature, and P is pressure. In the case of these simulations, pressure is maintained constant at 1 atm and temperature is varied from 500 K to 4000 K. This results in a particular molecular distribution of species at each temperature step within the temperature range and an area plot for each element can be created using temperature and the relative prevalence of each species. The atomic species present and their relative quantities must be specified, and this is determined using mass and volume throughputs of a typical process condition. The

constituent elements present are nitrogen for the carrier gas, iron and aluminum as powders for core formation, and potentially a small amount of oxygen (contaminant from leaks in the system, oxide layer on the powder, or as a trace species in the nitrogen). The plasma (nitrogen) typically has a gas flow rate of 9 SLPM. Using the ideal gas law at standard conditions, the molar flow rate of nitrogen can be determined:

$$\dot{n}_{N_2} = \frac{n}{V} Q_0 = \frac{P}{RT} Q_0. \tag{C.2}$$

In the above equation, $\dot{n}$ is molar flow rate, n is the number of moles, V is volume, Q_0 is the volumetric flow rate at standard conditions, P is pressure, R is the ideal gas constant, and T is temperature. Using a flow rate of 9 litres per minute at standard conditions (1 atm and 293 K), the throughput of nitrogen is determined to be 0.3744 mol_{N_2} min^{-1}. Regarding metals, powder is introduced into the system at a rate of approximately 30 mg min^{-1} and has a molar ratio of 2 mol_{Fe} : 1 mol_{Al}. This corresponds to a mass ratio of 4.14 g_{Fe} : 1 g_{Al} The individual molar flow rates of iron ($\dot{n}_{Fe}$) and aluminum ($\dot{n}_{Al}$) can be determined:

$$\dot{n}_{Fe} = \frac{\dot{n}_{met} x_{Fe}}{M_{m,Fe}}, \tag{C.3}$$

$$\dot{n}_{Al} = \frac{\dot{n}_{met} x_{Al}}{M_{m,Al}}, \tag{C.4}$$

where $\dot{n}_{met}$ is the total molar throughput of metal, M_m is molar mass, and x is the mass fraction of a particular metal. With the above conditions, the molar throughputs of iron and aluminum are 4.327×10^{-4} mol_{Fe} min^{-1} and 2.163×10^{-4} mol_{Al} min^{-1} respectively. Finally, a flow of oxygen was introduced to account for any contamination or leakage. This was set as 0.5 sccm. Adapting the equation in C.2 for the oxygen flow rate results in $\dot{n}_{O_2} = 2.080 \times 10^{-5}$ mol_{O_2} min^{-1}. Accounting for the fact that there are twice as many moles of oxygen and nitrogen atoms as their diatomic counterparts, the overall molar ratio for these conditions is 18 000 N : 10 Fe : 5 Al : 1 O.

Figure C.1 displays the results of the thermodynamic equilibrium calculations for (a) iron, (b) aluminum, (c) oxygen, and (d) nitrogen. Subscripts indicate solid (s), liquid (L), gas (g), and in the case of iron, the alpha (α, magnetic and non-magnetic), gamma (γ), and delta (δ) phases are shown. In the case of nitrogen, nearly all atoms are contained in the N_2 carrier gas even at equilibrium (>99.9% for all temperatures), so the plot in Figure C.1d displays the distribution of nitrogen atoms outside the N_2 fraction. In other words, the entire population shown here constitutes less than 0.1% of all nitrogen atoms in the system.

Examination of the iron and aluminum plots in Figure C.1a and b respectively reveals that the species that will be first to nucleate will be liquid iron which begins to condense at approximately 2100 K. At 1730 K, aluminum begins to condense as

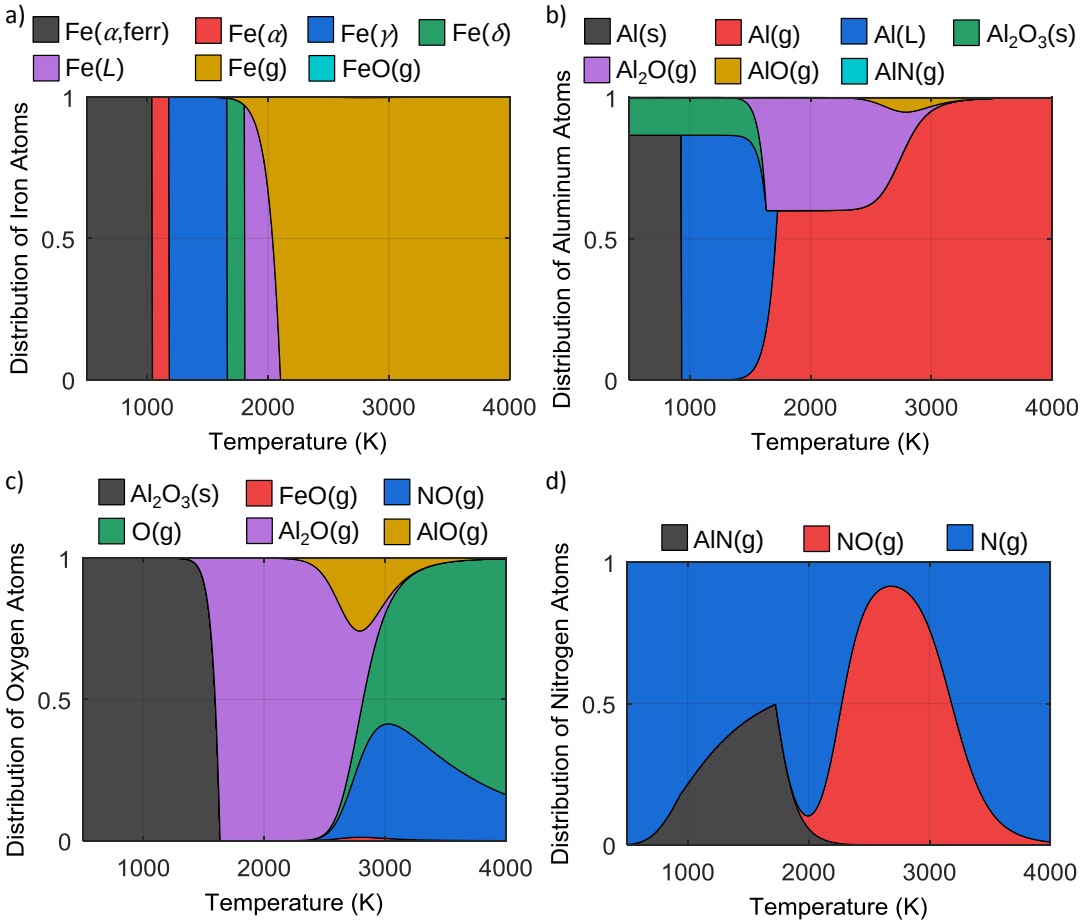

Fig. C.1 Distribution of atoms at thermodynamic equilibrium for (a) iron, (b) aluminum, (c) oxygen, and (d) nitrogen, not including those contained in N_2

reduced liquid metal, followed by solid Al_2O_3 nucleation at approximately 1600 K. Note from Figure C.1c that while a small amount of the oxygen will exist as FeO between 2500 K and 3300 K, the remainder exists in aluminum compounds, NO and O. Therefore, an important conclusion is that with modest oxygen contamination in the process, the iron should still exist as reduced metal at all temperatures and is therefore able to grow CNTs. Secondly, these results indicate that it would be difficult to fully oxidize the iron for optimal energy storage capacity unless all the aluminum has first been oxidized. As such, an ex-situ oxidation step with excess oxygen would be a more effective method of ensuring maximum oxygen content in the material, and indeed this was found to be the case from TGA results presented in section 5.2.3.